NNT :

Thèse de doctorat de l'Université Paris-Saclay et de l'Université de Turin préparée à l'Université Paris-Sud

CEA/Irfu/DPhP

École doctorale n°576

Particules, Hadrons, Énergie, Noyau, Instrumentation, Imagerie, Cosmos et Simulation (PHENIICS)

Spécialité de doctorat: Physique des particules

par

Giulia NEGRO

Search for heavy neutrinos with the CMS experiment and studies for the upgrade of its electromagnetic calorimeter

Thèse présentée et soutenue à l'Orme de Merisiers le 28 septembre 2018

Composition du jury :

M.	Fabrice HUBAUT,	CPPM, Marseille	Rapporteur
Pr.	Daniele DEL RE,	Université de Rome,	Rapporteur
M.	Stephane LAVIGNAC,	CEA-Saclay,	Examinateur
M.	Federico FERRI,	CEA-Saclay,	Encadrant
M.	Marc BESANCON,	CEA-Saclay,	Co-Directeur de thèse
Pr.	Stefano ARGIRO,	Université de Turin,	Co-Directeur de thèse

Contents

Introduction **1**

1 Theory overview and previous studies **1**
1.1 The Standard Model of particle physics 1
1.1.1 Particles and their interactions 1
1.1.2 The Standard Model formalism 3
1.1.3 The Higgs mechanism 8
1.2 Beyond the Standard Model 13
1.2.1 Neutrino masses 14
1.2.2 Heavy neutrinos 15
1.3 Left-Right Symmetric Models 16
1.3.1 Phenomenology of LRS model 20
1.3.2 Previous studies 22

2 The Compact Muon Solenoid Experiment at LHC **27**
2.1 The Large Hadron Collider 27
2.1.1 LHC design and detectors 27
2.1.2 LHC operations for pp collisions 32
2.1.3 HL-LHC 35
2.2 The CMS experiment 37
2.2.1 The tracker 40
2.2.1.1 The pixel detector 42
2.2.1.2 The strip detector 45
2.2.2 The electromagnetic calorimeter 46
2.2.2.1 ECAL pulse shape reconstruction 51
2.2.2.2 ECAL laser monitoring system 52
2.2.2.3 ECAL calibration 54
2.2.3 The hadronic calorimeter 58
2.2.4 The muon system 60
2.2.4.1 Drift Tubes chambers 62

2.2.4.2 Cathode Strips Chambers . . . 62
2.2.4.3 Resistive Plate Chamber . . . 63
2.2.5 Trigger system and Data Acquisition . . . 64
2.2.5.1 The Level-1 trigger . . . 65
2.2.5.2 The High Level Trigger (HLT) . . . 67
2.2.5.3 The Data Acquisition System (DAQ) . . . 68
2.2.6 Event reconstruction . . . 69
2.2.7 CMS upgrade for HL-LHC . . . 71

3 Upgrade studies of ECAL 75
3.1 ECAL upgrade strategy . . . 75
3.1.1 Current and new EB electronics . . . 76
3.1.2 Requirements for EB upgrade . . . 79
3.2 Test beam . . . 81
3.2.1 Test beam setup . . . 84
3.2.2 Test beam analysis . . . 88
3.2.3 Test beam results . . . 96
3.3 Conclusions . . . 98

4 Search for a heavy right-handed W boson and a heavy neutrino at 13 TeV 101
4.1 Signal and background definition . . . 102
4.2 Strategy . . . 103
4.3 Datasets and triggers . . . 103
4.3.1 Data samples . . . 103
4.3.2 Simulated samples . . . 104
4.3.2.1 Signal samples . . . 104
4.3.2.2 Background samples . . . 107
4.3.3 Triggers . . . 107
4.4 Object definition, identification and corrections . . . 114
4.4.1 Jets . . . 116
4.4.1.1 Reconstruction . . . 116
4.4.1.2 Identification . . . 116
4.4.1.3 Corrections . . . 117
4.4.2 Electrons . . . 117
4.4.2.1 Reconstruction . . . 117
4.4.2.2 Identification . . . 119
4.4.2.3 Energy corrections . . . 120
4.4.3 Muons . . . 121
4.4.3.1 Reconstruction . . . 121

4.4.3.2 Identification . . . 122
4.4.3.3 Momentum corrections . . . 123
4.5 Event selection . . . 125
4.6 Background estimation . . . 128
4.6.1 Top background estimation . . . 131
4.6.2 DY+jets background estimation . . . 135
4.7 Statistical analysis and systematic uncertainties . . . 146
4.7.1 Systematic uncertainties . . . 152
4.8 Results . . . 157
4.8.1 Comparison with 2015 results . . . 165
4.9 Conclusions . . . 170

5 Outlook and perspectives **177**
5.1 Other searches at CMS . . . 177
5.1.1 Search for heavy neutral leptons in trilepton channel . . . 177
5.1.2 Search for heavy neutral leptons in dilepton-dijet channel . . . 178
5.1.3 Search for heavy neutrinos in diτ-dijet channel . . . 178
5.2 Direct searches at future experiments . . . 183
5.2.1 SHiP . . . 185
5.2.2 HL-LHC . . . 190
5.2.3 FCC-ee . . . 196
5.2.4 ILC . . . 199
5.3 Conclusions . . . 204

Conclusions **207**

Appendices **207**

Appendix A Drell–Yan Monte Carlo studies **207**

Appendix B Statistics of DY aMC@NLO sample **211**

Appendix C Punzi mass range optimization **215**

Bibliography **233**

Chapter 1

Theory overview and previous studies

1.1 The Standard Model of particle physics

The Standard Model (SM) of particle physics [1, 2] is a quantum field theory developed in the early 1970s that describes the fundamental constituents of matter and the interactions between them. So far it has been extremely successful at explaining the experimental data collected over the years and at predicting a wide variety of phenomena. One of the fundamental predictions of the SM was the existence of a new scalar field with an associated particle, the Higgs boson, considered responsible for the masses of all known elementary particles. This particle was observed at a mass of about 125 GeV by the ATLAS and CMS experiments in 2012, during the Run 1 of the CERN Large Hadron Collider (LHC) at a center-of-mass energy $\sqrt{s} = 7$–8 TeV [3–5].

1.1.1 Particles and their interactions

The subatomic elementary particles are described by the SM [6] along with their interactions: the electromagnetic, weak and strong forces. The gravitational interaction, whose strength at the typical energy scale of particle physics is much smaller with respect to the other fundamental interactions, is not included in the SM.

Fermions

Fermions are twelve particles with spin 1/2 that describe the matter. According to their interactions, they are classified into two categories, *leptons* and *quarks*, and divided into three generations, each made of two leptons with electric charge -1 and 0 and two quarks with electric charge $+2/3$ and $-1/3$, as shown in Table 1.1. All fermions can interact via weak forces, while only the charged fermions can interact via the electromagnetic force, and only the quarks can interact via the strong force.

Table 1.1: *Mass and charge of leptons and quarks.*

Fermions	Quarks		Leptons	
1^{st} generation	up (u) m=$2.2^{+0.6}_{-0.4}$ MeV	down (d) m=$4.7^{+0.5}_{-0.4}$ MeV	electron (e) m=0.511 MeV	electron neutrino (ν_e) m<2 eV
2^{nd} generation	charm (c) m=1.27 ± 0.03 GeV	strange (s) m=96^{+8}_{-4} GeV	muon(μ) m=105.7 MeV	muon neutrino(ν_μ) m<2 eV
3^{rd} generation	top (t) m=$173.21 \pm 0.51 \pm 0.71$ GeV	bottom (b) m=$4.18^{+0.04}_{-0.03}$ GeV	tau (τ) m=1777 MeV	tau neutrino (ν_τ) m<2 eV
charge	$+2/3$	$-1/3$	-1	0

Each fermion has two additional quantum numbers associated with the weak interaction: the hypercharge (Y) and the isospin ($I3$). Quarks have also the color charge (C), associated with the strong interaction.
Each fermion has an associated antiparticle with opposite quantum numbers.

Bosons

The gauge bosons, integer-spin particles, are the mediators of the three interactions described in the SM:

- the *photon* (γ) is massless and neutral and carries the electromagnetic interaction, responsible for the cohesion of atoms with an infinite range of action;
- the $W^{\pm}$, charged, and the Z^0, neutral, bosons are massive and carry the weak interaction, responsible for nuclear decays with a range of action of $\approx 10^{-18}$ m;
- the *gluons* (g) are 8 massless and colored mediators carrying the strong interaction, responsible for the cohesion of nucleus and hadrons inside the atoms with a range of action of $\approx 10^{-15}$ m.

The main characteristics of the gauge bosons are summarized in Table 1.2.
The quantum field model of electromagnetic and weak (electroweak) interactions predicted the existence of massive gauge bosons: the neutral Z boson, confirmed by observations of neutral current scattering between neutrinos in 1973 [7] and by the UA1 and UA2 collaborations at CERN in 1983 [8, 9], and the charged W bosons, also confirmed by the UA1 and UA2 collaborations in 1983 [10–12]. Precise measurements of electroweak coupling strengths and of W and Z gauge boson masses, performed at LEP [13–16] and Tevatron [17–19], set indirect limits on the Higgs boson mass, confirmed by its observation [3, 4].

Since in nature it is not possible to observe single, isolated and colored quarks, when two quarks move away and reach a separation distance of $\approx 10^{-15}$ m (diameter of a hadron) their strong interaction is so great that quark-antiquark pairs are produced. These pairs are combined in different ways through "hadronization" forming colorless composite particles made of quarks, called *hadrons*:

Table 1.2: *Mass of gauge bosons and coupling constant of their corresponding interaction.*

Interaction	Electromagnetic	Weak		Strong
Quantum mediator	photon (γ)	$W^{\pm}$	Z	gluons (g)
Mass (GeV)	0	80.363 ± 0.020	91.1876 ± 0.0021	0
Coupling constant	$\alpha(Q^2 = 0) \approx \frac{1}{137}$	$G_F \approx 1.2 \cdot 10^{-5}$ GeV^{-2}		$\alpha_s(m_Z) \approx 0.1$

- *mesons* are made of quark-antiquark pairs, e.g. π^0 is a combination of $\frac{u\bar{u}-d\bar{d}}{\sqrt{2}}$;
- *baryons* are made of 3 quarks or antiquarks, e.g. uud compose a proton and udd a neutron.

QCD predicts also the existence of bound states composed of 2 quarks and 2 antiquarks (called *tetraquarks*) and of 4 quarks and 1 antiquark bound together (called *pentaquarks*), for which the $Z(4430)$ state composed of $c\bar{c}d\bar{u}$, and the X state composed of $uudc\bar{c}$ and coming from the decay of bottom Lambda baryons Λ_b^0, reported by the LHCb collaboration at CERN [20, 21], are candidate examples.
Some hadrons have small lifetimes, e.g. $\approx 10^{-17}$ s for π^0, and can be assumed to decay immediately from an experimental point of view, while others have bigger lifetimes, e.g. $\approx 10^{-8}$ s for K_L^0, and decay with a displaced vertex. The proton, with a lifetime greater than 2.1×10^{29} years, and the neutron, with a lifetime of ≈ 15 minutes, are considered stable from the experimental point of view.

1.1.2 The Standard Model formalism

The SM has 19 free parameters, corresponding to 6 quark masses, 3 charged lepton masses, 2 parameters of the Higgs potential (usually the vacuum expectation value and the Higgs boson mass), 3 gauge couplings, 3 mixing angles, the phase related to charge-parity (CP) violations of the Cabibbo-Kobayashi-Maskawa (CKM) matrix [22], and the CP-violating phase of strong interactions.
The CKM matrix is a unitary matrix that determines the strength of quark mixing in weak decays. The mass eigenstates of the quarks are not the same as the weak eigenstates, leading to the only flavor changing interactions in the SM. Initially conceived as a 2×2 matrix with a single *"Cabibbo angle"* θ_C [23] to explain mixing with the strange and later with the charm quarks, it was further generalized to a 3×3 matrix to include the third generation when evidence for CP violation made the introduction of an additional phase necessary. To describe the neutrino mixing between flavor and mass eigenstates, Pontecorvo, Maki, Nakagawa, and Sakata proposed a similar matrix, the PMNS matrix [24], which introduces three mixing angles (θ_{12}, θ_{23}, and θ_{13}) and a CP-violating phase (δ_{CP}).
Once the SM parameters are measured, the model can be completely determined, allowing to make predictions. With the discovery of the Higgs boson [3, 4] the final free parameter of the SM corresponding to the Higgs mass has been measured. Its couplings to the

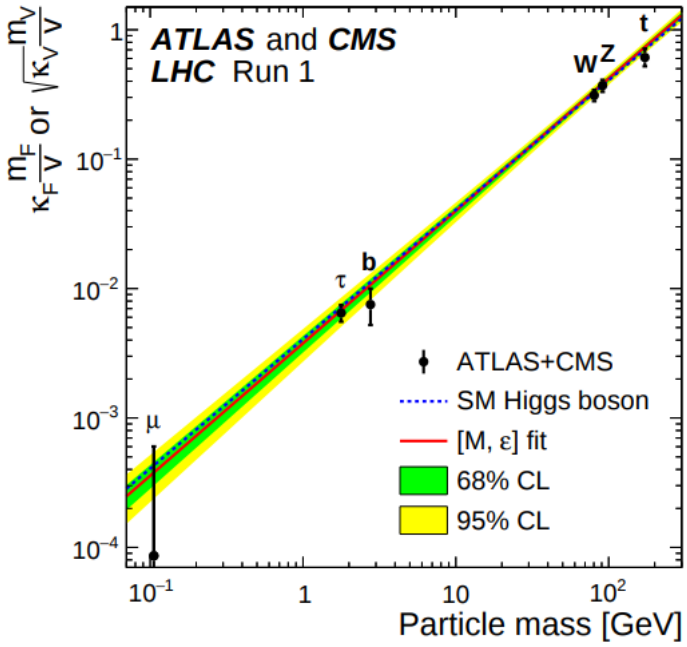

Figure 1.1: *Couplings of the Higgs boson to different particles as function of their mass, computed using data from ATLAS and CMS experiments collected during LHC Run 1 [25].*

fermion fields are proportional to their squared masses, as shown in Figure 1.1, and can be measured as a further test of the SM.

The SM is a perturbatively renormalizable quantum field theory (QFT) which describes each particle with a field $\psi(x,t)$, dependent on position and time, and each gauge boson with an interaction field. Relativistic fermions fields are described by four component spinors ψ:

$$\psi = \begin{pmatrix} \psi_R \\ \psi_L \end{pmatrix}$$

where ψ_L and ψ_R are the left and right chirality components, according to:

$$\psi_{L,R} = \frac{(1 \mp \gamma^5)}{2}\psi$$

where γ_5 is a Dirac matrix.
The QFT is based on the local gauge symmetries associated with the electroweak and strong interactions, corresponding to invariances under the weak isospin and hypercharge symmetry groups $SU(2)_L \times U(1)_Y$ for the unified weak and electromagnetic forces and under the color symmetry group $SU(3)_C$ for the strong force. The $U(1)$ symmetry group

acts only on fields with non-zero hypercharge Y and is therefore noted $U(1)_Y$, while, as described below, only the left-handed fields are doublets and therefore the $SU(2)$ group is noted as $SU(2)_L$. This leads to a

$$SU(3)_C \times SU(2)_L \times U(1)_Y$$

symmetry group for the SM. The generators of these symmetry groups correspond to eight gluons fields G_A^μ $(A = 1, 2, ...8)$ for $SU(3)_C$, three boson fields W_α^μ $(\alpha = 1, 2, 3)$ for $SU(2)_L$, and a single boson field B^μ for $U(1)_Y$. The γ, W and Z bosons are obtained by linear combinations of W_α^μ and B^μ, as detailed later in the text.

The SM describes the strong interaction through the Quantum Chromo-Dynamics (QCD), based on the $SU(3)_C$ gauge group, while the theory of electromagnetic (EM) interaction, the Quantum Electro-Dynamics (QED), is based on the gauge group $U(1)_{EM}$, associated with the conserved quantum number Q (electric charge). In this case, the condition of local invariance under the $U(1)_{EM}$ group leads to the existence of a massless vector boson, the *photon*. The gauge theory for weak interactions is conceived as an extension of the QED. The unification of the electromagnetic and the weak interaction is then described by the Glashow-Weinberg-Salam (GWS) model, extending the gauge symmetry of QED to the electroweak gauge group $SU(2)_I \times U(1)_Y$.
The quantum numbers corresponding to the third component (I_3) of the weak isospin operator, generator of $SU(2)_I$, and to the weak hypercharge operator (Y), generator of $U(1)_Y$, satisfy the Gell-Mann-Nishijima formula

$$Q = I_3 + \frac{Y}{2}.$$

The values of I_3, Y and Q for all fermions are reported in Table 1.3.
In the SM, the left and right chirality fermions have different interactions due to the parity violation in weak interactions, thus they can be divided in doublets of left-handed particles and singlets of right-handed quarks and charged leptons:

$$L_L = \begin{pmatrix} \nu_{\ell,L} \\ \ell_L \end{pmatrix}, \ell_R,\ Q_L = \begin{pmatrix} u_L \\ d_L \end{pmatrix}, u_R, d_R, \tag{1.1}$$

where $\ell = e, \mu, \tau$, $u = u, c, t$, and $d = d, s, b$. The right-handed neutrinos are not needed in the SM, since due to the chiral structure of the electroweak force there are no right-handed neutral leptons singlets.

The most general Lagrangian of the SM to describe matter particles and their interactions is given by:

$$\mathcal{L} = \mathcal{L}_{Yang-Mills} + \mathcal{L}_{Dirac} + \mathcal{L}_{Higgs} + \mathcal{L}_{Yukawa},$$

Table 1.3: *Isospin (I_3), hypercharge (Y) and electric charge (Q) of all fermions.*

Fermions	I_3	Y	Q
$\begin{pmatrix} \nu_{\ell,L} \\ \ell_L \end{pmatrix}$	$\begin{pmatrix} \frac{1}{2} \\ -\frac{1}{2} \end{pmatrix}$	$\begin{pmatrix} -1 \\ -1 \end{pmatrix}$	$\begin{pmatrix} 0 \\ -1 \end{pmatrix}$
ℓ_R	0	-2	-1
$\begin{pmatrix} u_L \\ d_L \end{pmatrix}$	$\begin{pmatrix} \frac{1}{2} \\ -\frac{1}{2} \end{pmatrix}$	$\begin{pmatrix} \frac{1}{3} \\ -\frac{1}{3} \end{pmatrix}$	$\begin{pmatrix} \frac{2}{3} \\ -\frac{1}{3} \end{pmatrix}$
u_R	0	$+\frac{4}{3}$	$+\frac{2}{3}$
d_R	0	$-\frac{2}{3}$	$-\frac{1}{3}$

where $\mathcal{L}_{Yang-Mills}$ represents the kinematics of the gauge fields, $\mathcal{L}_{Dirac}$ describes the fermions and their interactions with the gauge bosons, $\mathcal{L}_{Higgs}$ introduces the Higgs field allowing to describe the electroweak spontaneous symmetry breaking, and $\mathcal{L}_{Yukawa}$ represents the interaction between the Higgs field and the fermion fields.

Yang-Mills Lagrangian

The Yang-Mills Lagrangian is described by:

$$\mathcal{L}_{Yang-Mills} = -\frac{1}{4g'^2} B_{\mu\nu} B^{\mu\nu} - \frac{1}{4g^2} W^{\alpha}_{\mu\nu} W^{\alpha\mu\nu} - \frac{1}{4g''^2} G^{A}_{\mu\nu} G^{A\mu\nu}$$

where

- g, g', and g'' are the couplings associated with I, Y, and C respectively;
- $B_{\mu\nu} = \partial_\mu B_\nu - \partial_\nu B_\mu$ is the hypercharge tensor;
- $W^{\alpha}_{\mu\nu} = \partial_\mu W^{\alpha}_{\nu} - \partial_\nu W^{\alpha}_{\mu} - \epsilon^{abc} W^{b}_{\mu} W^{c}_{\nu}$ is the isospin tensor, with ϵ^{abc} the asymmetric structure of $SU(2)_L$;
- $G^{A}_{\mu\nu} = \partial_\mu G^{A}_{\nu} - \partial_\nu G^{A}_{\mu} - f^{ABC} G^{B}_{\mu} G^{C}_{\nu}$ is the color tensor, with f^{ABC} the asymmetric structure constants of $SU(3)_C$.

Dirac Lagrangian

The term in the Dirac free Lagrangian described by:

$$\mathcal{L} = \bar{\psi} i \gamma_\mu \partial^\mu \psi,$$

is not invariant under local gauge transformations $\psi(x) \to e^{i\alpha(x)}\psi(x)$, where α is a scalar, and then the $\partial^\mu \psi$ term is not invariant under $U(1)$ transformations. The invariance is achieved by adding a compensating field B_μ in a way that the covariant derivative is

written as:

$$\partial_\mu \rightarrow D_\mu = \partial_\mu - ig' B_\mu.$$

The requirement of local gauge invariance under the $SU(2)_I \times U(1)_Y$ group introduces then four massless vector fields, W_μ^α and B_μ, which couple to fermions with two different coupling constants, g and g', representing the weak and the electromagnetic interaction coupling strengths. The gauge-invariant Lagrangian for fermion fields coupling to gauge fields can then be written as:

$$\mathcal{L} = \bar{\Psi}_L \gamma^\mu \big(i\partial_\mu + g\tau_\alpha W_\mu^\alpha - \frac{1}{2} g' Y B_\mu\big)\Psi_L + \bar{\psi}_R \gamma^\mu \big(i\partial_\mu - \frac{1}{2} g' Y B_\mu\big)\psi_R, \tag{1.2}$$

where τ_α are the Pauli $SU(2)$ matrices and

$$\Psi_L = \begin{pmatrix} \Psi_L^1 \\ \Psi_L^2 \end{pmatrix},$$

with Ψ_L and ψ_R summed over all the possibilities of 1.1.

For the invariance under the $SU(3)_C$ group, eight massless vector fields, G_μ^A, coupling to fermions with the g'' constant, are introduced. The term

$$-i\gamma^\mu \frac{1}{2} g'' G_\mu^A \lambda_A$$

where λ_A are the Gell-Mann $SU(3)$ matrices, is then added to the Lagrangian for the quarks terms.

The physical fields are not represented by the gauge fields W_μ^α and B_μ, but by linear combinations of them. The charged bosons W^+ and W^- correspond to:

$$W_\mu^\pm = \frac{1}{\sqrt{2}}(W_\mu^1 \mp i W_\mu^2),$$

while the neutral bosons γ and Z correspond, respectively, to:

$$A_\mu = B_\mu \cos\theta_W + W_\mu^3 \sin\theta_W,$$

$$Z_\mu = -B_\mu \sin\theta_W + W_\mu^3 \cos\theta_W,$$

obtained by mixing the neutral fields W_μ^3 and B_μ with a rotation angle θ_W, named *Weinberg angle*. Using these fields, the interaction term between gauge fields and fermions of the Lagrangian in Equation 1.2 becomes:

$$\mathcal{L}_{int} = \frac{1}{2\sqrt{2}} g\big(J_\alpha^+ W^{(+)\alpha} + J_\alpha^- W^{(-)\alpha}\big) + \frac{1}{2}\sqrt{g'^2 + g^2}\, J_\alpha^Z Z^\alpha + e J_\alpha^{EM} A^\alpha,$$

where J^{EM} is the electromagnetic current connected to the photon field, while J^+, J^- and J^Z are the three weak isospin currents. Since A^α is identified with the photon field, we get

$$g \sin\theta_W = g' \cos\theta_W = e.$$

The GWS model thus predicts the existence of two charged gauge fields, which only couple to left-handed fermions, and two neutral gauge fields, which interact with both left- and right-handed components, with the Z boson interacting differently with right and left part. To preserve the gauge invariance of $SU(2)_L \times U(1)_Y$, the W and Z bosons have to be massless.
In fact, within the SM formalism all the particles have to be massless, since a mass term for the gauge bosons in the electroweak Lagrangian would violate gauge invariance, needed to ensure the renormalizability of the theory. The W and Z bosons have however a mass, as described in Section 1.1.1, then the electroweak symmetry must be broken, leading to a

$$SU(3)_C \times SU(2)_L \times U(1)_Y \rightarrow SU(3)_C \times U(1)_{EM}$$

symmetry group.

Accidental symmetries, like the lepton and baryon number in any SM process, come from the renormalizable terms of the Lagrangian and are broken by non-renormalizable terms at higher order. Decays that could violate lepton number conservation, such as $\mu \rightarrow e^+e^-e^+$, are looked for by experiments [26], together with searches [27] for the Majorana nature of neutrinos that could lead to physics beyond the SM.

1.1.3 The Higgs mechanism

The spontaneous electroweak symmetry breaking [28] is associated with the Brout-Englert-Higgs (BEH) mechanism [29–31], that explains the origin of the mass of the gauge bosons, and of the fermions through their Yukawa couplings. The Higgs field originates from this mechanism, and its quantum excitation, the Higgs boson, is a scalar particle that interacts with other particles. This occurs without explicitly breaking the gauge invariance, thus preserving the renormalizability of the theory, in which the mass of the Higgs boson, m_H, is a free parameter.
The Higgs mechanism was developed to explain the masses of the $W^\pm$ and Z bosons and it introduces a doublet of complex scalar fields

$$\phi = \begin{pmatrix} \phi^+ \\ \phi^0 \end{pmatrix} = \frac{1}{2} \begin{pmatrix} \phi^1 + i\phi^2 \\ \phi^3 + i\phi^4 \end{pmatrix},$$

with four scalar bosons affecting only the $SU(2)_L$ group symmetry of the electroweak theory, since the photons should remain massless.

Table 1.4: *Isospin (I_3), hypercharge (Y) and electric charge (Q) of ϕ.*

	I_3	Y	Q
$\begin{pmatrix} \phi^+ \\ \phi^0 \end{pmatrix}$	$\begin{pmatrix} \frac{1}{2} \\ -\frac{1}{2} \end{pmatrix}$	$\begin{pmatrix} 1 \\ 1 \end{pmatrix}$	$\begin{pmatrix} 1 \\ 0 \end{pmatrix}$

The Higgs field ϕ is characterised by the quantum numbers presented in Table 1.4.

According to the Goldstone theorem [32, 33], there is a massless Goldstone boson for every spontaneously broken symmetry. Four degrees of freedom are postulated for ϕ: three are Goldstone bosons consumed to give mass to the $W^{\pm}$ and Z bosons, and the fourth predicts the existence of a massive spin-zero particle, the Higgs boson.
The Lagrangian for the masses of the gauge bosons can be written as:

$$\mathcal{L}_{Higgs} = (D^{\mu}\phi)^{\dagger} D_{\mu}\phi - V(\phi^{\dagger}\phi), \tag{1.3}$$

where $D_{\mu} = \partial_{\mu} - ig\tau_{\alpha}W_{\mu}^{\alpha} + \frac{i}{2}g'YB_{\mu}$ is the covariant derivative, representing the propagation of the Higgs doublet ϕ, its couplings to the $SU(2)_L$ and $U(1)$ generators τ^{α} and Y, and the massless vector fields W_{μ}^{α} and B_{μ}. Since the kinetic part is written in terms of covariant derivatives and the Higgs potential V only depends on the product $\phi^{\dagger}\phi$, this Lagrangian is invariant under $SU(2)_L \times U(1)_Y$ transformations. The ϕ field transforms as $\phi \to e^{i\alpha_i\tau_i}\phi$ under $SU(2)_L$ transformations, and as $\phi \to e^{iY\beta}\phi$ for $U(1)_Y$ transformations.
As shown in Figure 1.2, the effective potential of the Higgs field has a local maximum at $\phi = 0$, but at $|\phi| > 0$ there is an infinite number of global minima representing the vacuum. At high energies, the gauge bosons are located at $\phi = 0$ and the local gauge symmetry of the SM is conserved. At lower energies, the symmetry is spontaneously broken when a specific minimum of the potential is choosen.
The potential term can be written as

$$V(\phi^{\dagger}\phi) = -\mu^2\phi^{\dagger}\phi - \lambda(\phi^{\dagger}\phi)^2.$$

With $\mu^2 < 0$ and $\lambda > 0$, the spontaneous symmetry breaking appears with a minimum vacuum expectation value given by:

$$\phi^{\dagger}\phi = \frac{1}{2}\left(\phi_1^2 + \phi_2^2 + \phi_3^2 + \phi_4^2\right) = -\frac{\mu^2}{2\lambda} = \frac{v^2}{2},\ v^2 = -\frac{\mu^2}{\lambda}.$$

The choice of (ϕ^+, ϕ^0) corresponding to the ground state is arbitrary, and the chosen point is not invariant under rotations in the (ϕ^+, ϕ^0) plane. If the ground state is fixed on the ϕ^0 axis to choose a vacuum not charged, the vacuum expectation value of ϕ is

$$\langle\phi\rangle = \frac{1}{\sqrt{2}}\begin{pmatrix} 0 \\ v \end{pmatrix}. \tag{1.4}$$

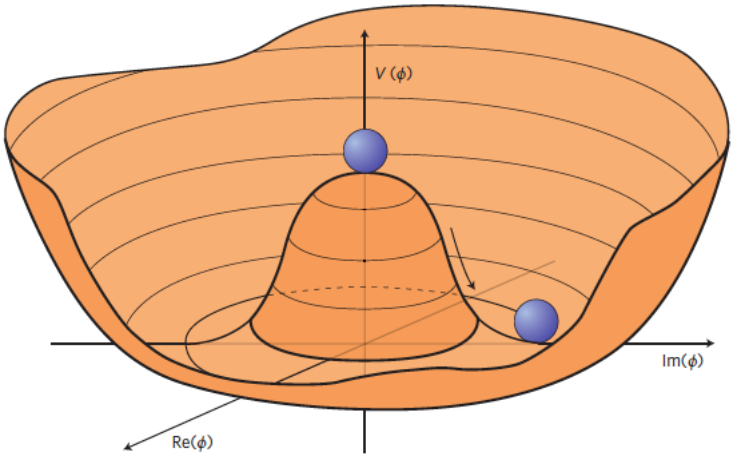

Figure 1.2: *Shape of the Higgs potential. At high energies, particles are located at $\phi = 0$, not interacting with the Higgs field. At lower energies, particles choose a distinct ground state of the potential and the symmetry is spontaneously broken.*

The ϕ field can thus be rewritten, in terms of its vacuum expectation value, in a generic gauge:

$$\phi = \frac{1}{\sqrt{2}} e^{\frac{i}{v}\phi^\alpha \tau_\alpha} \begin{pmatrix} 0 \\ H + v \end{pmatrix},$$

where the three fields ϕ^α ($\alpha = 1, 2, 3$) are called *Goldstone fields* and H is the Higgs boson scalar field. These three Goldstone fields, corresponding to three massless bosons, can be eliminated by choosing a *unitary gauge* given by the transformation

$$\phi \to \phi' = e^{-\frac{i}{v}\phi^\alpha \tau_\alpha} \phi = \frac{1}{\sqrt{2}} \begin{pmatrix} 0 \\ H + v \end{pmatrix}. \tag{1.5}$$

The remaining field, the *Higgs field*, has now a zero expectation value. With the ϕ field in the unitary gauge, the Lagrangian in Equation 1.3 can be written as:

$$\mathcal{L}_{Higgs} = \frac{1}{2}\partial_\mu H \partial^\mu H - \frac{1}{2} m_H^2 - \sqrt{\frac{\lambda}{2}} m_H H^3 - \frac{\lambda}{4} H^4 + \left[m_W^2 W^{+\mu} W_\mu^- + \frac{m_Z^2}{2} Z^\mu Z_\mu \right] \left(1 + \frac{H}{v}\right)^2,$$

where

$$m_H = \sqrt{2\mu^2} = \sqrt{2\lambda} v.$$

This Lagrangian now contains mass terms for the $W^\pm$ and Z fields: each of the three gauge bosons has acquired mass and an additional degree of freedom, corresponding to the longitudinal polarization. The total number of degrees of freedom is still preserved, since the three Goldstone bosons have disappeared from the Lagrangian $\mathcal{L}_{Higgs}$: the degrees related to the missing Goldstone bosons have become the longitudinal degrees of the vector

bosons. Only the H scalar field, the Higgs boson, is still present, acquiring mass itself. The Higgs boson is neutral since the Higgs field does not interact with the electromagnetic field.

Vector boson masses and couplings

The masses of the $W^{\pm}$ and Z vector bosons are related to the vacuum expectation value v and to the electroweak coupling constants:

$$\begin{cases} m_W = \frac{1}{2}vg \\ m_Z = \frac{1}{2}v\sqrt{g^2+g'^2} \end{cases} \rightarrow \frac{m_W}{m_Z} = \frac{g}{\sqrt{g^2+g'^2}} = \cos\theta_W.$$

The vector bosons couplings to the Higgs boson depend on the square of m_W and m_Z:

$$g_{H-W} = \frac{1}{2}vg^2 = \frac{2}{v}m_W^2$$

$$g_{H-Z} = \frac{1}{2}v(g^2+g'^2) = \frac{2}{v}m_Z^2.$$

A relation between the decay ratios of the Higgs boson to a pair of W bosons and to a pair of Z bosons can be derived from the above equations:

$$\frac{BR(H\rightarrow W^+W^-)}{BR(H\rightarrow ZZ)} = \left(\frac{g_{H-W}}{\frac{1}{2}g_{H-Z}}\right)^2 = 4\left(\frac{m_W^2}{m_Z^2}\right)^2 \approx 2.4.$$

The Fermi constant G_F allows to directly determine the energy scale of the electroweak symmetry breaking through the vacuum expectation value [1, 34, 35]:

$$v = (\sqrt{2}G_F)^{-\frac{1}{2}} \approx 246 \text{ GeV}.$$

Yukawa Lagrangian

As shown in 1.1, quarks and charged leptons exist in left- and right-handed states that are degenerate in mass, so a "Dirac mass term" like

$$m\bar{\psi}\psi = m\psi_L^\dagger\psi_R + m\psi_R^\dagger\psi_L, \tag{1.6}$$

which contains the product of left- and right-handed fields, should be used to give mass to the fermions in the SM. However, since it is clear that ψ_L and ψ_R behave differently under $SU(2)$ transformations, a Dirac mass term is not gauge invariant and thus it is not possible to introduce it explicitly in the fermion Lagrangian.
The electromagnetic gauge invariance allows the coupling between fermions and scalars, then the Higgs doublet introduced in the GWS model allows a gauge invariant interaction

that looks like a fermion mass term when the Higgs gets its vacuum expectation value, called *Yukawa coupling*. Thus the Higgs field generates masses also for fermions through their Yukawa couplings.

The Lagrangian for the Yukawa interaction with the Higgs field can be written as:

$$\mathcal{L}_{Yukawa} = h^u_{ij}\bar{Q}^i_L u^j_R \tilde{\phi} + h^d_{ij}\bar{Q}^i_L d^j_R \phi + h^\ell_{ij}\bar{L}^i_L \ell^j_R \phi$$

where $\tilde{\phi}$ is the charge-conjugate Higgs field defined as

$$\tilde{\phi} = \frac{1}{\sqrt{2}} \begin{pmatrix} H+v \\ 0 \end{pmatrix},$$

$h^{u,d,\ell}_{ij}$ (or λ_ψ) are the Yukawa couplings proportional to the mass of the fermions interacting with the Higgs field and to the average value of the vacuum expectation value, and $i, j = 1, 2, 3$ are flavor indices. The down quarks (d, s, b) have the same Yukawa coupling term of the leptons. The up quarks (u, c, t) need instead to use the charge-conjugate of the Higgs field, since for them the vacuum expectation value of the Higgs field is placed in the down part of the doublet, as shown in Equation 1.4.
The mass terms appear with the development of the Yukawa Lagrangian around its minimum:

$$\mathcal{L}_{mass} = m^u_{ij}\bar{u}^i_L u^j_R + m^d_{ij}\bar{d}^i_L d^j_R + m^l_{ij}\bar{\ell}^i_L \ell^j_R + h.c.$$

where *h.c.* is the hermitian conjugate.
Using the unitary gauge of Equation 1.5, the terms proportional to v lead to:

$$\frac{\lambda_\psi v}{\sqrt{2}}(\bar{\psi}_L\psi_R + \bar{\psi}_R\psi_L) = \frac{\lambda_\psi v}{\sqrt{2}}\bar{\psi}\psi \rightarrow m_\psi = \frac{\lambda_\psi v}{\sqrt{2}}.$$

From this equation it is visible that the fermions acquire a mass proportional to v.
Fermions can get their mass from spontaneous symmetry breaking, like the W and Z vector bosons: the mass is proportional to λ_ψ, which is the strength of the coupling of the fermion ψ to the Higgs. In the electroweak sector of the SM, this mechanism is the only known source of CP violation.

Neutrinos, neutral and massless fermions that only interact through the weak interaction, play a special role in the SM. Due to parity violation in the weak interaction, neutrinos are always left-handed and anti-neutrinos are always right-handed. In the SM, the mass of a fermion can only be assigned through a Dirac mass term like the one in Equation 1.6, which depends on the product of left- and right-handed fields, then the Dirac mass term for a neutrino yields a mass of zero if there are no right-handed neutrinos. To account for the experimental observation of massive neutrinos an extension of the SM is thus required.

1.2 Beyond the Standard Model

Despite the many successful predictions of the SM, there are indications that the SM is not a complete theory [36].

Gravitational interaction

The SM is a low-energy effective theory, deriving from a Grand Unified Theory (GUT), valid up to some energy scale Λ but it does not include gravity. In fact, the effect of gravity at small scales is extremely weak. The strength of the gravitational attraction at the quantum level is expected to be comparable to the other forces at the Planck scale, $m_{\text{Planck}} \approx 10^{19}$ GeV, which is well beyond the one that can be probed in the current experiments. Therefore, theories that incorporate gravity are not easily testable.

Dark Matter

The total energy content of the entire universe is made of the matter described by the SM only for $\approx 5\%$ [37]. Approximately 20% of the remaining 95% consists of dark matter and the rest is dark energy, an unknown form of energy, not very dense and known to interact only through gravity, which tends to accelerate the expansion of the universe. Dark matter is not only dark to electromagnetic interactions, but it also does not interact strongly with any of the forces described by the SM. Its presence is inferred from its gravitational interaction with baryonic matter. From a particle physics point of view, this new type of matter should come from a new particle. A candidate for dark matter is proposed by many models, including supersymmetry (SUSY) [38], as a weakly interactive massive particle (WIMP). This is a very active area of research at collider experiments as well as at direct [39] and indirect [40] detection experiments.

Baryon Asymmetry

In the observable universe, there is an imbalance between baryonic matter and antibaryonic matter. After the Big Bang, equal amounts of matter and antimatter have been produced but now there is a prevalence of matter, thus a break of symmetry due to some unknown mechanism must have taken place in the early universe. The SM does not predict the baryon-antibaryon asymmetry experimentally observed, then an extension of the SM is required to take this into account.

Right-handed neutrinos

The weak force only couples particles of a specific chirality and only left-handed particles couple with right-handed antiparticles. In the SM, only left-handed neutrinos are present, then some other theory beyond the standard model should come into play to add

right-handed neutrinos. One proposed theory, known as the Left-Right symmetry model and described in Section 1.3, introduces an additional symmetry in the SM that mirrors the one of the weak force. This theory predicts the existence of additional heavy particles similar to the W and Z bosons, as well as a new kind of neutrinos.

Moreover, within the electroweak sector, the SM does not describe the neutrino flavor oscillations, suggested in 1967 by Pontecorvo [41] and experimentally confirmed from the 1990s [42–47]. These evidences motivate extensions to the SM and support models with massive neutrinos, described in Section 1.2.2.

1.2.1 Neutrino masses

Neutrinos were first proposed in 1929 to preserve energy conservation in beta decays and were first confirmed by experimental evidence with the observation of a neutrino in 1953 [48], later identified as the electron neutrino. After the discovery of a second neutrino in 1962 [49], later identified as the muon neutrino, the initial theory that only one neutrino existed was rejected. Theories that predicted that each charged lepton had a corresponding neutrino were then formulated and later confirmed by experimental evidence. The tau neutrino was finally observed in 2001 [50].
Advances in the understanding of neutrino physics and weak interactions often coincided, since neutrinos were predicted to interact only through weak interactions.
A theoretical model of the weak interaction was proposed in 1932 to explain beta decay, including a massless neutral lepton later identified as the electron neutrino. Experimental measurements of hadron decay rates through weak interaction, like $K^+ \to 2\pi, 3\pi$, performed in the 1950s motivated new parity violating models of the weak interaction, experimentally observed in 1957 [51].
Experimental measurements of neutrinos performed in the 1970s and earlier, like ν energy spectra in beta decays and ν-nucleon interaction cross sections, were consistent with massless neutrinos within experimental uncertainties. The SM was then developed with massless neutrinos and with the weak interaction modeled as a parity violating quantum field theory.
However, in the last 20 years it has been confirmed that neutrinos have a very small mass. In particular, the neutrino flavor oscillations, observed in experiments such as SNO (Sudbury Neutrino Observatory) [52] and Super-Kamiokande [53], implied that neutrinos have mass, motivating extensions to the SM.
These experiments measured an oscillation between electron neutrinos and muon neutrinos, coming from the sun and from the atmosphere of the earth. Since this oscillation is possible only if there is a difference in mass between the neutrino mass eigenstates, they proved that neutrinos have mass.

In particular, the squared mass differences between the neutrinos are estimated as [54]:

$$\Delta m^2_{21} \simeq 7.5 \times 10^{-5}\, eV^2,$$

$$|\Delta m^2_{23}| \simeq 2.5 \times 10^{-3}\, eV^2,$$

with m_i the mass of the ith neutrino mass eigenstate. The Δm^2_{21} is equivalent to the Δm^2_{sol} of solar neutrinos, while the $|\Delta m^2_{23}|$ is identified as the Δm^2_{atm} of atmospheric neutrinos, linked by the relation:

$$\Delta m^2_{sol} = \Delta m^2_{21} \ll |\Delta m^2_{23}| \simeq |\Delta m^2_{13}| \simeq \Delta m^2_{atm}.$$

For the mass spectrum there are two possibilities:

- the "*normal hierarchy*", with $m_1 < m_2 < m_3$ and $\Delta m^2_{23} < 0$;
- the "*inverted hierarchy*", with $m_3 < m_1 < m_2$ and $\Delta m^2_{23} > 0$.

The experiments studying neutrino oscillations provide also a measurement of the mixing angles:

- $\theta_{12} \approx 33.6°$, estimated from solar neutrino detectors like SNO or Super-Kamiokande;
- $\theta_{23} \approx 41.6°$, estimated from detectors measuring atmospheric neutrino flux such as Super-Kamiokande or from long-baseline accelerator neutrino experiments such as MINOS (Main Injector Neutrino Oscillation Search) [55], OPERA (Oscillation Project with Emulsion-tRacking Apparatus) [56], T2K (Tokai-to-Kamioka) [57], and NOvA (NuMI Off-Axis ν_e Appearance) [58];
- $\theta_{13} \approx 8.5°$, estimated from long-baseline accelerator neutrino experiments such as T2K or reactor experiments such as Daya Bay [47], RENO (Reactor Experiment for Neutrino Oscillations) [59] and Double Chooz [60].

An upper limit on the absolute mass scale of neutrinos was also placed from cosmological observations [61–63], which provide $\Sigma m_{\nu_i} < 0.12$ eV. These masses are very small compared to any other mass scale in the SM.
As already said in Section 1.2, neutrinos are only produced in left-handed states in the SM, so for a Lorentz invariant theory an extension with massive neutrinos, like the Left-Right symmetry model described in Section 1.3, is needed.

1.2.2 Heavy neutrinos

The SM can accommodate massive, fermionic neutrinos in several ways. In one of the simplest extensions, neutrinos are Majorana fermions, which are their own anti-particles.

Two Majorana masses m_L and m_R, generated through an extended Higgs model, are defined in the Lagrangian :

$$\mathcal{L}_M = -m_L \chi_L^\dagger \chi_L - m_R \chi_R^\dagger \chi_R.$$

Majorana neutrinos allow neutrinoless double beta decay, a process violating the lepton number by two units. This has not been observed yet [64, 65].
The Left-Right symmetric model, which predicts massive fermionic neutrinos that have not yet been observed in experiments, is one of these alternatives, as described in Section 1.3. Massive neutrinos could also be introduced with the neutrino Minimal Standard Model (νMSM), proposed by T. Asaka and M. Shaposhnikov in 2005 [66, 67]. The νMSM introduces three sterile heavy neutrinos that interact only with the light active SM neutrinos through their mixing, where the mixing angle is given by the ratio of the active and sterile neutrino masses: $\theta^2 \approx m_\nu / m_N$. This model could explain some of the unresolved phenomena in particle physics while remaining consistent with the observation of neutrino oscillations and with the cosmological data on neutrino masses and mixing. In fact, it could provide a dark matter candidate with the first lightest heavy neutrino, N_1 ($m_{N_1} \approx 1$ keV), explain the matter-antimatter asymmetry of the universe with the other two neutrinos, N_2 and N_3 ($1 < m_{N_2,N_3} < 100$ GeV), massive enough to be searched for at the LHC, and explain the origin of the SM neutrino masses through the "see-saw" mechanism [68, 69].

Production modes

Heavy neutrinos can be produced through meson decays (π, K, D, B) if their mass is small enough, or, if they have higher mass, through the decay of a W (or W_R) boson into a lepton and its associated heavy neutrino. This is the case considered in the analysis described in Chapter 4. Additionally, heavy neutrinos can be produced through the decay of a Z or Higgs boson into a light neutrino and a heavy neutrino, which is very challenging from the experimental point of view.

Decay modes

Heavy neutrinos can decay into a W (or W_R) boson and a lepton, with the W boson decaying into a lepton and a light neutrino or into a pair of quarks as shown in Figure 1.3, or into a Z or Higgs boson and a light neutrino. Their lifetime can vary from very short to macroscopic values, possible for lower couplings at low masses.

1.3 Left-Right Symmetric Models

The Left-Right Symmetric (LRS) model [70–72], extension of the SM, introduces massive neutrinos preserving the SM predictions supported by experimental evidence. First

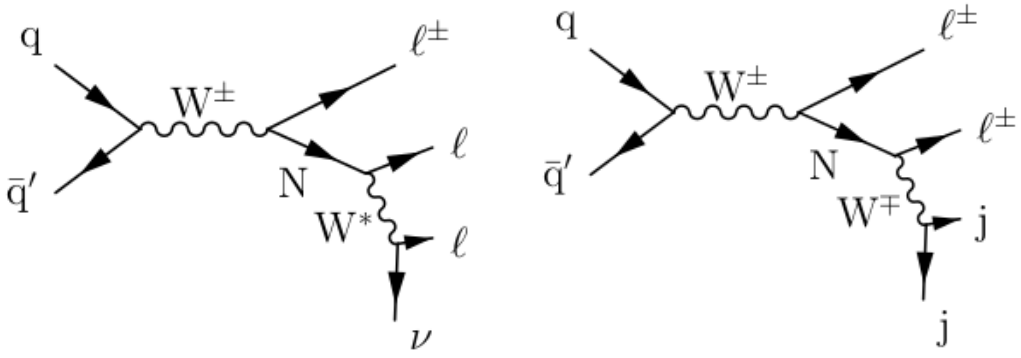

Figure 1.3: *The Feynmann diagram for the heavy neutrino decay into a W boson and a lepton, with the W decaying into a lepton and a light neutrino (on the left) or into a pair of quarks (on the right).*

proposed in 1974 [73], the LRS model predicts an electroweak interaction, existed in the very early universe, conserving parity and mediated by seven massless gauge bosons. These massless bosons are transformed into the SM electroweak bosons and into the heavier $W_{\mathrm{R}}^{\pm}$ (W_{R}) and Z' gauge bosons through an extension of the SM BEH mechanism.
The right-handed neutrinos are missing from the SM fields listed in 1.1, then completing these fields and restoring the chiral symmetry of the SM are the main motivations of the LRS model. These neutrinos are obtained introducing new gauge heavy bosons and additional Higgs multiplets through an additional $SU(2)_R$ symmetry, leading to a

$$SU(3)_C \times SU(2)_L \times SU(2)_R \times U(1)_{L-B}$$

gauge symmetry group. Leptons and quarks are then completely left-right symmetric:

$$L_{L,R} = \begin{pmatrix} \nu_\ell \\ \ell \end{pmatrix}_{L,R}, \; Q_{L,R} = \begin{pmatrix} u \\ d \end{pmatrix}_{L,R}.$$

The electromagnetic charge is now defined as

$$Q_{EM} = I_{3L} + I_{3R} + \frac{B-L}{2},$$

since there is an accidental symmetry of $B - L$ rather than individual baryon and lepton number conservation as in the SM.

The SM electroweak sector, described by the $SU(2)_L \times U(1)_Y$ group, is extended by the LRS model adding the $SU(2)_R$ gauge group and three heavy right-handed neutrinos N_{R}. This group introduces three massless vector fields $W_{R\mu}^{j}$, which become massive bosons through an extended BEH mechanism in two stages. This mechanism ultimately yields

one massless and six massive gauge bosons mediating the electroweak interactions.
The first stage [74] introduces two chiral, complex Higgs doublets

$$\chi_{L,R} = \begin{pmatrix} \chi^+_{L,R} \\ \chi^0_{L,R} \end{pmatrix} \tag{1.7}$$

with bosonic fields that couple independently to the left- and right-handed gauge bosons. The propagation and interaction of these new fields with other massless bosons is described by the Lagrangian:

$$\mathcal{L}_{H,LRS} = \frac{1}{2}(D_\mu \chi_L)^\dagger D^\mu \chi_L + \frac{1}{2}(D_\mu \chi_R)^\dagger D^\mu \chi_R - V(\chi_{L,R}) \tag{1.8}$$

where the covariant derivative $D_\mu = \partial_\mu + ig_L \tau^j W^j_{L\mu} + ig_R \tau^j W^j_{R\mu} + i\frac{g'}{2} Y B_\mu$ contains the massless boson fields $W^j_{L\mu}$, $W^j_{R\mu}$, and B_μ multiplied respectively by the generators of the $SU(2)_L$, $SU(2)_R$, and $U(1)$ groups. The coupling strengths g_R and g_L are assumed to be equal in the simplified LRS model considered here, and are denoted as g.
The potential $V(\chi_{L,R})$ depends on a constant U_R, respecting the LRS model symmetries. To minimize $V(\chi_{L,R})$, the $\chi_{L,R}$ fields equilibrate at

$$\left\langle \chi^+_{L,R} \right\rangle = 0,\ \langle \chi^0_L \rangle = 0,\ \langle \chi^0_R \rangle = U_R.$$

Subsequently the new fields

$$W^\pm_{R\mu} = \frac{1}{\sqrt{2}}(W^1_{R\mu} \mp i W^2_{R\mu}),\ Z'_\mu = \frac{1}{\sqrt{g'^2 + g^2}}(-g' B_\mu + g W^3_{R\mu})$$

are created with masses

$$m_{W_\mathrm{R}} = \frac{1}{2} g U_R,\ m_{Z'} = \frac{1}{2} U_R \sqrt{g'^2 + g^2},$$

while all the other bosons remain massless. The new charged weak boson W_R couples to N_R and all right-handed SM fermions.
The second stage [74, 75] introduces in the Higgs sector two complex Higgs doublets ϕ_1 and ϕ_2 through the multiplet

$$\Phi = \begin{pmatrix} \phi^0_1 & \phi^+_2 \\ \phi^-_1 & \phi^0_2 \end{pmatrix}$$

that interacts with the left- and right-handed $SU(2)$ boson fields. These interactions are described by a Lagrangian $\mathcal{L}_{H_2,LRS}$ that is similar to the one in Equation 1.8 but has additional terms for the second Higgs doublet and a potential $V(\phi_1, \phi_2)$. The multiplet Φ

naturally adopts a non-zero expectation value

$$\langle \Phi \rangle = \begin{pmatrix} v_1 & 0 \\ 0 & v_2 \end{pmatrix}, \tag{1.9}$$

where $v_{1,2}$ are real positive numbers, that minimizes $V(\phi_1, \phi_2)$. At equilibrium, the SM W and Z bosons, and the W_{R}, Z' bosons have masses

$$m_W = \frac{1}{2} g v,\ m_{W_{\mathrm{R}}} = \frac{1}{2} g U_R,\ m_Z = \frac{1}{2} \bar{g} v,\ m_{Z'} = \frac{1}{2} \bar{g} U_R$$

where

$$v^2 = v_1^2 + v_2^2,\ \bar{g}^2 = g^2 + g'^2.$$

Assuming $U_R \gg v$ and a negligible mixing between the left and right-handed leptons, the LRS model predicts the correct masses for the SM weak bosons, and ensures that the three new bosons are much heavier than the SM bosons.
It also ensures that the LR symmetry is broken down to the SM $SU(2)_L \times U(1)$ group, then the electroweak spontaneous symmetry breaking proceeds as before and the SM is recovered at low energies.
In the SM, the parity violation does not have a clear theoretical motivation, but in the LRS model it is indicated by the mass difference between the left-handed $W^{\pm}$ and Z bosons and the right-handed W_{R}, Z' bosons.

In the fermionic sector, with the addition of the $SU(2)_R$ group, the LRS model predicts new neutrinos with masses consistent with neutrino flavor oscillations. Three new right-handed neutrinos N_{R} arise naturally to form doublets of $SU(2)_R$ hypercharge with right-handed charged leptons. Using a mixture of Dirac (D_i) and Majorana (M_i, M_i') mass terms [68, 76], the Lagrangian

$$\mathcal{L} = \frac{1}{2} (\bar{\nu}_{L_i}\ \bar{\nu}_{R_i}) \begin{pmatrix} M_i' & D_i \\ D_i & M_i \end{pmatrix} (\nu_{L_i}\ \nu_{R_i})^T, \tag{1.10}$$

where i is the lepton generation and ν_L and ν_R are massive, pure left- and right-handed fermionic neutrino fields, leads the LRS model to predict non-zero masses for N_{R} and SM neutrinos.
The nonzero value of $\langle \Phi \rangle$ in Equation 1.9 leads to the Dirac masses D_i, and the expectation values of χ_L and χ_R defined in Equation 1.7 lead to the Majorana masses M_i' and M_i, resulting in

$$D_i \approx v,\ M_i' \approx 0,\ M_i \approx U_R \gg D_i,$$

which is consistent with $m_{W_{\mathrm{R}}} \gg m_W$.
Substituting v and U_R for the Dirac and Majorana masses and assuming negligible left-right

mixing, Equation 1.10 is diagonalized and yields the following neutrino mass eigenvalues:

$$\lambda_{i+} = M_i,\ \lambda_{i-} = \frac{D_i^2}{M_i}$$

The detectable states N_i and ν_i that participate in electroweak interactions are mixtures of the pure left- and right-handed neutrino fields:

$$\nu_i = \frac{1}{\sqrt{D_i^2 + M_i^2}}(M_i\nu_{L_i} - D_i\nu_{R_i}) = \nu_{L_i} - \frac{D_i}{M_i}\nu_{R_i}$$

$$N_i = \frac{1}{\sqrt{D_i^2 + M_i^2}}(D_i\nu_{L_i} + M_i\nu_{R_i}) = \nu_{R_i} + \frac{D_i}{M_i}\nu_{L_i}$$

with masses:

$$m_{\nu_i} = \lambda_{i-} = \frac{D_i^2}{M_i},\ m_{N_i} = \lambda_{i+} = M_i.$$

The LRS model predicts thus that the left-handed neutrinos ν_i have masses λ_{i-} and the right-handed neutrinos N_i have masses $\lambda_{i+} = M_i \gg D_i$, leading to a Majorana nature of these massive neutrinos.
Very light left-handed neutrinos, very heavy right-handed neutrinos, and negligible mixing between left- and right-handed states (suppressed by $\approx \frac{D_i}{M_i} \ll 1$), consistent with the experimental evidence [72, 77], are obtained with appropriate choices for D_i and M_i.
An explanation for how three generations of heavy N_{R} mix with the SM light neutrinos, and how the light neutrinos acquire masses that are inversely proportional to the mass of the N_{R}, is given by the "see-saw" mechanism [68, 69].

After the spontaneous symmetry breaking, the Yukawa interaction between quarks and the Higgs multiplet generates mass matrices that can be diagonalized such that

$$m_u = U_{uL} m_u U_{uR}^{\dagger},\ m_d = U_{dL} m_d U_{dR}^{\dagger}.$$

The CKM matrix $V_{CKM} = U_{uL}^{\dagger} U_{dL}$ has then been recovered and the right-handed analogue $V_R = U_{uR}^{\dagger} U_{dR}$, matrix that controls the branching ratios of the right-handed W into SM quarks and leptons, has been constructed. No constraints on the values of the matrix are put from the theory, then it is convenient to assume that they are similar to those of the CKM matrix.

1.3.1 Phenomenology of LRS model

The LRS model discussed here predicts massive Majorana neutrinos, provides an explanation for the parity violation in the weak interaction, and explains the baryon-antibaryon asymmetry of the universe while preserving all the aspects of the SM. Through interactions

mediated by the W_{R} and Z' boson, the LRS model predicts in fact more processes violating CP than the ones in the SM [78], predicting thus an asymmetry between the number of baryons and antibaryons that is closer to observations.
These features are maintained by specific realizations of the LRS model and distinguished by unique values of the free parameters of the model: the weak coupling constant g_R, the left-right symmetric energy scale U_R that sets the W_{R} mass, the masses M_i and D_i that set the N_{R} and SM ν masses, the three mixing angles θ_i, and the CP violating phase δ_R that define the W_{R} analogue of the CKM quark mixing matrix.
As stated before, the coupling g_R is assumed to be the same for all lepton flavors and equal to the SM weak coupling g_L in the simplified LRS model considered.
Unitarity constrains both the W_{R} and N_{R} masses to be $\lesssim 3000$ TeV [79] and the measured neutral kaon $K_L - K_S$ mass difference [80] excludes W_{R} bosons with $m_{W_{\mathrm{R}}} < 2.5$ TeV at 95% confidence level (CL).
The mass of N_{R} can be above or below $m_{W_{\mathrm{R}}}$, but as $m_{N_{\mathrm{R}}}$ decreases both the rate of mixing between the N_{R} and SM ν, and the left-handed component of N_{R} increases. The larger left-handed component of N_{R} thus increases the rate of $N_{\mathrm{R}} \to W^{\pm}\ell^{\mp}$.
If the mass of N_{R} is close to the Z boson mass, energetic SM neutrinos from $Z \to \nu\nu$ decays could mix into N_{R} states, producing a charged lepton through $pp \to Z \to \nu\nu \to \nu N_{\mathrm{R}} \to \nu W^{\pm}\ell^{\mp}$. So far, measurements sensitive to the $Z \to \nu\nu$ rate [81, 82] have not seen any deviations from SM predictions, so it is expected that $m_{N_{\mathrm{R}}} \gtrsim 90$ GeV.
At the LHC energies, only some specific realizations of the LRS model can be tested, given the following assumptions:

- the SM quarks and all right-handed leptons couple to the W_{R} and Z' bosons with the same strength as to the SM weak bosons. The W_{R} analogue of the CKM matrix is thus constrained to match the SM CKM matrix;
- the right-handed neutrinos N_{R} are lighter than the W_{R} boson, hence the W_{R} decays to the N_{R};
- the decay of the N_{R} preserves the flavor, hence only the processes $W_{\mathrm{R}} \to eN_e \to eeW_{\mathrm{R}}^{*}$ and $W_{\mathrm{R}} \to \mu N_\mu \to \mu\mu W_{\mathrm{R}}^{*}$ are allowed.

The W_{R} and Z' bosons can be searched for using data from proton-proton collisions produced at the LHC. The Z' boson has been searched for at LEP [83], which excluded masses below ≈ 1.65 TeV, as well as at LHC [84, 85], which excludes masses below ≈ 4.5 TeV, but since the W_{R} boson is lighter than the Z' boson, it is more likely to have a mass within the energy reach of LHC. The LRS model realizations are then tested by searching for evidence of the W_{R} boson, where the W_{R} decays to a pair of quarks or to a charged lepton and a heavy neutrino N_{R}.
The W_{R} decay to a quark pair has the highest branching fraction, $\mathcal{B}(W_{\mathrm{R}} \to qq) \approx 60\%$, but does not allow a measurement of the neutrino mass $m_{N_{\mathrm{R}}}$, while the W_{R} decay to a

charged lepton and a heavy neutrino N_R, with a branching ratio $\mathcal{B}(W_R \to \ell N_R) \approx 6-8\%$, allows a N_R mass measurement.
The search for the W_R boson in the $W_R \to \ell_1 N_R$ decay is the main subject of this thesis, as described in Chapter 4. In this decay, the N_R can decay to a Z boson and a light ν, or to a second charged lepton ℓ_2 and a virtual W_R^*.
The decay of the N_R to a charged lepton and two quarks through a virtual W_R^*, $N_R \to \ell_2 W_R^* \to \ell_2 q_1 q_2$, is the one considered in this analysis since it has the highest branching fraction, with $\mathcal{B}(N_R \to \ell qq) \approx 50\%$ and $\mathcal{B}(W_R \to \ell N_R \to \ell\ell qq) \approx 3-4\%$. Furthermore, it is possible to reconstruct the W_R invariant mass since, as a result of the absence of neutrinos in the final state, there is no energy loss. This decay also provides good m_{N_R} resolution because the energies of ℓ_2, q_1, and q_2 can be measured directly.
The production and decay of a W_R boson, $pp \to W_R \to \ell_1 N_R \to \ell_1 \ell_2 q_1 q_2$, with $\ell_1\ell_2 =$ ee, $\mu\mu$, is expected to produce events with two same flavor leptons and two quarks that hadronize into two jets, as shown in Figure 1.3 on the right.
Based on prior searches [86, 87], the W_R is also expected to be heavier than 2 TeV, so it decays to high energy leptons and jets. The mass of the W_R can be extracted from the dilepton-dijet invariant mass ($m_{\ell\ell jj}$), found by measuring the energies and trajectories of the leptons and jets.

1.3.2 Previous studies

The CMS Collaboration has performed Run 1 searches for W_R bosons at a center-of-mass energy of $\sqrt{s} = 7$ TeV [86] and 8 TeV [87]. The 8 TeV analysis has excluded W_R masses up to approximately 3 TeV at 95% CL, as shown in Figures 1.4 and 1.5. An excess of events in the data with respect to the prediction of only SM processes with a local significance of 2.8σ was observed in the $W_R \to$ eejj decay mode at $m_{eejj} \approx 2.1$ TeV, as shown in Figure 1.6. The excess did not appear to be consistent with signal events from the LR symmetric theory, shown by the red line for $m_{W_R} = 2.5$ TeV.
In the Run 2 search performed with data collected in 2015 [88], this excess was not confirmed and the observed number of events appeared to be consistent with the SM prediction, as shown in Figure 1.7. The analysis has excluded W_R bosons up to 3.3 TeV (3.5 TeV) in the electron (muon) channel with a N_R mass between 10% and 90% of the W_R mass at a 95% CL, as shown in Figures 1.8 and 1.9.
The ATLAS Collaboration has also carried out similar searches with similar results at $\sqrt{s} = 7$ TeV [89] and 8 TeV [90].

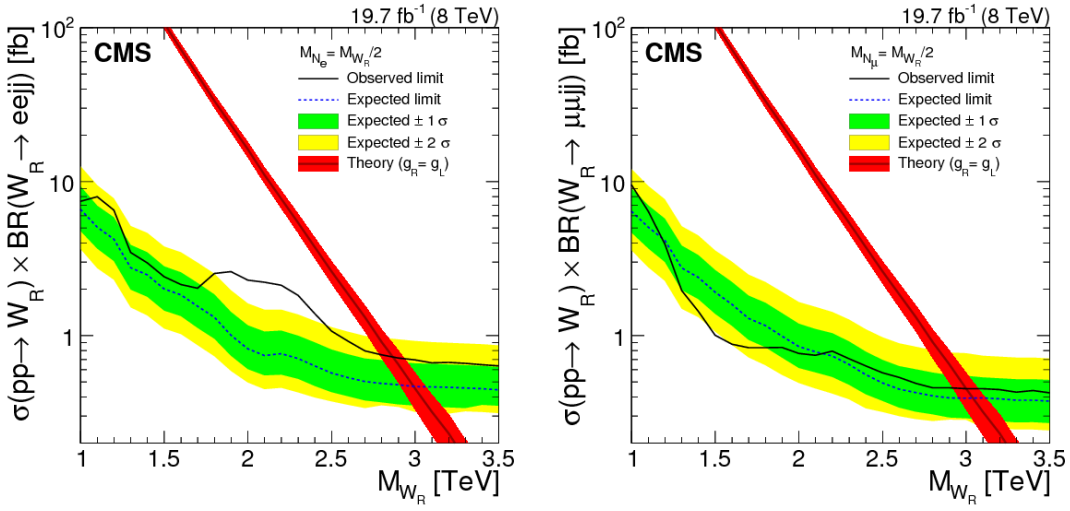

(a) *Electrons* (b) *Muons*

Figure 1.4: *The 95% CL exclusion limit for W_{R} boson production cross section times branching fraction, computed as a function of $m_{W_{\mathrm{R}}}$ assuming the right-handed neutrino has half the mass of the W_{R} boson, for the* 8 TeV *analysis. The signal cross section PDF uncertainties (red band surrounding the theoretical W_{R} boson production cross section curve) are included for illustration purposes only.*

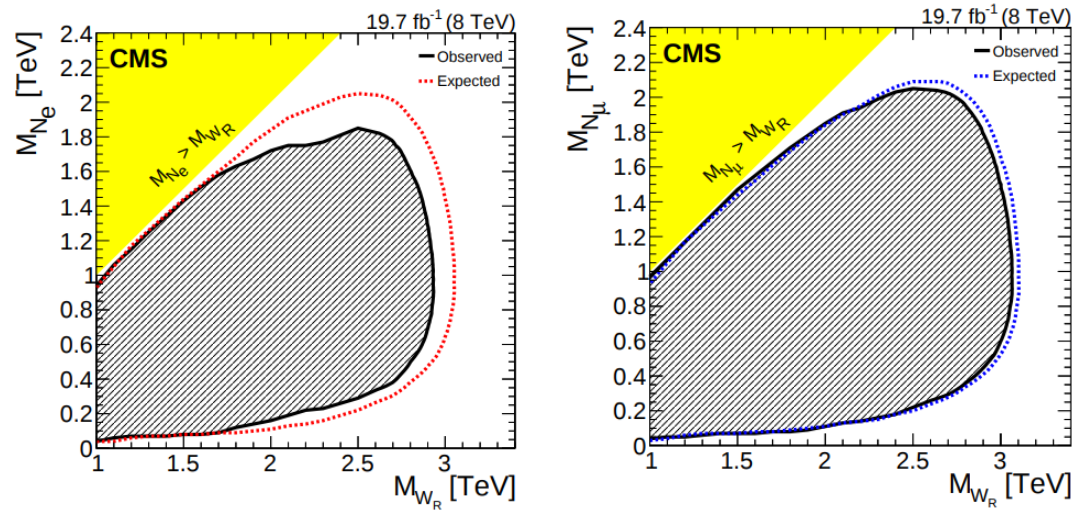

(a) *Electrons* (b) *Muons*

Figure 1.5: *The 95% CL exclusion region (hatched) in the ($m_{W_{\mathrm{R}}}$,$m_{N_{\mathrm{R}}}$) plane for the* 8 TeV *analysis. Neutrino masses greater than $m_{W_{\mathrm{R}}}$ (yellow shaded region) are not considered in this search.*

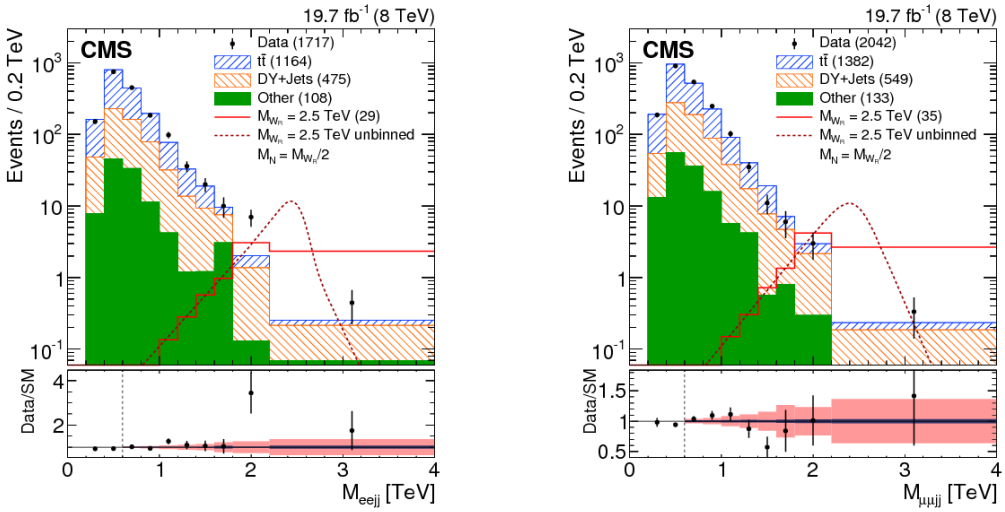

(a) *Electrons* (b) *Muons*

Figure 1.6: *Distribution of the invariant mass $m_{\ell\ell jj}$ for events in data (points with error bars) with $m_{\ell\ell} > 200$ GeV and for background contributions (hatched stacked histograms) from data control samples ($t\bar{t}$) and simulation for the 8 TeV analysis. The signal mass point $m_{W_R} = 2.5$ TeV, with $m_{N_R} = \frac{1}{2} m_{W_R}$, is included for comparison (open red histogram, and dotted line for the unbinned signal shape). The numbers of events from each background process and the expected number of signal events are included in parentheses in the legend, where the contributions from diboson and single top quark processes have been collected in the "Other" background category. The data are compared with SM expectations in the lower portion of the figure. The total background uncertainty (light red band) and the background uncertainty after neglecting the uncertainty due to background modeling (dark blue band) are included as a function of $m_{\ell\ell jj}$ for $m_{\ell\ell jj} > 600$ GeV (dashed line).*

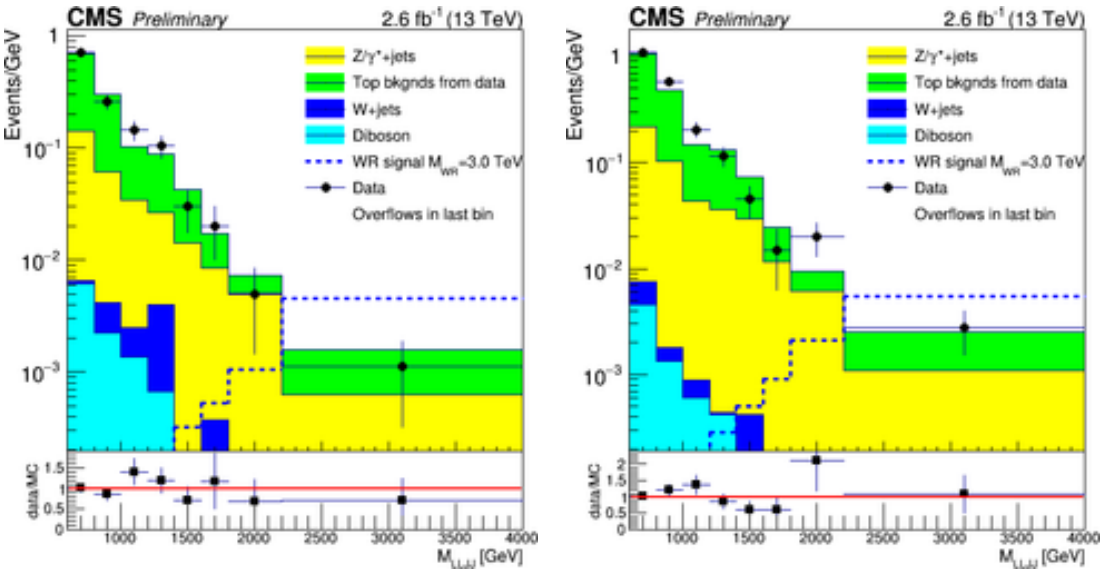

(a) *Electrons* (b) *Muons*

Figure 1.7: *The $m_{\ell\ell jj}$ distribution in the signal region for the 2015 analysis. For the W_{R} signal shown, $m_{N_{\mathrm{R}}} = \frac{1}{2} m_{W_{\mathrm{R}}}$ is assumed. The plot uses* 200 GeV *wide bins from* 600 *to* 1800 GeV*, then one bin spans* 1800 *to* 2200 GeV*, and finally the last bin includes all events above* 2200 GeV*. In addition, the bin contents are divided by the bin widths.*

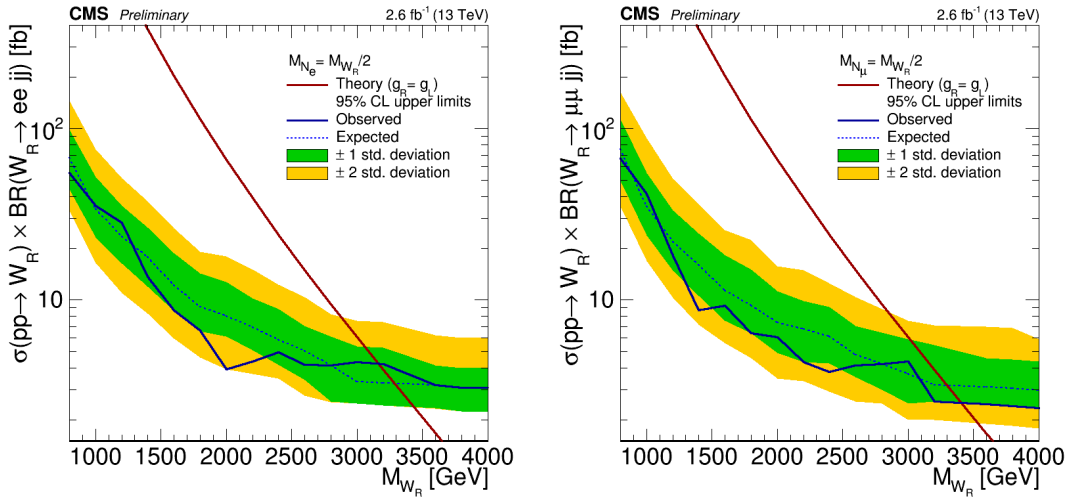

(a) *Electrons* (b) *Muons*

Figure 1.8: *The 95% CL exclusion limit for W_{R} boson production cross section times branching fraction, computed as a function of $m_{W_{\mathrm{R}}}$ assuming $m_{N_{\mathrm{R}}} = \frac{1}{2} m_{W_{\mathrm{R}}}$, for the 2015 analysis.*

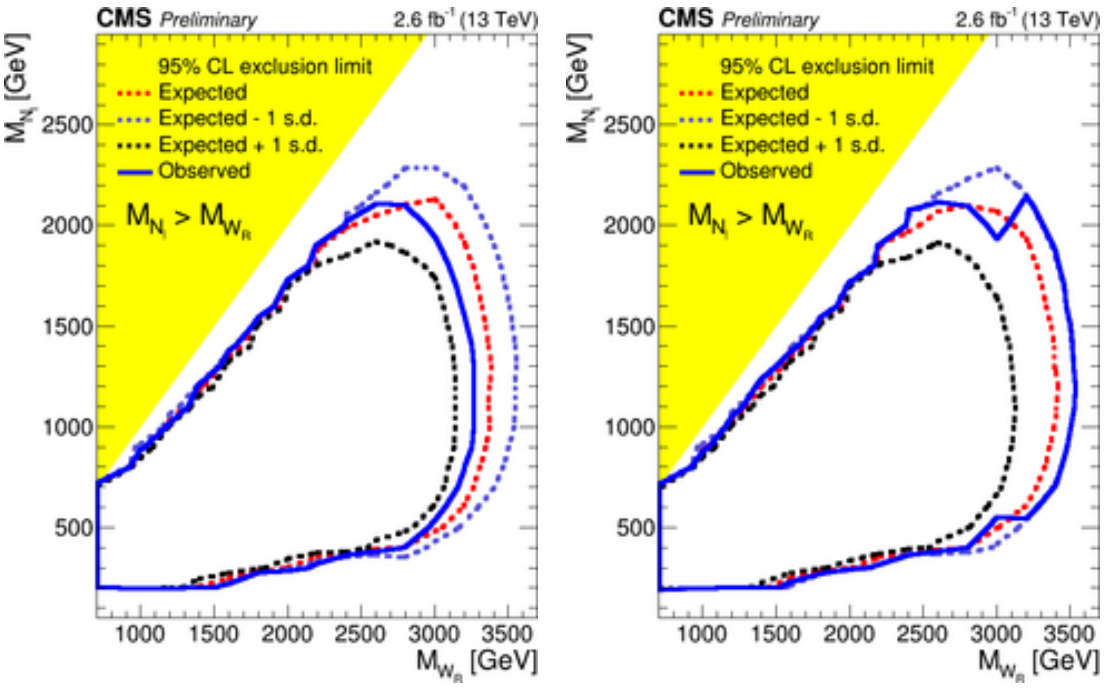

(a) *Electrons* (b) *Muons*

Figure 1.9: *The 95% CL exclusion region in the (m_{W_R},m_{N_R}) plane for the 2015 analysis. Neutrino masses greater than m_{W_R} (yellow region) are not considered in this search.*

Chapter 2

The Compact Muon Solenoid Experiment at LHC

2.1 The Large Hadron Collider

The Large Hadron Collider (LHC) [91, 92] is the most powerful particle accelerator ever built, designed to collide opposing particle beams of protons or heavy ions. Proposed and realized by the European Organization for Nuclear Research (CERN) from 1998 to 2008, it was built in order to look for an answer to the most fundamental questions of particle physics. It is an unprecedented machine in terms of energy, luminosity, size, complexity of experiments, cost, and involvement of human resources.
The primary goal of the LHC was to search for the Higgs boson, discovered in 2012 by the CMS and ATLAS Collaborations [93, 94]. Now it is to perform precision measurements of the Higgs properties in order to study the electroweak symmetry breaking. Furthermore, searches for new physics are possible at the energies of few TeV reached by the collisions at LHC, since interactions not described by the SM could be observed in various production and decay processes.

2.1.1 LHC design and detectors

The LHC was designed to study proton-proton collisions at a center-of-mass energy of 14 TeV with an instantaneous luminosity ($\mathcal{L}$) up to 10^{34} cm^{-2}s^{-1}, and lead-lead collisions at 2.76 TeV per nucleon with luminosity up to 10^{27} cm^{-2}s^{-1}.
The collider is placed in a circular tunnel 27 km long built between 1983 and 1988 for the Large Electron Positron Collider (LEP) and situated at a depth of about 100 m underground at the boundary between France and Switzerland, near the city of Geneva. The tunnel contains two adjacent and parallel beam pipes, where proton (or ion) beams travel in opposite directions around the ring. The two beams cross in four different points where

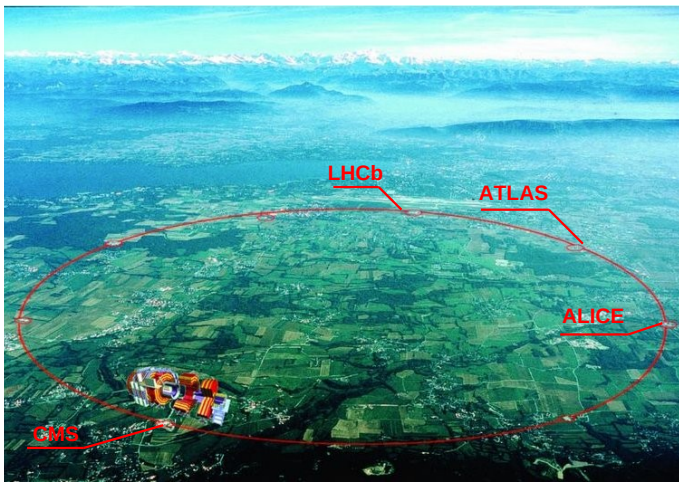

Figure 2.1: *View of the CERN site: the LHC tunnel with the four experiments located at each interaction point.*

the main experimental detectors are placed, as shown in Figure 2.1.
The use of two separate beams and the collisions between particles of the same charge require opposite magnet dipole fields in the two acceleration cavities. In total, over 1600 superconducting magnets are installed: 1232 dipole magnets 15 meters long and made of copper-clad niobium-titanium keep the beams on their circular path, while additional 392 quadrupole magnets 5–7 meters long are used to keep the beams focused, in order to maximize the chances of interaction in the four points where the two beams cross. Approximately 96 tonnes of liquid helium is needed to keep the superconducting magnets at their operating temperature of 1.9 K. The field in the magnets increases from 0.53 T to 8.3 T while the protons are accelerated from 450 GeV to 6.5 TeV.

In order to probe new physics up to the TeV energy scale, the following design features are needed:

- hadron collider: high energy collisions require massive particles with low synchrotron radiation (e.g. a proton loses about 7 keV per turn). In a $\sqrt{s} = 14$ TeV pp collision each parton carries a fraction $x \approx 0.15$–0.2 of the proton momentum, so the energy range which can be explored is $\sqrt{\hat{s}} = \sqrt{x_1 x_2 s} \simeq 1$–$2$ TeV. With respect to lepton colliders, hadron colliders have the advantage that proton acceleration to great energies is easier and that proton collisions, being quarks or gluons collisions, can scan a wide range of collision energies;

- proton-proton collisions: processes like Higgs production are dominated by gluon fusion, therefore the cross section is approximately the same for pp and $p\bar{p}$ collisions, but high intensity beams of protons are easier to accumulate with respect to proton-

Parameter	p-p	Pb-Pb
Circumference [km]	26.659	
Beam radius at interaction point [μm]	15	
Dipole peak field [T]	8.3	
Design center-of-mass energy [TeV]	14	1148
Design Luminosity [$\mathrm{cm^{-2}s^{-1}}$]	10^{34}	10^{27}
Luminosity lifetime [h]	15	4.2
Number of particles per bunch	$1.1 \cdot 10^{11}$	$7 \cdot 10^{7}$
Number of bunches	2808	592
Bunch length [mm]	53	75
Time between collisions [ns]	24.95	$124.75 \cdot 10^{3}$
Bunch crossing rate [MHz]	40.08	0.008

Table 2.1: *LHC design parameters for p-p and Pb-Pb collisions.*

antiproton beams;

- high luminosity: the cross section σ of a given process is determined by the formula $\sigma = R/\mathcal{L}$, where R is the event rate of the process which represents the number of collisions per unit of time and per cross-sectional area of the beams. The luminosity is specific to the collider parameters and it can be written as:

$$\mathcal{L} = \frac{f_{rev} \cdot n_b \cdot N_1 N_2 \cdot \gamma_r}{A} \cdot F$$

where $f_{rev} = 11$ kHz is the revolution frequency of the n_b proton bunches per beam, N_1 and N_2 are the number of protons in the colliding bunches, $A = 4\pi\epsilon_n\beta*$ is the transverse area of the proton beams, with ϵ_n the normalized transverse beam emittance and $\beta* = O(0.5)$ m the beta function at the collision point which measures the beam focalization, γ_r is the relativistic gamma factor which correct $\beta*$, and F is the geometric luminosity reduction factor ($\approx$ 0.8–0.9). This reduction factor is due to the crossing angle between the two beams at the interaction point, needed to reduce the long-range interactions between the beams through electromagnetic fields to an acceptable level. To compensate for the low cross section of the interesting processes, the LHC must have a very high luminosity, reached through a high number of bunches per beam ($n_b = 2808$) and a high number of protons per bunch ($N_1 = N_2 = 1.15 \times 10^{11}$) colliding with a very short bunch crossing interval of 25 ns (bunch crossing rate of 40 MHz).

The main parameters of the LHC are summarized in Table 2.1 and the cross sections for different known SM processes in proton-proton collisions at the LHC are shown in Figure 2.2 as a function of the center-of-mass energy.

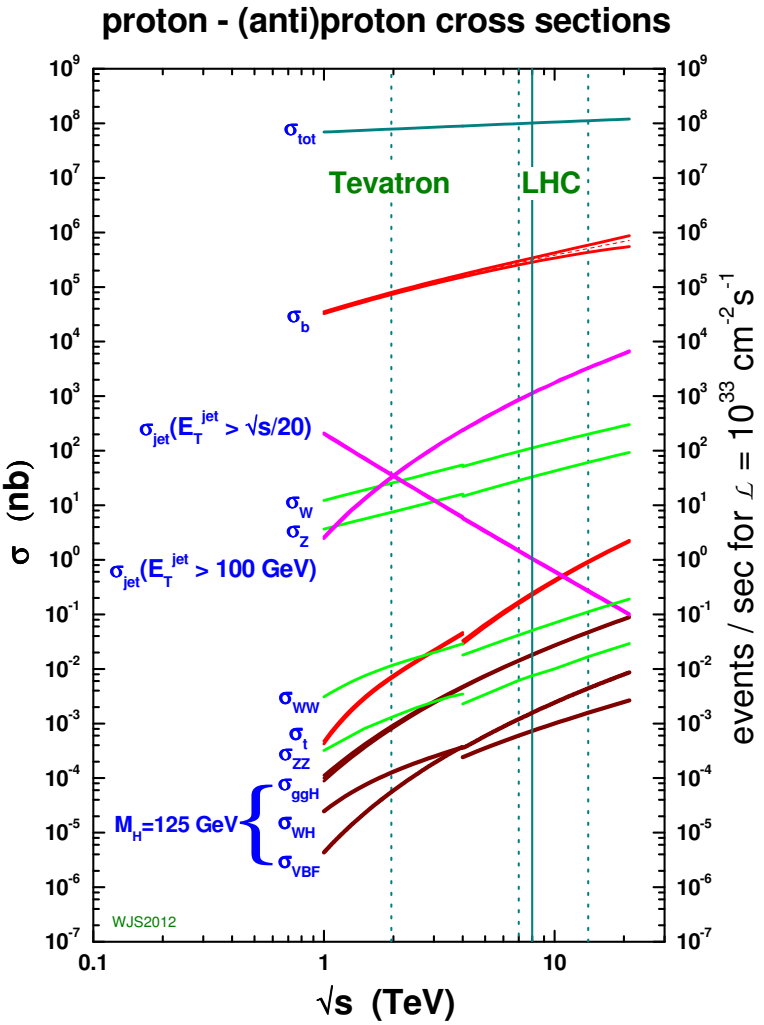

Figure 2.2: *Expected production cross section for signal and background processes at hadron colliders as a function of the center-of-mass energy [95].*

The record-breaking collision parameters of the LHC have important consequences on the design of the detectors. Under nominal conditions, the number of inelastic collision events is of the order of 10^9 per second, with approximately 20 collisions per bunch crossing. The occurrence of such overlapping proton-proton interactions is called *in-time pileup* and to distinguish particles coming from different interactions a high granularity is required in the detectors. Fast response and good time resolution are also needed in order to distinguish events from consecutive crossings happening every 25 ns, i.e. avoiding the phenomena of consecutive signals overlap called *out-of-time pileup*.

The LHC is the final stage of a succession of accelerators, as shown in Figure 2.3. Each accelerator boosts the speed of a beam of particles, before injecting it into the next one in the sequence.
Considering proton-proton collisions, the protons are obtained removing the electrons from hydrogen atoms. They are first accelerated to an energy of 50 MeV in the linear accelerator (LINAC2) and to 1.4 GeV in the Proton Synchrotron Booster (PSB). They then reach 26 GeV in the Proton Synchrotron (PS) and 450 GeV in the Super Proton Synchrotron (SPS), before finally reaching the LHC. Protons are accelerated by 16 radio-frequency cavities in the LHC, where the electromagnetic field oscillates at 400 MHz for about 20 minutes before reaching the maximum energy.
Considering lead-lead collisions, lead ions for the LHC start from a source of vaporised lead and enter LINAC3 before being collected and accelerated in the Low Energy Ion Ring (LEIR). Then they follow the same route to maximum acceleration as the protons.
At the CERN complex there are beam extraction lines that provide dedicated beams to various experiments, and the proton or ion beam from the PS and the SPS can be sent to a fixed target providing secondary beams of electrons, muons and pions to several areas dedicated to fixed target experiments or detector testing, e.g. for LHC upgrade project or for R&D.

The LHC hosts four main experiments. Each one has a different subdetector composition and geometry, specialized to study an area of particle physics:

- ATLAS (*A large Toroidal LHC ApparatuS*) is a general-purpose detector designed to cover a wide physics program with optimized sensitivity for Higg boson searches and possible physics BSM at the TeV scale. It is built with a cylindrical geometry surrounding the beam pipe and it uses a toroidal magnetic field of 2–4 T produced by three sets of air-core toroids complemented by a small solenoid in the inner region;

- CMS (*Compact Muon Solenoid*) is a general-purpose detector and has a cylindrical geometry, like ATLAS. Their subdetectors are optimized for the reconstruction of high energy objects with great efficiency and accuracy. It differs from ATLAS because it bends the charged particle trajectories using a solenoidal field of 3.8 T generated by the world's largest superconducting solenoid;

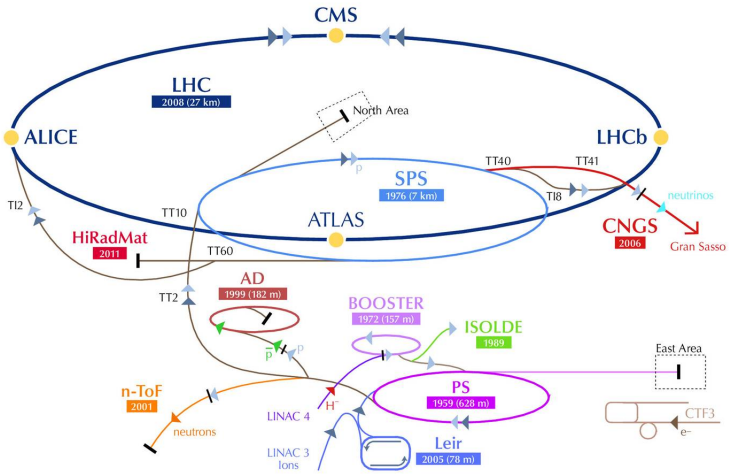

Figure 2.3: *CERN accelerator complex.*

- LHCb (*Large Hadron Collider beauty experiment*) studies the heavy quark and heavy meson physics with a particular attention to the b quark and its mesons, and aims to perform precision measurements on CP violation. It does not surround the entire collision point, but it stretches for 20 m along the beam pipe covering the forward region;

- ALICE (*A Large Ion Collider Experiment*) is a heavy-ion dedicated detector. It has been conceived to study the physics of strongly interacting matter at extreme energy densities and high temperature, where the formation of a new phase of matter, the quark-gluon plasma, is expected. The existence of such a phase and its properties are key issues in QCD for the understanding of quarks and gluons confinement.

Two of these main experiments, ATLAS and CMS, are designed for a high luminosity regime, in order to catch the rare events of their physics programs. Furthermore, at ≈ 100 m from the interaction points of CMS and ATLAS, two forward detectors are placed: TOTEM (*TOTal cross section, Elastic scattering and diffraction dissociation Measurement*) and LHCf (*LHC forward experiment*). They are conceived to study the physics processes in the region very close to the particles beam, at extremely low angles. This forward physics is useful in particular to study the underlying events, energy and particle flow distributions, and photon-induced processes.

2.1.2 LHC operations for pp collisions

The first proton-proton collisions were produced by the accelerator in 2009 and the first collisions at a center-of-mass energy of 7 TeV, the highest ever reached at a particle

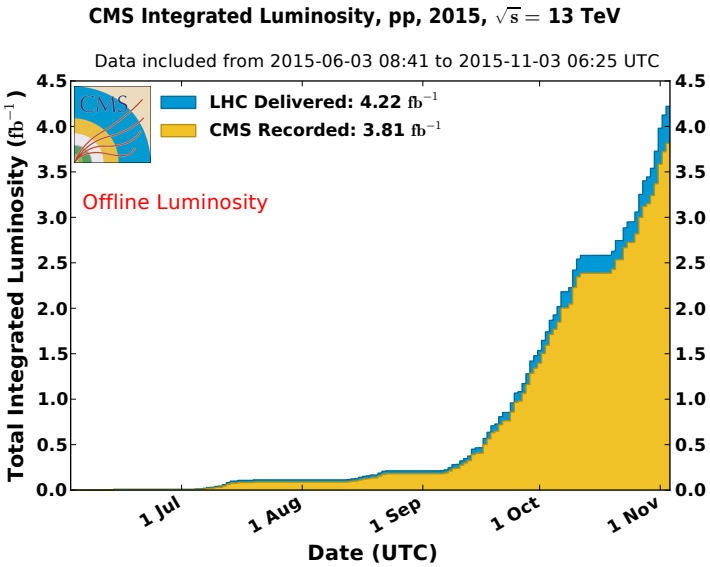

Figure 2.4: *Integrated luminosity delivered by the LHC (in blue) and recorded by CMS (in yellow) in 2015 proton-proton collisions.*

collider, were recorded at the beginning of 2010. The LHC has operated through the rest of 2010 at the same $\sqrt{s} = 7$ TeV increasing the instantaneous luminosity by increasing the intensity of the beam current and the number of bunches per beam, keeping a 50 ns bunch spacing and having $\approx 2-4$ pileup interactions. The total integrated luminosity delivered in 2011 was 6.1 fb^{-1} and it reached 23.3 fb^{-1} in 2012, incrementing the center-of-mass energy up to 8 TeV. This first data taking, with $\approx 10-30$ pileup interactions, was referred to as Run 1 and the first 5 fb^{-1} of 2012 allowed to accomplish the Higgs boson discovery.

A two years upgrade period called Long Shutdown 1 (LS1) was used to technically prepare LHC for running at $\sqrt{s} = 13$ TeV, upgrading the subdetectors system of the various detectors installed at LHC to improve their performance in view of the higher energy and luminosity runs.

The first Run 2 beams at 13 TeV were obtained in 2015, started with 50 ns collisions before moving to the nominal bunch spacing of 25 ns. In total, a data sample corresponding to 4.2 fb^{-1} was delivered in 2015, as shown in Figure 2.4, with $\approx 10-20$ pileup interactions. In 2016 the LHC, at $\sqrt{s} = 13$ TeV and with a bunch spacing of 25 ns, was able to reach even more than its nominal luminosity of 1.4×10^{34} cm^{-2}s^{-1}. The proton-proton data taking ended with a total delivered integrated luminosity of 41.1 fb^{-1}, as shown in Figure 2.5, and with $\approx 20-40$ pileup interactions. The 2017 proton-proton data taking, still with $\sqrt{s} = 13$ TeV and bunch spacing of 25 ns, delivered a total integrated luminosity of 50 fb^{-1}, as shown in Figure 2.6, with $\approx 20-60$ pileup interactions.

Figure 2.7 shows the cumulative integrated luminosity delivered to the CMS experi-

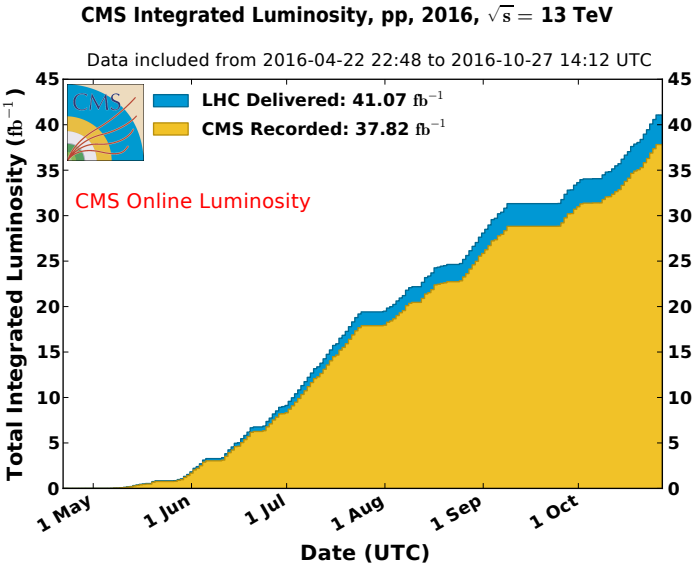

Figure 2.5: *Integrated luminosity delivered by the LHC (in blue) and recorded by CMS (in yellow) in 2016 proton-proton collisions.*

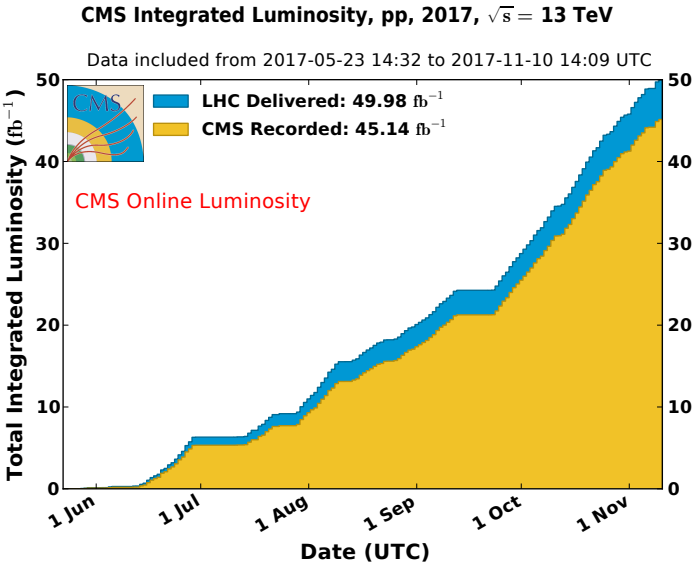

Figure 2.6: *Integrated luminosity delivered by the LHC (in blue) and recorded by CMS (in yellow) in 2017 proton-proton collisions.*

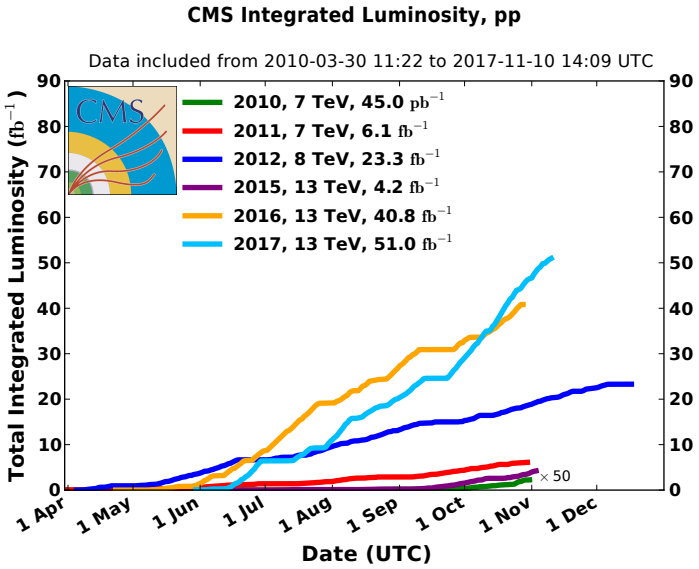

Figure 2.7: *Cumulative integrated luminosity delivered by LHC to CMS during stable beams for proton-proton collisions.*

ment in every year of data taking. The luminosity recorded by the CMS experiment is $\approx 90\%$ of the one delivered by the LHC but not all data are used for physics analyses. The data certified as good for physics, taken when all subdetectors, triggers and physics objects (tracks, electrons, muons, photons, jets, and missing energy) show the expected performance, are $\approx 85\%$ of the delivered ones.

The LHC Run 2 is scheduled till 2018 and it will be followed by the Long Shutdown 2 (LS2), period during which the machines will be upgraded to deliver designed center-of-mass energy ($\sqrt{s} = 14$ TeV) and instantaneous luminosity of 2×10^{34} cm^{-2}s^{-1}.

The LHC Run 3, which will end the LHC Phase I delivering a total integrated luminosity of about 300 fb^{-1} to the experiments, will last from 2021 till 2023, then from 2024 there will be the Long Shutdown 3 (LS3), after which the LHC Phase II in preparation of the High Luminosity LHC (HL-LHC) will start, as shown in Figure 2.8. In this second phase of the LHC physics program, the accelerator will provide the experiments an additional integrated luminosity of about 3000 fb^{-1} over 10 years of operations, allowing to enlarge the search region for new particles and to extend the properties studies of the Higgs boson.

2.1.3 HL-LHC

The LHC program foresees a high-luminosity phase (HL-LHC) [96] starting from 2026. The proposed operating scenario for the upgrade of the LHC accelerator complex is to

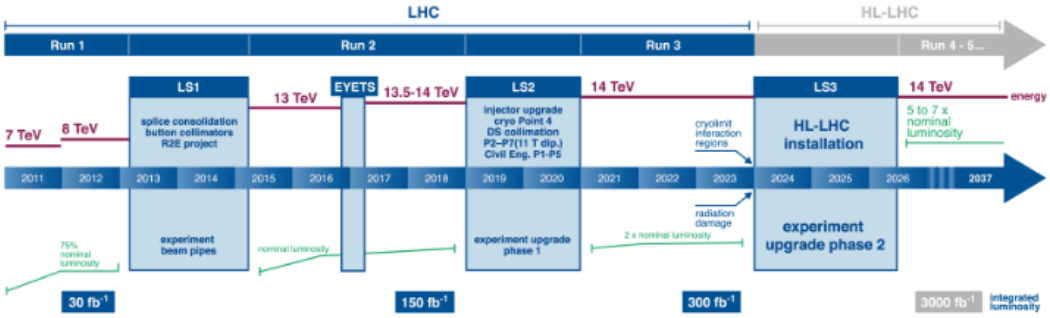

Figure 2.8: *Timeline for LHC and HL-LHC.*

	Design	**Current state**	**Upgrade**
E_{beam} [TeV]	7	6.5	7
L_{inst} [$\mathrm{cm^{-2}s^{-1}}$]	10^{34}	(1.0–1.4) $\times 10^{34}$	5×10^{34}
L_{int} [$\mathrm{fb^{-1}}$] 10 years operation	300	300–500 (≈ 50/year)	3000 (≈ 250/year)
β^* [cm]	50	30–40	15
PU	20	40–60	140–200

Table 2.2: *LHC design, current and upgrade parameters.*

provide collisions with an instantaneous luminosity of at least 5×10^{34} $\mathrm{cm^{-2}}$ $\mathrm{s^{-1}}$ and to accumulate a total dataset of about 3000 $\mathrm{fb^{-1}}$. The integrated luminosity, needed for new physics searches and for precise measurements of the Higgs boson couplings and other rare SM processes, will then be about ten times the expected luminosity of the first twelve years of the LHC.

The peak luminosity of 7.5×10^{34} $\mathrm{cm^{-2}}$ $\mathrm{s^{-1}}$, which is roughly four times the current value, will be achieved by increasing the beams intensities and by squeezing the two beams more at the interaction points. This will lead to a higher number of collisions occurring within the same bunch crossing, increasing the average number of collisions (pileup) to 140–200 at HL-LHC, a factor of four larger than the current Run 2 values of 40–60.

The main parameters of the LHC for the current state and the upgrade are summarized in Table 2.2.

The HL-LHC will be an highly challenging environment also for the unprecedented levels of radiation, up to six times higher than for LHC. The detectors will then need an upgrade for the HL-LHC to maintain performance comparable to Run 2 in an environment with high levels of pileup and radiation, improving the event reconstruction and the radiation resistance of the detectors components.

2.2 The CMS experiment

The Compact Muon Solenoid experiment [93, 97] is designed to investigate a wide range of particle physics processes and thus it requires excellent reconstruction and identification for leptons, photons, jets, and missing energy, together with excellent momentum and energy resolution. Moreover, the high flux of particles coming from proton-proton collisions can damage some detector components, especially in the inner tracker and forward calorimeters, thus the detector has to be radiation resistant. In order to handle the LHC bunch spacing of 25 ns, it has to provide good timing resolution requiring high-performance readout electronics, and, in order to distinguish particles coming from the main proton-proton interaction from particles coming from pileup interactions, it requires a high number of channels.

The CMS detector consists of a series of subdetectors which allow an excellent reconstruction of the charged particle tracks and measurement of their momentum resolution thanks to a high quality tracking system, a precise measurement of photons and electrons energy with a high resolution scintillating crystals-based electromagnetic calorimeter (ECAL), a good measurement of charged and neutral hadrons energy with a sampling hadronic calorimeter (HCAL), and a reliable identification of the muons by a combination of inner tracking and information from muon chambers. The inner tracking system also allows a precise localization of the vertex of the primary interaction, which is an essential feature in the scenario of high luminosity collisions causing high pileup of events.
A schematic view of the detector is shown in Figure 2.9. The detector structure of CMS is made of several cylindrical layers coaxial to the beam axis (the *barrel layers*) closed at both ends by detector disks orthogonal to the beam direction (the *endcaps*) to ensure optimal hermeticity, in order to capture every particle emerging from the collisions.

The main feature of the CMS detector is the 12.5 m long superconducting solenoid. It is the central device around which the experiment is organized, leading to a very compact design of the total apparatus which has overall length of 21.6 m, diameter of 14.6 m and total weight of about 14000 tons. The purpose of the magnet is to bend the trajectories of the particles emerging from the vertex where the high-energy collisions take place. In order to achieve a good momentum resolution for momenta up to 1 TeV, a strong solenoidal magnetic field, combined with high-precision position measurement in the tracker and in the muon system, is needed. The superconducting magnet has been designed to reach a 4 T magnetic field in the inner region, storing about 2.5 GJ of energy (Figure 2.10), and operates at a temperature of 4 K, ensured by the liquid helium cooling system. At such temperatures, the niobium-titanium cable becomes superconducting, allowing a 20 kA current to flow without appreciable loss over time. The magnet coil, with a diameter of 5.9 m, is large enough to accommodate the tracking system and the calorimeters within its volume and is contained in a vacuum cylinder that isolates it from the external environment. The steel return yoke, placed outside the cylinder and consisting of five barrel layers and

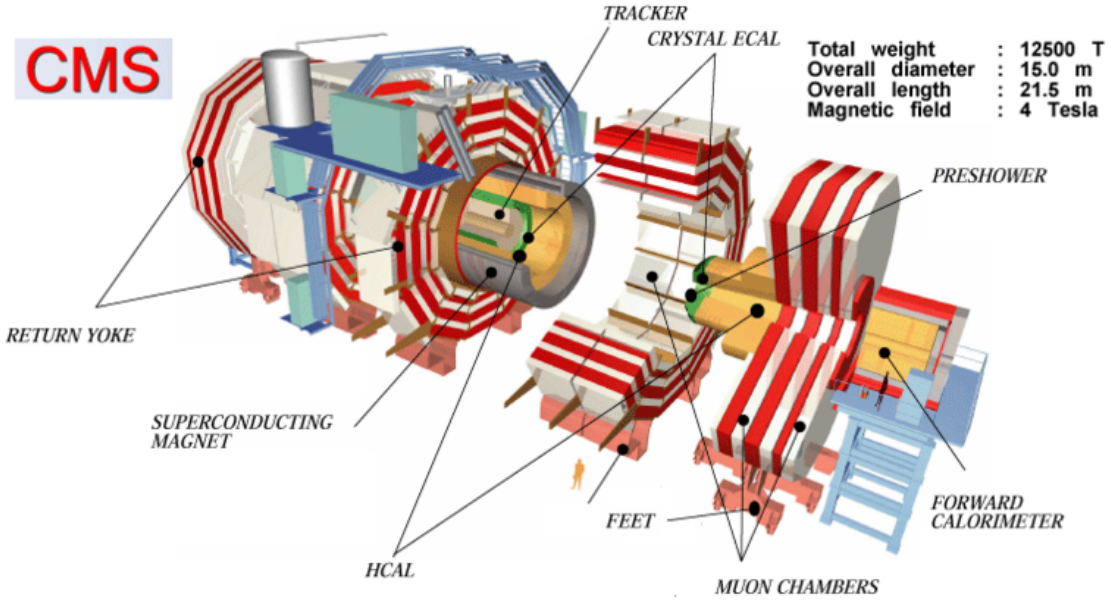

Figure 2.9: *Schematic picture of the CMS experiment at the LHC: the beams travel in opposite directions along the central axis of the CMS cylinder colliding in the middle of the CMS detector.*

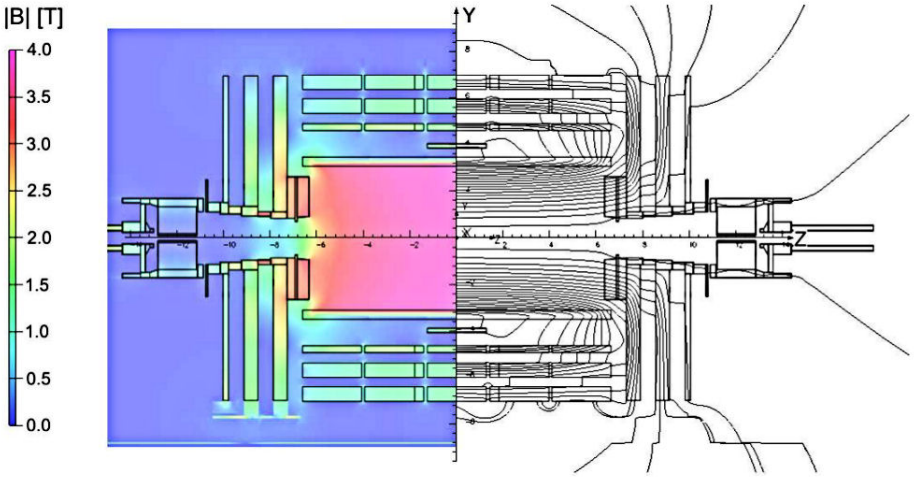

Figure 2.10: *The superconducting magnet and the generated magnetic field.*

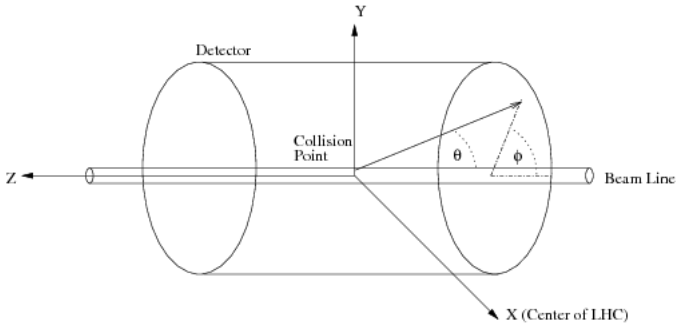

Figure 2.11: *Coordinate system of the CMS detector.*

three disks for each endcap, is necessary to contain and to guide the return magnetic field of 1.8 T present outside the solenoid volume, which otherwise would get lost. It contains the muon detectors, composed by 4 stations of drift tube detectors in the barrel region, 4 stations of cathode strip chambers in the endcaps, and 9 layers of resistive plate chambers, 6 in the barrel and 3 in the endcaps.

Coordinate conventions

The CMS experiment uses a cylindrical coordinate system whose origin is at the nominal interaction point inside the detector, as shown in Figure 2.11. The direction of the z axis is chosen along the beam and it is referred to as longitudinal. The x axis is horizontal and points towards the center of the LHC ring while the y axis is vertical and points upwards. The $x-y$ plane, orthogonal to the beam line, is called transverse plane and the radial coordinate is denoted by r. According to these definitions, the momentum of a particle can be divided in two components: the longitudinal momentum p_z and the transverse momentum p_T, which can be written as $p_T = \sqrt{p_x^2 + p_y^2}$, with $\vec{p_T} = (p_x, p_y)$. The *rapidity* of a particle of energy E is defined as:

$$y = \frac{1}{2} \ln \frac{E + p_z}{E - p_z}$$

and it is used for describing angular distribution of particle momentum. For ultrarelativistic particles ($p \gg m$) it can be approximated by the *pseudorapidity*:

$$\eta = -\ln(\tan \frac{\theta}{2})$$

which only depends on the polar angle θ of the particle momentum, measured with respect to the z axis with values in $[0, \pi]$. The angular distance between two particles can be

defined as:

$$\Delta R = \sqrt{\Delta\phi^2 + \Delta\eta^2}$$

where ϕ is the azimuthal angle, measured in the $x-y$ plane from the x axis, with values $[-\pi, \pi]$.
In proton-proton collisions, the interacting partons carry an unknown fraction of the proton momentum. Experimentally, it is thus not possible to define the total energy of an event and its missing energy (the imbalance of the total energy measurement in the collision). All the interesting physics observables are then measured in the plane transverse to the beamline. The transverse energy is defined as $E_T = E\sin\theta$ and the missing transverse energy is denoted with E_T^{miss}. Likewise, the transverse momentum $p_T = p{\cdot}\sin\theta$ is measured instead of the longitudinal momentum $p_z = p{\cdot}\cos\theta$. The transverse momentum of a particle of charge $Q = z \cdot e$ going through a magnetic field B with an helicoidal trajectory of radius R can be expressed by the relation:

$$p_T[GeV] = 0.3 \cdot z \cdot B[T] \cdot R[m]\,.$$

2.2.1 The tracker

The inner tracking system [98] is the CMS innermost subdetector and the closest to the interaction point. It extends in the region of $|\eta| < 2.5$, with $4.3 < r < 120$ cm and $|z| < 270$ cm, and it is based on several layers of silicon semiconductor detectors that cover a total surface of 210 m^2. It has a concentric layout, as shown in Figure 2.12: silicon pixel detectors are placed closest to the interaction point ($r \leq 10$ cm) in order to provide the most precise 3D position measurement in a region with a high particle density, silicon microstrips are used in the region $20 < r < 55$ cm where the particle flux decreases, and larger pitch microstrips are placed in the outermost region of the tracker ($r > 55$ cm).
The main purpose of the CMS tracker is an efficient reconstruction of charged tracks and interaction vertices together with the measurement of charged particles momentum, important tools for identifying signal events and rejecting background. Its major requirements are:

- robustness of its components to the radiation exposure, since the large number of particles created in the collisions exposes the tracking system to a large radiation damage. In order to limit this damage, both pixel and microstrip detectors are kept at a working temperature of $-10°$C;
- fast response of the detectors, given the high track population during the LHC collisions with one event every 25 ns;
- minimization of the crossed material, with the aim of reducing photons conversion, electrons energy loss via bremsstrahlung, and the multiple Coulomb scattering of

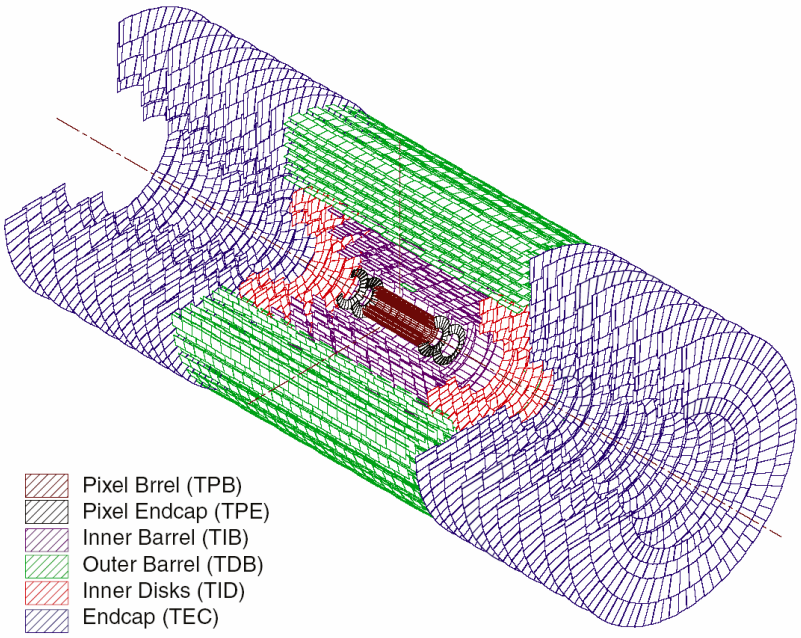

Figure 2.12: *View of the silicon tracker.*

charged particles crossing the detector, that adversely affect the position resolution of the tracker;

- perfect alignment, internal of its components and with the muon system, in order to provide a reliable measurement of the particle momentum;
- fine spatial granularity, requested by the need to achieve a high precision in the measurements of the tracks.

The tracker detector was designed in order to fulfill these requirements, allowing:

- high tracking efficiency, of at least 95% for charged tracks with $p_T > 10$ GeV, and low rate of fake tracks (i.e. reconstructed tracks that do not correspond to any real track) in the region $|\eta| < 2.5$;
- high momentum resolution for isolated tracks:

$$\frac{\delta p_T}{p_T} = (1.5 \cdot p_T[TeV] \oplus 0.5)\% \quad \text{for } |\eta| < 1.6\,,$$

$$\frac{\delta p_T}{p_T} = (6.0 \cdot p_T[TeV] \oplus 0.5)\% \quad \text{for } |\eta| < 2.5\,,$$

as measured in data [99];

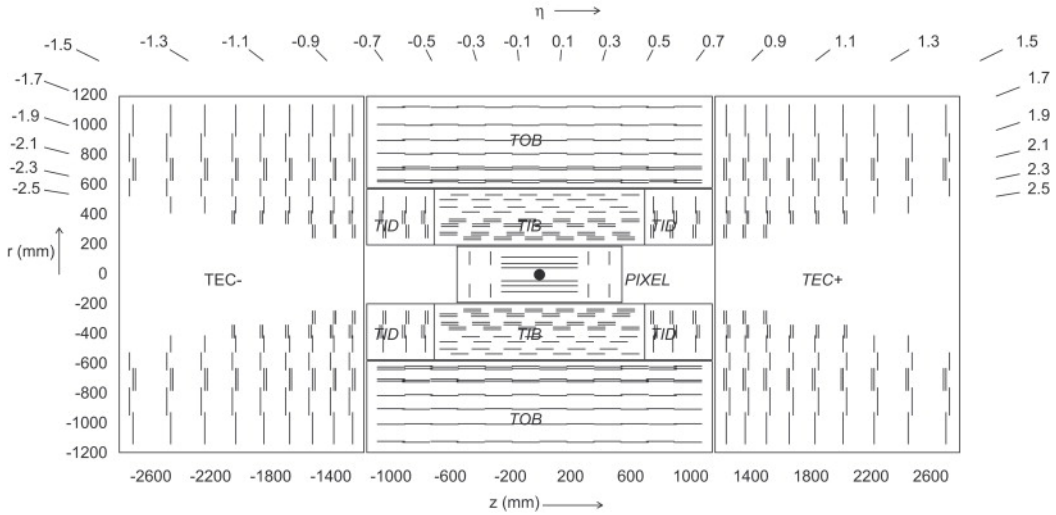

Figure 2.13: *Overview of the CMS tracker, where each line represents a detector module.*

- high spatial resolution, from 10 μm to 20 μm;
- fast (below 10 ns) collection of the charge deposited by the particles on the sensitive elements;
- high resolution for both transverse and longitudinal impact parameter: $\sigma(d_{xy}) = 35$ μm and $\sigma(d_z) = 75$ μm.

A scheme of the tracking system is shown in Figure 2.13.
A relatively large amount of material in the detector results from the large amount of silicon in the inner tracker combined with the required electronics, which lead to a substantial requirement for cabling and cooling services. The estimated material budget is shown in Figure 2.14 as a function of pseudorapidity: it ranges from about 0.4 radiation lengths in the very central barrel to a peak of about 1.8 radiation lengths in the vicinity of $|\eta| = 1.5$, near the barrel-endcap transition region.

2.2.1.1 The pixel detector

The pixel tracker consists of three 53.3 cm long barrel layers and two endcap disks on each side of the barrel section, as shown in Figure 2.15.
The innermost barrel layer has a radius of 4.4 cm, while for the second and third layer the radii are 7.3 cm and 10.2 cm, respectively, extending in $|z| < 26.5$ cm. The layers are composed of modular detector units (called *modules*) placed on carbon fiber supports (called *ladders*). Each ladder includes eight modules, consisting of thin (285 μm) segmented

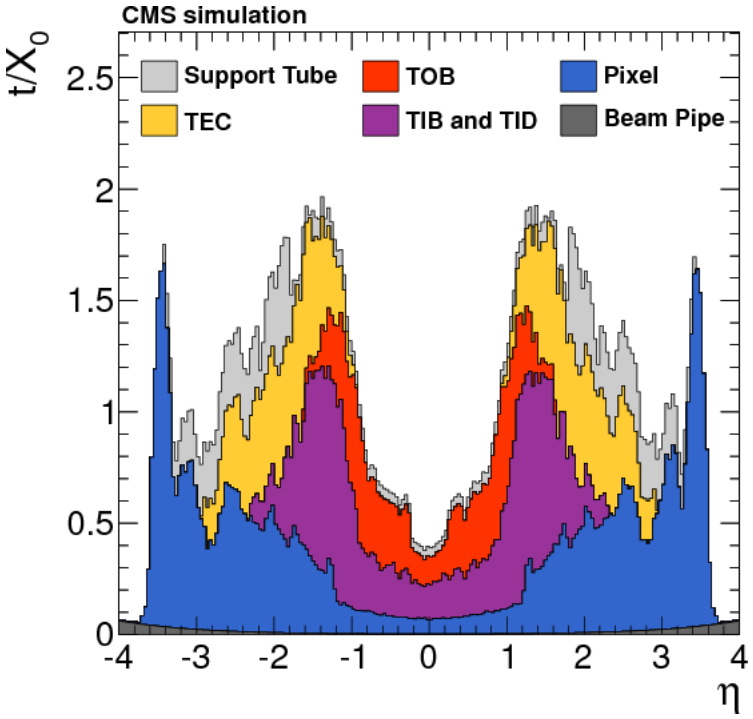

Figure 2.14: *Total thickness t of the material of each of the subsystems of the CMS tracker, together with contributions from the beam pipe and from the support tube that surrounds the tracker, expressed in units of radiation length X_0 as a function of pseudorapidity η. The configuration shown in the picture reflects the one prior the 2017 upgrade of the pixel detector, that significantly reduces the material budget in the forward region.*

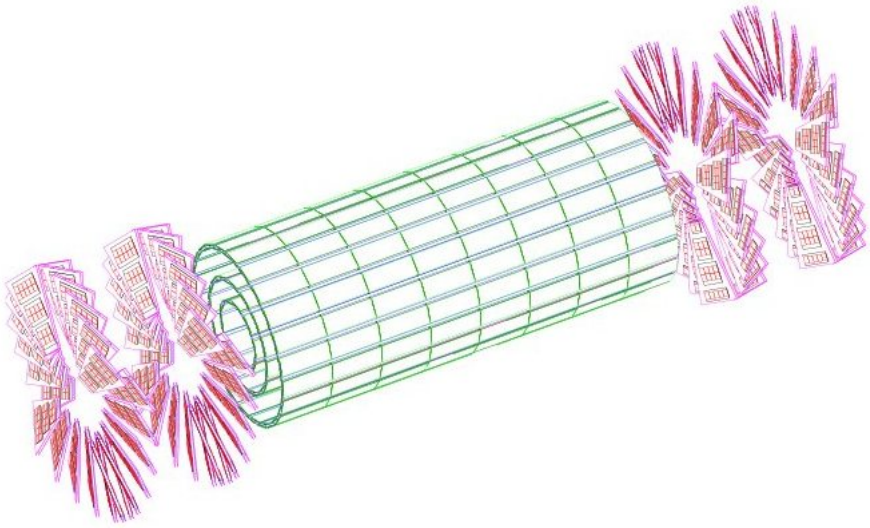

Figure 2.15: *The pixel detector: the barrel section and the two disks of the endcaps.*

silicon sensors with highly integrated readout chips (ROC) connected by Indium bump-bonds. Each ROC serves a 52×80 array of pixels. The total area covered with pixels is about 0.92 m^2.

The Barrel Pixel (BPIX) region is composed of 672 full modules and 96 half modules, each including 16 and 8 ROCs, respectively. The number of pixels per module is 66560 (full modules) or 33280 (half modules) and the total number in the barrel section is 47923200. The Forward Pixel (FPIX) endcap disks, extending from 6 cm to 15 cm in radius, are placed at $z = \pm 34.5$ cm and $z = \pm 46.5$ cm. Disks are split into half-disks, each including 12 trapezoidal blades arranged in a turbine-like geometry. Each blade is a sandwich of two back-to-back panels. Rectangular sensors of five sizes are bump-bonded to arrays of ROCs, forming the so-called "plaquettes". Three (four) plaquettes are arranged on the front (back) panels with overlap to provide full coverage for charged particles originating from the interaction point. The endcap disks include 672 plaquettes (270 μm thick), for a total of 17971200 pixels. The minimal pixel cell area is dictated by the readout circuit surface required for each pixel.

The pixel tracker is composed of approximately 66 million pixel cells with a size of 150 μm $\times$100 μm and spread across 1440 modules, allowing a fine 3D vertex reconstruction. Both transverse ($r\phi$) and longitudinal (z) coordinates are important in localizing secondary decay vertices, and this is why a nearly square pixel shape is adopted.
The deposited charge of a charged particle crossing the module is often shared among several pixels, with the amount of charge deposited in each pixel inversely related to the

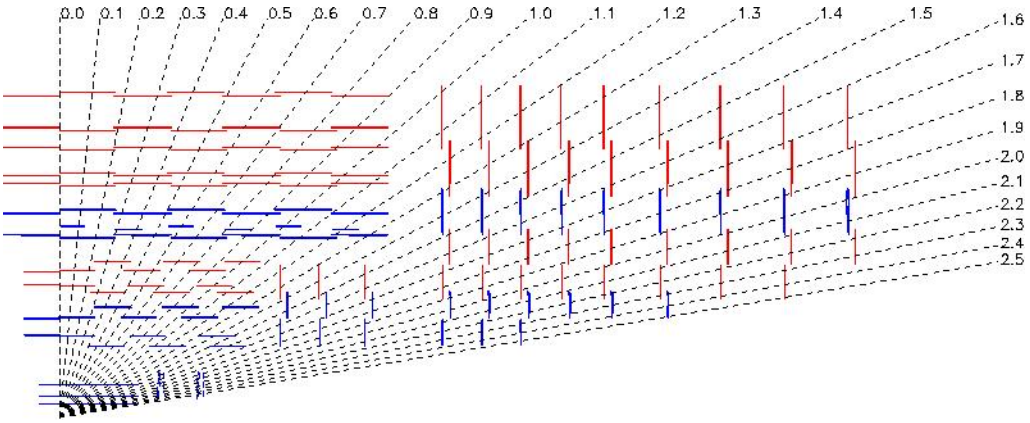

Figure 2.16: *Schematic view of the strip tracker.*

distance between the particle position and the pixel. A measurement of the charge sharing between adjacent pixels enables the interpolation between pixels and then improves the spatial resolution, allowing the single hit position resolution to be smaller than the dimension of a single pixel.

2.2.1.2 The strip detector

Outside the pixel detector, the strip tracker is made of 10 layers of silicon microstrip sensors, as shown in Figure 2.16. The full tracker consist of about 9.3 million strips across 15148 modules and provides precise measurements in only two-dimensions, with most strips oriented perpendicular to the ϕ direction.

The barrel region ($|\eta| < 1.6$) is divided into two parts: the Tracker Inner Barrel (TIB), covering $20 < r < 55$ cm, and the Tracker Outer Barrel (TOB), covering $55 < r < 120$ cm. The TIB is composed of 4 layers of silicon sensors with a thickness of 320 μm and a inter-strip distance (strip pitch) which varies from 81 to 118 μm. The first two layers are made with double sided modules, composed by two detectors mounted back to back with the strips tilted by 100 mrad. This kind of sensors provides a measurement in both $r\phi$ and $r - z$ coordinates with a single point resolution between 23–34 μm and 230 μm respectively. The TOB is made of 6 layers of thick (550 μm) silicon sensors with a strip pitch which varies from 120 to 180 μm. In this region the radiation levels are smaller and thicker silicon sensors (500 μm) can be used to maintain a good signal-to-noise ratio for longer strip length. Also, the first two layers of the TOB provide a measurement with a single point resolution which varies from 35 μm to 52 μm in the $r - \phi$ plane and is 530 μm in the z direction.

The endcap region ($|\eta| > 1.6$) is covered by the Tracker Inner Disks (TID) and by two Tracker End Caps (TEC+ and TEC-). Each TEC is made of 9 disks that extend

into the region $120 < |z| < 280$ cm, carrying up to 7 rings of silicon microstrip detectors: the three innermost rings are made of sensors 320 μm thick, while in the remaining disks they are 500 μm thick. The TID comprises 3 disks and the thickness of the sensors is 320 μm. The three disks of the TID fill the gap between the TIB and the TEC in the region $80 < |z| < 90$ cm.

In both trackers the modules are arranged in rings, centered on the beam line, their strips point towards the beam line (radial topology) and their pitch is variable. Various types of sensor geometries are used: rectangular sensor types for TIB and TOB, and wedge-shaped sensor types for TEC and TID. These sensors can be made quite large, so in the innermost barrel their dimension is 6×12 cm^2, while in the outmost barrel is 10×9 cm^2.

2.2.2 The electromagnetic calorimeter

The primary aim of the Electromagnetic Calorimeter (ECAL) [100] is the identification and the accurate measurement of energy and position of photons and electrons created in the collisions, through their interaction with the material and the collection of the energy released. The strictest requirements on its performance are imposed by the Higgs decay into two photons $H \to \gamma\gamma$, which needs excellent energy and position resolution. In order to achieve a 1% resolution on the diphoton invariant mass, an homogeneous design which optimizes energy resolution is chosen for ECAL.

It is made of 75848 lead tungstate ($PbWO_4$) scintillating crystals arranged in a cylindrical structure around the beampipe: 61200 crystals are mounted in the central barrel part, closed by 7324 crystals in each of the two endcaps. The lead tungstate crystals are chosen because of their excellent energy resolution, essential to reconstruct the decay into two photons of a Higgs boson. Lead tungstate is a fast, radiation-hard scintillator: it is a transparent material characterized by a high density ($\rho = 8.28$ g/cm^3), a short radiation length ($X_0 = 0.89$ cm) and a small Molière radius ($R_M = 2.2$ cm), that allows good shower containment in the limited space available for the detector. These features allow a very compact shape and a fine granularity, necessary because of the high particle density produced at the LHC. Moreover, these crystals have a trapezoidal shape and are characterized by a very short scintillation decay time, that allows the electronics to collect about 80% of the light within 25 ns, so that they can be used at the crossing rate of 40 MHz. The length of the crystals is 23 cm (25.8 X_0) in the barrel and 22 cm (24.7 X_0) in the endcaps, with a front face area of 2.2×2.2 cm^2 and 2.9×2.9 cm^2 respectively.

The longitudinal view of one quarter of the ECAL is shown in Figure 2.17. The ECAL barrel (EB) covers the central rapidity region $0 < |\eta| < 1.479$, while the pseudorapidity range $1.479 < |\eta| < 3$ is covered by the two endcaps (EE). The EB, located at $r = 1.3$ m from the interaction point, is composed of 36 supermodules that cover half of the barrel length and 20° in ϕ, with each supermodule made of four modules and containing 400

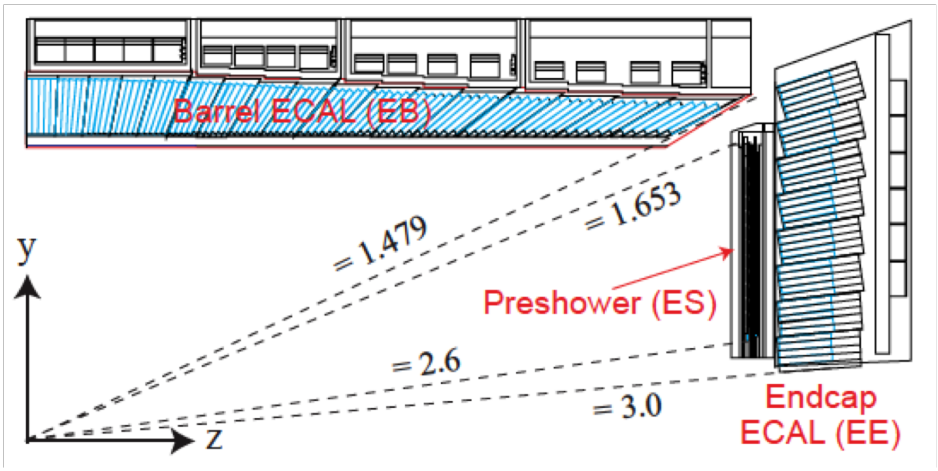

Figure 2.17: *Schematic view of the ECAL.*

or 500 crystals in an alveolar structure, while each EE, installed at $|z| = 3.1$ m, is made of two semi-circular dees containing 3662 crystals. This structure is illustrated in Figure 2.18. The crystals are arranged in a $\eta - \phi$ grid in the barrel and in a $x - y$ grid in the endcaps and they are pointing to the nominal interaction point: the axes are tilted at 3° in the barrel and at 2°–5° in the endcaps with respect to the line from the nominal vertex position.

The scintillation light is collected by fast, radiation-tolerant photodetectors which amplify the small light yield of the particles traversing them. Different photodetectors are used in EB and EE due to different magnetic field configurations and expected radiation levels: silicon avalanche photodiodes (APDs) in the barrel and vacuum phototriodes (VPTs) in the endcaps. In order to preserve the energy resolution, a cooling system has to stabilize the temperature of both crystals and photodetectors to 18°C, since the crystal response is temperature-dependent.
APDs are fast (≈ 2 ns of rise time), highly insensitive to magnetic field and radiation resistant detectors with very good quantum efficiency (70%–80% at $\lambda = 420$ nm). Two APDs, each with 5×5 mm^2 active area, are glued to the back of each crystal. Their structure is shown in Figure 2.19.
In the endcaps, where the radiation is higher, VPT detectors, one for each crystal, are used instead of APDs because the latter are insufficiently radiation hard. The VPT structure is shown in Figure 2.20. The photocathode is semitransparent and made of radiation-hard glass. They have a large effective area of ≈ 280 mm^2, making the total detector response almost the same for barrel and endcap.

A preshower device (ES), consisting of two disks of lead absorber at 2 X_0 and 3 X_0 and of two planes of silicon strip detectors, is installed in front of the endcaps and covers

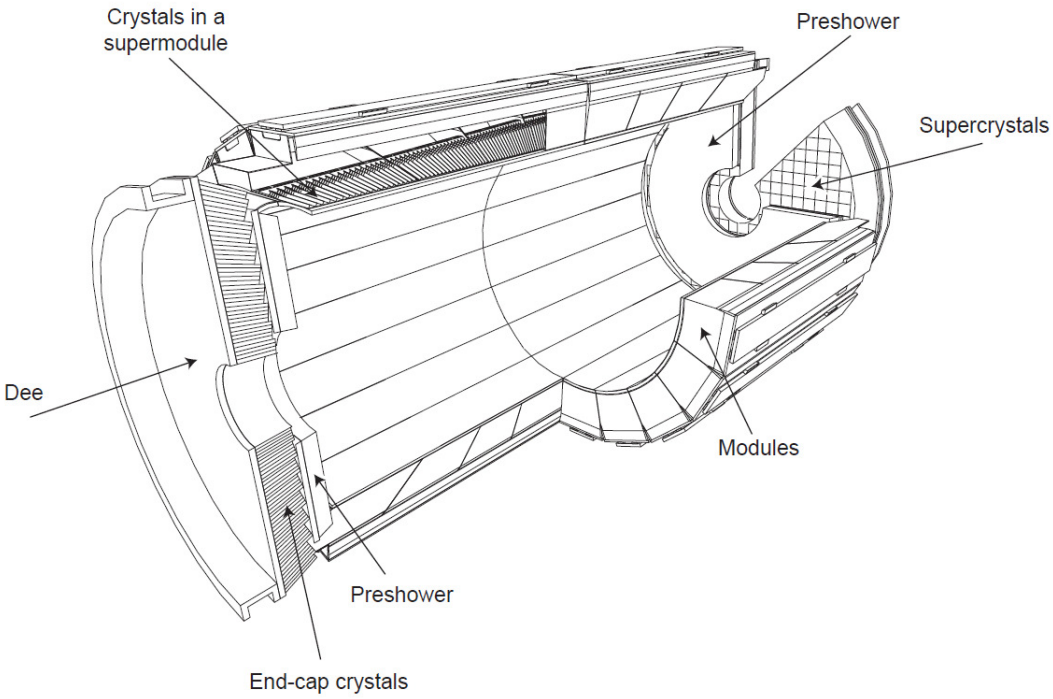

Figure 2.18: *Layout of the ECAL with the barrel supermodules, the two endcaps and the preshower subdetectors.*

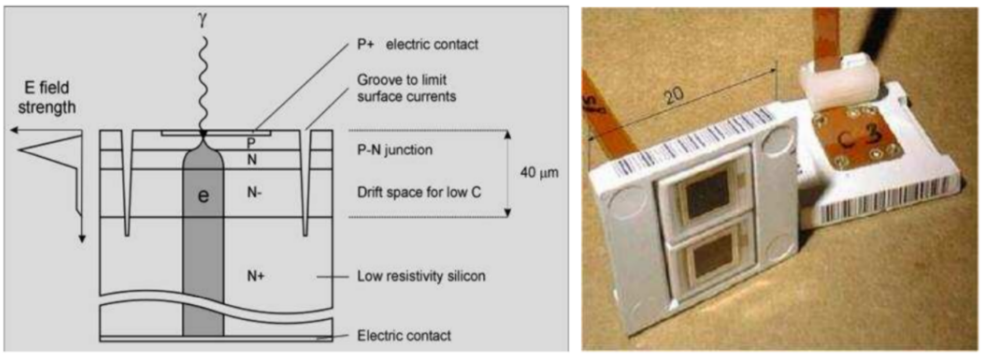

Figure 2.19: *Left: APD layout. Right: Photo of APDs.*

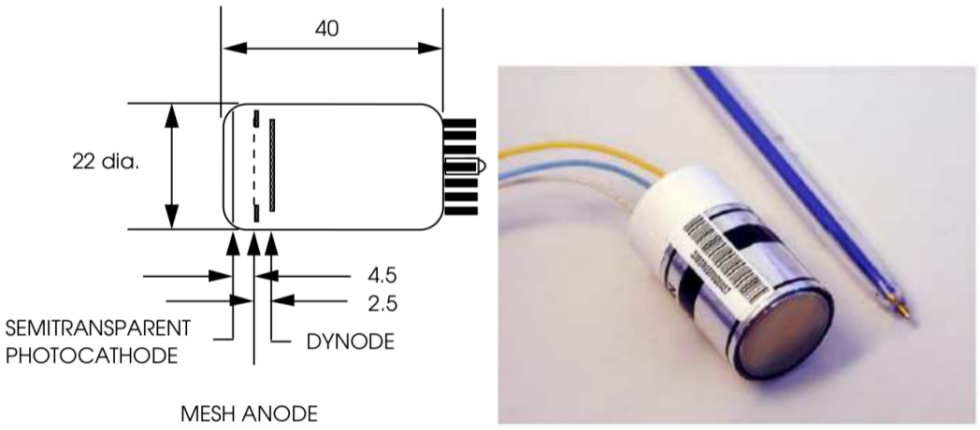

Figure 2.20: *Left: VPT layout. Right: Photo of a VPT detector.*

the $1.653 < \eta < 2.6$ region with about 140000 read-out channels. Electromagnetic showers from incoming particles are initiated by the lead layers, while the silicon strip sensors measure the deposited energy and the transverse shower profiles. The ES allows the rejection of photon pairs from π^0 decays, improves the estimation of the direction of photons to enhance the measurement of the two photon invariant mass, and helps in identifying electrons from minimum ionizing particles.

The energy resolution of a calorimeter is a function of the energy E of the incident particle and it is usually parametrized as:

$$\frac{\sigma_E}{E} = \frac{S}{\sqrt{E}} \oplus \frac{N}{E} \oplus C$$

where S is the stochastic term that includes statistical effects, N is the noise due to electronics and pileup, and C is a constant term related to the calibration of the calorimeter. To measure the ECAL performance, test beams with ideal conditions (no magnetic field and material in front of the calorimeter) were performed using electrons with energy ranging from 20 to 250 GeV. The EB energy resolution was found to be:

$$\frac{\sigma_E}{E} = \frac{2.8\%}{\sqrt{E(GeV)}} \oplus \frac{12.8\%}{E(GeV)} \oplus 0.3\%$$

where the stochastic term is due to shower development, statistical fluctuations in the number of photo-electrons produced in the APDs, and statistical fluctuations of the containment losses, the electronic noise term is measured by applying the amplitude reconstruction procedure to data taken with a random trigger and no electron signal ("pedestal

runs"), and the constant term dominating the energy resolution for high-energy electrons and photons is due to stability, longitudinal non-uniformity effects of the crystal response, monitoring and calibration effects.

Electrons and photons produce electromagnetic showers depositing energy over several crystals surrounding the one hit by the particle. For a uniform impact on the crystal front face, 70% of the energy is deposited in one crystal, 94% in a 3×3 array, and 97% in a 5×5 array. Photon conversions and electron bremsstrahlung processes take place in the tracker and, due to the intense magnetic field, spread the radiated energy along ϕ. The energy of an electron or a photon is then collected by clustering algorithms that at first form *basic clusters*, corresponding to a local maximum of the energy deposits, and then merge them together into a *supercluster*, which is extended in ϕ to recover the radiated energy. Different clustering algorithms are used for the barrel and endcaps, due to the different geometric arrangement of the crystals in these two regions, and achieve a rather complete ($\approx 95\%$) reconstruction of the energy of photons and electrons, even for those undergoing conversion and bremsstrahlung in the material in front of the ECAL. The energy in an electromagnetic cluster is obtained by summing the single energy deposits of each crystal belonging to the supercluster:

$$E_{e,\gamma} = F_{e,\gamma} \cdot \left[G \cdot \sum_i \left(S_i(t) \cdot c_i \cdot \mathcal{A}_i \right) + E_{ES} \right].$$

The $F_{e,\gamma}$ are corrections to the supercluster energy that take into account several energy containment effects, like the electromagnetic shower leakage and the clustering of energy emitted by bremsstrahlung or photon conversions in the tracker, biases in the energy reconstruction related to the geometry of the detector, and different developments of the electron and photon showers. G is a scale coefficient that convert the digital scale measured in ADC counts to the energy scale expressed in GeV, $S_i(t)$ are time dependent corrections that account for the changes in response of the crystals, explained in Section 2.2.2.2, c_i are intercalibrations constants that take into account differences in the crystals response, $\mathcal{A}_i$ are pulse amplitudes in ADC counts estimated as described in Section 2.2.2.1, and E_{ES} is the preshower energy, summed to that of the ECAL supercluster only for electrons or photons in the acceptance region of the ECAL preshower.

The current period of data taking, LHC Run 2, is characterized by an instantaneous luminosity of up to 1.5×10^{34} cm^{-2} s^{-1} and by an average number of concurrent interactions per bunch crossing (pileup) of up to 50, with an average of 23 and a root mean square of ≈ 6 in 2016. These values are approximately a factor of two larger than those experienced in Run 1 and exceed the original design parameters of the LHC, so the performance of the ECAL have to deal with the LHC luminosity and pileup increases.

2.2.2.1 ECAL pulse shape reconstruction

New techniques have been developed to maintain the ECAL energy resolution and trigger performance at higher pileup, like a more efficient electromagnetic trigger algorithm and a new method for pulse shape reconstruction.
The scintillation light measured by the photodetectors is read out as an analog signal by the front-end electronics. The signal is pre-amplified, shaped and processed by a multi-gain amplifier. The output is digitized by a 12 bit ADC running at 40 MHz, which records 10 consecutive samples, then used to reconstruct the signal amplitude.
A *multifit* pulse shape reconstruction, a template fit with multiple components, mitigates the effect of out-of-time (OOT) pileup events under the high luminosity conditions of Run 2. The pulse shape is modeled as the sum of the in-time signal amplitude and up to 9 OOT amplitudes (one per bunch crossing), estimated minimizing the χ^2 distribution:

$$\chi^2 = \sum_{i=1}^{10} \frac{(\sum_{j=1}^{M} \mathcal{A}_j \times p_{ij} - S_i)^2}{\sigma_{S_i}^2},$$

using a non-negative-least-squares technique for a better description of the in-time shape. The $\mathcal{A}_j$ are the amplitudes from the pulse at bunch cross j, the p_{ij} are the pulse templates, corresponding to energy deposits within a range of -5 to $+4$ bunch crossings around the time of the in-time signal, the S_i are the digitized amplitudes of the total electronic noise and the σ_{S_i} are the noise covariance matrix. Examples of a fitted pulse shape for signals in the barrel and in the endcaps are shown in Figure 2.21.

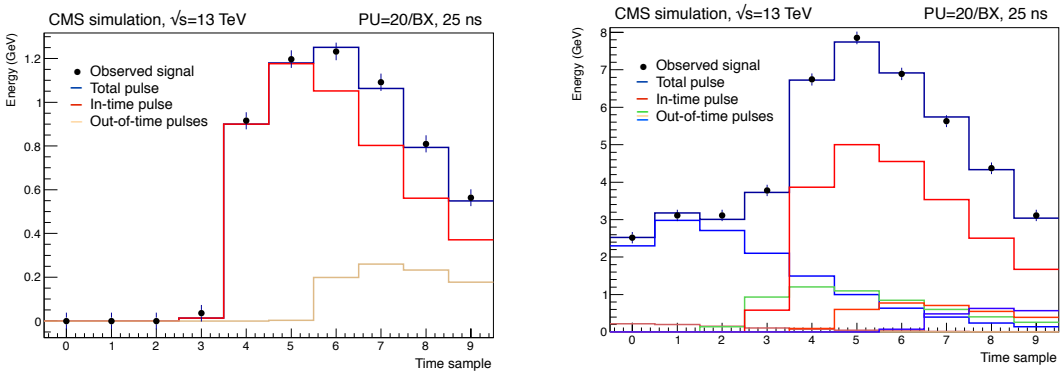

Figure 2.21: *Example of fitted pulses for simulated events with* 20 *average pileup interactions and* 25 *ns bunch spacing, for a signal in the barrel (left) and in the endcaps (right). Dots represent the* 10 *digitized samples, the red distributions (other light colors) represent the fitted in-time (out-of time) pulses with positive amplitude. The dark blue histograms represent the sum of all the fitted contributions.*

2.2.2.2 ECAL laser monitoring system

A stable and precise laser monitoring system plays an important role in the ECAL calibration, allowing the computation of the intercalibration correction coefficients needed to stabilize the response of the detector after the radiation-induced crystal transparency variation. The ionizing electromagnetic radiation produces color centers in the crystals which affect the optical transmission within crystals, reducing their transparency and therefore their measured response to the deposited energy. This transparency loss process is not permanent, since the color centers partially anneal with thermal energy, leading to a recovery which is evident in absence of irradiation, during machine inter-fills and shut-downs. The loss in transparency depends then on the dose rate, which varies with η.

The laser light pulses are injected into each ECAL crystal via a multi-level optical-fibre distribution system every 40 minutes, either during the CMS data-taking and during periods between LHC fills. The laser wavelengths available are three: the blue one (447 nm) to follow the crystals radiation damages, the green one (527 nm) to perform systematic studies of the evolution of the calorimeter, and the infrared one (796 nm) to disentangle the electronics instability from the radiation-induced fluctuations. The signal received on the associated photo-detector, APD in the barrel and VPT in the endcaps, is compared with the signal given by a photo-detector (PN diode) that sees directly the light sent to the crystals. The transparency of each crystal can be measured through the ratio between the APDs or VPTs amplitude and the one measured with the PN diode.

The variation of the relative crystal response to laser light injected in the ECAL crystals, shown in Figure 2.22, has been measured during 2011-2012 (LHC Run 1) and 2015-2016-2017-2018 (LHC Run 2) and it is averaged over all crystals in bins of pseudorapidity. The response variation observed in the ECAL channels is up to 10% in the barrel, it reaches up to 50% at $\eta \approx 2.5$, the limit of the tracker acceptance, and it is up to 90% in the region closest to the beam pipe. The recovery of the crystal response during the periods without collisions (e.g. Long Shutdown 1) is visible, even if the response was not fully recovered, particularly in the region closest to the beam pipe.

The monitoring corrections are obtained and applied promptly within ≈ 48 hours, in time for the CMS prompt reconstruction of the events. The stability of the response after applying the monitoring corrections is assessed with collisions data comparing the energy measured in ECAL to the track momentum measured in the silicon tracker (E/p) for isolated electrons from $W \to e\nu$ and $Z \to e^+e^-$ decays and examining the stability of the reconstructed invariant mass of $\gamma\gamma$ pairs in $\pi^0 \to \gamma\gamma$ decays.
The stability plot obtained with the E/p method using 2015 dataset is shown in Figure 2.23, where the E/p relative scale versus time is shown before and after applying the laser corrections. The stability plot obtained with the π^0 method using 2017 dataset is shown in Figure 2.24.

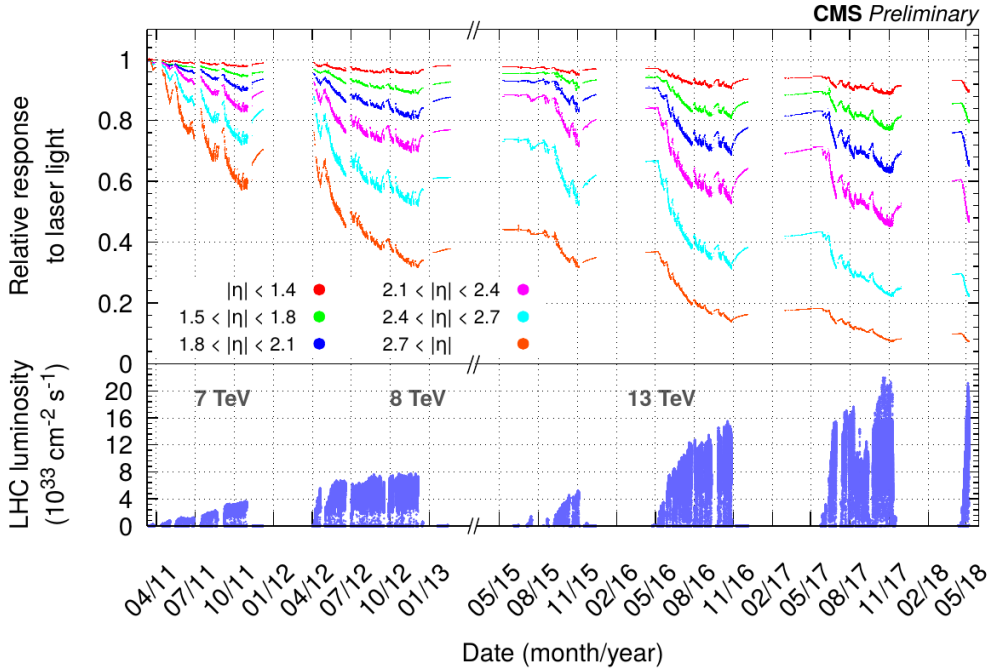

Figure 2.22: *Relative response to laser light injected (440 nm in 2011 and 447 nm from 2012 onwards) in the ECAL crystals, measured by the ECAL laser monitoring system, averaged over all crystals in bins of pseudorapidity, for the 2011, 2012, 2015, 2016, 2017 and 2018 data taking periods with magnetic field at 3.8 T. This plot includes measurements, performed every 40 minutes and used to correct the physics data, taken up to May 2018. The bottom plot shows the instantaneous LHC luminosity delivered during this time period.*

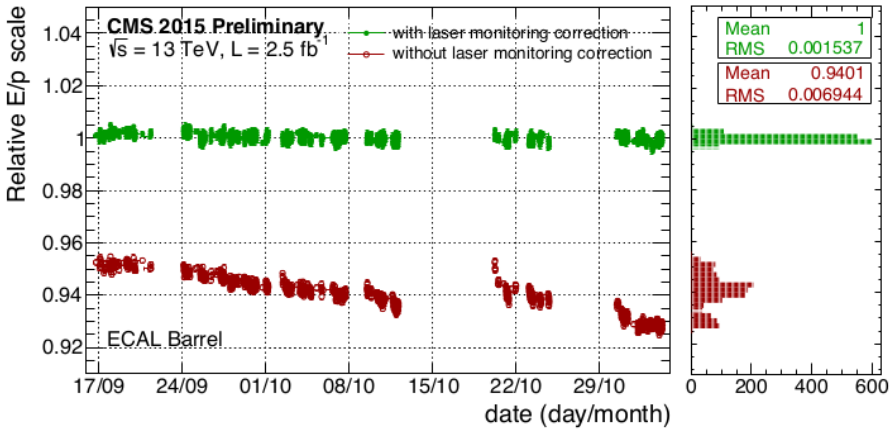

Figure 2.23: *History plot for 2015 data of the ratio of electron energy E, measured in the ECAL barrel, to the electron momentum p, measured in the tracker. The dataset corresponds to the prompt-reconstruction with the 2015 startup calibrations. Each point in the plot is computed from 5000 selected events with the reconstructed electron located in the ECAL barrel. The E/p distribution for each point is fitted to a template E/p distribution measured from data (using the entire 2015 dataset) in order to provide a relative scale for the E/p measurement versus time. The history plots are shown before (red points) and after (green points) corrections to ECAL crystal response variations due to transparency loss are applied. A stable energy scale is achieved throughout 2015 run after applying laser corrections: the average signal loss is $\approx 6\%$, and the RMS stability after corrections is $\approx 0.14\%$.*

2.2.2.3 ECAL calibration

The energy response of the detector is precisely calibrated and monitored at regular intervals. To equalize the response of each crystal to the deposited energy, relative and absolute calibrations are performed. The relative crystal-by-crystal intercalibrations use three different methods:

- the *ϕ-symmetry* method equalizes the average energy in channels located at a constant value of η, based on the expectation that the total deposited transverse energy (ΣE_t) should be the same in all crystals at the same pseudorapidity (η-ring). The intercalibration in ϕ is performed by comparing the ΣE_t deposited in one crystal with the total transverse energy collected by crystals at the same value of η ($\Sigma E_t(ring)$);

- the *π^0/η mass* method exploits the invariant mass of unconverted photons arising from π^0 and η decays to intercalibrate the channel response. The π_0/η invariant mass distribution, shown in Figure 2.25, is fitted with a Gaussian function for the signal, and a fourth-order polynomial for the background. The intercalibration constants are updated iteratively to correct the fitted mass value in each channel;

- the *E/p* method compares the energy measured in ECAL to the momentum measured in tracker for isolated electrons from W and Z boson decays. The crystals belonging

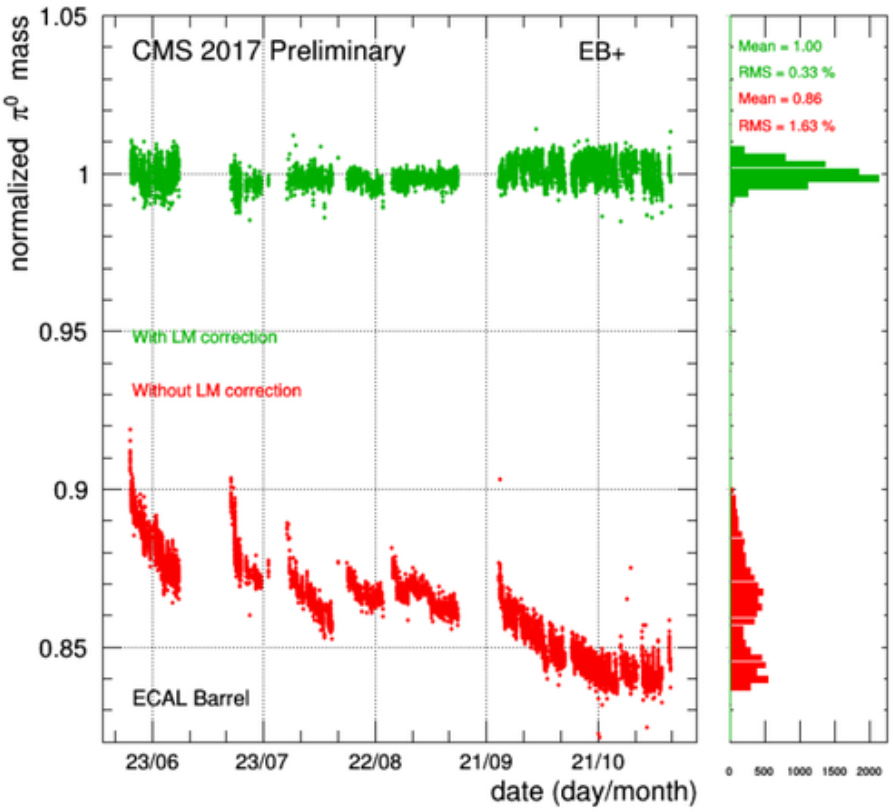

Figure 2.24: *Stability of the relative energy scale measured from the invariant mass distribution of $\pi^0 \to \gamma\gamma$ decays in the ECAL barrel. The energy scale is measured by fitting the invariant mass distribution of approximately 500000 photon pairs in the mass range of the π^0 meson. Each point is obtained from a fit to approximately 5 minutes of data taking. The error bars represent the statistical errors on the fitted peak position. The energy scale is plotted as a function of time over the 2017 data taking period. The plot shows the data with (green points) and without (red points) light monitoring (LM) corrections applied. The right-hand panel shows the projected relative energy scales.*

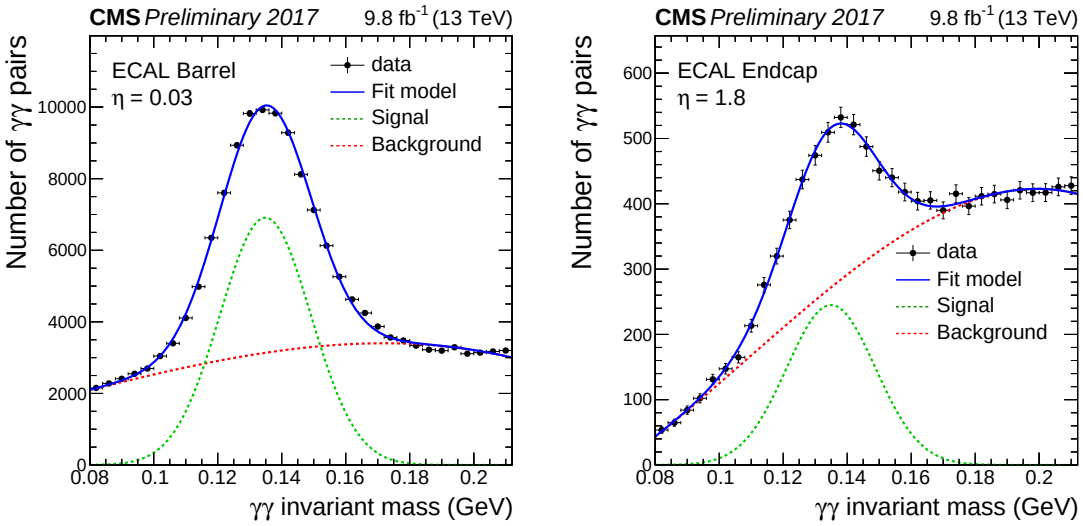

Figure 2.25: *Examples of the invariant mass of photon pairs in the mass range of the π^0 with one photon in one fixed crystal of the ECAL barrel at $\eta = 0.03$ (left plot), and of the ECAL endcap at $\eta = 1.8$ (right plot). Data collected in 2017 and corresponding to an integrated luminosity of approximately 9.8 fb^{-1} are used. These events are collected by CMS with a dedicated trigger at a rate of 7 (2) kHz in the barrel (endcap). The high trigger rate is made possible by a special stream at HLT that saves only a minimal amount of information of the events, in particular energy deposits in the ECAL crystals surrounding a possible π^0 candidate. For the candidates in the endcaps in the region covered by the preshower ($1.7 < \eta < 2.6$), the position of the ES is used. These π^0 invariant mass plot are built with uncalibrated energy scale. These events are used as prompt feedback to monitor the effectiveness of the laser monitoring, as shown in Section 2.2.2.2, and to intercalibrate the energy of ECAL crystals.*

to each electron supercluster are intercalibrated iteratively minimizing the difference $E/p - 1$.

The intercalibration constants from each method are then combined to provide a weighted average intercalibration constant for each channel.

The precision of the inter-calibration constants in the ECAL barrel after the combination of the three methods is shown in Figure 2.26, as a function of pseudorapidity, for the 2017 dataset. For central EB crystals ($|\eta| < 1$), the combined intercalibrations precision is $\approx 0.3\%$ and it goes up to 1% for the rest of the EB, up to $|\eta| = 1.48$. The variation of the precision with pseudorapidity arises partly from the size of the data sample, and partly from the amount of material in front of the ECAL.

The $Z \to ee$ events are exploited to correct the relative scale between different η-rings, fitting the dielectron invariant mass distribution around the Z peak selecting electrons pairs belonging to different η-rings.

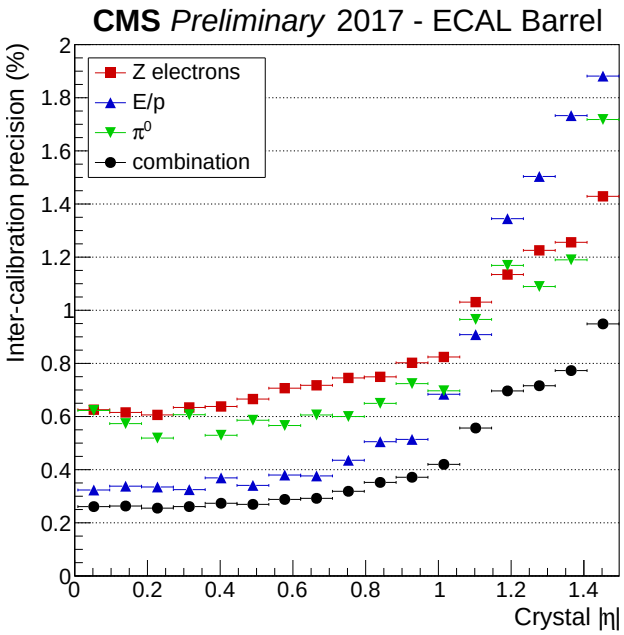

Figure 2.26: *The precision for measuring the channel inter-calibration constants from $Z \to ee$, $\pi \to \gamma\gamma$ decays, and electrons arising from W and Z boson decays compared to the tracker response (E/p), is shown as a function of $|\eta|$ in the ECAL barrel detectors using the data collected in 2017. The precision of the $Z \to ee$ inter-calibrations, in red, is at the level of the systematic errors. The precision of the E/p inter-calibrations, in blue, is still dominated by the statistical errors for $|\eta| > 1$. The green points represent the precision of the intercalibration constants obtained using photons from $\pi^0 \to \gamma\gamma$ decays. The black points represent the precision of the combination of the three methods (weighted average).*

The global energy scale is also given by the $Z \to ee$ invariant mass, used to fix the overall absolute calibration matching data to a detailed simulation of the detector for EB and EE separately.
The supercluster energy is corrected using a multivariate approach that maximally exploits η, ϕ, and cluster shapes variables of electrons and photons. These energy corrections are optimized using a Boosted Decision Tree (BDT) implementation trained on Monte-Carlo simulation and are tuned separately for electrons and photons to account for the differencies in the way they interact with the material in front of the ECAL, shown in Figure 2.14.

The energy resolution achieved with the fully calibrated and corrected clusters has been compared between collision data and Monte Carlo simulation. The ECAL response in the simulation is tuned to match test beam results. The electron energy resolution is estimated from the $Z \to e^+e^-$ peak width using an unbinned maximum likelihood fit to the invariant mass distribution of e^+e^- pairs, with a Breit- Wigner function convoluted with a Gaussian as the signal model.

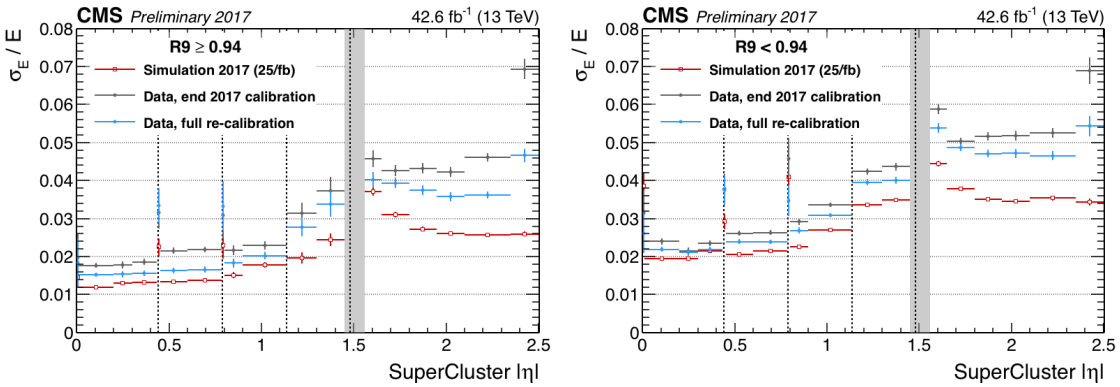

Figure 2.27: *Relative electron energy resolution in bins of pseudorapidity for the barrel and the endcaps, using electrons from $Z \to ee$ decays. The resolution is shown for very low bremsstrahlung electrons (named "golden", with $R_9 > 0.94$) on the left, and for high bremsstrahlung electrons ($R_9 < 0.94$) on the right, plotted separately for data and MC events. The relative resolution σ_E/E is extracted from an unbinned likelihood fit to $Z \to ee$ events, using a Voigtian (a Landau convoluted with a Gaussian) as the signal model. The ECAL conditions used in the simulation (red points) reflect the status of the detector as predicted after 25fb^{-1} of data-taking in 2017. The resolution is affected by the amount of material in front of the ECAL and is degraded in the vicinity of the ECAL modules boundaries, indicated by the vertical dashed lines in the plot. Also, the resolution improves significantly after a dedicated calibration using the full 2017 dataset (blue points) with respect to the end-of-year (EOY) 2017 calibration (gray points) for which only time dependent effects were corrected for. The grey band at $|\eta| \approx 1.5$ marks the barrel-endcap transition region excluded from the photon fiducial region used in the $H \to \gamma\gamma$ analysis.*

The energy resolution obtained using 2017 data samples corresponding to an integrated luminosity of 25 fb^{-1} is shown in Figure 2.27, for low bremsstrahlung electrons ($R_9 > 0.94$) on the left and for high bremsstrahlung electrons ($R_9 < 0.94$) on the right, with $R_9 = E_{3\times3}/E_{SC}$. For low bremsstrahlung electrons, the energy resolution is around 1.5%–1.8% in the central barrel ($|\eta| < 1$) and it varies between 3% and 5% in the endcaps, while for high bremsstrahlung electrons, the energy resolution is around 2%–2.8% in the central barrel and it varies between 4% and 5.5% in the endcaps.

2.2.3 The hadronic calorimeter

The Hadronic Calorimeter (HCAL) [101] surrounds the electromagnetic calorimeter and its design is strongly influenced by the following aims: the identification and measurement of charged and neutral hadrons by estimating the energy and the direction of hadronic jets, the accurate determination of total transverse energy and the neutrino detection by measuring the missing transverse energy of the event. In order to be able to capture as many particles as possible to achieve these goals, one of the main design requirements is a high hermeticity, which means that the detector must cover a portion of the solid angle

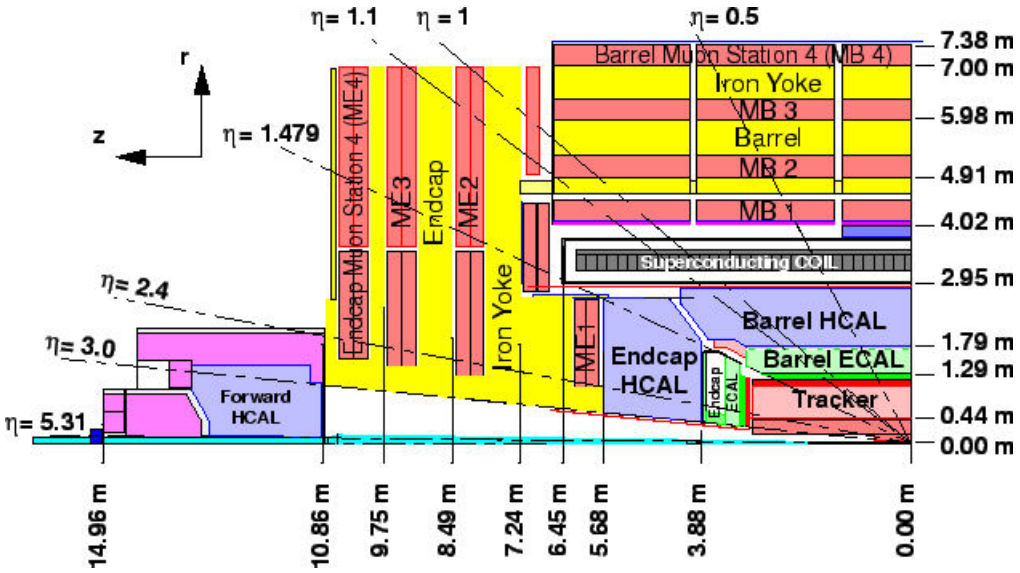

Figure 2.28: *Schematic view of the detector showing the different η coverage of the various parts of the HCAL.*

as big as possible. In particular, since the identification of forward jets is very important for the rejection of many backgrounds and for the evidence of BSM signatures, the HCAL angular coverage must include the very forward region. In the forward region beyond the coverage of the ECAL, the HCAL system is also responsible for the measurement of electromagnetic energy.

As shown in Figure 2.28, the HCAL is divided in four parts, allowing a good segmentation, a moderate energy resolution, and a full angular coverage. Its dimensions are constrained by the ECAL and the surrounding magnet coil, which have $r = 1.77$ m and $r = 2.95$ m, respectively. The barrel hadronic calorimeter (HB) covers the central pseudorapidity region up to $|\eta| = 1.3$, while the endcap regions are covered up to $|\eta| = 3$ by the two endcap hadron calorimeters (HE). To satisfy the hermeticity requirements and to reduce the mis-identification of hadronic jets as muons, the barrel and endcap parts installed inside the solenoid magnet are complemented by a very forward calorimeter (HF) which is placed outside the magnet return yokes 11 m far from the interaction point, extending the pseudorapidity coverage up to $|\eta| = 5.3$. Finally, an array of scintillators, referred to as the outer hadronic calorimeter (HO) and located outside the magnet in the region covered by the HB, is used to improve the central shower containment. In the barrel a full shower containment is not possible within the magnet volume, but HO increases the material thickness in the barrel region such that the hadronic showers are fully absorbed before reaching the muon system.

The HCAL is a sampling calorimeter, finding particles position, energy, and arrival time using alternating layers of *absorber* and *scintillator* materials. The active part is made of plastic scintillator tiles interleaved with brass absorber plates and coupled with wavelength shifting fibers and clear fibers carrying the light to the readout system. In particular, brass (70% Cu and 30% Zn) has been chosen as absorber material thanks to its non magnetic behavior and its quite short interaction length ($\lambda_I \approx 151$ mm). To maximize the amount of absorber before the magnet, the space devoted to the active medium is minimized. In the Cherenkov-based HF calorimeter, the absorber is made of steel while the active elements are quartz fibers parallel to the beam and the signal originated from them is Cherenkov light. The photodetection readout is based on multi-channel hybrid photodiodes (HPDs) that can operate in a high magnetic field and give an amplified response, proportional to the original signal, for a large range of particle energies. The HPDs are housed within the calorimeter volume. Both barrel and endcap are read out in towers with a size of $\Delta\eta \times \Delta\phi = 0.087 \times 0.087$ up to $\eta < 1.6$ and $\Delta\eta \times \Delta\phi = 0.17 \times 0.17$ for $\eta > 1.6$.
The HCAL energy resolution measured in data is:

- $\frac{\sigma_E}{E} \simeq 65\%\sqrt{E} \oplus 5\%$ in the barrel;
- $\frac{\sigma_E}{E} \simeq 85\%\sqrt{E} \oplus 5\%$ in the endcap;
- $\frac{\sigma_E}{E} \simeq 100\%\sqrt{E} \oplus 5\%$ in the very forward calorimeter.

The energy resolution of the ECAL-HCAL system was evaluated with a combined test beam with high energy pions [102] and is given by $\frac{\sigma_E}{E} \simeq \frac{84.7\%}{E} \oplus 7.4\%$.

2.2.4 The muon system

The aim of the muon system is the identification of muons and the measurement of their transverse momentum, in combination with the inner tracker. The efficient detection of muons is of primary importance as they represent a clear signature for a large number of physics processes. For this reason the muon spectrometer [103] must provide a robust trigger and an accurate measurement of the muons momentum and charge, even without the contribution of the tracker. The muons can penetrate several meters of iron without being stopped, so they have to be detected by muon chambers placed in the outermost part of the experiment. The muon detection system, shown in Figure 2.29, is therefore set outside the magnetic coil, embedded in the iron return yoke which shields the detectors from charged particles different from muons.

The redundancy of the muon detection, performed first in the inner tracker and then in the muon system, allows a sensible improvement in the resolution of high-momentum particles, for which spatial resolution dominates, while for lower momenta (up to p_T values of 200 GeV) the resolution is dominated by multiple scattering in the material before the chambers and the inner silicon tracker is sufficient to obtain the best resolution. An overall

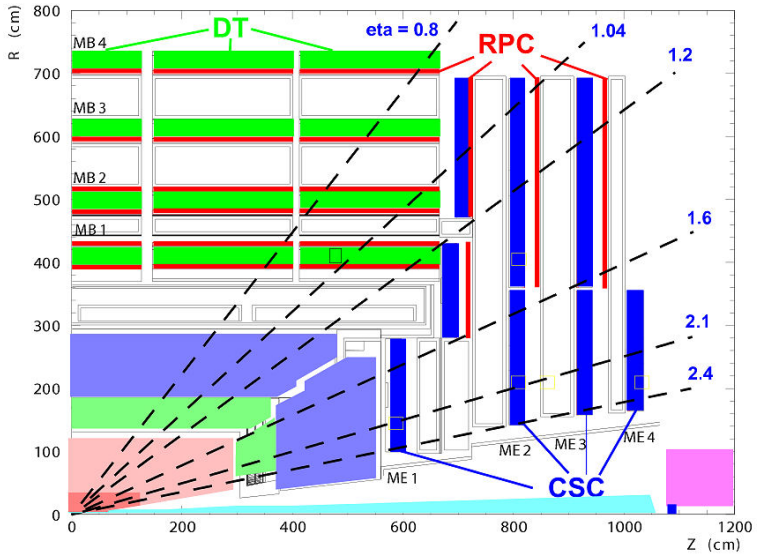

Figure 2.29: *Layout of a quarter of the muon system, showing the four DT stations in the barrel (MB1-MB4, in green), the four CSC stations in the endcap (ME1-ME4, in blue), and the RPC stations in the barrel and in the endcap (in red).*

muon momentum resolution of 5–8% at 10 GeV and of 20–40% at 1 TeV can be obtained using only the muon system, where the measurement of the momentum of muons varies with pseudorapidity. This measurement is performed through the determination of the muon bending angle at the exit of the coil, taking the interaction point (known with a precision of $\simeq 20$ μm) as the origin of muons. When the combination of the inner tracker and outer muon system is used, the values improve significantly to 1–1.5% at 10 GeV and to 6–17% at 1 TeV. The trajectory beyond the return yoke can be extrapolated back to the beam-line, thanks to the compensation of the bend before and after the coil. The minimum value of the muon transverse momentum required to reach the system is 3 GeV.

The muon spectrometer is composed by three different types of gas-ionization chambers for a total of 25000 m^2 of detection planes:

- Drift Tube (DT) chambers in the barrel, covering the region $|\eta| < 1.2$;
- Cathode Strip Chambers (CSC) in the endcaps, used in the region $0.9 < |\eta| < 2.4$;
- Resistive Plate Chambers (RPC) in both the barrel and the endcaps, covering the range of $|\eta| < 1.6$.

The reason for these different technologies lies in the different particle rates and expected occupancies, both higher in the endcaps, and in the intensity of the stray magnetic field, which is lower in the barrel.

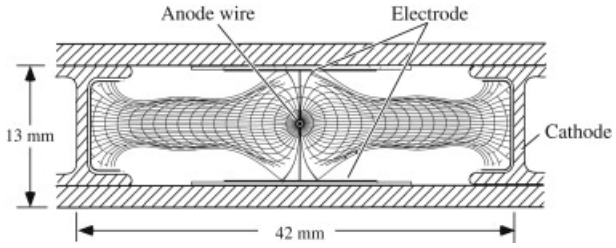

Figure 2.30: *Section of a drift tube cell.*

2.2.4.1 Drift Tubes chambers

In the barrel region ($|\eta| < 1.2$), where the track density and the residual magnetic field are low, four layers of drift tube chambers (MB1-MB4, shown in Figure 2.29) are chosen as detection elements. In this region the detector stations are interleaved with the iron plates of the yoke. The chamber segmentation follows that of the iron yoke, consisting of five wheels along the z axis, each one divided into 12 azimuthal sectors. There are 12 chambers in each of the 3 inner layers, while in the fourth layer the top and bottom sectors host 2 chambers each, leading to a total of 14 chambers per wheel.

The basic detector element is a drift tube cell, whose section is shown in Figure 2.30. A layer of cells is made of parallel aluminum plates, with cells obtained with perpendicular I-shaped aluminum cathodes and anodes of 50 μm diameter steel wires placed between the cathodes. The internal volume is filled with a gas mixture of Ar (85%) and CO_2 (15%) at atmospheric pressure, which provides good quenching properties and a saturated drift velocity of about 5.6 cm/μs. A muon passing through a cell ionizes the gas mixture that fills the cell volume and the drift time of the resulting electrons is then used to measure the distance between the muon track and the wire.

The DTs provide a precise track measurement in the bending plane; their maximum drift time is about 400 ns with a time resolution of about 1 ns. A single cell has a resolution of about 180 μm and an efficiency close to 100%, since in order to eliminate any dead spot the drift cells of each chamber are offset by a half-cell width with respect to their neighbor.

2.2.4.2 Cathode Strips Chambers

In the two endcaps ($0.9 < |\eta| < 2.4$), where the muon rate and the residual magnetic field are higher, four stations of cathode strip chambers (ME1-ME4, shown in Figure 2.29) are used, being the detector technology more indicated in a region suffering high particle rates and large residual magnetic field between the plates of the yoke. In each of the endcaps, the cathode strip chambers are arranged in 4 disks perpendicular to the beam and in concentric rings formed by 18 or 36 trapezoidal chambers: 3 rings in the innermost station and 2 in the others. Each CSC, multiwire proportional chamber with a good spatial and time resolution, is made of 6 gas gaps with planes of cathode strips in the

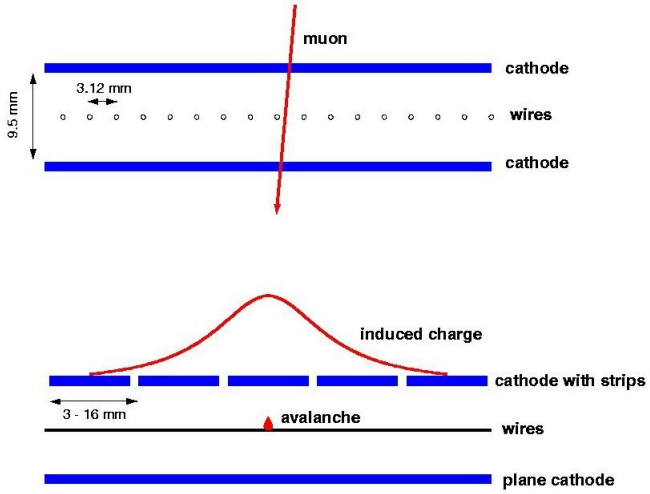

Figure 2.31: *Orthogonal section of a cathode strip chamber.*

radial directions and anode wires almost perpendicular to the strips.

The ionization of a charged particle passing through the planes causes an avalanche developing near the wire, that induces a distributed charge on the cathode plane. The orthogonal orientation of the cathode strips with respect to the wires allows the determination of two coordinates from a single detector plane, as shown in Figure 2.31.

Most CSCs are overlapped in ϕ in order to avoid gaps in acceptance and have a spatial resolution of about 200 μm (100 μm for the chambers belonging to the first station) and an angular resolution in $r - \phi$ of about 10 mrad. The wires resolution is of the order of about 0.5 cm, while for the strips is about 50 μm.

2.2.4.3 Resistive Plate Chamber

A system of resistive plate chambers is installed in both the barrel and the endcaps ($|\eta| < 1.6$) to assure redundancy to the muon trigger. RPC detectors are composed of 4 bakelite planes forming 2 coupled gaps 2 mm thick, as shown in Figure 2.32. The gaps are filled with a mixture of 90% $C_2H_2F_4$ (freon) and 5% i-C_4H_{10} (isobutane). They operate in avalanche mode, obtained with a lower electric field across the gap which allows the detectors to sustain high rates. An improved electronic amplification is required, since the gas multiplication is reduced. In the barrel, the RPC chambers follow the segmentation of DT chambers. Each DT chamber has 1 or 2 RPCs coupled to it before installation, depending on the station. A total of six layers of RPCs are present in the barrel, while

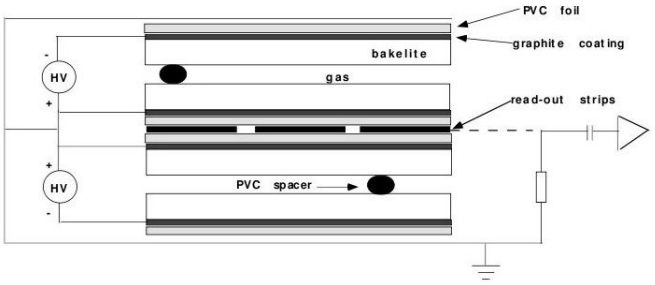

Figure 2.32: *Section of a double gap resistive plate chamber.*

there are three layers in the endcap.

The robustness of the muon spectrometer is guaranteed by the different sensitivity of DTs, RPCs and CSCs to the background. The main sources of background particles in the LHC environment are represented by secondary muons produced in pion and kaon decays, from punch-through hadrons and from low energy electrons originating after slow neutron capture by nuclei with subsequent photon emission. This neutron induced background is the responsible of the major contribution to the occupancy level in the muon detectors. CSC and DT chambers, in contrast with RPC detectors, are characterized by a layer layout which helps in reducing the effect of background hits: the request of correlation between consecutive layers is particularly effective against them. Both DTs and CSCs can then trigger muons independently with good efficiency and background rejection, while RPCs provide a complementary trigger system with a limited spatial resolution, but an excellent time resolution of few ns, allowing unambiguous bunch crossing identification even at the largest LHC luminosities.

2.2.5 Trigger system and Data Acquisition

At the instantaneous luminosity reached by jproton-proton collisions at LHC, the interaction rate produces 10^9 interactions/s but only a small part of them can be stored, since no storage system presently available is capable of recording this large amount of data. Moreover, the LHC high luminosity causes several interactions overlap in the same bunch crossing (pileup), as well as overlap of signals from different bunch crossings, due to the limited speed of detector response and read-out. There are therefore several technical difficulties in handling, storing and processing this huge amount of data and a selection of events has to be applied by the trigger and the data acquisition systems. As a consequence, a good triggering system with a large rejection of the less interesting particles maintaining at the same time a high efficiency on the (potential) interesting events is necessary.

The typical data size of a raw event is $\approx$ 1 MB and just a rate of $\approx$ 1 kHz can be stored for offline analysis. In order to fulfill this data reduction, the CMS trigger system performs an online event selection via two successive layers described in the following sections: the Level-1 trigger (L1), implemented on custom designed hardware, and the High-Level Trigger (HLT), implemented at software level. The data are then transmitted to the CMS Tier-0 computing center for storage and offline processing.

2.2.5.1 The Level-1 trigger

The hardware-based Level-1 trigger [104], implemented in the readout electronics of each subsystem except for the tracker, has to take an accept-reject decision for each bunch crossing (every 25 ns) reducing the rate of selected events down to 100 kHz, limit imposed by the CMS readout electronics. The high bunch crossing rate does not allow the full readout of the detector, mainly because of the slowness of the tracker algorithms, so only segmented data from calorimeters and muon detectors are used. The full high-resolution data are stored in pipelines of processing elements, waiting for the trigger decision to keep or discard the data from a certain event.

The L1 trigger electronics is placed partly on the sub-detectors and partly in the underground control room located at a distance of about 20 m from the CMS detector site. The L1 selection relies on a programmable menu made of 128 algorithms (*seeds*), each of which selects a particular type of objects. A prescale value p is assigned to each seed, making it accept only $1/p$ events passing its specific selection criteria. The prescales are adjusted to the LHC instantaneous luminosity during data taking, in order to restrict the output rate to the 100 kHz upper limit. The maximum latency allowed is 4 μs: this time is used to decide if accept or reject an event and includes also the transit of data from the detector front-end electronics to Level-1 trigger processors and back.

As shown in Figure 2.33, the information is processed using two separate flows. The "Calorimeter Trigger" identifies the best four candidates (called *trigger primitives*) of electrons, photons, taus, central jets, forward jets and so on from the shape of the energy deposited in the ECAL and HCAL *trigger towers*, five strips of five crystals along the azimuthal direction forming a 5×5 array of crystals in ECAL and $\Delta\eta \times \Delta\phi = 0.087 \times 0.087$ towers in HCAL. Moreover, it determines the total transverse energy E_T, the missing energy and the scalar transverse energy sum of all jets (H_T) above a programmable threshold. For the "Muon Trigger", all the three trigger systems – RPCs, CSCs, and DTs – take part in computing the muon trigger primitives from track segments and hit patterns: the CSC and DT track finders join the segments to complete the tracks and to assign physical values to them, while the RPC trigger chambers, thanks to their high timing resolution, deliver their own track candidates. The informations from the various muon sub-detectors are then combined to improve the momentum resolution and the efficiency of the muon candidates with respect to the individual systems.

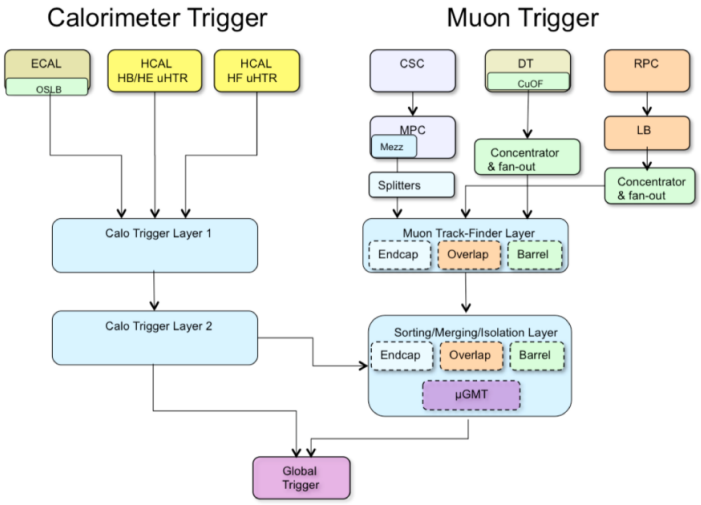

Figure 2.33: *Scheme of the L1 trigger system.*

All the information about these objects are then sent to the "Global L1 Trigger", which finally takes the decision to reject or to accept the event, based on the algorithm calculations and on the readiness of the sub-detectors and the DAQ. If the L1 accepts the event, the data are moved to be processed by the HLT for further evaluation.

For the high instantaneous luminosities and pileup levels of the LHC Run 2, the L1 trigger system was not able to keep low trigger thresholds staying within the 100 kHz bandwidth. To maintain the good performance also during the LHC luminosity increase, several updates were then introduced [105]. For the "Calorimeter Trigger", a previous subsystem called "Global Calorimeter Trigger" was replaced by a new data processing card with better data throughput and computational power, allowing the execution of improved algorithms and the inclusion of event-by-event pileup subtraction; new optical links were used to improve the data communication from ECAL, and two new layers of data processors, with a new time-multiplexed architecture, were used to read the events. The position and energy resolution of jets, photons, electrons and tau candidates were improved, providing the additional background rejection required by the increased instantaneous luminosity and pileup. The "Muon Trigger" was also upgraded combining all the three muon systems to perform an integrated track finding and to allow for a more precise p_T measurement.

2.2.5.2 The High Level Trigger (HLT)

The High Level Trigger [106] is based on the raw data events accepted by the L1 trigger and performs a full readout of the CMS detector, reconstructing all main classes of physics objects, such as electrons, muons, photons, taus, missing transverse energy and jets, and including also some more advanced techniques like b-tagging or jet substructure study. The reconstruction is done with the same software used for offline processing, but with a optimized configuration two orders of magnitude faster. The maximum processing time per event is of $\approx$ 200 ms per event for a L1 input rate of 100 kHz. In order to keep the rate under control and retain the subset of events more relevant to subsequent data analysis, specific selection criteria are applied to the reconstructed objects, exploiting the full precision of the CMS detector data with offline-quality algorithms. The HLT software system reduces the output rate from about 100 to about 1 kHz.

The HLT runs on a single dedicated farm of commercial computers, with approximately 16000 CPU cores. This event filter farm has "builder" units that collect and assemble individual event fragments from the detector, and "filter" units that unpack the raw data into detector-specific data structures, performing event reconstruction and trigger filtering. Its computing power has been increased by about 50% since Run 1 to cope with pileup and code complexity. Data processing at the HLT is structured around a predefined sequence of algorithms, called *path*, that processes steps of increasing complexity, reconstructing and applying selections to a certain type of physics objects, such that the events are classified accordingly to their topology (i.e. events with a muon pair, electron pair, large E_T^{miss}, ...). These paths can be prescaled as the L1 seeds and the set of all paths used at a given time is called *menu*. All paths are run in parallel and independently of each other, but common modules and sequences are shared among different paths. The successive reconstruction modules and selection filters are organized so that the fastest selections, such as those relying on information from the calorimeters and muon detectors, are run first, reducing the event rate before considering CPU-expensive steps such as track reconstruction. All events selected by at least one path are then directed to one of various data streams, illustrated in Figure 2.34. The main physics data stream transmits events as full raw detector data, for prompt offline event reconstruction and permanent mass storage. Its maximum average rate has been increased from 400 Hz in Run 1 to about 1 kHz in Run 2. Other physics streams include data parking, the storage of full event content from special loose HLT paths for a delayed offline reconstruction during LHC long shutdowns, and data scouting, the storage of reduced, non-reprocessable event content from very loose HLT paths. Some special streams are dedicated to data quality monitoring (online and offline) and to detector alignment and calibration workflows, and some to physics.

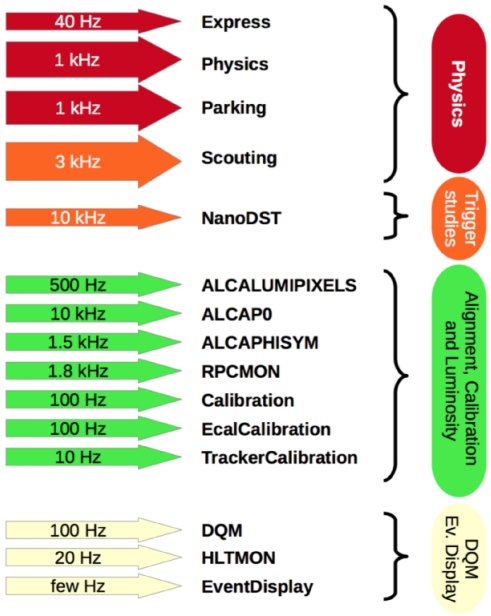

Figure 2.34: *Schematic representation of the HLT system.*

2.2.5.3 The Data Acquisition System (DAQ)

Like the HLT, the crucial function of the Data Acquisition System is to read the CMS detector information for the events selected by the Level-1 Trigger and to select the most interesting ones for output to mass storage. Therefore it must sustain a data flow of ≈ 100 GB/s (≈ 1 MB/evt) coming from ≈ 650 data sources (each with an average event fragment size of ≈ 2 kB for pp collisions at the design luminosity of 10^{34} cm^{-2}s^{-1}) and must provide enough computing power for the HLT to reduce the rate of stored events from 100 kHz to 1 kHz. All events that pass the Level-1 Trigger are sent to the Event Filter that performs physics selections to filter events and achieve the required output rate. Each sub-detector has a front-end system (FES) that stores data in pipelined buffers. There are approximately 700 FESs in the CMS readout. When a L1 trigger arrives, the Timing-Trigger-Control (TTC) system pulls out the corresponding data from the front-end buffers and pushes them into the DAQ system via the Front-End Drivers (FEDs), which are located in the underground counting room at a distance of 70 m from the detector. Here the Front-end Read-out Links (FRLs) read the data. The event builder assembles the event fragments belonging to the same L1 from all FEDs into a complete event and transmits it to one Filter Unit (FU) in the Event Filter for further processing. The collection of networks that provide the interconnections between the Read-out and the Filter Systems is known as Builder Network. The DAQ system can be deployed in up to 8 nearly autonomous systems,

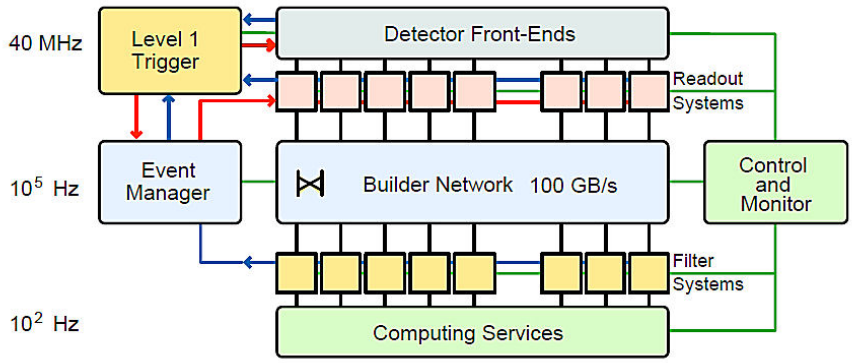

Figure 2.35: *Scheme of the DAQ system.*

each capable of handling event rate up to 12.5 kHz. The total rate of data produced by the online trigger system, which needs to be stored for further processing and analysis, is about 230 MB/s. The scheme of the CMS DAQ system is shown in Figure 2.35.

2.2.6 Event reconstruction

The CMS event reconstruction relies on the so called Particle-Flow (PF) algorithm [107, 108], whose aim is to reconstruct and identify each stable particle in the event (leptons, photons, charged and neutral hadrons) combining information from the different subdetectors. Tracks and calorimeter clusters, topologically linked into blocks which are finally interpreted as particles, are the fundamental elements of the PF algorithm.

An iterative tracking reconstruction [109] is used to achieve a high tracking efficiency. At first, tracks are seeded and reconstructed with very tight criteria. The hits are reconstructed from zero-suppressed signals from the pixel and the strip tracker: in the pixel detector, adjacent pixels form clusters whose position is calculated by a weighted average of the charge collected in each pixel; in the strip detector, hit seeds from a strip combined with the charge of neighbor strips form clusters whose position is determined as the charge-weighted strip position. The next steps are performed iteratively using the Combinatorial Track Finder (CTF) software [109], where the hits assigned to the reconstructed tracks in each iteration are removed in subsequent iterations, and the track seeding criteria are progressively loosened. The prompt tracks coming from the interaction point and with high p_T are reconstructed in the first iteration, while the low p_T ones are reconstructed in the second iteration. The displaced tracks, usually coming from a secondary vertex, are reconstructed in the remaining iterations.
To determine the trajectory of a charged particle, a first set of parameters can be estimated from a "track seed" that, given the high granularity and resolution of the pixel sensors, is

usually made from three pixel hits, or from two pixel hits together with the beamspot as constraint. This seed is accepted and used for track finding, based on the Kalman Filter method [110–112] in the CTF algorithm, if the parameters estimated from the seed are consistent with those of a good track. These parameters are then updated by adding hits consistent with the predicted trajectory, taking into account multiple scattering effects and energy loss. At each layer there can be multiple compatible hits, thus a single seed can produce multiple track candidates. To prevent too many candidates, only 5 candidates are considered at each step.
After collecting all hits compatible with a track, a final refit using a Kalman Filter method is performed to calculate the track parameters, starting with a four-hit seed and updating as new hits are added. A Runge-Kutta propagator [113] is used to optimize the precision, taking into account the detector material and the inhomogeneous magnetic field.
Many of the fake tracks produced in the track finding step are then removed with a final selection, that can considerably reduce them with requirements on the number of hits, the quality of the fit, and the parameter significance.
Tracks determine also the position of the interaction vertices in collision events, reconstructed by fitting clustered tracks and using the z coordinate to distinguish particles coming from the hard interaction vertex from those of additional pileup interactions. An interaction vertex is required to have at least two reconstructed tracks originating within 2 mm of the vertex position.

A clustering algorithm of calorimeter energy deposits is designed to reconstruct neutral particles such as photons or neutral hadrons and to measure their energy and the one of electrons, recovering energy loss by bremsstrahlung or photon conversion.

Several elements (charged-particle tracks, calorimeter clusters, muon tracks) are expected from a single particle in the event, so they need to be connected by a link algorithm which reconstructs each particle avoiding possible double counting from different detectors and defines a distance between pairs of elements in the event, quantifying the quality of their link. This algorithm, following a set of criteria depending on the element types, decides whether these elements are linked or not, creating blocks made of several elements. For each block, the algorithm proceeds through the following sequence:

- a "global muon", defined in Section 4.4.3, is reconstructed when its momentum is compatible with that determined from the inner tracker within 3 standard deviations. Muon tracks, as well as calorimetric energy deposits of muons, are then removed from the considered block;

- an electron, primarily reconstructed as energy cluster in the ECAL, is reconstructed if it passes identification criteria defined by an algorithm that exploits tracking and calorimetric variables. Electron tracks and ECAL clusters are then removed from the block;

- the energy deposits in ECAL and HCAL clusters undergo a calibration procedure, correcting for zero-suppression effects and for the non-linear response function of the calorimeters to hadronic showers;

- when there is absence of signal in the muon detectors and the ECAL and HCAL clusters are linked together with a track, if their calibrated combined energy is compatible with the momentum measurement in the tracker a charged hadron is reconstructed, otherwise a neutral hadron or a photon is created from the excess of calorimeter energy. The associated tracks and clusters are then removed from the block;

- the remaining ECAL clusters are associated to photons, and the HCAL energy clusters not matched to charged particle trajectories are associated to neutral hadrons.

For each event, a final collection of individual particles of five possible types is obtained. Charged and neutral hadrons are clustered into jets using various algorithms specific to different analyses. The energies of charged hadrons are determined combining the momentum measurement of the tracker with the energy measurement of the ECAL and HCAL, improving the overall energy resolution on hadronic jets. The energies of neutral hadrons are obtained from the corresponding ECAL and HCAL corrected energies.
Leptons and photons are distinguished from jets by requiring isolation criteria.
The PF reconstruction gives also the best estimate for global event quantities, such as the missing transverse energy calculated as $-\Sigma\vec{E}_T^{miss}$, where the sum runs over all the objects reconstructed by combining all the system information using the PF algorithm.

2.2.7 CMS upgrade for HL-LHC

In order to fully exploit the operation environment of the HL-LHC providing the same high quality data as in Run 1 and Run 2, the CMS detectors will be upgraded.
The CMS upgrade for the Phase II [114] foresees:

- the complete replacement of the current tracker [115]. The silicon tracker will be severely damaged by radiation by the time of the LS3 of the LHC in 2023, thus it will be replaced by a new, light and radiation tolerant detector. A fourth pixel layer increasing the outer radius covered by the pixel detector has already been added during the 2016/2017 end-of-year shutdown. With four silicon pixel layers for a precise vertex reconstruction surrounded by silicon strips for a measurement of the charged particle momentum, the tracker has a finer granularity, which will mitigate the increased tracks overlap, and a pixel coverage extended from the current $|\eta| = 2.5$ to $|\eta| = 3.8$, which will provide a larger acceptance for the analyses in the context of HL-LHC. At variance with the current system, the new tracker will introduce the tracking at the Level-1 trigger level, providing to the L1 system information that will be exploited to compute isolation quantities and to improve the energy resolution on

jets and E_T^{miss}. Improving the event selection already at the L1 trigger, with energy thresholds lower than the ones currently in use, will allow to control the trigger rate and to provide a larger acceptance especially for precision measurements of rare SM processes;

- a completely new dedicated electronics for the Level-1 trigger system [116]. In order to keep only the events where interesting physics could be happening and discard the rest, a highly selective trigger system is necessary, thus it will be redesigned to cope with the much higher instantaneous luminosity. The trigger rate will increase from the current 100 kHz to 750 kHz, with a 40 MHz selective readout for hardware trigger and an HLT output of 7.5 kHz events registered. This higher rate will be matched by the upgraded electronics of the other subdetectors;

- a replacement of the electronics in the barrel calorimeters [117]. For the ECAL barrel, the details are reported in Section 3.1. For the HCAL barrel, the replacement of scintillators and fibers will not be necessary since their expected radiation damage will be negligible for the full HL-LHC. The HPDs will be replaced during Long Shutdown 2 with silicon photomultipliers (SiPMs) that will continue to be used for the HL-LHC period thanks to their higher photo-detection efficiency. The current back-end electronics will not be able to sustain the 750 kHz L1 trigger rate planned for Phase II, thus new electronics based on the design developed for the ECAL barrel will be installed;

- the complete replacement of the endcap calorimeter system [118]. The current endcaps of the ECAL and HCAL will not be able to survive the high radiation levels of the HL-LHC, since the radiation damage will be more than 1.5×10^{15} n_{eq}/cm^2 in the parts closer to the beam line and will affect too much the active components of ECAL ($PbWO_4$ crystals) and HCAL (scintillating tiles and photo-detectors). The endcaps of the calorimeters will then be replaced with a silicon based high granularity sampling calorimeter (HGCAL) with tungsten absorbers in the electromagnetic part and lead absorbers in the hadronic one. It will be radiation tolerant with an excellent timing resolution for the silicon sensors: ≈ 50 ps resolution per layer in electromagnetic showers, where multiple layers can be combined for a better resolution. Overlapping energy deposits will be discriminated by the longitudinal segmentation;

- new detectors in the muon system [119]. New RPC forward chambers ($1.6 < \eta < 2.4$) and the GEM based detectors already inserted in the magnet return yoke will extend the muon system acceptance up to $|\eta| = 2.8$. Precision measurement of the Higgs boson properties through its decay in four muons ($H \to ZZ \to 4\mu$) will benefit from this extended coverage. The electronics of the DT and CSC detectors will also be upgraded;

- a new minimum ionizing particles (MIP) timing detector [120]. A new detector with crystals and silicon photomultipliers (SiPMs) in the barrel and low gain avalanche diodes in the endcap will be able to measure the time of flight of charged particles. It has been proposed in order to reconstruct the time of the interaction vertex and the time of energy deposits in the calorimeters. The inclusion of this information will improve the event reconstruction since the collisions overlapping in space within the luminous region can be separated in time with a resolution of the order of 10 ps. Moreover, exploiting the information of the production time at the interaction point, the energy deposits in the calorimeters coming from neutral particles can be assigned to the correct collision.

With these upgrades, the maintenance and improvement of the CMS performance will be possible even in the harsh environment of the HL-LHC.

Chapter 3

Upgrade studies of ECAL

The excellent energy resolution of the CMS electromagnetic calorimeter (ECAL) played a key role in the discovery of the Higgs boson in LHC Run 1 through the $H \to \gamma\gamma$ decay channel and in the measurement of its couplings to other particles [121]. A high performance electromagnetic calorimetry is crucial also for many analyses involving physics beyond the SM, such as high-mass resonances or detection of final states with energetic photons or electrons [122], and for SM precision measurements [123]. The ECAL must thus provide a high energy resolution, a high position resolution for reconstructed deposits, a good timing resolution, and a fast and efficient readout for online selection.

3.1 ECAL upgrade strategy

The High Luminosity LHC (HL-LHC) will enable to reach about 3000 fb^{-1} of luminosity during 10 years of operation, ten times the luminosity reached by the end of Run 3, as shown in Figure 3.1. The expected pileup is a factor four larger than the current Run 2 values, and unprecedented levels of radiation, up to six times higher than for LHC, will be experienced. The HL-LHC will then be a highly challenging environment. To retain a performance comparable to Run 2, the trigger rate will need to be increased up to 750 kHz and the detectors need to be upgraded. The components that are necessary to upgrade the LHC to HL-LHC will be installed during the long shutdown 3 (LS3).
The ECAL needs an upgrade strategy different for barrel (EB) and endcaps (EE), since the radiation dose will be 100 times bigger in the EE. The radiation-induced loss of crystal response in the forward regions of CMS will require a complete replacement of the ECAL endcaps, prior to the start of HL-LHC. The EE will then be fully replaced by a high-granularity silicon calorimeter (HGCAL) [124], as described in Section 2.2.7.
The luminosity increase poses significant challenges to the operation of the barrel photodetectors. The EB crystals and APDs [125] will remain operational, but there will be a substantial upgrade of the electronics, that will necessitate the removal, re-installation

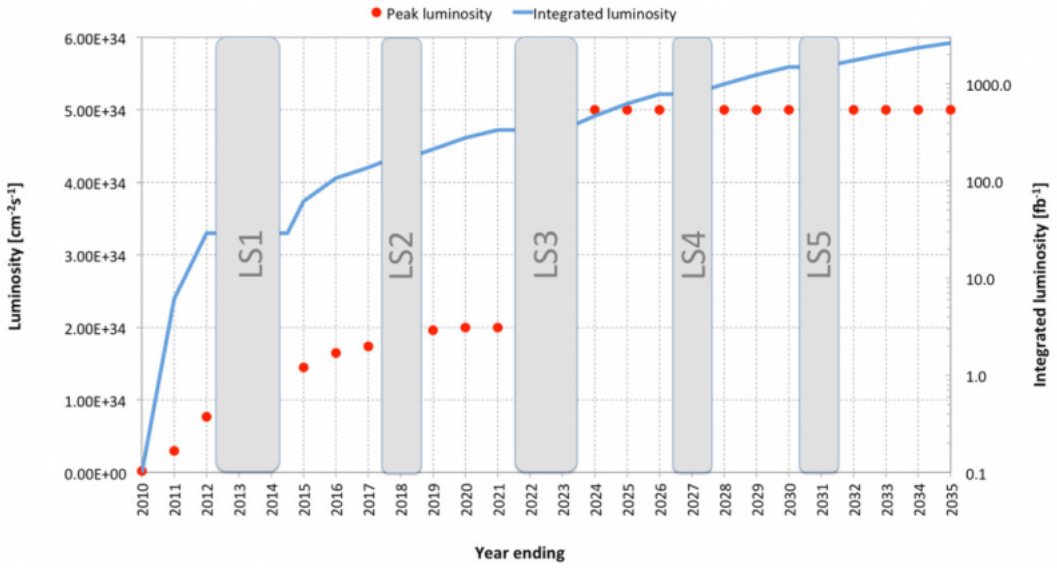

Figure 3.1: *Timeline and luminosity reached by LHC and HL-LHC.*

and re-commissioning of the 36 EB super-modules during the LS3.

3.1.1 Current and new EB electronics

The current EB electronics is composed of readout units, very-front-end (VFE), and front-end (FE) boards, shown in Figure 3.2.
The basic readout unit, the motherboard, is linked to a 5×5 crystal matrix and is the building block for the on-detector electronics. It distributes the LV to the VFE and hosts 5 VFE cards.
Each VFE board readouts 5 channels with a multi gain pre-amplifier (MGPA) ASIC with about 43 ns shaping time, and a 12 bits analog-to-digital converter (ADC) with sampling rate of 40 MHz.
The FE electronics takes care of data pipeline and transmission, generates trigger information with 5×5 crystals granularity, and separates the readout for data and trigger. As shown in Figure 3.3, the FE cards are equipped with a FENIX chip that sums the energy of 5 crystals within a strip, analyzes the digitized signal, and performs trigger and readout functions.
The access to the motherboards is very complex since they are mounted under the water cooling block for the electronics boards, thus replacing them would be a long and risky operation. Since their replacement is not necessary, as confirmed by accelerated ageing and irradiation tests, the motherboard, the APDs, and the crystals will be kept in place, while the VFE and FE boards will be replaced.

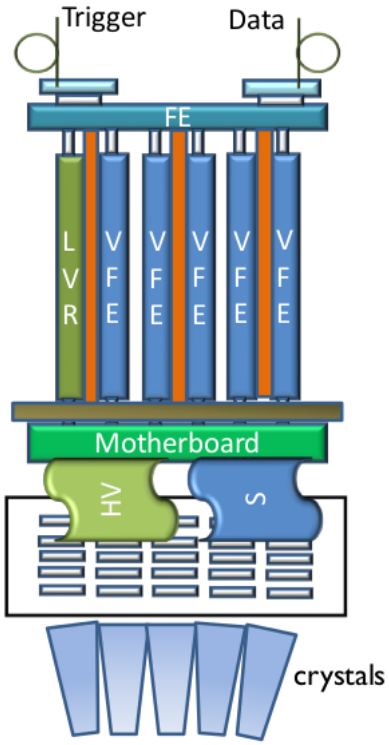

Figure 3.2: *Scheme of electronics used currently in the ECAL EB: motherboard, VFE and FE boards.*

The new electronics scheme is shown in Figure 3.4. The VFE boards contain the readout of 5 channels, each composed by:

- a CATIA pre-amplifier, a Trans Impedance Amplifier (TIA) with 50 MHz bandwidth and a 2-gain (×1-×10) output;
- a data transfer unit (LiTE-DTU) that will send data to the FE, implementing a data compression from 2.08 Gb/s to 1.28 Gb/s with a gain selection logic and a lossless data compression algorithm;
- two 12 bits ADCs with 160 MHz sampling frequency, integrated in the LiTE-DTU, that will receive the two analog signals from the two gains of the preamplifier output and convert them to a digital representation of the pulse.

The FE boards design will provide fast and radiation tolerant optical links to transmit data off-detector through CERN lpGBT and Versatile+ links, as shown in Figure 3.5. At variance with respect to the Phase 1 electronics, providing trigger information with a granularity of 5×5 crystals, the new electronics will provide trigger information based on single crystal data to the L1 calorimeter trigger. Therefore the FE card will not compute

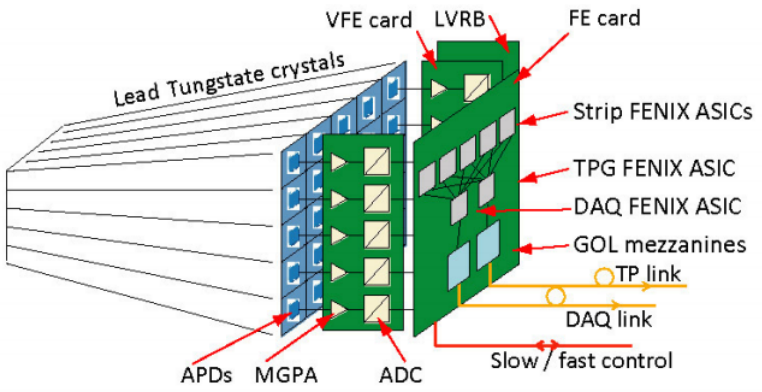

Figure 3.3: *Layout of the legacy system.*

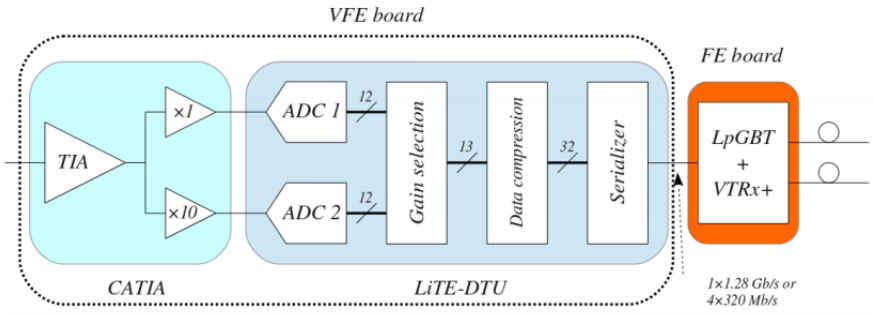

Figure 3.4: *Layout of the new electronics for phase 2.*

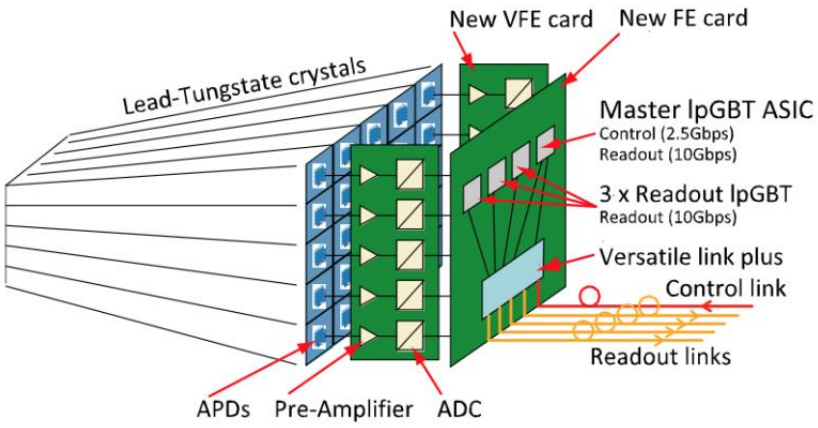

Figure 3.5: *Layout of the phase 2 system.*

trigger primitives anymore but will only act as "pass-through" for data and as distributor of the clock.
The low voltage regulator cards (LVR), one every 5×5 crystals, are based on the radiation and magnetic field tolerant DC-DC converters developed by CERN [126]. These highly efficient and compact devices provide very low noise output and 1.2 and 2.5 voltages.
For the off-detector electronics, one board will combine all functions: DAQ, trigger, and control of FE boards.

3.1.2 Requirements for EB upgrade

In order to maintain the Run 2 performance at the higher luminosity and pileup of the HL-LHC, the EB electronics must comply with the CMS Level-1 (L1) trigger requirements, provide more precise timing resolution, and mitigate the increasing noise from the photodetectors.

The main motivation for the EB upgrade is the trigger requirement necessary to achieve a L1 trigger accept rate of about 750 kHz, about 7.5 times higher than the current one, as described in Section 2.2.7. The new on-detector and off-detector electronics will then be replaced to satisfy a trigger latency of 12.5 μs, with an increase of about a factor three with respect to the current one of 4 μs.

The new on-detector ASICs is being designed to perform pulse amplification, shaping, and digitization of the signal at a sampling rate of 160 MHz, and will allow to maintain the best possible energy resolution for the HL-LHC. The new design of the VFE boards involves also a shortening of the signal shaping time (t) from 43 ns to about 20 ns. These characteristics will enable better timing resolution, reduced APD noise, which goes like $\sqrt{t}$, and improved pileup mitigation at L1.

In the most irradiated regions of the ECAL barrel, the predicted neutron fluence at the HL-LHC is about 2×10^{14} n/cm^{-2}. Recent studies [127] have shown that the APDs will remain operational under such conditions, however the dark current increases linearly with the neutron fluence, and the readout noise will have an increase of about a factor 10 after 3000 fb^{-1}, corresponding to ≈ 400 MeV/channel.
To mitigate the APD radiation-induced increase of the leakage current, a reduction of the operating temperature from the current 18°C to $8-10$°C is foreseen, which will reduce the induced noise by about 35%, as shown in Figure 3.6. The temperature reduction will not require an upgrade of the ECAL cooling system, but the ECAL cooling plant, currently supplied with water at 14°C, will be required to have chilled water at 6°C for operations at 9°C.

The new ASICs will also improve the suppression of signals caused by direct ionization of the APDs, called *"spikes"*. These signals are energy deposits in a single APD: since the scintillation signal is missing, they have a shorter pulse than the one of signals compatible with an electromagnetic shower, which is also spread over several crystals.

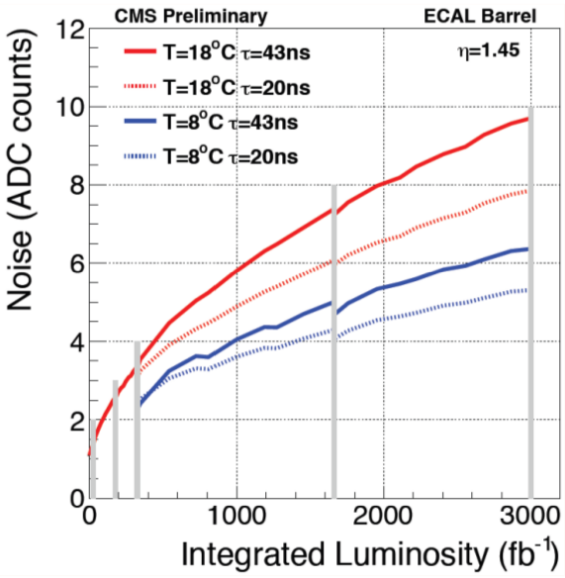

Figure 3.6: *Noise of APDs as a function of integrated luminosity. The dark current for APDs operating at* 18°C *(*9°C*) is shown by the red (blue) curve. The solid (dashed) lines show a shaping time of* 43 *(*20*) ns. The vertical gray lines indicate the long shutdowns periods.*

The performance of the current spike rejection algorithm at L1, based on topological requirements on the shower shape, will not be sufficient at the HL-LHC, where the expected spike rate in ECAL is as much as one per bunch crossing, dominating the available trigger bandwidth. A reduction of the pulse shaping time from 43 to about 20 ns, an increased sampling rate to 160 MHz, and a better isolation provided by the use of single crystals information at the L1 trigger will greatly improve the pulse shape discrimination between scintillation signals and spikes. They will also increase the granularity of the topological discrimination, providing additional handles to keep a similar performance as the one obtained during Phase 1 operations. The improvement in the rejection of APD spikes is shown in Figure 3.7.

Recent developments in radiation hard optical links (lpGBT) will permit the amplification, digitization, and transmission of data from all ECAL readout channels to new off-detector electronics, capable of processing these data with more complex and better-performing algorithms than are currently possible. For instance, a more granular clustering, a better spatial resolution, and a new tracks-cluster association whith approximated tracks available at L1 thanks to the new tracker system, explained in Section 2.2.7, will be used. The off-detector electronics will have to accommodate higher transfer rates and to generate trigger primitives. This will allow the exploitation of the full ECAL granularity at the Level-1 trigger.

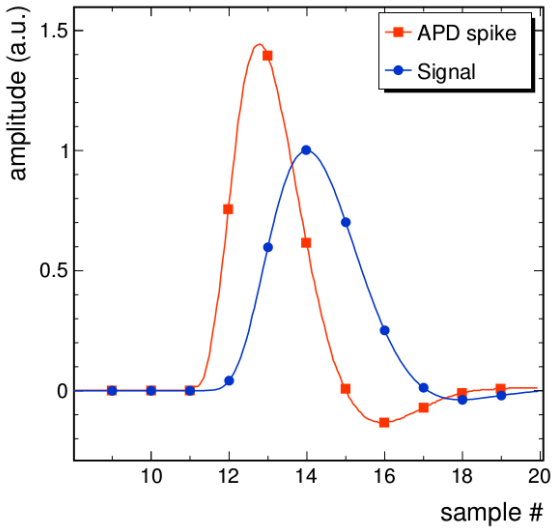

Figure 3.7: *Average pulse shapes from APD spike (red) and scintillation signal (blue). The amplitude samples from the digitization at* 160 *MHz sampling frequency are shown as dots and squares.*

The on-detector readout chain is being designed also with the aim of exploiting the excellent intrinsic timing resolution of the crystals, in order to discriminate between energy deposits arising from different overlapping events in the same bunch crossing based on their time-of-flight. The short shaping time (20 ns) and the fast sampling rate (160 MHz) will allow to approach the intrinsic timing capacity of the detector of $\approx 20 - 30$ ps, as given from test beam measurements and shown in Figure 3.8.
Timing of high energy photons with 30 ps precision can be exploited to keep the same $H \to \gamma\gamma$ vertex assignment efficiency as in Run 2. In the $H \to \gamma\gamma$ analysis, the primary vertex is identified through a MVA exploiting the kinematic properties of the tracks associated with the $H \to \gamma\gamma$ vertex and their correlation with the diphoton system. The identification efficiency of this method is $\approx 80\%$ at a pileup of 30 events, while it drops below 40% at 140 pileup events and is $\approx 30\%$ at 200 pileup events. A precise time measurement of both photons would enable to determine the vertex position along the beam direction via triangulation, and thus mitigate this efficiency loss.
More information about the ECAL HL-LHC upgrade can be found in [117].

3.2 Test beam

To test the new prototypes of the HL-LHC readout electronics and evaluate the energy and time resolution of the calorimeter, some beam test campaigns were performed at the H4 beam line in the SPS North Area of CERN during 2015, 2016, 2017 and 2018.

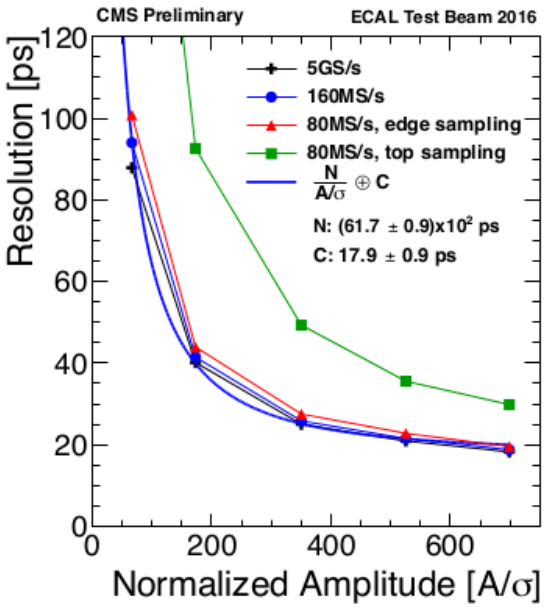

Figure 3.8: *Timing resolution as a function of normalized amplitude for different sampling frequencies. The* 160 *MHz sampling rate is shown in blue.*

In the 2015 campaign, the impact of the shaping time was studied, comparing the performance of the current (43 ns) and the reduced (20 ns) shaping time.
In 2016, the performance of a TIA prototype were tested. The prototype, used to readout a matrix of crystals with APDs and linked to a digitizer with a 5 GHz sampling frequency, was constructed using discrete components and its sampling frequencies were emulated at analysis level.
In 2017, a VFE prototype with discrete components and a commercial ADC was studied, while in 2018 the first prototype of CATIA, with 160 and 120 MHz readouts and a commercial ADC, was tested. The 2018 test beam campaign is described in details in the following sections, together with its data analysis.
The beam is made of high energy electrons with energies between 20 and 250 GeV, with a beam purity of 99% and a relative momentum spread ($\Delta p/p$) that can be as low as 0.5% while keeping an acceptable event rate for measurements. The beam line can also provide a equally pure pion beam.
Created from the primary SPS proton beam, which hits a metallic target producing a variety of particles selected through a system of magnets, collimators, and additional targets, as shown in Figures 3.9 and 3.10, this secondary electron beam is composed of several bunches extracted with a converter in an interval of $4-5$ s every $14-48$ s, depending on the SPS cycle configuration. In order to provide a uniform and less intense beam to the test area, the bunch scheme of the SPS beam is destroyed by the extraction line.
More details about the test beam can be found in [128].

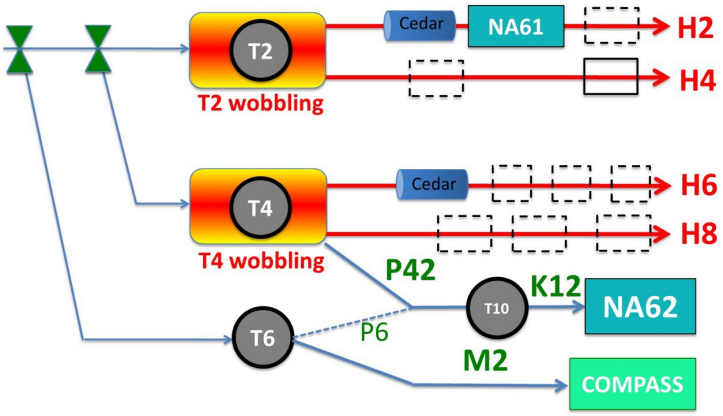

Figure 3.9: *Layout of the SPS secondary beam line: the* 400 GeV *primary proton beam is split into three beams directed towards the T2, T4, and T6 targets. Thanks to the T2 "Wobbling station", the two H2 and H4 secondary beams are derived.*

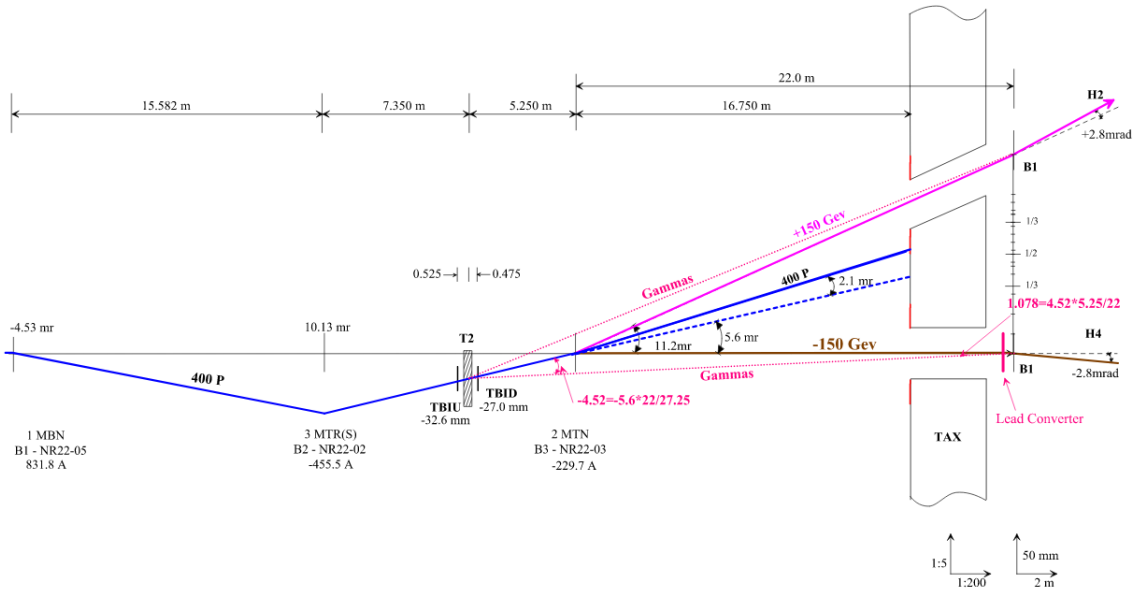

Figure 3.10: *Detail of the H4 beam line, produced by the proton beam targeting the T2 target.*

3.2.1 Test beam setup

The experimental setup of the 2018 test beam campaign consists of:

- a matrix of 5×5 crystals, similar to those installed in the ECAL barrel, shown in Figure 3.11;
- 5 VFE boards, shown in Figure 3.12, equipped with a Calorimeter Trans Impedance Amplifier (CATIA) chip, VFE adapters to custom-made FE boards, and a commercial 12-bit ADC operated at 120 and 160 MHz;
- an external digitizer CAEN V1742 VME board, shown in Figure 3.13, with a sampling frequency of 5 GHz;
- two micro-channel plate (MCP) detectors placed in front of the matrix and serving as reference for timing measurements, given their typical resolution of $\approx 20 - 30$ ps;
- two planes of scintillating fibers hodoscopes placed ≈ 3 m upstream of the crystals and the MCP, each composed of 64 fibers and with a spatial resolution of 0.5 mm, used to measure the position of the particles hitting the experimental setup in the plane transverse to the beam direction ($x - y$ plane).

To avoid light-induced noise in the photo-detectors, the crystal matrix and the readout electronics are kept inside a closed box, shown in Figure 3.13. The box is mounted on a movable, computer controlled table, and thermalized by a dedicated cooling system surrounding the matrix and driven by a water chiller. The nominal operating temperature has been of 18°C, but measurements have been made also at 9°C. A schematic view of the setup is shown in Figure 3.14.
Since the beam divergence is negligible, the particle transverse position measured by the hodoscopes corresponds to the impact point on the crystals face, as shown in Figure 3.15. The incoming particles are detected by three plastic scintillators of 6×6 cm^2, 3×3 cm^2, and 1×1 cm^2, placed few meters upstream of the crystals position. The trigger for the acquisition system is build as a coincidence of these three scintillation signals.

The goals of these test beam (TB) were to test the new CATIA chip with the 160 MHz ADC and to check the performance of the new electronics with timing resolution measurements. These can be performed comparing the time measured by the crystal hit by the electron to the one measured by an external reference, provided by the MCP, when the beam is centered in the middle of the crystal, as shown in Figure 3.16 on the left. Alternatively, the beam can be centered between two crystals, as shown in Figure 3.16 on the right, and the timing resolution can be derived from the time difference of the two crystals.

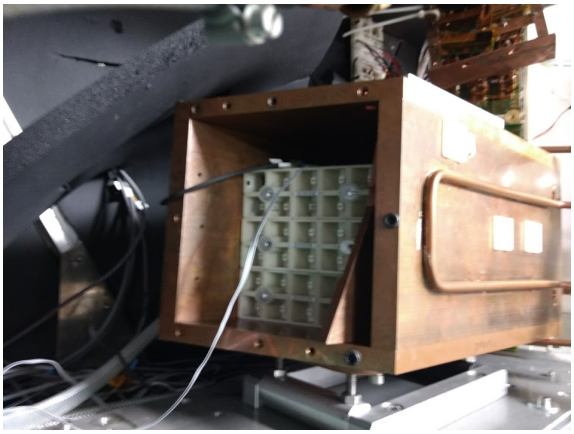

Figure 3.11: *Picture of the matrix of* 5×5 *crystals used for the test beam.*

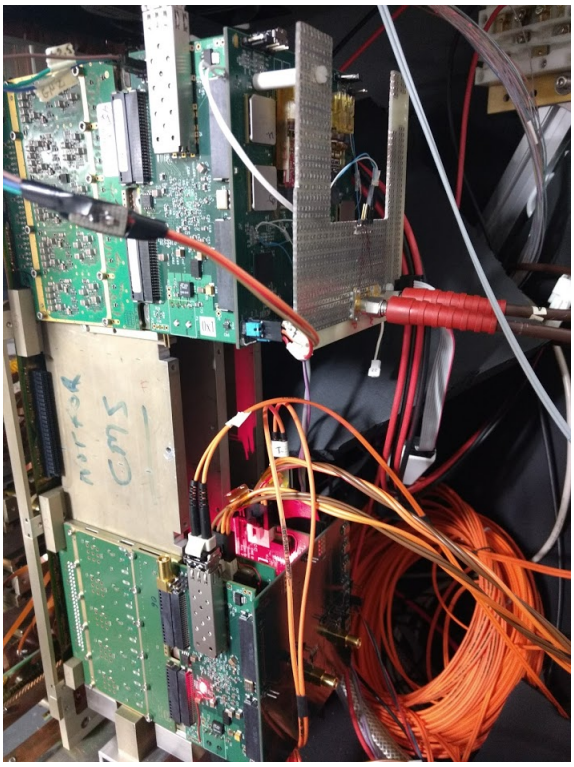

Figure 3.12: *Picture of the electronic boards used in the test beam: the VFE board is on the bottom left, next to it there is the VFE adapter to the custom-made FE board, placed transversely. The VFE adapters and the custom-made FE boards will be replaced with the final FE prototype.*

Figure 3.13: *Picture of the test beam setup: the digitizer is on the left, while on the right there is the box in which the crystal matrix, the VFE and FE boards are installed.*

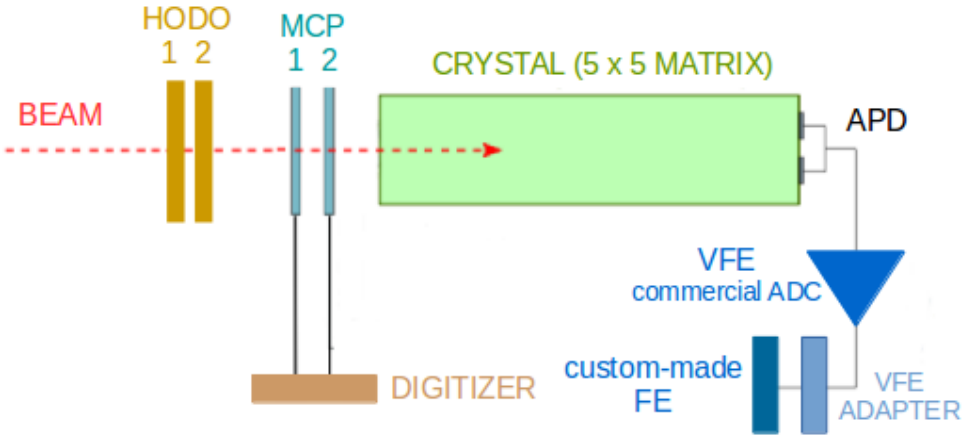

Figure 3.14: *Schematic view of the test beam setup: the electron beam comes from the left side and intersects subsequently the hodoscopes and the MCPs, arriving then in the crystal, drawn in green. The signals from the two APDs glued on the rear face of the crystal are merged before the pre-amplifier in the VFE, sampled with a commercial ADC. Data are send to digitzer through the VFE adapter and the custom-made FE.*

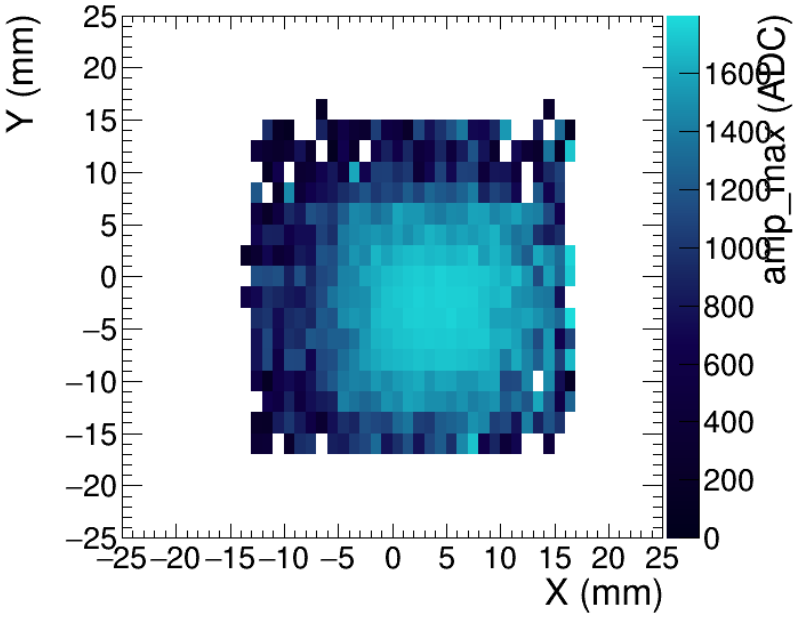

Figure 3.15: *Distribution of the signal amplitude of a single crystal as a function of the transverse impact position for a* 50 GeV *electron beam.*

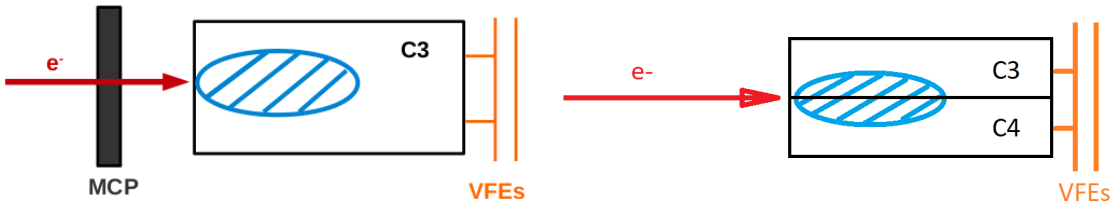

Figure 3.16: *Schematic representation of a beam centered in the middle of the crystal (left) for the timing resolution measurement between one crystal and the MCP, and of a beam centered between two crystals (right) for the timing resolution measurement between two adjacent crystal.*

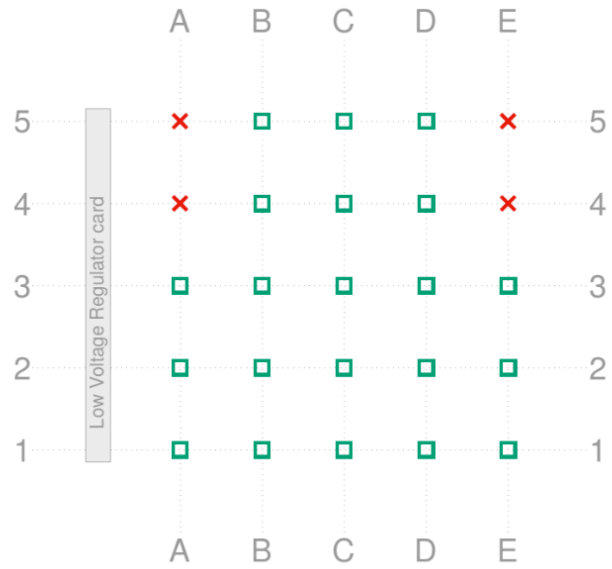

Figure 3.17: *Scheme of the crystals matrix used in the June 2018 test beam.*

3.2.2 Test beam analysis

The analysis of the June 2018 campaign is described here. The scheme of the crystals matrix used in this test beam is represented in Figure 3.17.

Amplitude and time reconstruction

The CAEN digitizer with a sampling frequency of 5 GHz acquires 1024 samples, one every 200 ps, for each event and for each of its channels. After passing through an VME bus and an optical interface, the samples arrive to a computer used for the acquisition, where a specific software synchronize the events between the digitizer and the hodoscopes. The MCP signal is very fast, ≈ 4 ns, and its amplitude is estimated as the value of the maximum sample. The amplitude of the MCP, A_{MCP}, shown in Figure 3.18 on the left, is required to be > 150 ADC counts to ensure a good time measurement. The time of the MCP, t_{MCP}, shown in Figure 3.18 on the right, is extracted with a fit to the MCP shape using a sigmoid function:

$$f(t) = A \cdot [1 + tanh((t - t_0)/B)]/2 + C.$$

For the APD signal, the amplitude and time, shown in Figure 3.19 on the left and on the right respectively, are estimated through a template fit to the signal shape. The pulse shapes are estimated with a Fourier-transform technique and a different template is generated for each crystal and for each energy.

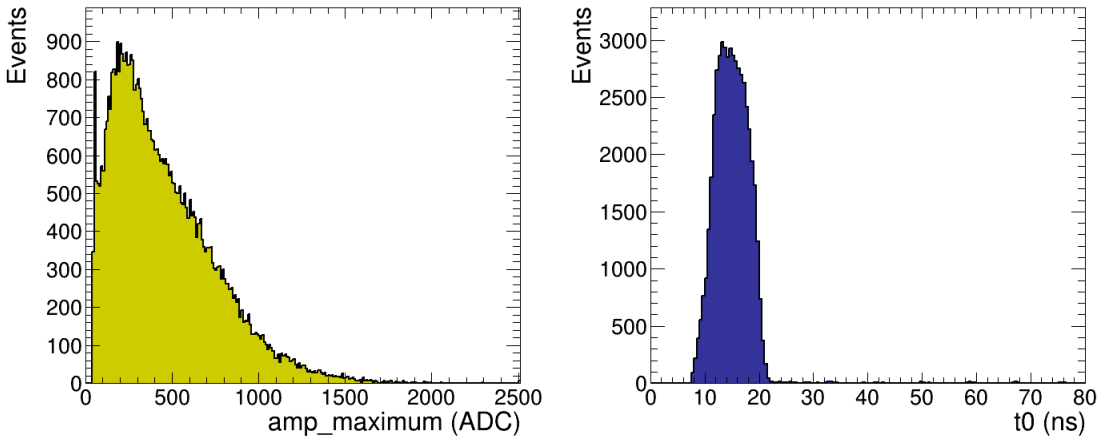

Figure 3.18: *Amplitude (on the left) and time (on the right) of the MCP.*

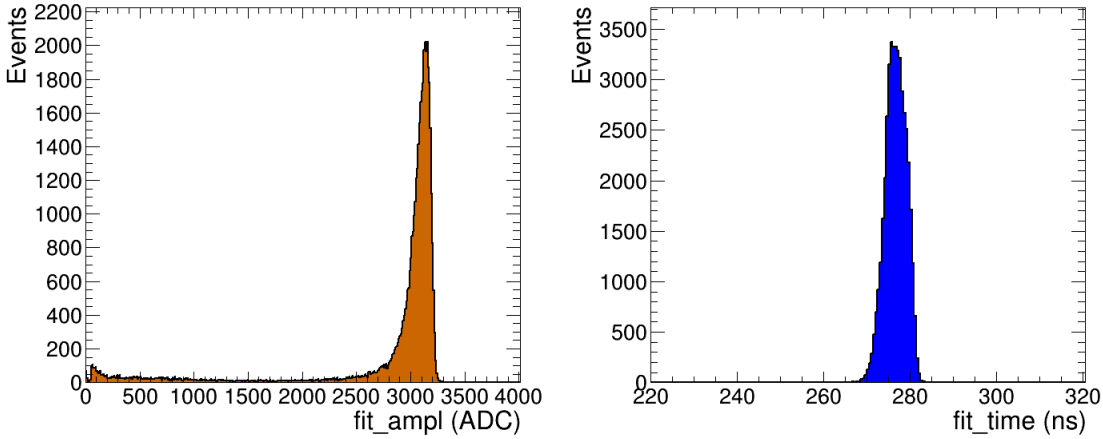

Figure 3.19: *Amplitude (on the left) and time (on the right) of the crystal estimated from the template fit. The tail at low energy in the amplitude plot is due to events coming from pions present in the beam: the purity of the beam can be estimated of* $\approx 95\%$.

The template fit to data is performed on the samples around the maximum sample minimizing the following distribution:

$$\chi^2 = \Sigma_i \frac{[A_i - A_0 \cdot F_{tmpl}(t_i - t_0)]^2}{\sigma_n^2},$$

where A_0 e t_0 are the amplitude and time values corresponding to the maximum sample. The templates generated for different energies are very similar in the same crystal, as shown in Figure 3.20. However, performing the ratio between each template and the template corresponding to the 150 GeV energy, small disagreements are visible in the tails of the fit range, as shown in Figure 3.21. For each energy run, the corresponding template is thus used.
To compare the crystal timing with the MCP one, the VFE clock needs to be synchronized with the CAEN digitizer. Each rising edge of the clock distribution, shown in Figure 3.22, is fitted to measure the period and the phase of the clock, visible in Figure 3.23 on the left and on the right, respectively.

Time resolution

The time resolution of the crystals plus APDs system can be extracted from the time difference between the most energetic crystal and the MCP, or between the two most energetic crystals of the same electromagnetic shower, where shower fluctuation effects cancels out.
For the first case, the time resolution is given by:

$$\sigma(t_{crystal} - t_{MCP}) = \left(\frac{N}{A/\sigma_n}\right) \oplus C \oplus C_{MCP}, \tag{3.1}$$

where $t_{crystal}$ and t_{MCP} are the times measured by the crystal and by the MCP, respectively, A is the average amplitude of the crystal signal at a given energy, σ_n is the RMS of the noise, N represents the noise term, C the constant term, and C_{MCP} the time resolution of the MCP.
For the second case, the time resolution is given by:

$$\sigma(t_1 - t_2) = \left(\frac{N}{A_{eff}/\sigma_n}\right) \oplus \sqrt{2} \cdot C, \tag{3.2}$$

where $t_{1,2}$ refers to the times measured by the two crystals, and A_{eff} is the effective amplitude given by:

$$A_{eff} = \frac{\sqrt{2}A_1A_2}{\sqrt{A_1^2 + A_2^2}},$$

with $A_{1,2}$ the amplitudes of the two crystals.

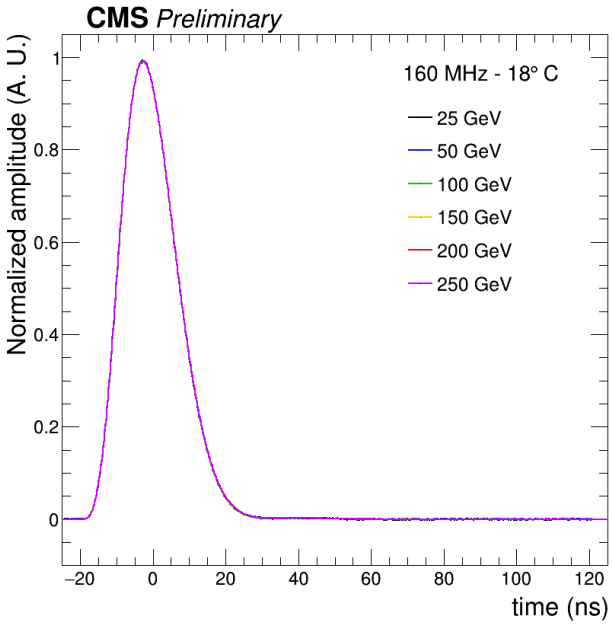

Figure 3.20: *Templates for C3 crystal at different energies.*

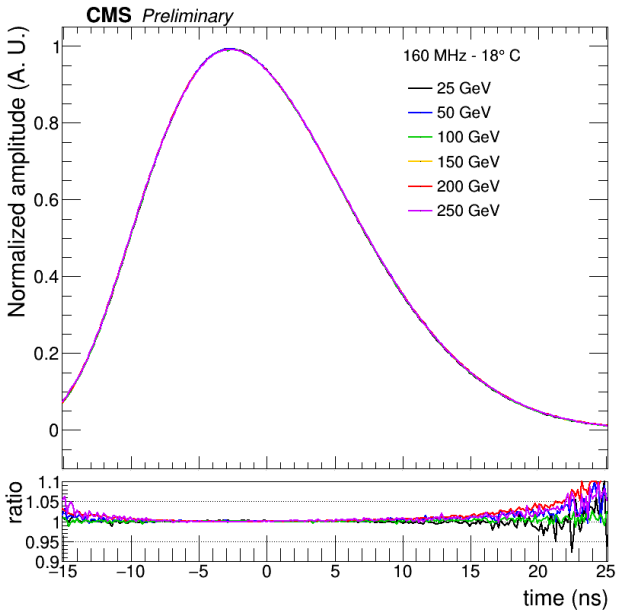

Figure 3.21: *Templates for C3 crystal at different energies in the template fit range, and ratio of each template with respect to the* 150 GeV *template.*

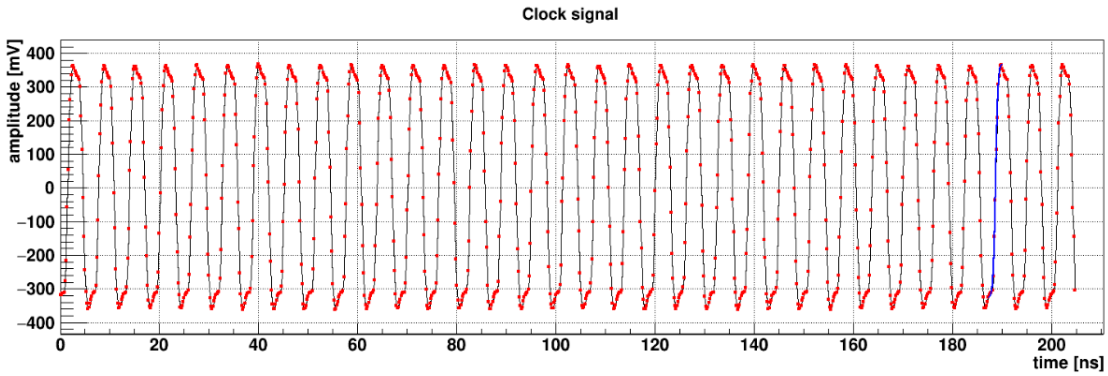

Figure 3.22: *Clock distribution. The fit performed to a rising edge is shown in blue.*

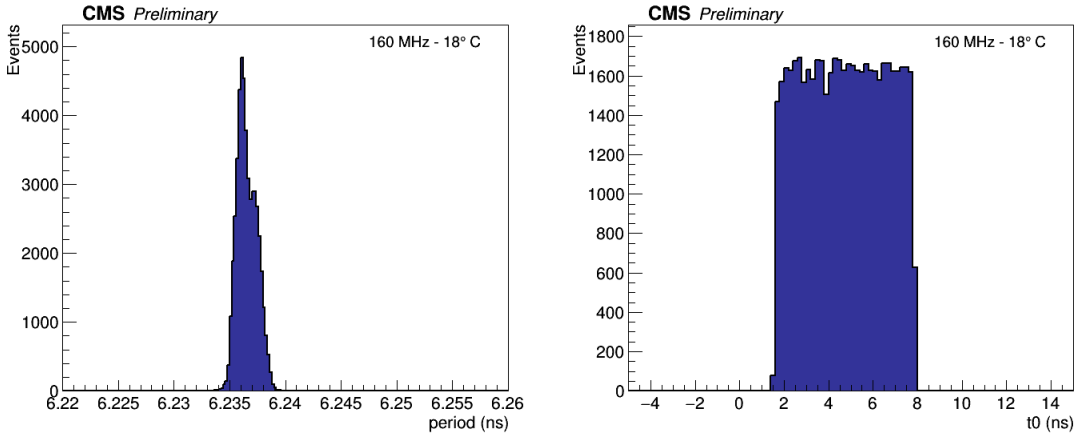

Figure 3.23: *Period (on the left) and phase (on the right) of the clock distribution.*

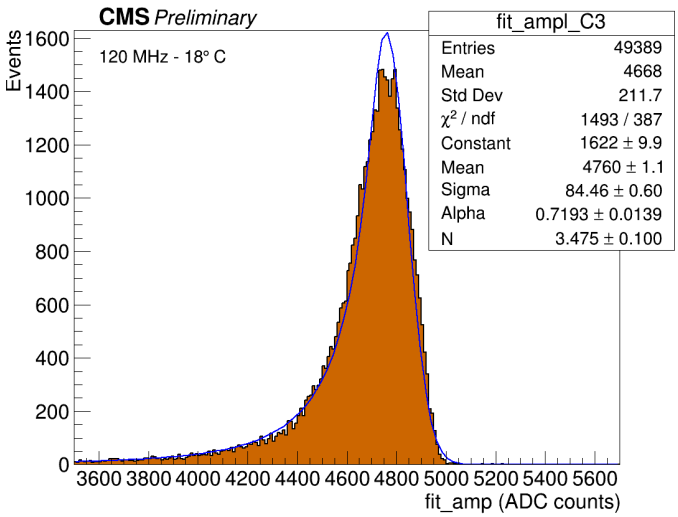

Figure 3.24: *Crystal-Ball fit (blue line) to the amplitude peak of the crystal.*

The amplitude of the crystal signal is extracted from a Crystal-Ball fit around the amplitude peak, as shown in Figure 3.24. The noise, σ_n, is taken from the RMS of the first 10 samples, and shown in Figure 3.25.

The timing resolution performed here uses the MCP as external time reference, so runs with beam centered in the middle of the crystal C3 are considered.
The time resolution $\sigma(t_{crystal} - t_{MCP})$ is estimated by the standard deviation extracted from a Gaussian fit to the time difference distribution between a crystal and one MCP, shown in Figure 3.26.
This operation is performed at different energies: 25, 50, 100, 150, 200, and 250 GeV. To select good events around the beam impact point, only events in which the electron hitting the crystal is within a region of 3×3 mm^2 around the center of the front face were considered.
Two MCPs were used as external reference in the timing resolution measurement. In order to get the resolution of the VFE, the resolution of the MCPs has thus to be removed from $\sigma(t_{crystal} - t_{MCP})$. To get the MCPs resolution, the 2D plot of the time difference between the two MCPs as a function of their effective amplitude:

$$A_{eff} = \frac{\sqrt{2} A_{MCP_1} A_{MCP_2}}{\sqrt{A^2_{MCP_1} + A^2_{MCP_2}}},$$

shown in Figure 3.27, is considered. The $\sigma(t_{MCP_1} - t_{MCP_2})$ is taken from Gaussian fits performed in each vertical bin of that plot, and is then fitted as a function of A_{eff} with

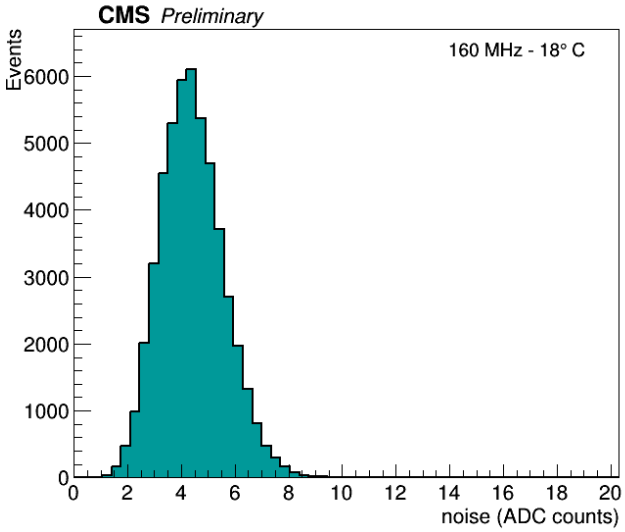

Figure 3.25: *Noise distribution of the crystal.*

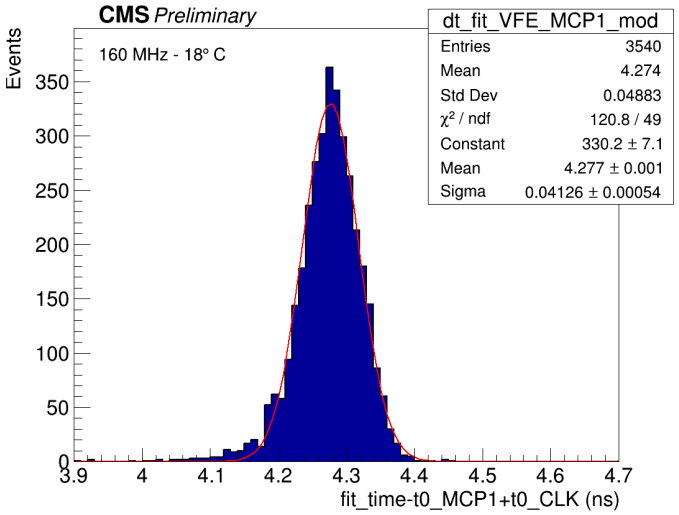

Figure 3.26: *Time difference distribution between C3 crystal and MCP1 for a run at* 200 GeV. *The Gaussian fit is represented by the red line.*

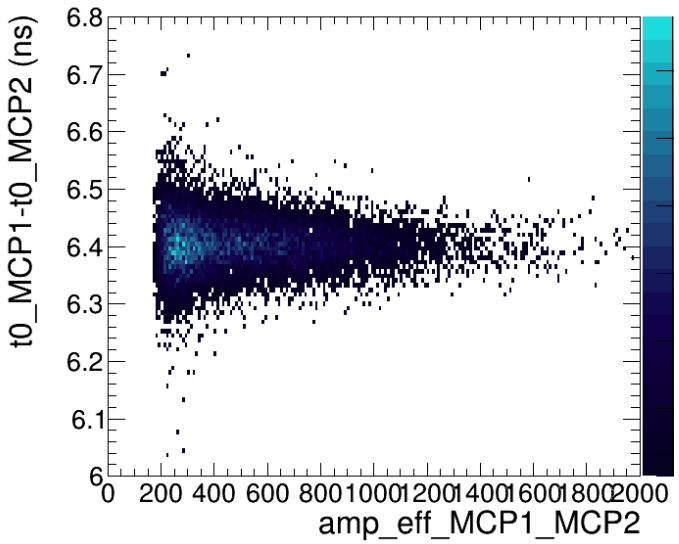

Figure 3.27: *Time difference distribution between the two MCPs as a function of their effective amplitude.*

the following function:

$$\sigma(t_{MCP_1} - t_{MCP_2}) = \frac{\sqrt{2}N_{MCP}}{A_{eff}} \oplus \sqrt{2} \cdot C_{MCP}. \tag{3.3}$$

From the fit, shown in Figure 3.28, the resolution of the two MCPs is estimated from the constant term $C_{MCP} \approx 20$ ps.
The MCPs resolution is estimated event-by-event for each energy run using the parametrized function of Equation 3.3.

The timing resolution between a crystal and a single MCP is thus given by:

$$\sigma(t_{crystal} - t_{MCP_{1/2}}) = \sqrt{\sigma^2_{crystal-MCP} - \sigma^2_{MCP_{1/2}}}.$$

For the time difference between a crystal and a MCP, the timing resolution is then fitted as a function of A/σ_n by the function:

$$\sigma(t_{crystal} - t_{MCP_{1/2}}) = \left(\frac{N}{A/\sigma_n}\right) \oplus C,$$

from where the N and C coefficients are estimated.

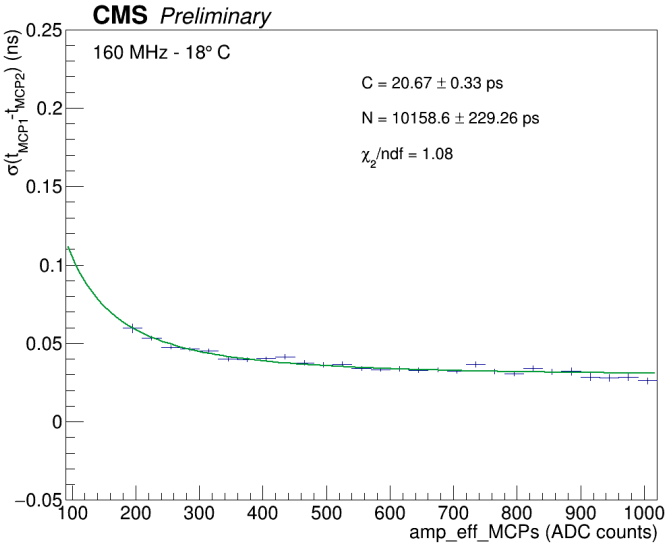

Figure 3.28: *Distribution of the resolution of the two MCPs as a function of their effective amplitude for runs at* 160 *MHz and* 18°C. *The fit is represented by the green line.*

3.2.3 Test beam results

The results of the June 2018 test beam campaign are reported here for different configurations of temperature, following the same procedure described in the previous Section:

160 **MHz -** 18° **C:** the timing resolution estimated using an MCP as external reference is shown in Figure 3.29 for the first MCP and in Figure 3.30 for the second one.
The results of the analysis considering the first MCP as external reference give a constant term $C \approx 26.8 \pm 1.0$ ps and a noise term $N \approx 10.2 \pm 0.3$ ns. Considering instead the second MCP, the constant term is $C \approx 26.3 \pm 1.0$ ps and the noise term is $N \approx 10.3 \pm 0.3$ ns.
The results obtained with the two MCPs are very similar, thus in the following only the results referring to MCP2 are considered since it has a better efficiency than MCP1.

160 **MHz -** 9°C**:** the timing resolution estimated using MCP2 as external reference is shown in Figure 3.31. The constant term is $C \approx 25.7 \pm 1.2$ ps and the noise term is $N \approx 13.2 \pm 1.2$ ns.

Table 3.1: *Timing resolution results for* 160 *MHz and* 18°/9° *C.*

		18° C		9° C	
		MCP1	MCP2	MCP1	MCP2
160 MHz	C (ps)	26.8 ± 1.0	26.3 ± 1.0	25.9 ± 1.2	25.7 ± 1.2
	N (ns)	10.2 ± 0.3	10.3 ± 0.3	12.7 ± 1.2	13.2 ± 1.2

The results are summarized in Table 3.1 and in Figure 3.32. The fit parameters are similar for 18°C and 9°C at 160 MHz, as expected.
During the 2016 campaign, which used a TIA prototype with discrete components, a 5 GHz digitizer, and a simulated sampling rate of 160 MHz, the asymptotic timing resolution was estimated at $\approx$ 18 ps, as shown in Figure 3.8. In 2016, the same clock (on the digitizer) was used for the VFE and the MCP, while now a different clock is used for the VFE and the MCP. The MCP still uses the digitizer, while for the VFE, the clock arrives at the ADC passing through an FPGA which typically introduces jitters of $\approx$ 15 ps. The timing resolution obtained in 2018 is then given by the difference in quadrature between the value calculated and the jitter:

$$\sigma_{2018} = \sqrt{\sigma^2_{\text{crystal-MCP}} - \text{jitter}^2} \approx 21\text{ps}.$$

The 2018 results are thus compatible within the uncertainties with the 2016 ones.

The values of maximum amplitude for the C3 crystal are listed in Table 3.2 for the different configurations of temperature and sampling rate, while the values of time resolution between C3 crystal and MCP1 (MCP2) are reported in Table 3.3 (3.4).
The amplitude values at 9°C are $\approx$ 20% bigger than the values at 18°C, as expected from the temperature dependence of light emission, typically of $\approx$ 2%/°C for $PbWO_4$ crystals at $\approx$ 18°C [100].

Table 3.2: *Maximum amplitude values (in ADC counts) for C*3 *crystal for* 160/120 *MHz and* 18°/9° *C.*

	25 GeV	50 GeV	100 GeV	150 GeV	200 GeV	250 GeV
160 MHz - 18° C	765	1565	3135	4725	6265	7685
160 MHz - 9° C	-	1835	3725	5605	7415	9165
120 MHz - 18° C	775	1565	3185	4745	6285	-
120 MHz - 9° C	935	1885	3895	5725	7555	-

Table 3.3: *Values of σ (in ps) of time difference between C3 crystal and MCP1 for 160MHz and 18°/9° C.*

	25 GeV	50 GeV	100 GeV	150 GeV	200 GeV	250 GeV
160 MHz - 18° C	71.3	51.8	43.8	41.9	41.3	40.5
160 MHz - 9° C	-	49.4	43.3	41.8	40.6	38.3

Table 3.4: *Values of σ (in ps) of time difference between C3 crystal and MCP2 for 160 MHz and 18°/9° C.*

	25 GeV	50 GeV	100 GeV	150 GeV	200 GeV	250 GeV
160 MHz - 18° C	71.3	52.1	43.9	41.2	40.4	39.6
160 MHz - 9° C	-	48.9	43.4	41.3	40.7	40.3

3.3 Conclusions

The CMS electromagnetic calorimeter, crucial for many physics analyses thanks to its precise measurements of electrons and photons energies, has been giving excellent performance throughout LHC Run 2 data taking.
To maintain performance comparable to Run 2 also during the High Luminosity LHC, in an environment with unprecedented levels of pileup and radiation, an upgrade of the detector is needed.
The main changes for the ECAL EB will be the replacement of VFE, FE and off-detector electronics, an upgrade of the cooling system with an operating temperature of $8 - 10$°C, the use of single crystal information in the Level-1 trigger, a new design for VFE electronics with a shorter pulse shaping at 20 ns and a faster sampling rate of 160 MHz, 12-bit ADCs with two gains, and new FE boards with radiation hard optical links (lpGBT).
Test beam campaigns are being carried out to test the prototype devices and extrapolate the future performance.
During the test beam of June 2018, the new CATIA chip with a commercial ADC operated at 160 and 120 MHz was tested, both at 18°C and 9°C.
The timing resolution performed between one crystal and one MCP with the ADC at 160 MHz and 18°C or 9°C gives a constant term of $\approx$ 26 ps, result compatible, within the uncertainties, with the 2016 one.

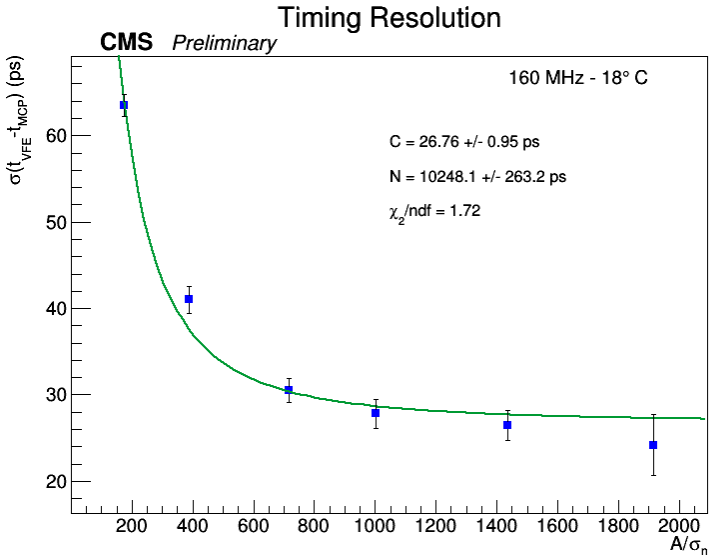

Figure 3.29: *Time resolution given by the difference between a crystal and the first MCP as a function of the normalized amplitude for* 160 *MHz and* 18°C. *The fit is represented by the green line.*

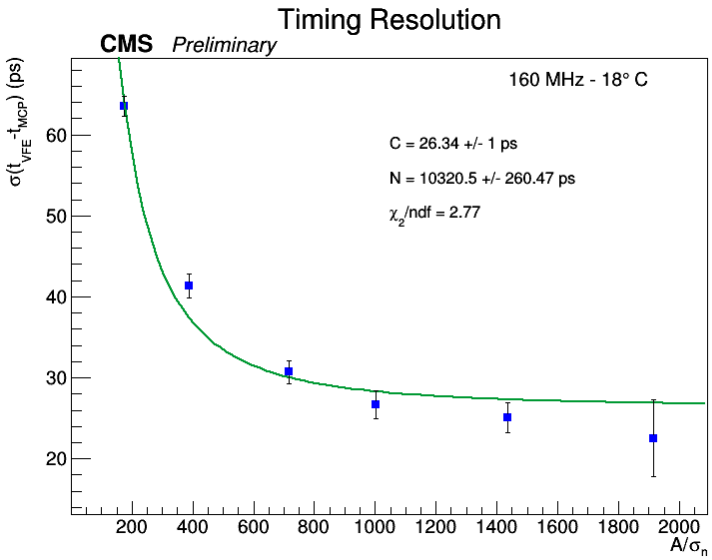

Figure 3.30: *Time resolution given by the difference between a crystal and the second MCP as a function of the normalized amplitude for* 160 *MHz and* 18°C. *The fit is represented by the green line.*

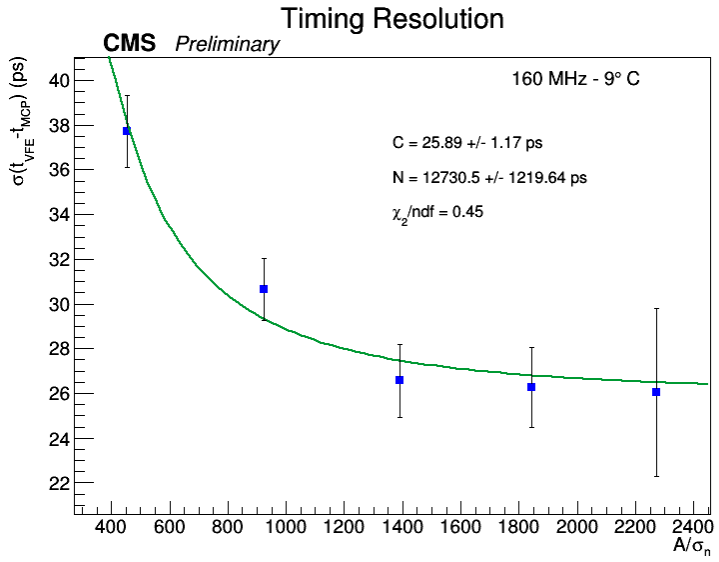

Figure 3.31: *Time resolution given by the difference between a crystal and the second MCP as a function of the normalized amplitude for* 160 *MHz and* 9°C. *The fit is represented by the green line.*

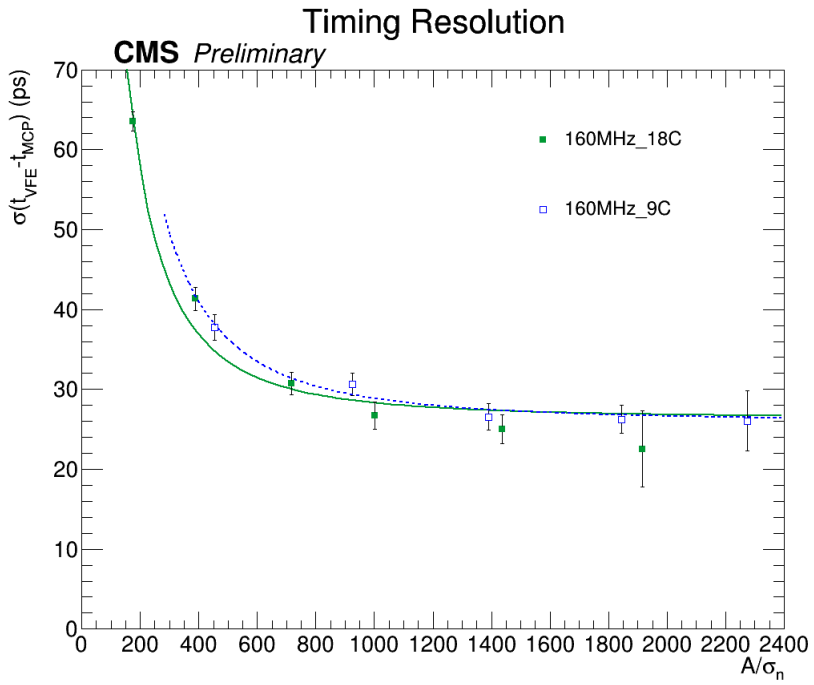

Figure 3.32: *Time resolution given by the difference between a crystal and the second MCP as a function of the normalized amplitude for* 160*MHz and* 18°/9° *C.*

Chapter 4

Search for a heavy right-handed W boson and a heavy neutrino at 13 TeV

In this chapter, the data analysis for the search of a heavy right-handed W boson (W_{R}) and a heavy neutrino in events with two same-flavor leptons and two jets at $\sqrt{s} = 13$ TeV is presented.

Heavy right-handed W bosons are predicted by BSM models, like the left-right (LR) symmetric model described in Section 1.3, which extends the electroweak sector of the SM lagrangian by a right-handed $SU(2)$ group [129–134]. These models explain the parity violation observed in weak interactions as the consequence of spontaneous symmetry breaking at a multi-TeV mass scale. In addition to the gauge bosons, LR models usually include heavy right-handed Majorana neutrinos (N_{R}) [135, 136]. The existence of these heavy neutrinos can explain the very small masses of the SM neutrinos as a consequence of the "see-saw" mechanism [68, 69, 137].

As explained in Section 1.3, the W_{R} is produced through an interaction between two quarks and can decay in many ways, e.g. into a pair of quarks or into a charged lepton and a heavy N_{R}.

As described in Section 1.2.2, heavy neutrinos can be produced through the decay of a W_{R} boson into a lepton and a heavy neutrino or through the decay of a Z or Higgs boson into a light neutrino and a heavy neutrino. They can subsequently decay into a Z or Higgs boson and a light neutrino or into a W_{R}^{*} boson and a lepton, with the W_{R}^{*} boson decaying into a lepton and a light neutrino or into a pair of quarks, which is experimentally the most accessible.

The W_{R} decay considered in this analysis is the one into a heavy N_{R} and a SM charged lepton. Subsequently, the N_{R} decays to a second SM charged lepton and an off-shell W_{R}

which decays hadronically, producing the decay chain

$$W_{\mathrm{R}} \to \ell N_{\mathrm{R}} \to \ell\ell W_{\mathrm{R}}^{*} \to \ell\ell qq', \ \ell = \mathrm{e} \text{ or } \mu.$$

The quarks hadronize into jets that can be observed by the CMS detector. Only first and second generation leptons (electrons and muons) are considered in the final state. The Feynman diagram for this process is shown in Figure 4.1.

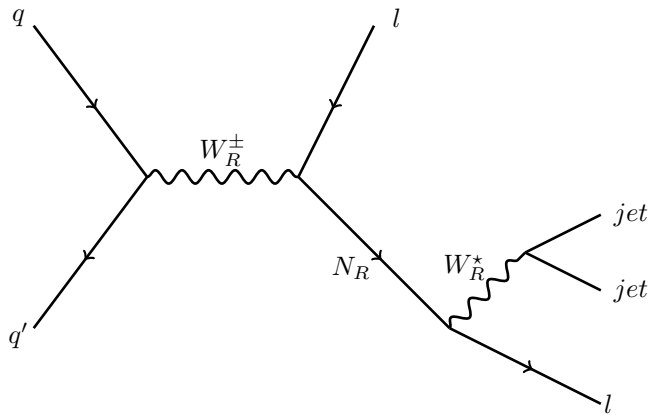

Figure 4.1: *Feynman diagram for the production of the heavy neutrino through W_{R} boson decay.*

4.1 Signal and background definition

The signal signature considered in this analysis is given by events with two leptons (electrons or muons) with the same flavor and two jets in the final state.
The main backgrounds for this analysis are represented by SM processes that produce events with the same final-state particles of the signal model. They include Drell–Yan (DY) production of lepton pairs with additional jets in the final state, and $t\bar{t}$ and diboson (WZ, ZZ, WW) production. Backgrounds where object misidentification leads to events with two leptons and two jets in the final state, like W boson production with additional jets, t-channel single top quark production, and QCD multijet events, are also considered. The DY+jets and $t\bar{t}$ production are irreducible background processes making up the bulk of the background events in the signal region. W+jets, WW, WZ, ZZ, single top quark, and QCD events are instead reducible backgrounds, because the diboson contribution can be suppressed by a dilepton mass requirement ($m_{\ell\ell} > 200$ GeV) and the contribution of the remaining processes is suppressed by the low lepton fake rates.

4.2 Strategy

This analysis uses the data collected in 2016 by the CMS detector in proton-proton collisions at $\sqrt{s} = 13$ TeV, and corresponding to an integrated luminosity of 35.9 fb^{-1}.
The W_{R} is assumed to have a mass ($m_{W_{\mathrm{R}}} \gg m_W$) between 800 and 6000 GeV, and the N_{R} to have a mass between 100 GeV and the W_{R} mass. In addition, as explained in Section 1.3, the couplings in the right-handed sector are assumed to be the same as those in the left chiral SM $SU(2)_L$ group, so the W_{R} interacts with the SM particles with a coupling constant g_{R} which is the same as the SM one, g_{L}, and the right-handed quark mixing matrix is assumed to be the same as the Cabibbo–Kobayashi–Maskawa matrix. No flavor changing is assumed in the process and consequently the flavor of the two final state leptons is the same. Also, to preserve acceptance to a wider class of models, no charge requirement is imposed on the leptons, although the Majorana nature of the right-handed neutrinos in the LR model implies that the charged leptons in the final-state can have the same sign.
While the W_{R} production and decay model represent the benchmark signal, the search for evidence of the W_{R} model is not the sole focus of this analysis. This search is designed to be sensitive to any heavy resonance which can be produced through proton proton interactions and decay to two muons or electrons and two jets. To make this analysis as model independent as possible, specific details of the W_{R} decay chain and correlations between final state particles are not exploited.
The discriminating variable is the invariant mass $m_{\ell\ell\mathrm{jj}}$ constructed from the two leptons and two jets with the largest transverse momenta. We search for an excess of events above the SM prediction for different W_{R} mass hypotheses in windows of $m_{\ell\ell\mathrm{jj}}$.
The analysis presented in this chapter is conducted in the *electron* (eejj) and *muon* ($\mu\mu$jj) *channels*, analyzed independently using the same strategy as in the 2015 iteration of the search, described in Section 1.3.2.
Different regions of phase-space, signal and control regions (CR) described in Section 4.5, are defined to look for the W_{R} signal and to estimate the contributions from the different SM backgrounds: the *flavour-sideband* is used to estimate the $t\bar{t}$ contribution, the *low-*$m_{\ell\ell}$ CR to check the agreement between data and simulation on the DY+jets contribution, and the *low-*$m_{\ell\ell jj}$ CR to check the agreement between data and simulation in events with high dilepton mass.

4.3 Datasets and triggers

4.3.1 Data samples

The 2016 data considered in this analysis include seven data-taking eras, corresponding to Runs B, C, D, E, F, G, and H. These eras are divided into two sets certified separately

Table 4.1: *Datasets used in this analysis.*

eejj channel	$\mu\mu$jj channel
DoubleEG/Run2016B-03Feb2017_ver2-v2	SingleMuon/Run2016B-03Feb2017_ver2-v2
DoubleEG/Run2016C-03Feb2017-v1	SingleMuon/Run2016C-03Feb2017-v1
DoubleEG/Run2016D-03Feb2017-v1	SingleMuon/Run2016D-03Feb2017-v1
DoubleEG/Run2016E-03Feb2017-v1	SingleMuon/Run2016E-03Feb2017-v1
DoubleEG/Run2016F-03Feb2017-v1	SingleMuon/Run2016F-03Feb2017-v1
DoubleEG/Run2016G-03Feb2017-v1	SingleMuon/Run2016G-03Feb2017-v1
DoubleEG/Run2016H-03Feb2017_ver2-v1	SingleMuon/Run2016H-03Feb2017_ver2-v1
DoubleEG/Run2016H-03Feb2017_ver3-v1	SingleMuon/Run2016H-03Feb2017_ver3-v1

by the CMS data quality assurance team[1] for a total integrated luminosity of $\mathcal{L} = 35.9$ fb^{-1}. The data datasets used are shown in Table 4.1.

4.3.2 Simulated samples

Samples for both the W_R signal final states (eejj and $\mu\mu$jj) and the background processes were produced with Monte Carlo (MC) simulation during an official production campaign[2] with the pileup conditions expected for Run 2 (PU= 20–30). In this simulation, the response of the CMS detector is modeled using the GEANT4 package [138].
The simulated samples are weighted with a factor that makes the simulated distribution of the number of pileup events match the one observed in the data. The distributions for number of vertices in data and simulation are shown for both the electron and the muon channel in Figure 4.2, after the pileup reweighting procedure.

4.3.2.1 Signal samples

Two sets of W_R signal samples were generated with the PYTHIA 8.212 program [139] with the NNPDF2.3 [140] parton distribution functions (PDFs), each with the eejj and $\mu\mu$jj final states generated separately. A left-right symmetry model is included in the PYTHIA package with the W_R mass, N_R mass, and couplings as input parameters. The assumptions for this search are those described in Section 4.2.
A first set of samples was generated with the W_R mass ranging from 800 GeV to 6 TeV in steps of 200 GeV, the N_R mass was set to half of the W_R mass, and the couplings between W_R and N_R were set to be the same as the couplings between SM W boson and SM neutrinos. The complete list of these signal samples, that were fully reconstructed, is given in Table 4.2.
A second set of signal samples was generated "ad-hoc" for this work to extend the analysis

[1] In CMS jargon, the "SeptReReco json" and the "Prompt json" files are used, respectively.
[2] In CMS jargon, the "Moriond17" campaign.

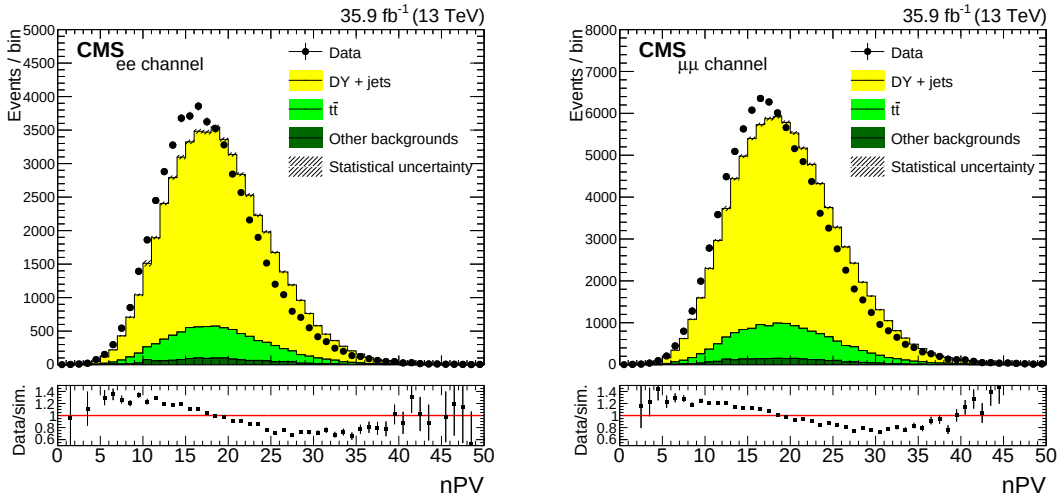

(a) *Electrons* (b) *Muons*

Figure 4.2: *Distributions of number of vertices in data and simulation events after applying the pileup reweighting.*

to a wider range of W_{R} and N_{R} mass combinations, needed to estimate the 2D limits described in Section 4.8. This set was produced at the generation (GEN) level only, with the W_{R} mass ranging from 800 GeV to 6 TeV in steps of 100 GeV and the N_{R} ranging from 100 GeV to $m_{W_{\mathrm{R}}}$ in steps of 100 GeV, and it was used to evaluate the changes in acceptance for other possible W_{R} and N_{R} mass combinations. The results obtained with the fully simulated (RECO) samples at $m_{N_{\mathrm{R}}} = \frac{1}{2}m_{W_{\mathrm{R}}}$ were scaled by the relative GEN efficiency between $m_{N_{\mathrm{R}}} = \frac{1}{2}m_{W_{\mathrm{R}}}$ and the other $m_{W_{\mathrm{R}}}$ and $m_{N_{\mathrm{R}}}$ combinations, assuming the ratio between RECO and GEN efficiencies constant as a function of $m_{N_{\mathrm{R}}}$, as described in Section 4.8.

Generation and validation of signal samples

In order to start comparison studies between data and MC samples while waiting for the official signal samples not yet produced at that time, a production of fully reconstructed signal MC samples with $m_{N_{\mathrm{R}}} = \frac{1}{2}m_{W_{\mathrm{R}}}$ was done for few mass points ($m_{W_{\mathrm{R}}} = 800$, 1600, 2400, 3200, 4000, 4600, 5400, and 6000 GeV) for both the electron and muon channels, with 50000 events for each sample. The validation of these samples was initially done comparing them with the official 2015 signal samples already produced, and then, once available, with the official 2016 ones.
The comparison with the official 2015 samples is shown for both the electron and the muon channels using 15000 events for three mass points: $m_{W_{\mathrm{R}}} = 2400$ GeV in Figure 4.3,

Table 4.2: *MINIAOD datasets, cross-sections, and number of events for fully reconstructed signal samples.*

Dataset	Cross-section (pb)	Events
/WRToNuEToEEJJ_MW-800_MNu-400_TuneCUETP8M1_13TeV-pythia8/RunIISummer16MiniAODv2-PUMoriond17_80X_mcRun2_asymptotic_2016_TrancheIV_v6-v1	4.262e+00	50000
/WRToNuEToEEJJ_MW-1000_MNu-500_TuneCUETP8M1_13TeV-pythia8/RunIISummer16MiniAODv2-PUMoriond17_80X_mcRun2_asymptotic_2016_TrancheIV_v6-v1	1.672e+00	50000
/WRToNuEToEEJJ_MW-1200_MNu-600_TuneCUETP8M1_13TeV-pythia8/RunIISummer16MiniAODv2-PUMoriond17_80X_mcRun2_asymptotic_2016_TrancheIV_v6-v1	7.594e-01	50000
/WRToNuEToEEJJ_MW-1400_MNu-700_TuneCUETP8M1_13TeV-pythia8/RunIISummer16MiniAODv2-PUMoriond17_80X_mcRun2_asymptotic_2016_TrancheIV_v6-v1	3.768e-01	49835
/WRToNuEToEEJJ_MW-1600_MNu-800_TuneCUETP8M1_13TeV-pythia8/RunIISummer16MiniAODv2-PUMoriond17_80X_mcRun2_asymptotic_2016_TrancheIV_v6-v1	2.019e-01	50000
/WRToNuEToEEJJ_MW-1800_MNu-900_TuneCUETP8M1_13TeV-pythia8/RunIISummer16MiniAODv2-PUMoriond17_80X_mcRun2_asymptotic_2016_TrancheIV_v6-v1	1.129e-01	50000
/WRToNuEToEEJJ_MW-2000_MNu-1000_TuneCUETP8M1_13TeV-pythia8/RunIISummer16MiniAODv2-PUMoriond17_80X_mcRun2_asymptotic_2016_TrancheIV_v6-v1	6.583e-02	49887
/WRToNuEToEEJJ_MW-2200_MNu-1100_TuneCUETP8M1_13TeV-pythia8/RunIISummer16MiniAODv2-PUMoriond17_80X_mcRun2_asymptotic_2016_TrancheIV_v6-v1	3.930e-02	50000
/WRToNuEToEEJJ_MW-2600_MNu-1300_TuneCUETP8M1_13TeV-pythia8/RunIISummer16MiniAODv2-PUMoriond17_80X_mcRun2_asymptotic_2016_TrancheIV_v6-v1	1.491e-02	50000
/WRToNuEToEEJJ_MW-2800_MNu-1400_TuneCUETP8M1_13TeV-pythia8/RunIISummer16MiniAODv2-PUMoriond17_80X_mcRun2_asymptotic_2016_TrancheIV_v6-v1	9.420e-03	49184
/WRToNuEToEEJJ_MW-3000_MNu-1500_TuneCUETP8M1_13TeV-pythia8/RunIISummer16MiniAODv2-PUMoriond17_80X_mcRun2_asymptotic_2016_TrancheIV_v6-v1	6.066e-03	50000
/WRToNuEToEEJJ_MW-3200_MNu-1600_TuneCUETP8M1_13TeV-pythia8/RunIISummer16MiniAODv2-PUMoriond17_80X_mcRun2_asymptotic_2016_TrancheIV_v6-v1	3.925e-03	50000
/WRToNuEToEEJJ_MW-3400_MNu-1700_TuneCUETP8M1_13TeV-pythia8/RunIISummer16MiniAODv2-PUMoriond17_80X_mcRun2_asymptotic_2016_TrancheIV_v6-v1	2.530e-03	50000
/WRToNuEToEEJJ_MW-3600_MNu-1800_TuneCUETP8M1_13TeV-pythia8/RunIISummer16MiniAODv2-PUMoriond17_80X_mcRun2_asymptotic_2016_TrancheIV_v6-v1	1.649e-03	49858
/WRToNuEToEEJJ_MW-3800_MNu-1900_TuneCUETP8M1_13TeV-pythia8/RunIISummer16MiniAODv2-PUMoriond17_80X_mcRun2_asymptotic_2016_TrancheIV_v6-v1	1.070e-03	49914
/WRToNuEToEEJJ_MW-4000_MNu-2000_TuneCUETP8M1_13TeV-pythia8/RunIISummer16MiniAODv2-PUMoriond17_80X_mcRun2_asymptotic_2016_TrancheIV_v6-v1	7.234e-04	50000
/WRToNuEToEEJJ_MW-4200_MNu-2100_TuneCUETP8M1_13TeV-pythia8/RunIISummer16MiniAODv2-PUMoriond17_80X_mcRun2_asymptotic_2016_TrancheIV_v6-v1	4.813e-04	50000
/WRToNuEToEEJJ_MW-4400_MNu-2200_TuneCUETP8M1_13TeV-pythia8/RunIISummer16MiniAODv2-PUMoriond17_80X_mcRun2_asymptotic_2016_TrancheIV_v6-v1	3.167e-04	50000
/WRToNuEToEEJJ_MW-4800_MNu-2400_TuneCUETP8M1_13TeV-pythia8/RunIISummer16MiniAODv2-PUMoriond17_80X_mcRun2_asymptotic_2016_TrancheIV_v6-v1	1.414e-04	49170
/WRToNuEToEEJJ_MW-5000_MNu-2500_TuneCUETP8M1_13TeV-pythia8/RunIISummer16MiniAODv2-PUMoriond17_80X_mcRun2_asymptotic_2016_TrancheIV_v6-v1	9.400e-05	49698
/WRToNuEToEEJJ_MW-5200_MNu-2600_TuneCUETP8M1_13TeV-pythia8/RunIISummer16MiniAODv2-PUMoriond17_80X_mcRun2_asymptotic_2016_TrancheIV_v6-v1	6.213e-05	49940
/WRToNuEToEEJJ_MW-5600_MNu-2800_TuneCUETP8M1_13TeV-pythia8/RunIISummer16MiniAODv2-PUMoriond17_80X_mcRun2_asymptotic_2016_TrancheIV_v6-v1	2.790e-05	50000
/WRToNuEToEEJJ_MW-5800_MNu-2900_TuneCUETP8M1_13TeV-pythia8/RunIISummer16MiniAODv2-PUMoriond17_80X_mcRun2_asymptotic_2016_TrancheIV_v6-v1	1.860e-05	49799
/WRToNuEToEEJJ_MW-6000_MNu-3000_TuneCUETP8M1_13TeV-pythia8/RunIISummer16MiniAODv2-PUMoriond17_80X_mcRun2_asymptotic_2016_TrancheIV_v6-v1	1.262e-05	48827
/WRToNuMuToMuMuJJ_MW-800_MNu-400_TuneCUETP8M1_13TeV-pythia8/RunIISummer16MiniAODv2-PUMoriond17_80X_mcRun2_asymptotic_2016_TrancheIV_v6-v1	4.290e+00	50000
/WRToNuMuToMuMuJJ_MW-1000_MNu-500_TuneCUETP8M1_13TeV-pythia8/RunIISummer16MiniAODv2-PUMoriond17_80X_mcRun2_asymptotic_2016_TrancheIV_v6-v1	1.677e+00	49352
/WRToNuMuToMuMuJJ_MW-1200_MNu-600_TuneCUETP8M1_13TeV-pythia8/RunIISummer16MiniAODv2-PUMoriond17_80X_mcRun2_asymptotic_2016_TrancheIV_v6-v1	7.684e-01	50000
/WRToNuMuToMuMuJJ_MW-1400_MNu-700_TuneCUETP8M1_13TeV-pythia8/RunIISummer16MiniAODv2-PUMoriond17_80X_mcRun2_asymptotic_2016_TrancheIV_v6-v1	3.776e-01	49572
/WRToNuMuToMuMuJJ_MW-1600_MNu-800_TuneCUETP8M1_13TeV-pythia8/RunIISummer16MiniAODv2-PUMoriond17_80X_mcRun2_asymptotic_2016_TrancheIV_v6-v1	2.019e-01	48806
/WRToNuMuToMuMuJJ_MW-1800_MNu-900_TuneCUETP8M1_13TeV-pythia8/RunIISummer16MiniAODv2-PUMoriond17_80X_mcRun2_asymptotic_2016_TrancheIV_v6-v1	1.135e-01	50000
/WRToNuMuToMuMuJJ_MW-2000_MNu-1000_TuneCUETP8M1_13TeV-pythia8/RunIISummer16MiniAODv2-PUMoriond17_80X_mcRun2_asymptotic_2016_TrancheIV_v6-v1	6.565e-02	50000
/WRToNuMuToMuMuJJ_MW-2200_MNu-1100_TuneCUETP8M1_13TeV-pythia8/RunIISummer16MiniAODv2-PUMoriond17_80X_mcRun2_asymptotic_2016_TrancheIV_v6-v1	3.922e-02	50000
/WRToNuMuToMuMuJJ_MW-2400_MNu-1200_TuneCUETP8M1_13TeV-pythia8/RunIISummer16MiniAODv2-PUMoriond17_80X_mcRun2_asymptotic_2016_TrancheIV_v6-v1	2.388e-02	50000
/WRToNuMuToMuMuJJ_MW-2600_MNu-1300_TuneCUETP8M1_13TeV-pythia8/RunIISummer16MiniAODv2-PUMoriond17_80X_mcRun2_asymptotic_2016_TrancheIV_v6-v1	1.503e-02	49720
/WRToNuMuToMuMuJJ_MW-2800_MNu-1400_TuneCUETP8M1_13TeV-pythia8/RunIISummer16MiniAODv2-PUMoriond17_80X_mcRun2_asymptotic_2016_TrancheIV_v6-v1	9.440e-03	49686
/WRToNuMuToMuMuJJ_MW-3000_MNu-1500_TuneCUETP8M1_13TeV-pythia8/RunIISummer16MiniAODv2-PUMoriond17_80X_mcRun2_asymptotic_2016_TrancheIV_v6-v1	6.048e-03	50000
/WRToNuMuToMuMuJJ_MW-3200_MNu-1600_TuneCUETP8M1_13TeV-pythia8/RunIISummer16MiniAODv2-PUMoriond17_80X_mcRun2_asymptotic_2016_TrancheIV_v6-v1	3.894e-03	49848
/WRToNuMuToMuMuJJ_MW-3400_MNu-1700_TuneCUETP8M1_13TeV-pythia8/RunIISummer16MiniAODv2-PUMoriond17_80X_mcRun2_asymptotic_2016_TrancheIV_v6-v1	2.535e-03	49442
/WRToNuMuToMuMuJJ_MW-3600_MNu-1800_TuneCUETP8M1_13TeV-pythia8/RunIISummer16MiniAODv2-PUMoriond17_80X_mcRun2_asymptotic_2016_TrancheIV_v6-v1	1.666e-03	50000
/WRToNuMuToMuMuJJ_MW-3800_MNu-1900_TuneCUETP8M1_13TeV-pythia8/RunIISummer16MiniAODv2-PUMoriond17_80X_mcRun2_asymptotic_2016_TrancheIV_v6-v1	1.105e-03	50000
/WRToNuMuToMuMuJJ_MW-4000_MNu-2000_TuneCUETP8M1_13TeV-pythia8/RunIISummer16MiniAODv2-PUMoriond17_80X_mcRun2_asymptotic_2016_TrancheIV_v6-v1	7.189e-04	50000
/WRToNuMuToMuMuJJ_MW-4200_MNu-2100_TuneCUETP8M1_13TeV-pythia8/RunIISummer16MiniAODv2-PUMoriond17_80X_mcRun2_asymptotic_2016_TrancheIV_v6-v1	4.808e-04	50000
/WRToNuMuToMuMuJJ_MW-4400_MNu-2200_TuneCUETP8M1_13TeV-pythia8/RunIISummer16MiniAODv2-PUMoriond17_80X_mcRun2_asymptotic_2016_TrancheIV_v6-v1	3.182e-04	50000
/WRToNuMuToMuMuJJ_MW-4600_MNu-2300_TuneCUETP8M1_13TeV-pythia8/RunIISummer16MiniAODv2-PUMoriond17_80X_mcRun2_asymptotic_2016_TrancheIV_v6-v1	2.124e-04	49588
/WRToNuMuToMuMuJJ_MW-4800_MNu-2400_TuneCUETP8M1_13TeV-pythia8/RunIISummer16MiniAODv2-PUMoriond17_80X_mcRun2_asymptotic_2016_TrancheIV_v6-v1	1.412e-04	49878
/WRToNuMuToMuMuJJ_MW-5000_MNu-2500_TuneCUETP8M1_13TeV-pythia8/RunIISummer16MiniAODv2-PUMoriond17_80X_mcRun2_asymptotic_2016_TrancheIV_v6-v1	9.449e-05	50000
/WRToNuMuToMuMuJJ_MW-5200_MNu-2600_TuneCUETP8M1_13TeV-pythia8/RunIISummer16MiniAODv2-PUMoriond17_80X_mcRun2_asymptotic_2016_TrancheIV_v6-v1	6.261e-05	49589
/WRToNuMuToMuMuJJ_MW-5400_MNu-2700_TuneCUETP8M1_13TeV-pythia8/RunIISummer16MiniAODv2-PUMoriond17_80X_mcRun2_asymptotic_2016_TrancheIV_v6-v1	4.223e-05	47921
/WRToNuMuToMuMuJJ_MW-5600_MNu-2800_TuneCUETP8M1_13TeV-pythia8/RunIISummer16MiniAODv2-PUMoriond17_80X_mcRun2_asymptotic_2016_TrancheIV_v6-v1	2.802e-05	50000
/WRToNuMuToMuMuJJ_MW-5800_MNu-2900_TuneCUETP8M1_13TeV-pythia8/RunIISummer16MiniAODv2-PUMoriond17_80X_mcRun2_asymptotic_2016_TrancheIV_v6-v1	1.870e-05	49783
/WRToNuMuToMuMuJJ_MW-6000_MNu-3000_TuneCUETP8M1_13TeV-pythia8/RunIISummer16MiniAODv2-PUMoriond17_80X_mcRun2_asymptotic_2016_TrancheIV_v6-v1	1.256e-05	50000

$m_{W_R} = 3200$ GeV in Figure 4.4, and $m_{W_R} = 4000$ GeV in Figure 4.5. The agreement is similar for all the other samples and kinematic variables.
The comparison with the official 2016 samples is shown in Figure 4.6 for the electron channel at $m_{W_R} = 1600$ GeV. A similar agreement is visible for all the other samples and kinematic variables.
Given the good agreement between these signal samples produced with $m_{N_R} = \frac{1}{2} m_{W_R}$ and the official ones, the "ad-hoc" signal samples produced with $m_{N_R} \neq \frac{1}{2} m_{W_R}$ were considered consistent. Moreover, since the official production was not done for three mass points in the electron channel ($m_{W_R} = 2400$ GeV, 4600 GeV, and 5400 GeV), the corresponding fully reconstructed signal samples privately produced were used in the analysis.

4.3.2.2 Background samples

The backgrounds samples are simulated with several MC event generators. The DY+jets and the $t\bar{t}$ samples are generated with aMC@NLO 2.3.3 [141] at next-to-leading order (NLO) using the NLO NNPDF3.0 [142] PDF set. Diboson (WZ, ZZ, and WW) samples are generated at leading order (LO) using PYTHIA 8.212 along with the LO NNPDF2.3 [140] PDFs, while W+jets events are generated with aMC@NLO 2.3.3 [141] at leading order (LO) and single top quark events are produced in the tW channel with POWHEG v1.0 [143–146]. The more precise NLO calculations are used to normalize the SM simulated samples of diboson, W+jets and single top quark events to NLO accuracy. The NNPDF3.0 PDFs are used for samples generated at NLO.
For all samples, PYTHIA 8.212 is used for parton showering, fragmentation and hadronization with the underlying event tune CUETP8M1 [147].
The DY+jets samples have one parton at the matrix element level, and the additional parton showering is modeled in PYTHIA. The potential double counting of partons generated using PYTHIA with those using aMC@NLO is minimized using the MLM [148] (FXFX [149]) matching scheme in the LO (NLO) samples.
The complete list of simulated samples used to estimate the background processes is given in Table 4.3. The QCD multijet samples, generated with PYTHIA 8.212, have also been taken into account, but they were not used in the analysis because their contribution was negligible, as described in Section 4.6.

4.3.3 Triggers

The benchmark W_R signal has high p_T leptons and jets in the final state, therefore events are selected with the following triggers:

muon channel: `HLT_Mu50` OR `HLT_TkMu50`, non-isolated and unprescaled single-muon triggers without ID requirements and with a minimum p_T requirement of 50 GeV applied to the muon, are used for the W_R search in the $\mu\mu$jj channel;

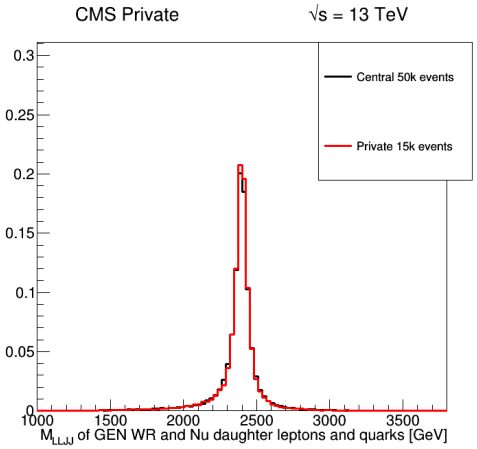

(a) *Electrons: four-object mass*

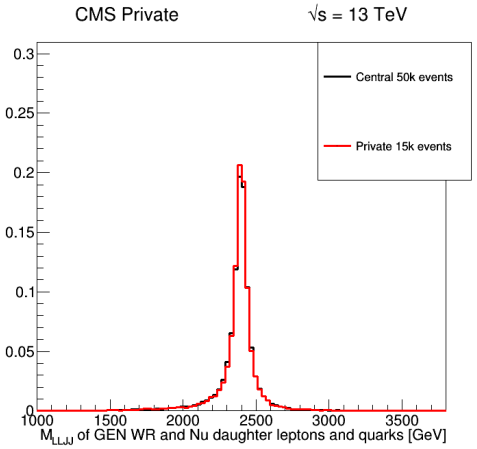

(b) *Muons: four-object mass*

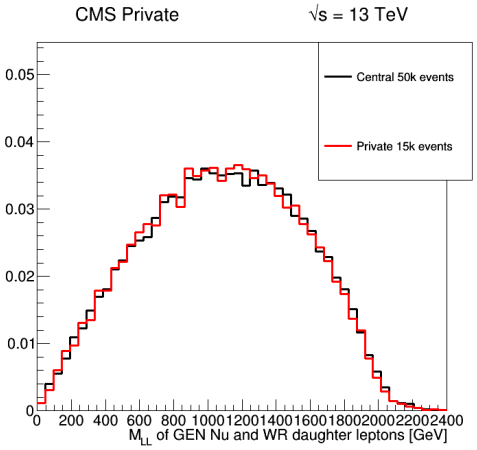

(c) *Electrons: dilepton mass*

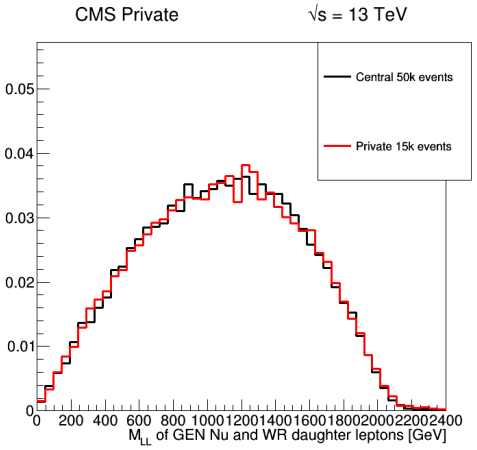

(d) *Muons: dilepton mass*

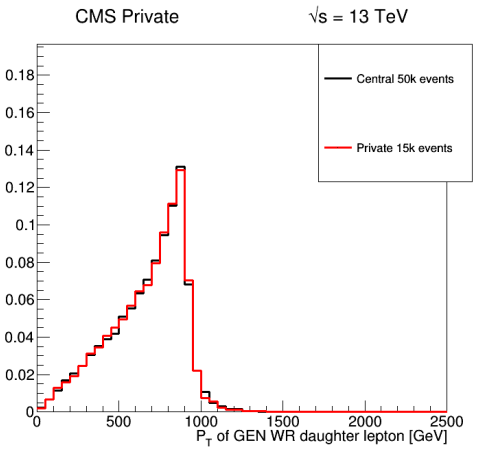

(e) *Electrons: leading lepton p_T*

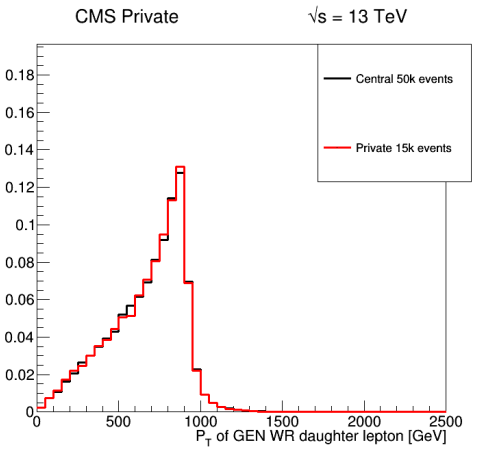

(f) *Muons: leading lepton p_T*

Figure 4.3: *Comparison of produced signal samples with the official 2015 ones for* $m_{W_R} = 2400$ GeV *for different kinematic variables in both electron (on the left) and muon (on the right) channels.*

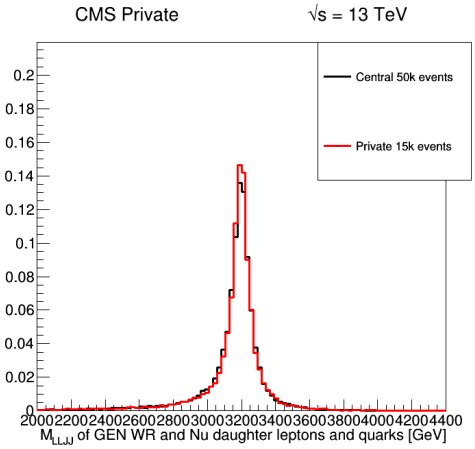

(a) *Electrons: four-object mass*

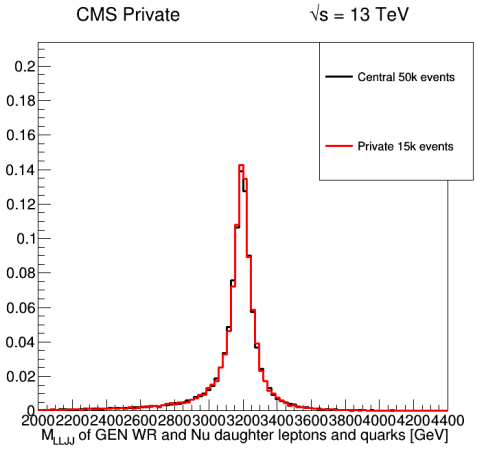

(b) *Muons: four-object mass*

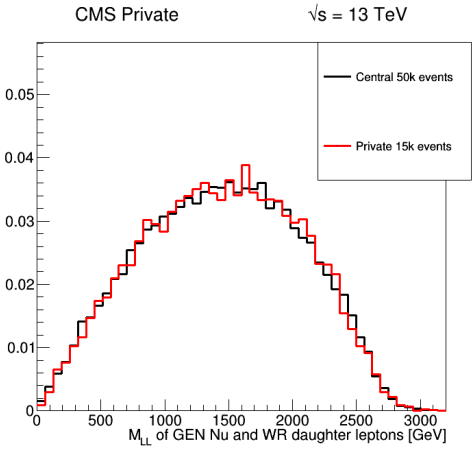

(c) *Electrons: dilepton mass*

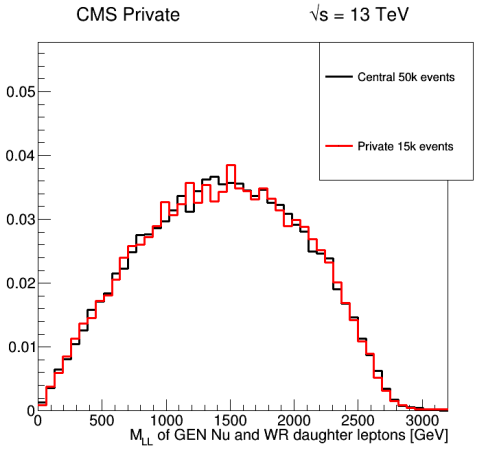

(d) *Muons: dilepton mass*

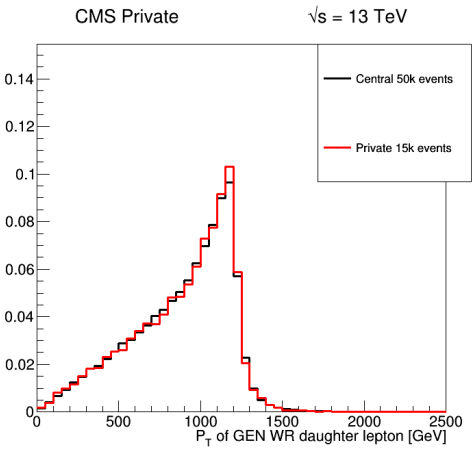

(e) *Electrons: leading lepton* p_T

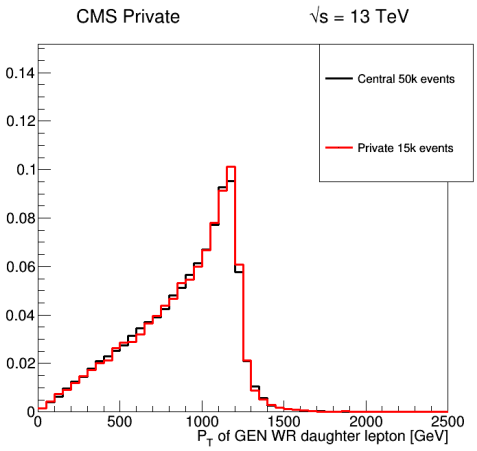

(f) *Muons: leading lepton* p_T

Figure 4.4: *Comparison of produced signal samples with the official 2015 ones for* $m_{W_R} = 3200$ GeV *for different kinematic variables in both electron (on the left) and muon (on the right) channels.*

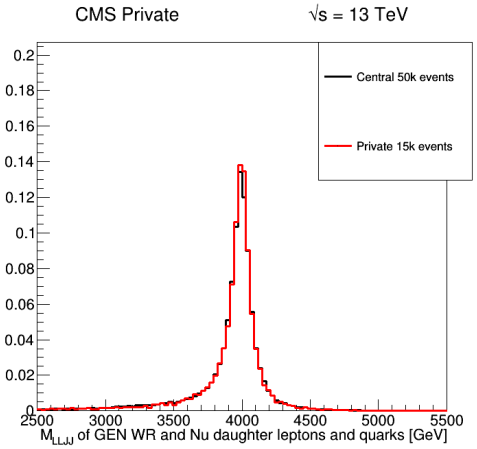

(a) *Electrons: four-object mass*

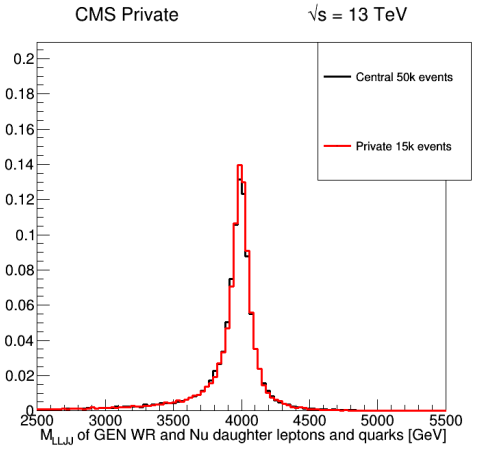

(b) *Muons: four-object mass*

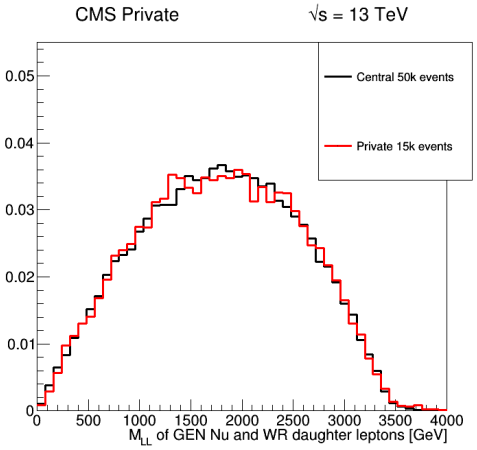

(c) *Electrons: dilepton mass*

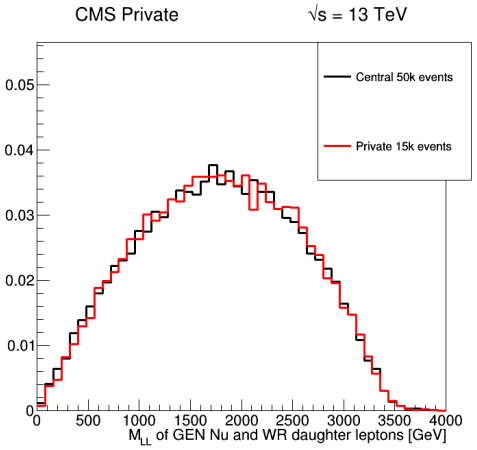

(d) *Muons: dilepton mass*

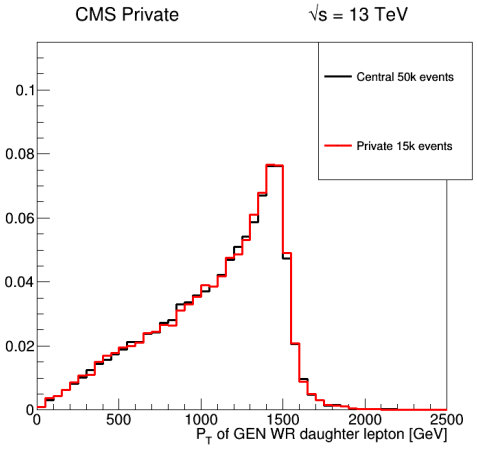

(e) *Electrons: leading lepton p_T*

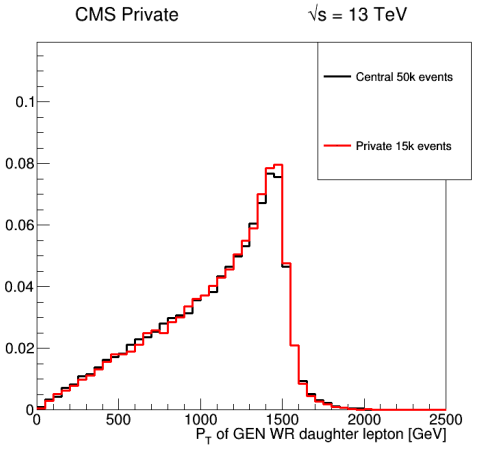

(f) *Muons: leading lepton p_T*

Figure 4.5: *Comparison of produced signal samples with the official 2015 ones for* $m_{W_R} = 4000$ GeV *for different kinematic variables in both electron (on the left) and muon (on the right) channels.*

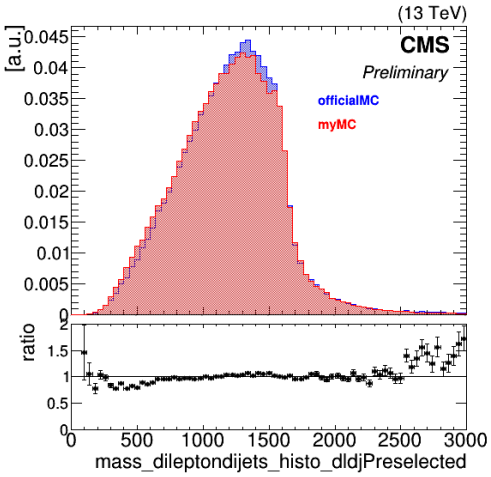

(a) *Four-object mass*

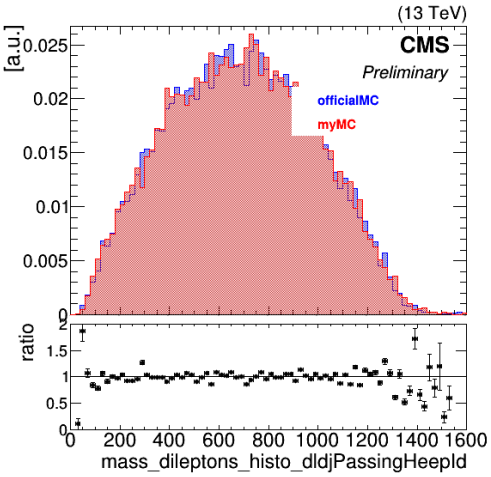

(b) *Dilepton mass*

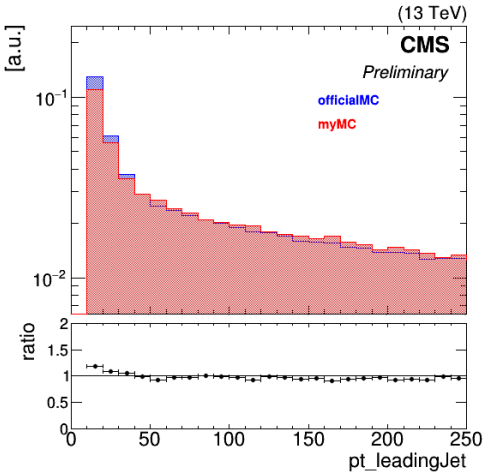

(c) *Leading jet* p_T

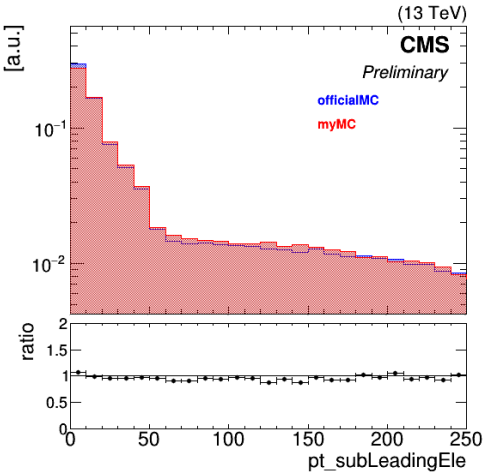

(d) *Subleading lepton* p_T

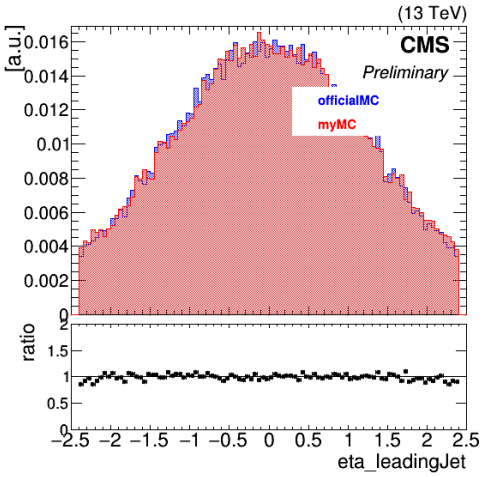

(e) *Leading jet* η

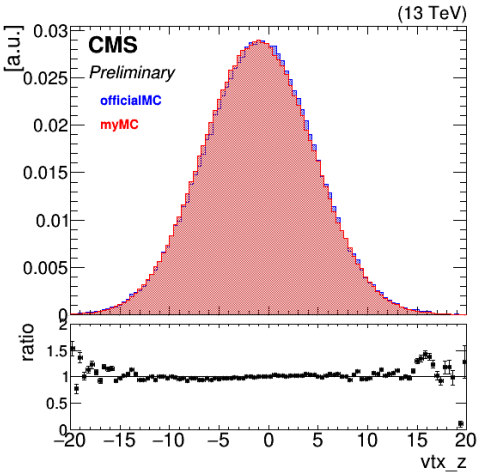

(f) *z of vertices*

Figure 4.6: *Comparison of produced signal samples with the official 2016 ones for* $m_{W_R} =$ 1600 GeV *for different kinematic variables in the electron channel.*

Table 4.3: *Datasets, generators, order of generation, cross sections, and number of events for background samples.*

Sample	Dataset	Generator	Order	σ (pb)	Events
DY+jets	DYJetsToLL_Pt-50To100_TuneCUETP8M1_13TeV-amcatnloFXFX-pythia8	aMC@NLO	NLO	3.467e+02	130582589
	DYJetsToLL_Pt-100To250_TuneCUETP8M1_13TeV-amcatnloFXFX-pythia8	aMC@NLO	NLO	8.13e+01	83686174
	DYJetsToLL_Pt-250To400_TuneCUETP8M1_13TeV-amcatnloFXFX-pythia8	aMC@NLO	NLO	2.98e+00	21185045
	DYJetsToLL_Pt-450To600_TuneCUETP8M1_13TeV-amcatnloFXFX-pythia8	aMC@NLO	NLO	3.837e-01	1625936
	DYJetsToLL_Pt-600ToInf_TuneCUETP8M1_13TeV-amcatnloFXFX-pythia8	aMC@NLO	NLO	3.558e-02	1627882
$t\bar{t}$	TTJets_Dilept_TuneCUETP8M2T4_13TeV-amcatnloFXFX-pythia8	aMC@NLO	NLO	7.795e+01	68209952
W+jets	WJetsToLNu_TuneCUETP8M1_13TeV-madgraphMLM-pythia8	aMC@NLO	NLO	6.153e+04	57026058
Diboson	WZ_TuneCUETP8M1_13TeV-pythia8	PYTHIA 8	NLO	4.713e+01	2995828
	ZZ_TuneCUETP8M1_13TeV-pythia8	PYTHIA 8	NLO	1.652e+01	998034
	WW_TuneCUETP8M1_13TeV-pythia8	PYTHIA 8	NLO	1.187e+02	6987124
Single Top	ST_tWll_5f_LO_13TeV-MadGraph-pythia8	POWHEG	NLO	1.104e-02	50000
	ST_tWnunu_5f_LO_13TeV-MadGraph-pythia8	POWHEG	NLO	2.112e-02	100000
	ST_tW_top_5f_inclusiveDecays_13TeV-powheg-pythia8_TuneCUETP8M1	POWHEG	NLO	3.809e+01	6952830
	ST_tW_antitop_5f_inclusiveDecays_13TeV-powheg-pythia8_TuneCUETP8M1	POWHEG	NLO	3.806e+01	6933094
QCD	QCD_Pt-20to30_EMEnriched_TuneCUETP8M1_13TeV_pythia8	PYTHIA	LO	5.520e+06	9218954
	QCD_Pt-30to50_EMEnriched_TuneCUETP8M1_13TeV_pythia8	PYTHIA	LO	6.967e+06	11498579
	QCD_Pt-50to80_EMEnriched_TuneCUETP8M1_13TeV_pythia8	PYTHIA	LO	2.156e+06	45811241
	QCD_Pt-80to120_EMEnriched_TuneCUETP8M1_13TeV_pythia8	PYTHIA	LO	4.174e+05	77695287
	QCD_Pt-120to170_EMEnriched_TuneCUETP8M1_13TeV_pythia8	PYTHIA	LO	7.604e+04	77771316
	QCD_Pt-170to300_EMEnriched_TuneCUETP8M1_13TeV_pythia8	PYTHIA	LO	1.878e+04	11540163
	QCD_Pt-300toInf_EMEnriched_TuneCUETP8M1_13TeV_pythia8	PYTHIA	LO	1.215e+03	7373633
	QCD_Pt_15to20_bcToE_TuneCUETP8M1_13TeV_pythia8	PYTHIA	LO	2.598e+05	2685602
	QCD_Pt_20to30_bcToE_TuneCUETP8M1_13TeV_pythia8	PYTHIA	LO	3.754e+05	10987947
	QCD_Pt_30to80_bcToE_TuneCUETP8M1_13TeV_pythia8	PYTHIA	LO	4.114e+05	15328096
	QCD_Pt_80to170_bcToE_TuneCUETP8M1_13TeV_pythia8	PYTHIA	LO	4.103e+04	14976689
	QCD_Pt_170to250_bcToE_TuneCUETP8M1_13TeV_pythia8	PYTHIA	LO	2.586e+03	9720760
	QCD_Pt_250toInf_bcToE_TuneCUETP8M1_13TeV_pythia8	PYTHIA	LO	7.148e+02	9773617
	QCD_Pt-20toInf_MuEnrichedPt15_TuneCUETP8M1_13TeV_pythia8	PYTHIA	LO	2.688e+05	22094081

electron channel: two separate double-electron triggers, unprescaled for the data taking period in which they are used, with a minimum p_T requirement of 33 GeV applied on each electron, are used for the W_R search in the eejj channel:

- `HLT_DoubleEle33_CaloIdL_MW`, used for runs excluding 276453 – 278822,
- `HLT_DoubleEle33_CaloIdL_GsfTrkIdVL`, used for runs 276453 – 278822 (inclusive);

***flavour-sideband*:** `HLT_Mu50` OR `HLT_TkMu50` are used to estimate $t\bar{t}$ in the eμjj channel; since the subleading lepton p_T cut, defined in Section 4.5, is above the p_T requirement of the single muon trigger, no bias is introduced by using this trigger for the *flavour-sideband*.

The `HLT_DoubleEle33_CaloIdL_MW` path, which requires an ECAL energy deposit with an associated track which must include at least one pixel hit, had to be prescaled in certain runs to maintain acceptable rates, therefore for the runs affected the `HLT_DoubleEle33_CaloIdL_GsfTrkIdVL` path had to be used in its place.
The triggers used for this search fire in more than 98% of simulated W_R events passing the offline selections described in Section 4.5. This efficiency is shown in Figure 4.7 for both the muon and the electron channel triggers.

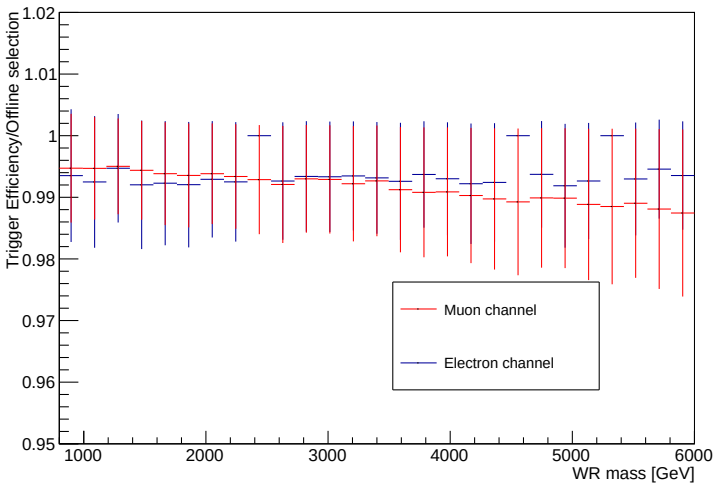

Figure 4.7: *Efficiency of electron and muon triggers in simulated W_R events with respect to offline selections as a function of W_R mass.*

The decline in the muon trigger efficiency with increasing W_R mass is caused by the L1 triggers which seed the `HLT_Mu50` trigger. As the W_R mass increases, the energies of muons produced by the W_R decay increase and as muon p_T increases, the probability that a muon will lose energy before the muon detectors due to the muon showering increases, reducing the L1 muon trigger efficiency. As the L1 muon trigger efficiency falls with increasing m_{W_R} and muon p_T, the `HLT_Mu50` efficiency falls. This high energy muons inefficiency is confirmed by measurements made by the $Z' \to \mu\mu$ analysis performed by the CMS experiment [84], and shown in Figure 4.8. In this figure, representing the efficiency as a function of muon p_T for the OR of the `HLT_Mu50` and `HLT_TkMu50` triggers with respect to the offline reconstructed muons passing identification and isolation requirements, the sharp turn-on is visible, together with an efficiency of $\approx 90\%$ for $p_T > 60$ GeV, and the slight efficiency decrease at high p_T. This inefficiency is partially recovered by choosing a single-muon trigger for the muon channel instead of a double muon trigger. Due to changing conditions during the 2016 data collection period, the official scale factors derived to correct the MC simulation are divided into two sets corresponding to Runs B-F and Runs G-H.

The high p_T electrons passing offline ID requirements pass the L1 and `HLT_DoubleEle33` triggers with lower efficiency in the endcap than in the barrel, as confirmed by the CMS $Z' \to$ ee analysis [84]. Figure 4.9 shows the efficiency of the $E_T > 33$ GeV requirement, where it is visible that the trigger is almost fully efficient by 35 GeV in the barrel and by 37 GeV in the endcap. These curves are used to weight simulated events to take into account the small efficiency loss at low E_T. The efficiency of the `CaloIdL` and `MW` (or `GsfTrkIdVL`) matching identification requirements are shown in Figure 4.10. As this effi-

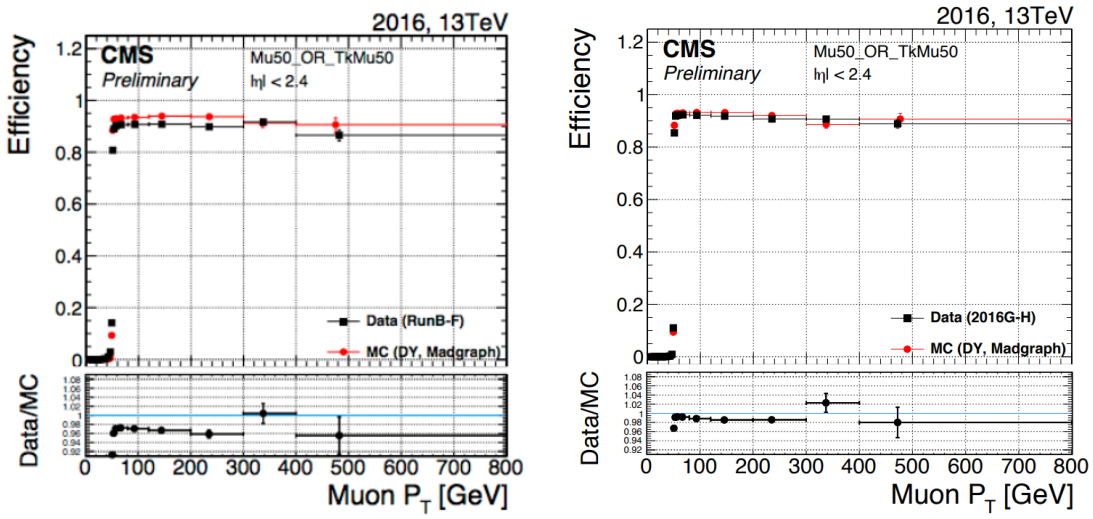

(a) *Runs B-F* (b) *Runs G-H*

Figure 4.8: *Efficiency of HLT_ Mu50 OR HLT_ TkMu50 triggers given offline muons passing high-p_T ID requirements as a function of muon p_T [84].*

ciency is flat versus E_T, there is no need to weight the simulated events with this factor as it will be automatically included in the Z peak normalization, described in Section 4.6.

4.4 Object definition, identification and corrections

The reconstruction, identification and corrections for efficiencies and energies of the three possible objects in the final state are described in this section.
The recommendations for the reconstruction and identification of high p_T objects given by the CMS Collaboration and described in the subsequent paragraphs were followed, together with the general prescriptions of the CMS "Physics Object Groups" for the specific data/MC corrections used for leptons and jets.
The global event reconstruction is performed using the particle-flow (PF) algorithm [107], which reconstructs and identifies each individual particle with an optimized combination of all the subdetectors information, as described in Section 2.2.6.
At least one reconstructed vertex is required to be found in the event. For events with multiple collision vertices from additional collisions in the same or adjacent bunch crossings (pileup interactions), the reconstructed vertex with the largest value of summed p_T^2 in the event, where the sum extends over all charged tracks associated with the vertex, is taken to be the primary pp interaction vertex (PV). A good offline-reconstructed PV, located within $|r| < 2$ cm and $|z| < 24$ cm from the nominal interaction point and with at least four tracks associated to it, is required.

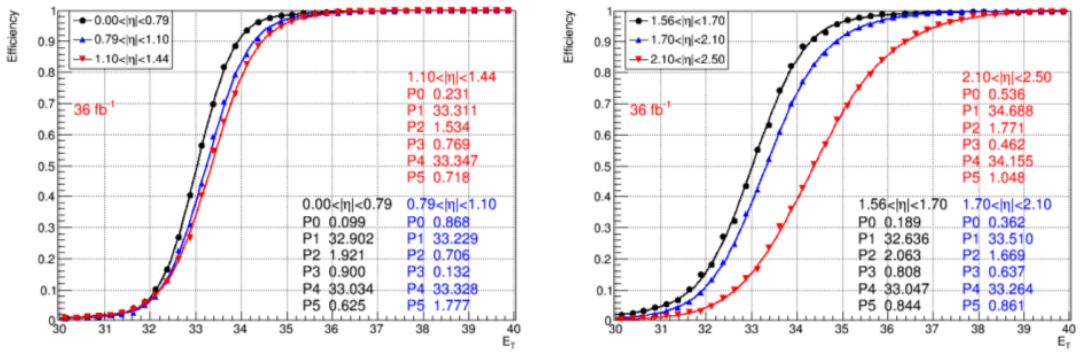

(a) *Barrel* (b) *Endcap*

Figure 4.9: *Efficiency of electrons passing offline ID requirements to match a L1 candidate with* $E_T > 33$ GeV *as a function of* E_T *[84].*

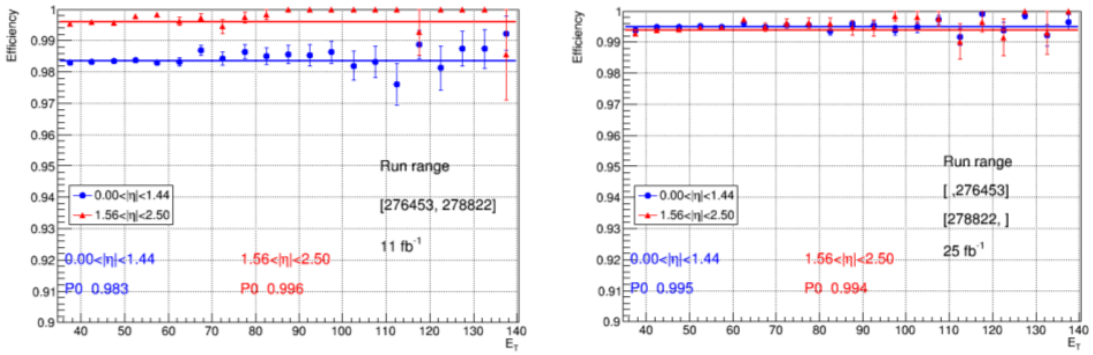

(a) *GsfTrkIdVL* (b) *MW*

Figure 4.10: *Efficiency of electrons in the barrel and endcaps passing offline ID requirements to pass the CaloIdL online ID requirement in the HLT_DoubleEle33 triggers as a function of* E_T *[84].*

4.4.1 Jets

Quarks and gluons, which are not directly detectable due to their color confinement, can be detected from the hadronic energy showers they produce, seen as tracks and energy clusters in the calorimeters. A collection of charged and neutral hadrons is called *jet* and there are multiple algorithms to reconstruct them [150, 151].

4.4.1.1 Reconstruction

Jet reconstruction is performed as part of the PF event reconstruction [152, 153]. The tracker information, crucial to the energy measurement since charged hadrons make up approximately two thirds of the energy in a jet, is taken from an iterative track reconstruction as described in Section 2.2.6. Calorimeter clusters are independently formed in each subdetector from high energy seeds, corresponding to single cells in the subdetectors, which are grown by adding neighboring cells with energy above a threshold. The PF tracks and calorimeter deposits are then linked into blocks of candidates by extrapolating tracks from their outermost position to the calorimeters and looking for nearby clusters, or by projecting an ECAL cluster to the less granular HCAL to find matching deposits. Jets are clustered from candidates by iteratively adding those that are within a certain distance from a seed, where the distance can be defined to take into account the energy of the candidate. In this analysis, jets were clustered using the "anti-k_T" clustering algorithm [151], which starts from the highest p_T particle and adds other particles to the jet based on their p_T and distance from the jet axis, with a jet cone size of $R = 0.4$. The energy of a jet is then taken as the sum of the energies of its constituents. Charged particles originating from pileup vertices were not included in the jet reconstruction, being removed from the list of reconstructed particles using the charged-hadron pileup subtraction algorithm [107], and neutral contributions to the jet energy from pileup vertices were removed by applying a residual average area-based correction [154].

4.4.1.2 Identification

In order to avoid selecting low quality jets or leptons that are misreconstructed as jets, a dedicated identification algorithm is used. Reconstructed jets passing the "`tightJet`" ID requirements with a lepton veto [155] are selected. The "`tightJet`" ID criteria are:

- the jets must have at least one constituent;
- the neutral and charged EM energy fractions must be less than 90%;
- the neutral hadronic energy fraction must be less than 90%;
- there must be at least one charged hadron in the jet and the charged hadronic fraction must be greater than zero;

- the muon energy fraction must be less than 80%.

These criteria showed an efficiency to identify jets of over 99% in the beginning of Run 1 [156], and the same level of performance was seen in the data collected in 2015 and 2016 [155].
Other jet identification algorithms [157] also remove contributions from calorimeter noise and beam halo to jets.

4.4.1.3 Corrections

The jet energy measured in the detector is typically inaccurate because of non-uniform and non-linear response of the CMS calorimeters, then jet energy corrections (JEC) are needed to get a better estimate of the true energy of the particle. A factorized multi-step procedure with three subsequent corrections has been developed. The first one, the *offset correction*, removes the excess energy coming from calorimeter electronic noise and multiple proton-proton collisions in the same and adjacent bunch crossings (pileup). The second one, the *relative correction*, removes variations in the detector response to hadrons as a function of jet $|\eta|$, while the third one, the *absolute correction*, removes variations in jet response as a function of jet p_T. The official "L1", "L2" and "L3" jet energy corrections[3], applied to both data and simulation, are derived from a detailed simulation of the detector, and are confirmed with in-situ measurements of the energy balance in dijet, multijet, γ+jet, and leptonically decaying Z+jet events [157]. An additional correction is also applied to data to correct for the small, remaining differences with the simulation.
Measurements show that the jet energy resolution (JER) in data is worse than in the simulation, then the reconstructed jets in MC need to be smeared with the JER corrections[4] [157] so that their p_T resolution matches the one observed in data.

4.4.2 Electrons

4.4.2.1 Reconstruction

Electrons are reconstructed by associating a charged-particle track from the PV reconstructed in the silicon detector with a so called "cluster" (a group of adjacent crystals hit at the same time) in the ECAL, described in Section 2.2.2.
To measure the initial energy of the electron accurately, it is essential to collect the energy of the radiated photons that mainly spreads along the ϕ direction because of the bending of the electron trajectory in the magnetic field. Dedicated algorithms are used to reconstruct the tracks matched to these highly-radiating electrons [158]. Electron tracks can be reconstructed in the tracker using the standard Kalman filter [110–112] track reconstruction used for all charged particles. However, this procedure is compromised by the large

[3] In CMS jargon, the "Spring16_V2" JEC is used.
[4] In CMS jargon, the "Spring16_25nsV10" JER is used.

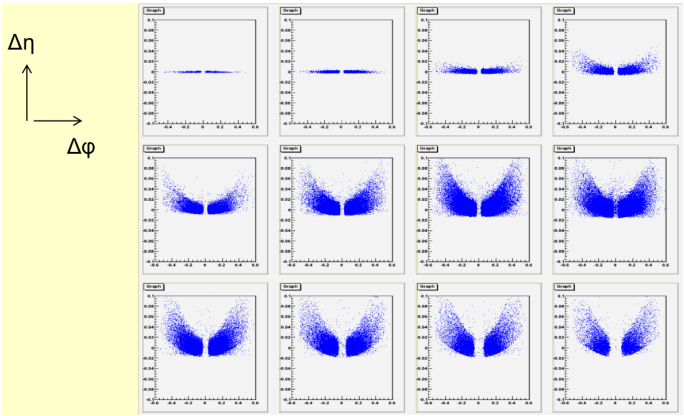

Figure 4.11: *The $\Delta\eta$ and $\Delta\phi$ distances between each cluster and the most energetic cluster are shown for $0 < |\eta| < 3$ with steps of $\eta = 0.25$, produced using simulated photons with $10 < p_T < 100$ GeV.*

radiative losses of electrons due to bremsstrahlung in the tracker material, that results in a loss of signal in the tracker. A dedicated track reconstruction is then used to recover these hits and provide a better estimate of the track parameters.
Two complementary seeding algorithms, finding and selecting the two or three first hits in the tracker from which the track can be initiated, are used.
The *"ECAL-based"* seeding starts from a "supercluster" (SC) of energy deposits. Clusters are reconstructed by aggregating all crystals with at least one side in common with a seed crystal with an energy above a given threshold, which represents about two standard deviations of the electronic noise in the ECAL (80 MeV in the barrel and up to 300 MeV in the endcaps). Clusters lying in the area between two p_T-η dependent parabolas, centered around the most energetic cluster, are dynamically merged into superclusters, giving them a mustache-like shape as shown in Figure 4.11. This "mustache clustering" is important especially when moving to higher $|\eta|$ regions and for low energy clusters, as the shape of the shower starts to extend not only in ϕ but also in η. The SC energy is the sum of the energy measured in the clusters and its position is calculated as an energy-weighted mean corrected by the depth of the shower produced by the electron. The SCs are used to estimate the trajectory of the electron in the first layers of the tracker. The electron seeds are then selected from all the reconstructed seeds.
The *"tracker-based"* seeding starts from tracks reconstructed using the general Kalman filter reconstruction for charged particles and complements the seeding efficiency, especially for low-p_T or non isolated electrons, as well as for electrons in the barrel-endcap transition region. When bremsstrahlung is negligible, the Kalman filter algorithm extrapolates the tracks towards the ECAL and matches them to an SC, measuring their momentum with good precision. Each track with direction compatible with the position of the SC has its seed selected for electron track reconstruction. If instead the bremsstrahlung is significant,

the Kalman filter (KF) algorithm produces low quality tracks because it cannot follow the change of curvature of the electron trajectory due to the bremsstrahlung. A dedicated Gaussian sum filter (GSF) [159] algorithm, a nonlinear generalization of the KF algorithm that utilizes multiple weighted Gaussian distributions to model the energy loss, is used to refit these tracks. This algorithm includes the information about energy loss at each layer into the track reconstruction, providing significant improvements to both momentum and angular resolution compared to the KF algorithm. The number of hits, the quality of the tracks, and the geometrical and energy matching of the ECAL and tracker information are used in a multivariate (MVA) analysis [160] to select the tracker seeds to be considered as electron seeds.
The electron seeds found using the two algorithms are combined, and are used to initiate the electron-track building, based on the combinatorial Kalman filter method that for each electron seed proceeds iteratively from the track parameters provided in each layer. Once the hits are collected, a GSF fit is performed to estimate the electron track parameters.
The electron candidates are then reconstructed from the association of a GSF track with an ECAL cluster by a geometrical matching or an MVA technique. The electron momentum is estimated by combining the energy measurement in the ECAL with the momentum measurement in the tracker.
Discrepancies in reconstruction efficiency between data and simulation are corrected with RECO SFs dependent on electron p_T and η, provided for the full 2016 dataset with a *Tag-and-probe* method [158].

4.4.2.2 Identification

Several electron identification algorithms are optimized for particular event topologies. In this analysis, an algorithm designed to select high momentum electrons, known as High Energy Electron Pairs (`HEEP`) identification [158], is used. Reconstructed electrons passing the `HEEP` ID (v7.0) criteria were selected. This identification requires a reconstructed electron to contain a high quality, isolated track spatially linked to an isolated ECAL energy deposit. Electrons must have $p_T > 35$ GeV and the pseudorapidity of the SC must be within the acceptance of the ECAL. The energy fraction in the hadronic calorimeter must be much smaller than the ECAL measurement. The electrons must be isolated from other tracks and calorimeter deposits, then the sum of the p_T of all tracks inside a cone of $R < 0.3$ centered on the electron candidate, not associated with the electron, and originating from the PV must be below 5 GeV. In addition, the shape of the ECAL energy deposit shower must be consistent with a true electromagnetic shower. The `HEEP` ID requirements are summarized in Table 4.4. [5]

[5] ρ is the amount of transverse energy from pileup interactions in the event; $|dxy|$ is the transverse impact parameter with respect to the primay vertex.

Table 4.4: *Summary of the HEEP v7.0 ID requirements.*

Variable	Barrel	Endcap
E_T	> 35 GeV	> 35 GeV
SC position	$\lvert\eta\rvert < 1.4442$	$1.566 < \lvert\eta\rvert < 2.5$
isEcalDriven	true	true
$\lvert\Delta\eta_{in}^{seed}\rvert$	< 0.004	< 0.006
$\lvert\Delta\phi_{in}\rvert$	< 0.06	< 0.06
H/E	$< 1/E + 0.05$	$< 5/E + 0.05$
full 5x5 $\sigma_{i\eta i\eta}$	n/a	< 0.03
full 5x5 E^{2x5}/E^{5x5}	> 0.94 OR $E^{1x5}/E^{5x5} > 0.83$	n/a
EM + Had Depth Isolation	$< 2 + 0.03 * E_T + 0.28 * \rho$	$\begin{cases} < 2.5 + 0.28 * \rho & \text{if } E_T < 50 \\ < 2.5 + 0.03 * (E_T - 50) + 0.28 * \rho & \text{otherwise} \end{cases}$
Track Isolation: track p_T	< 5 GeV	< 5 GeV
Inner Layer Lost Hits	≤ 1	≤ 1
$\lvert dxy\rvert$	< 0.02	< 0.05

Table 4.5: *Electron identification efficiency and SF for barrel and endcaps [84].*

	Barrel	Endcap
Eff. data	$86.13\% \pm 0.01\%(stat.)$	$83.38\% \pm 0.03\%(stat.)$
Eff. simulation	$88.65\% \pm 0.03\%(stat.)$	$84.85\% \pm 0.09\%(stat.)$
ID SF	$0.972 \pm 0.000(stat.) \pm 0.006(syst.)$	$0.983 \pm 0.001(stat.) \pm 0.007(syst.)$

Differences in electron ID efficiency between data and simulation were taken into account by applying a SF, shown in Table 4.5, estimated with a *Tag-and-probe* method [84]. The main sources of systematic uncertainties on the SF originate from non-DY processes.

4.4.2.3 Energy corrections

Discrepancies in energy scale and resolution between data and simulation were corrected following the official prescriptions for scales and smearings [158].
The energy measurement of electrons in data is not perfect and must be corrected with the $Z \to e^+e^-$ events. The electron energy scale in data is corrected by a multiplicative factor dependent on η and R_9[6] of the electron. To take into account the differences in resolution between data and simulation, the electron energy in simulated events was smeared by 1–3% using a Gaussian expression that varies as a function of η and R_9. Smearing and scaling factors were provided for the full 2016 dataset.
In Figure 4.12 the agreement between data and simulation for $Z \to e^+e^-$ events is shown after energy corrections and trigger, ID, and RECO SFs are applied. In this and in the following plots, all the expected SM backgrounds, except for DY+jets and $t\bar{t}$, are labelled as "*Other backgrounds*".

[6] R_9 is defined as the ratio of the energy in a 3×3 matrix of crystals centered around the most energetic one and the full energy collected by the SC: $R_9 = \frac{E_{3x3}}{E_{SC}}$.

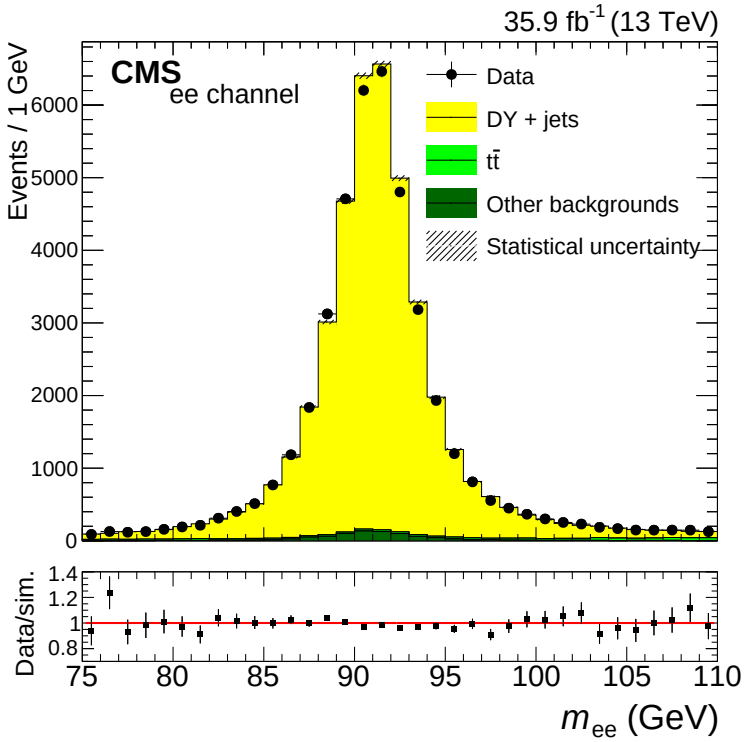

Figure 4.12: $Z \to e^+e^-$ *events in the* low-$m_{\ell\ell}$ *CR after application of ID, RECO, and DY normalization SFs and energy corrections. The uncertainty bands on the simulated background histograms only include statistical uncertainties. The uncertainty bars in the ratio plots represent the combined statistical uncertainties of data and simulation.*

4.4.3 Muons

4.4.3.1 Reconstruction

For the muon reconstruction, at first tracks are reconstructed independently in the inner tracker (*tracker track*) and in the muon system (*standalone-muon track*), then two complementary methods are used.
In the "Tracker Muon" reconstruction ("inside-out" approach), all the tracker tracks with $p_T > 0.5$ GeV and total momentum $p > 2.5$ GeV are considered as possible muon candidates and are extrapolated to the muon system. If at least one muon segment, either in the DTs or in the CSCs, matches the extrapolated track, the corresponding tracker track is considered a *tracker muon*.
The "Global Muon" reconstruction ("outside-in" approach) starts from a standalone-muon track and looks for a matching tracker track. If a compatible track is found, a *global muon* is reconstructed with the combined set of hits from the tracker and the muon system, using the Kalman Filter method to estimate the track parameters.

More information on muon reconstruction algorithms can be found in [99].
Each algorithm is best suited for a unique range of muon η and p_T values: the "Tracker Muon" reconstruction is more efficient for muons with low momentum ($p_T < 5$ GeV) because it requires only a single muon segment in the muon system, while the "Global Muon" reconstruction is more efficient for high-momentum muons penetrating through more than one muon station because it requires segments in at least two muon stations. At large transverse momenta, $p_T > 200$ GeV, the global-muon fit can improve the momentum resolution compared to the tracker-only fit. However, also the "Global Muon" reconstruction is not always the best for the high p_T muons studied in this analysis.
Dedicated reconstruction algorithms for high momentum muons were developed [99] to take into account the showering from interactions in the muon chambers. The *"Tracker-Plus-First-Muon-Station"* (TPFMS) algorithm starts from a *global muon* using only the information from the innermost station containing hits in the muon system. Then the *"Picky fit"* algorithm performs a fit using all the hits from the *global muon*, and discards those that are not consistent with the muon track based on the χ^2 fit. More muon stations are then included in the fit, as long as they are still compatible with a muon track, by the *" Dynamic Truncation fit"* (DYT), developed as an extension of the TPFMS algorithm. A momentum estimate for the muon is provided by each of the algorithms presented above. The best estimate for the p_T of each reconstructed muon is then determined between the tracker-only, the global, the TPFMS, the Picky, and the DYT fits by the *"TuneP"* algorithm. This algorithm chooses the momentum from the tracker-only fit for muons with $p_T < 200$ GeV, while for muons with $p_T > 200$ GeV it takes the momentum from the Picky fit comparing the goodness of this fit with the other fits, and then chooses the momentum from the fit with the most significant improvement.
The p_T of the high energy muons used in this analysis is then assigned by the *"TuneP"* algorithm.

4.4.3.2 Identification

An optimized identification algorithm to select high momentum muons, called "`isHighPtID`", was developed without relying on information from the calorimeters. Muons passing these high-p_T muon ID requirements were selected. The high-p_T muon criteria are:

- the muon is reconstructed as a *global muon*;
- at least one muon-chamber hit must be included in the global-muon track fit;
- there are muon segments in at least two muon stations;
- the p_T relative error, σ_{p_T}/p_T, of the muon best track is less than 0.3;
- to reject muons from cosmic rays and from decays in flight, the vertex position must be close to the interaction point: the transverse impact parameter must be less than

2 mm with respect to the primary vertex, and the longitudinal distance of the track must be less than 5 mm;

- the muon track has at least one pixel hit;
- at least 6 tracker layer hits are required in the reconstruction.

To reject muons originating from hadron decays or pion punch-through in jets, each muon must be isolated from other tracks. The energy of all tracks that originate from the PV and that are inside a cone of $R < 0.3$ around the muon, excluding the muon track, must be less than 10% of the muon p_T.
After muon ID and isolation requirements, simulated events were re-weighted according to the official prescriptions to account for differences in the ID and isolation efficiencies between data and simulations, using η-dependent SFs of 0.95–0.99 obtained with a *Tag-and-probe* method [99]. These SFs are run dependent, due to changing conditions during the 2016 data collection period. They are divided into two sets corresponding to Runs B-F and Runs G-H, and are applied weighted by the luminosity relative to the corresponding period.
To check possible dependences of the SFs from the muon momentum, to be considered with further systematic uncertainties, p-dependent scaling factors were also taken into account. Their impact on the final results is negligible since the effect of the muon trigger, ID and isolation uncertainties on the final signal and background yields considering these new SFs varies less than 1.4%, then no systematic uncertainties related to p-dependent SFs were considered.

4.4.3.3 Momentum corrections

The p_T of selected muons in data and simulated events were corrected with the Rochester corrections [161], developed to remove a bias of the muon momentum from any detector misalignment or any possible error of the magnetic field. These corrections bring the position and width of the $Z \to \mu\mu$ mass peak in simulations and data into better agreement, but their impact on the events studied in this analysis is very small because they are not relevant for high p_T muons. The muon p_T scale still shows a clear bias coming from the tracker in the endcaps. To compensate for these residual differences in the muon momentum scale, q/p_T corrections of the "generalized endpoint" method [84] were used.
The "generalized endpoint" method determines the values of the p_T bias found for high p_T muons as a function of both η and ϕ, comparing data and simulation. In order to describe the q/p_T distribution found in data, a constant bias minimizing the differences between the muon curvature distributions in bins of η and ϕ is injected in simulated events. The values of this bias, obtained for "TuneP" p_T assignment and for muons above 200 GeV in the region $|\eta| < 2.1$ and above 100 GeV in the forward region $|\eta| > 2.1$, are displayed in Figure 4.13. The correction is applied to each muon as a function of his charge, η, and

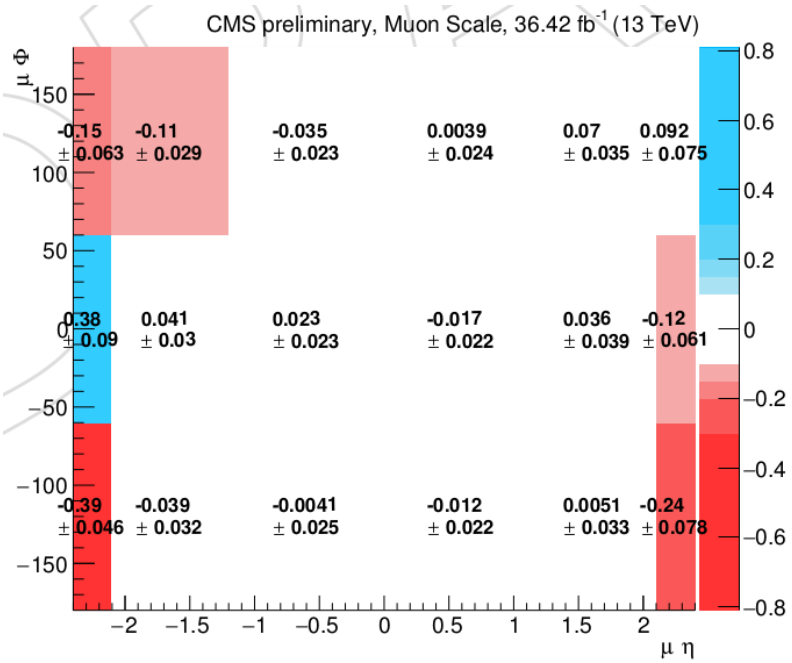

Figure 4.13: *Scale bias (in %) of the "generalized endpoint" method [84] for muons with* p_T $>$ 200 *(*100*)* GeV*in the region* $|\eta| < 2.1$ (> 2.1) *in different* η *and* ϕ *ranges.*

ϕ according to the values reported in Table 4.6. In simulated events, the shift is done according to a Gaussian distribution that takes the correction as central value and the uncertainty assigned on the measured bias as width. To correct data, the shift considers only the central correction without a Gaussian smearing. In the barrel, the p_T bias is consistent with zero with an uncertainty of 3%, while in the endcaps the p_T scale uncertainty is up to 9%.

For the muon momentum resolution in the high-p_T range ($p_T > 100$ GeV), studies using simulated samples and cosmic-ray muons, which allow testing the barrel region, or boosted dimuon events, for the endcaps, are performed. The p_T resolution in the barrel is better

Table 4.6: q/p_T *corrections of the "generalized endpoint" method [84], as a function of* η *and* ϕ *of the muon.*

	$-180 < \phi < -60$	$-60 < \phi < 60$	$60 < \phi < 180$
$-2.4 < \eta < -2.1$	-0.388122 ± 0.045881	0.376061 ± 0.090062	-0.153950 ± 0.063053
$-2.1 < \eta < -1.2$	-0.039346 ± 0.031655	0.041069 ± 0.030070	-0.113320 ± 0.028683
$-1.2 < \eta < 0$	0.0 ± 0.025	0.0 ± 0.025	0.0 ± 0.025
$0 < \eta < 1.2$	0.0 ± 0.025	0.0 ± 0.025	0.0 ± 0.025
$1.2 < \eta < 2.1$	0.005114 ± 0.033115	0.035573 ± 0.038574	0.070002 ± 0.035002
$2.1 < \eta < 2.4$	-0.235470 ± 0.077534	-0.122719 ± 0.061283	0.091502 ± 0.074502

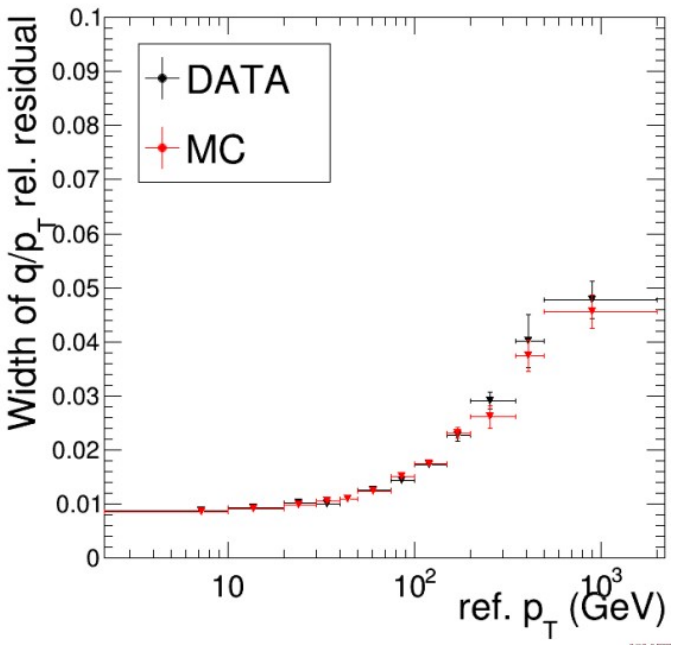

Figure 4.14: *Comparison of muon momentum resolution in data and simulation as a function of muon p_T.*

than 10% for muons with p_T up to 1 TeV [99]. As shown in Figure 4.14, the simulated samples reproduce quite well the resolution observed in data, so no corrections are applied. The uncertainty on the muon p_T resolution is given by a smearing of the muon p_T in simulated events of 1% in the barrel and 2% in the endcaps.

In Figure 4.15 the agreement between data and simulation for $Z \to \mu\mu$ events is shown after momentum corrections and trigger, ID, and isolation SFs are applied.

4.5 Event selection

Events are divided into signal region (one for each final state) and control regions (CR), as described in Section 4.2, according to the following criteria:

signal region: $\ell\ell$jj

- fire `HLT_DoubleEle33_CaloIdL_MW/GsfTrkIdVL` trigger if eejj channel, as described in Section 4.3.3;
- fire `HLT_Mu50` OR `HLT_TkMu50` trigger if $\mu\mu$jj channel, as described in Section 4.3.3;
- leading lepton with $p_T > 60$ GeV;

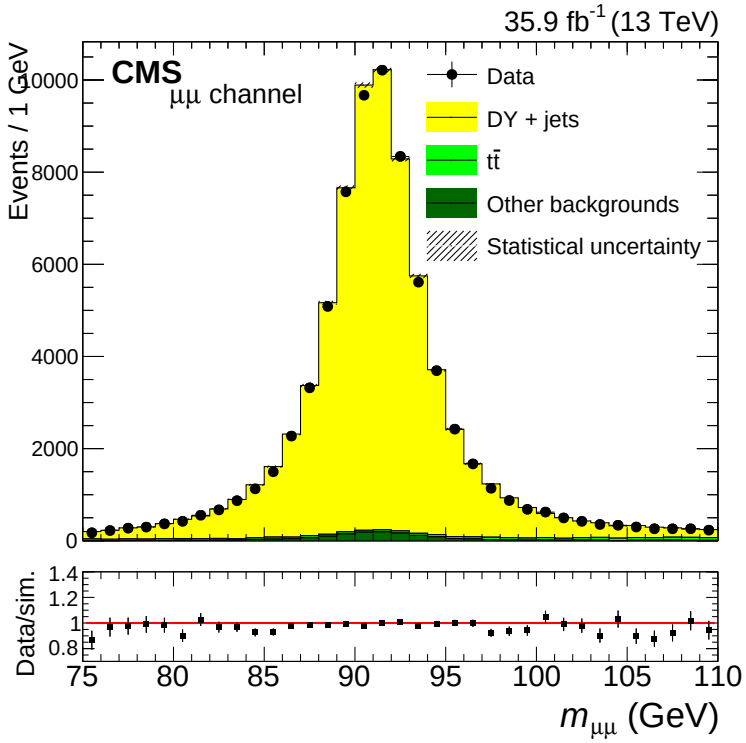

Figure 4.15: *$Z \to \mu\mu$ events in the* low-$m_{\ell\ell}$ *CR after application of trigger, ID, isolation, and DY normalization SFs and momentum corrections. The uncertainty bands on the simulated background histograms only include statistical uncertainties. The uncertainty bars in the ratio plots represent the combined statistical uncertainties of data and simulation.*

- subleading lepton with $p_T > 53$ GeV;
- at least two jets with $p_T > 40$ GeV, if more than two only the leading and subleading are considered in the following (event rejected if at least two jets with $p_T > 40$ GeV but leading and subleading leptons do not pass the selections);
- all leptons and jets with $|\eta| < 2.4$;
- $m_{\ell\ell} > 200$ GeV, to avoid contamination from resonant Z boson production;
- $R > 0.4$ between all objects in the final state (leptons and jets);
- $m_{\ell\ell \mathrm{jj}} > 600$ GeV, to ensure full efficiency of all kinematic requirements.

***flavour-sideband*:** CR used to estimate the $t\bar{t}$ contribution

- same as signal region $\ell\ell$jj but requiring one electron and one muon instead of two same-flavor leptons.

***low-$m_{\ell\ell}$* CR:** CR used to check the agreement between data and simulation on the DY+jets contribution

Table 4.7: *Signal/$\sqrt{Background}$ ratio ($S/\sqrt{B}$) with different p_T thresholds on final state particles in the muon channel analysis for $m_{W_R} = 2.2$ TeV and $m_{N_R} = 1.1$ TeV. Background rejection is improved requiring higher p_T final state particles with almost no impact to W_R signals with $m_{W_R} > 2$ TeV. The values used in this search are highlighted in bold.*

Final state particle	p_T threshold (GeV)	$S/\sqrt{B}$
Leading muon	53	17.3
	60	**17.4**
Subleading muon	40	17.1
	50	17.4
	53	**17.7**
Leading jet	30	15.4
	40	**17.4**

- same as signal region $\ell\ell$jj;
- $m_{\ell\ell} < 200$ GeV;
- no $m_{\ell\ell \mathrm{jj}}$ requirement.

***low-$m_{\ell\ell jj}$* CR:** CR used to check agreement between data and simulation in events with high dilepton mass

- same as signal region $\ell\ell$jj;
- $m_{\ell\ell \mathrm{jj}} < 600$ GeV.

Lowering the p_T thresholds with respect to the ones used in this analysis would introduce more background without an equivalent increase in signal, as shown in Table 4.7.

The $m_{\ell\ell} > 200$ GeV requirement applied in the W_R search performed in Run 1 to reduce the DY+jets and ZZ background, was adopted also by the 13 TeV W_R search. Its effect on the W_R signal efficiency varies with the W_R and N_R masses, as shown in Figure 4.16, but for W_R masses > 800 GeV and $m_{N_R} = \frac{m_{W_R}}{2}$ the efficiency is at least 81%.

All events are subjected to the $R > 0.4$ separation requirement between leptons and jets to make sure that the leptons are not in the cone size of the $anti - k_T$ algorithm used to reconstruct the jets. The R cut is applied to all the combinations between the two leading leptons and the two leading jets which pass p_T, η, and identification criteria. The two leptons are also required to be separated by at least $R > 0.4$ to suppress background from boosted Z. Events not satisfying this selection requirements are discarded.

The kinematic selections placed on leptons and jets have an effect on the $m_{\ell\ell \mathrm{jj}}$ background distribution. As shown in Figure 4.17, in the signal region the kinematic cuts result in a slowly increasing shape that spans $m_{\ell\ell \mathrm{jj}}$ from 300 to 550 GeV. A selection of $m_{\ell\ell \mathrm{jj}} > 600$ GeV is then applied. The effect of this requirement on W_R signal is negligible, as 99% of events from the lowest mass W_R sample ($m_{W_R} = 800$ GeV) pass the $m_{\ell\ell \mathrm{jj}} > 600$ GeV

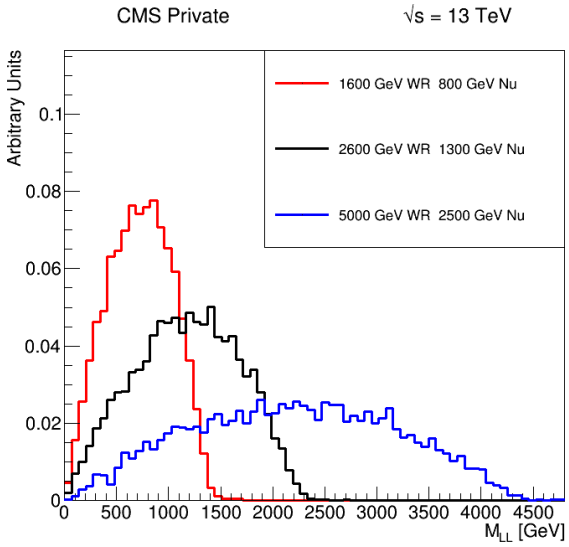

Figure 4.16: *Dilepton mass of leptons at generator level from the W_R decay chain for different m_{W_R} values. The area under each curve is normalized to 1.*

selection.

The efficiency of our selections on signal samples with $m_{N_R} = \frac{m_{W_R}}{2}$ is presented in Figure 4.18. At low W_R masses, it is less likely to produce two high-p_T leptons that would pass the selections. As the masses of the W_R and the N_R increase, the product of the acceptance and efficiency for W_R decays to the $\ell\ell$jj final state increases from 30% at $m_{W_R} = 1000$ GeV to 57% for $m_{W_R} > 3000$ GeV in the electron channel, and similarly from 40 to 75% in the muon channel. For both channels, the signal efficiency reaches a plateau at $m_{W_R} = 3000$ GeV. The electron channel has a 10% lower acceptance due to the exclusion of the gap region between the barrel and the endcap. When both leptons are in the barrel, there is a 10% difference in the efficiency. This residual difference is due to the lower efficiency of the electron identification, which is tighter with respect to the muon one. This leads to a total efficiency difference of approximately 20% for electrons and muons.

4.6 Background estimation

As $t\bar{t}$ and DY+jets have the same final state of the signal, they are the main sources of background in this analysis, representing respectively the 75% and 20% of the total background. The reducible backgrounds (W+jets, WW, WZ, ZZ, single top quark events, and QCD multijet events) do not significantly contaminate the signal region, defined in Section 4.5: the diboson backgrounds constitute $\approx$ 1.5% of the total background in the signal region, the W+jets $\approx$ 0.5%, the single top quark events $\approx$ 5%, and the QCD events

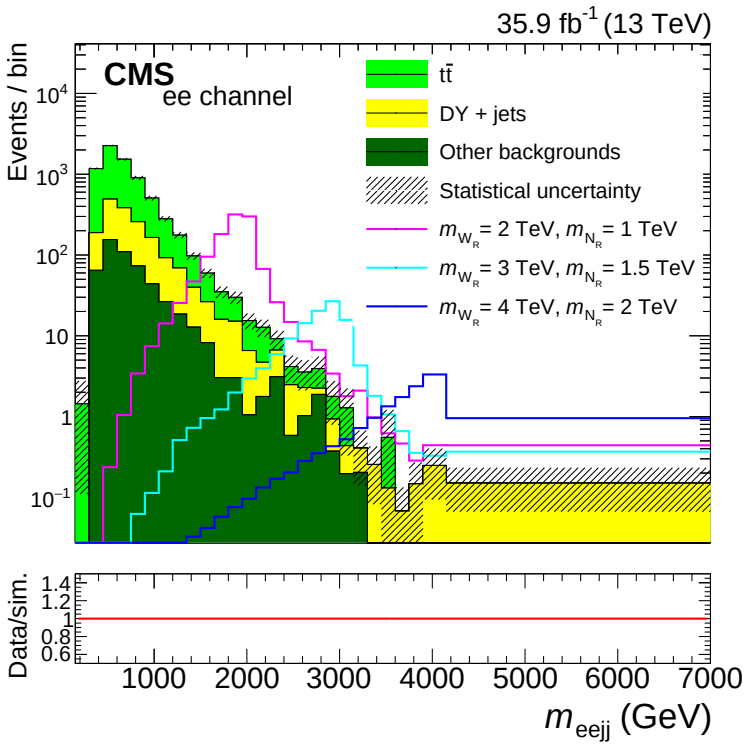

(a) Electron channel

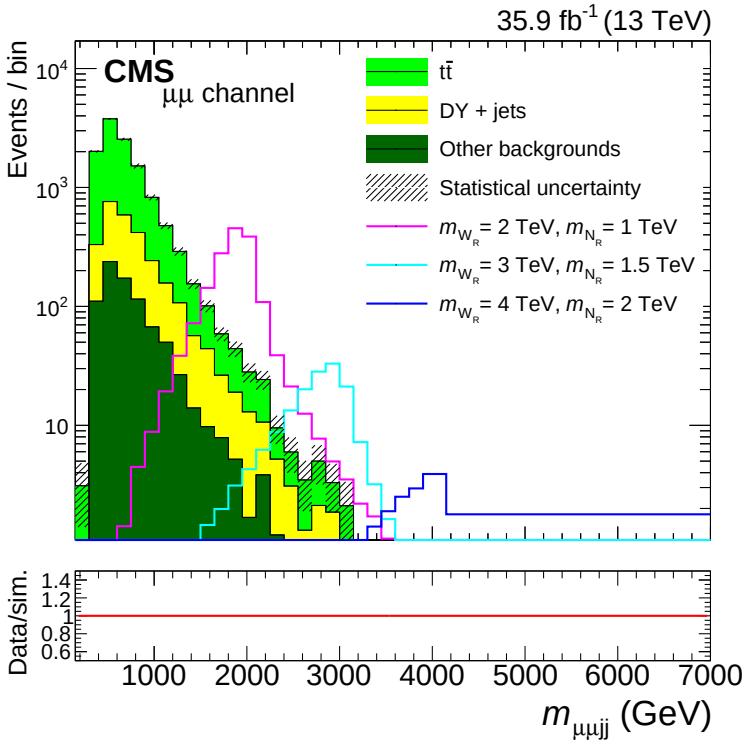

(b) Muon channel

Figure 4.17: *The $m_{\ell\ell jj}$ distribution in the signal region without the $m_{\ell\ell jj} > 600$ GeV requirement. The turn on curve is created by the lepton and jet kinematic selections. A few signal points are also plotted for comparison.*

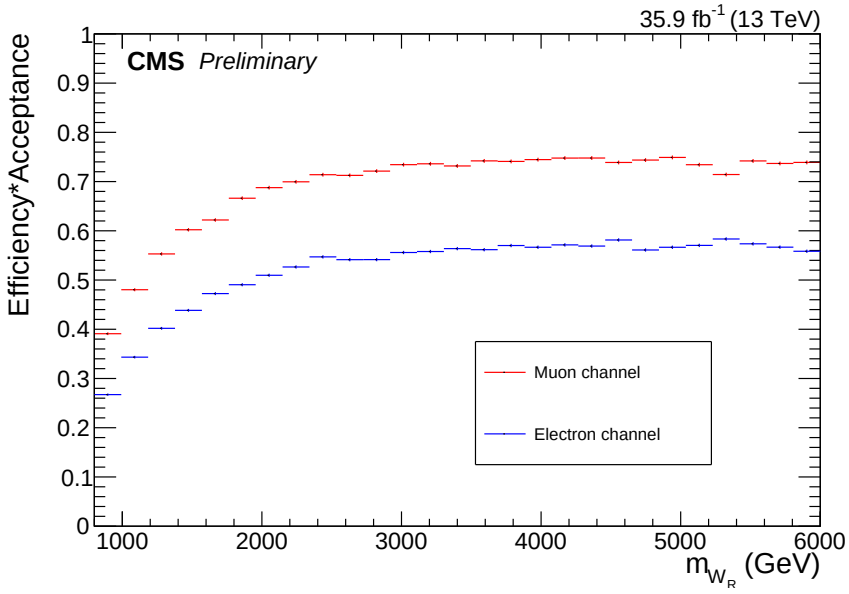

(a) Efficiency for all η

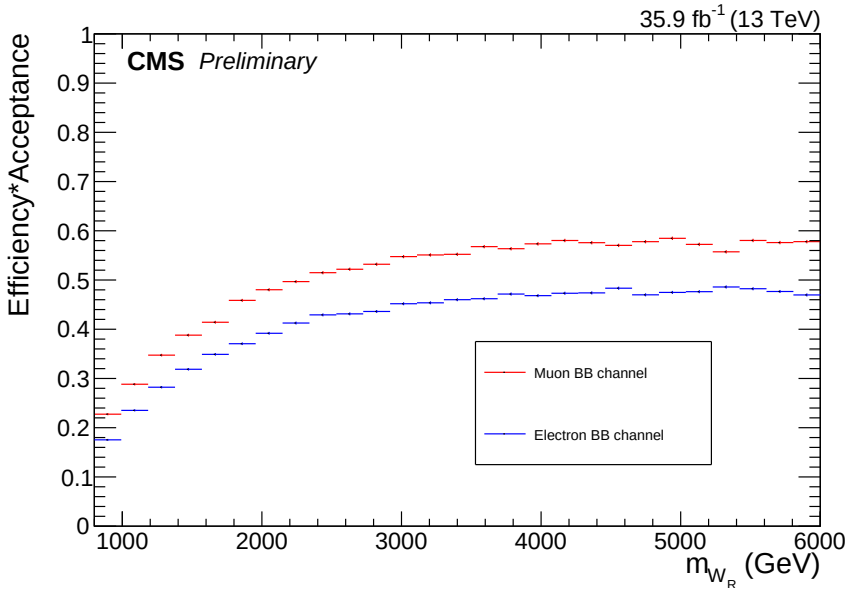

(b) Both leptons in the barrel

Figure 4.18: *Acceptance* $\times$ *efficiency for* $W_{\mathrm{R}} \to \ell\ell jj$ *events as a function of* W_{R} *mass, in the hypothesis of* $m_{N_{\mathrm{R}}} = \frac{m_{W_{\mathrm{R}}}}{2}$.

Table 4.8: *The functional approximation of the measured fake rate for HEEP electrons in the barrel and endcap as a function of E_T [84].*

region	E_T range (GeV)	functional form
barrel	$35 \leq E_T < 61.9$	$0.0628 - 0.000803 \times E_T$
	$61.9 \leq E_T < 152.2$	$0.0185 - 8.84 \times 10^{-5} \times E_T$
	$152.2 \leq E_T < 408.1$	$0.00505 - 6.51 \times 10^{-8} \times E_T$
	$E_T > 408.1$	$0.00181 + 7.88 \times 10^{-6} \times E_T$
endcap $\lvert\eta\rvert < 2.0$	$35 \leq E_T < 78.5$	$0.0955 - 0.000719 \times E_T$
	$78.5 \leq E_T < 226.8$	$0.0394 - 4.06 \times 10^{-6} \times E_T$
	$226.8 \leq E_T < 345.4$	$0.0229 + 6.86 \times 10^{-6} \times E_T$
	$E_T > 345.4$	0.0466
endcap $\lvert\eta\rvert > 2.0$	$35 \leq E_T < 57.3$	$0.100 - 0.000789 \times E_T$
	$E_T \geq 57.3$	$0.0513 + 6.29 \times 10^{-5} \times E_T$

$\approx 0.1\%$.
The QCD events are estimated with a data-driven method in the electron channel, following the procedure of the Z' dielectron analysis [84] where the electrons are required to fail the HEEP ID requirements and the data events are weighted with the fake rate as a function of the electron p_T and $|\eta|$ shown in Table 4.8, while they are taken directly from the simulation in the muon channel. The contribution from the QCD events is considered negligible, then these samples are not used in this analysis.
The contributions from the other reducible processes (W+jets, WW, WZ, ZZ, and single top quark events) are almost negligible and have been estimated with simulated samples by counting the number of events in the signal region.

4.6.1 Top background estimation

The $t\bar{t}$ background contribution was estimated directly from data in the *flavour-sideband* CR which has the same kinematic characteristics as the $t\bar{t}$ events in the signal region, as defined in Section 4.5. In Figure 4.19 the $m_{\ell\ell \mathrm{jj}}$ distribution is shown for data and simulation in the *flavour-sideband* CR. Additional comparison plots for variables used in the selection are shown in Figure 4.20.

To estimate this background in the signal region, the events in the *flavour-sideband* CR are used. The assumption made on the conservation of the lepton flavour in the decay ensures that there is no contamination from signal events. This assumption is valid since, at leading order, the decay of a W_{R} boson cannot yield events with an eμjj final state.
To calculate the number of events from $t\bar{t}$ in the eejj and the $\mu\mu$jj signal regions, simulated $t\bar{t}$ events are used to determine the transfer factor $R_{\ell\ell/\mathrm{e}\mu}$ ($\ell\ell$ = ee or $\mu\mu$) between the eμjj control region and the signal region. These factors were evaluated from the ratio of the

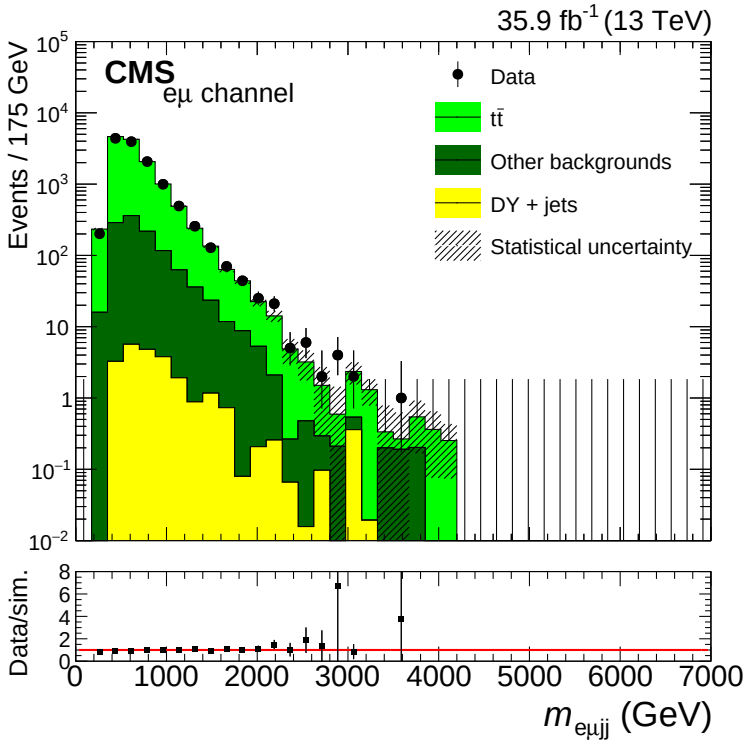

Figure 4.19: *The $m_{\ell\ell jj}$ distribution for data and simulated events in the* flavour-sideband *CR with all SFs applied. The uncertainty bands on the simulated background histograms only include statistical uncertainties. The uncertainty bars in the ratio plots represent the combined statistical uncertainties of data and simulation.*

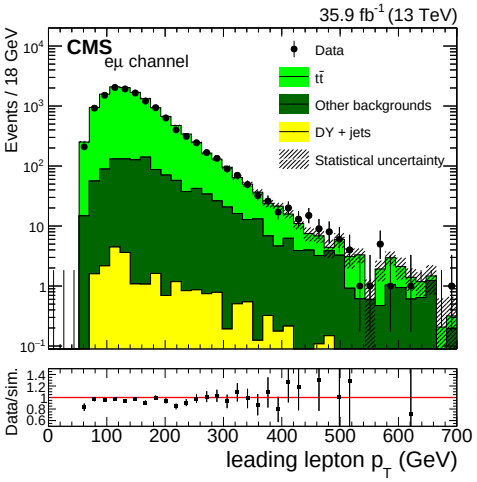

(a) *Leading lepton p_T*

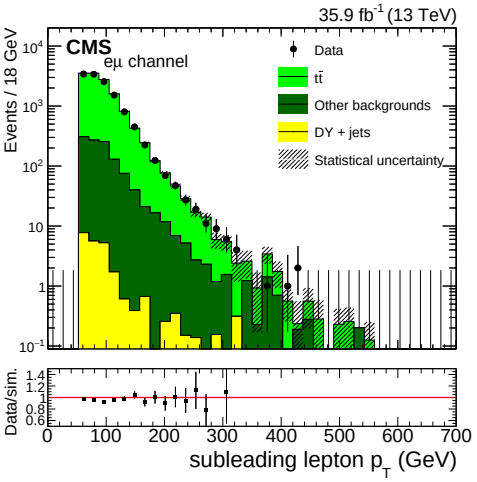

(b) *Subleading lepton p_T*

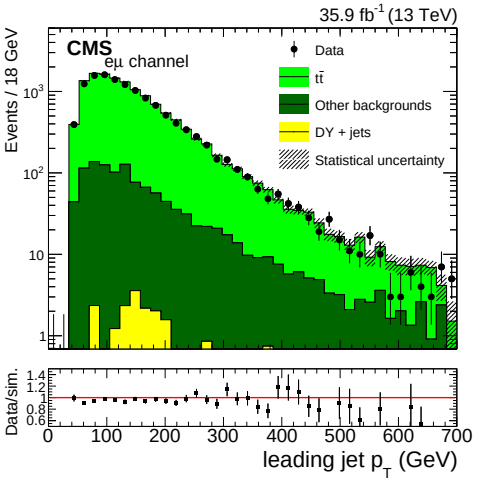

(c) *Leading jet p_T*

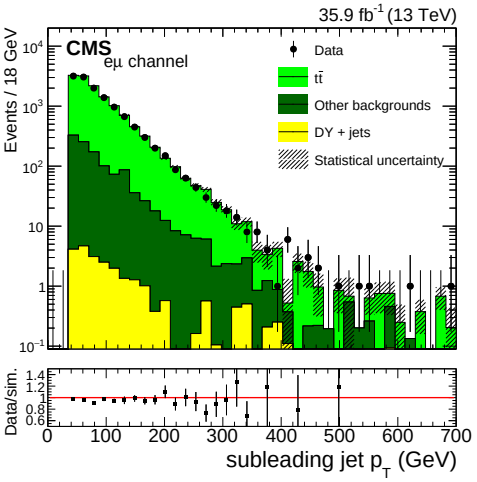

(d) *Subleading jet p_T*

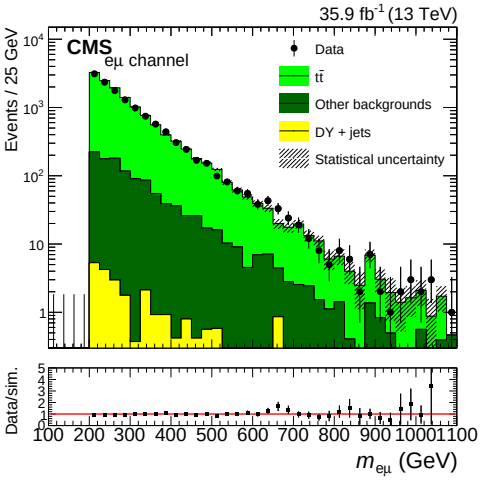

(e) *Dilepton mass*

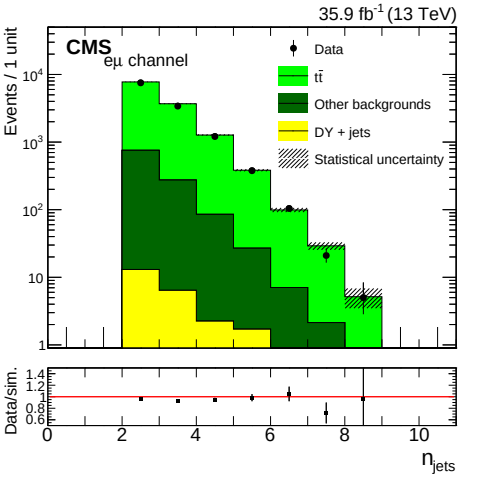

(f) *Number of jets*

Figure 4.20: *Data/MC comparison for different kinematic variables in the* flavour-sideband *CR with all SFs applied. The uncertainty bands on the simulated background histograms only include statistical uncertainties. The uncertainty bars in the ratio plots represent the combined statistical uncertainties of data and simulation.*

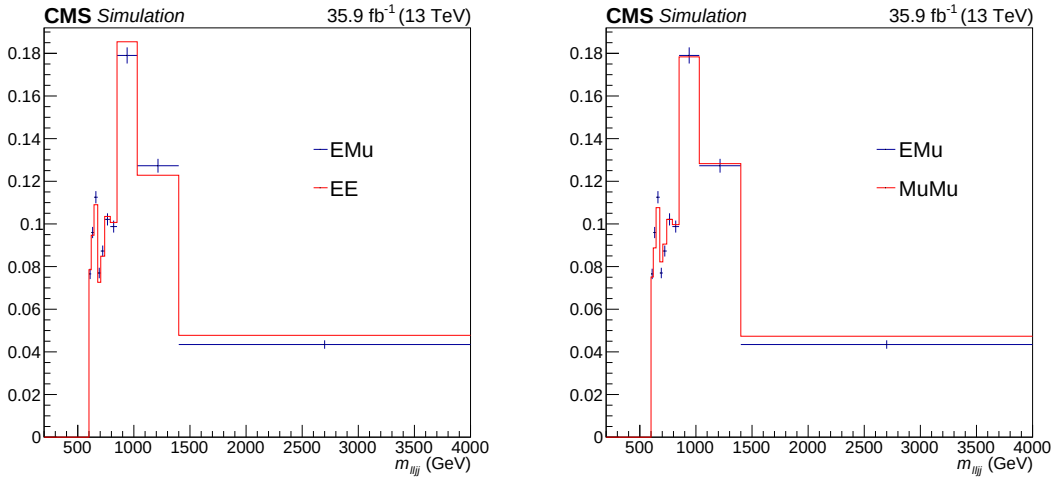

(a) m_{eejj} *and* $m_{\mathrm{e}\mu\mathrm{jj}}$ (b) $m_{\mu\mu\mathrm{jj}}$ *and* $m_{\mathrm{e}\mu\mathrm{jj}}$

Figure 4.21: *The* $m_{\ell\ell jj}$ *distribution for simulated* $e\mu jj$ *events in the* flavour-sideband *CR and for* $eejj$ $(\mu\mu jj)$ *events in the signal region on the left (right).*

number of simulated $t\bar{t}$ events in the distributions of m_{eejj} or $m_{\mu\mu\mathrm{jj}}$ in the signal region over the number of simulated $t\bar{t}$ events in the distribution of $m_{\mathrm{e}\mu\mathrm{jj}}$ in the *flavour-sideband* CR. The m_{eejj} and $m_{\mu\mu\mathrm{jj}}$ distributions in the signal region are presented, together with the $m_{\mathrm{e}\mu\mathrm{jj}}$ distribution in the *flavour-sideband* CR, in Figure 4.21.
The number of events in the signal region is thus given by:

$$N_{t\bar{t}}(\text{signal region}) = N_{t\bar{t}}(\text{flavor control region})\, R_{\ell\ell/\mathrm{e}\mu}.$$

The dependency of the $t\bar{t}$ extrapolation SF as a function of $m_{\ell\ell\mathrm{jj}}$ is checked with a bin-by-bin ratio, but no dependency has been found. As shown in Figure 4.22 for the electron and muon channels, the ratio of events as a function of the $m_{\ell\ell\mathrm{jj}}$ distribution is fit to a constant line from where the SF value is taken.
In order to evaluate a systematic uncertainty on the $t\bar{t}$ SF more conservative than the error on the fitted parameter, the ratio of the SFs as a function of $m_{\ell\ell\mathrm{jj}}$ was fitted with several functional forms: a constant line, a polynomial of first and second order, a logarithmic function and an exponential function, as shown in Figure 4.23 and in Figure 4.24. Since the fit with a polynomial of first order indicates there is no statistically significant slope and the rest of the functions have no physics motivation, we consider the first order polynomial to get the systematic uncertainty.
The difference between the values of the fitted line at high (4 TeV) and low (200 GeV) mass, shown in Figure 4.25, is used as systematic uncertainty on the $t\bar{t}$ SF since it is bigger than the error on the fitted parameter for every functional form studied. The values and

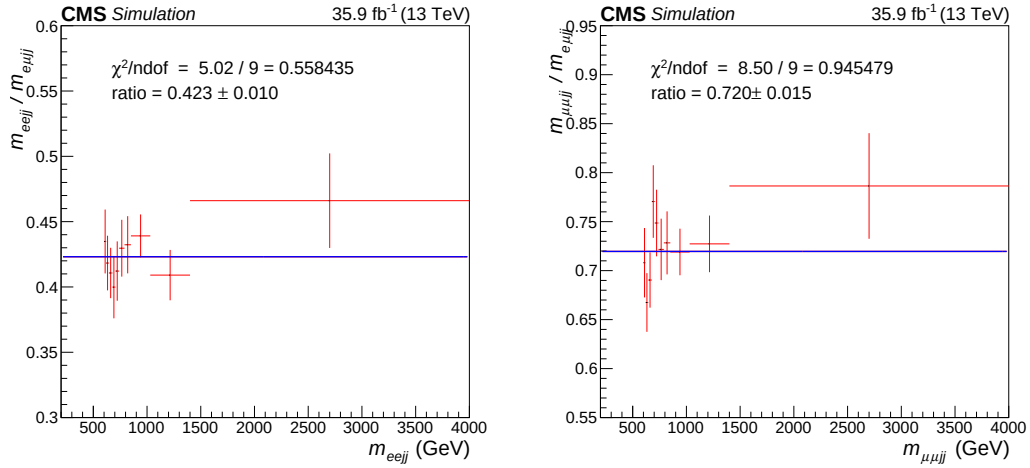

(a) *Ratio of* $m_{\mathrm{ee}\mathrm{jj}}$ *and* $m_{\mathrm{e}\mu\mathrm{jj}}$ (b) *Ratio of* $m_{\mu\mu\mathrm{jj}}$ *and* $m_{\mathrm{e}\mu\mathrm{jj}}$

Figure 4.22: *Bin-by-bin ratio of the* $m_{\ell\ell\mathrm{jj}}$ *and* $m_{\mathrm{e}\mu\mathrm{jj}}$ *distributions from* $t\bar{t}$ *simulations, where* ℓ *is an electron (left) or a muon (right). The blue horizontal line represents the SF value derived from a constant fit to the inclusive distribution. The* χ^2 *is calculated w.r.t. the blue line.*

the errors of the fitted parameters for the different functions are given in Table 4.9.

The values of the scale factors obtained with their statistical and systematic uncertainties are given in Table 4.10. Using these transfer factors we can account for the difference in efficiency and acceptance between electrons and muons in the final states. A difference related to the trigger is not explicitly taken into account, since selected events, with the triggers selection included, are used to calculate the ratio.

4.6.2 DY+jets background estimation

No high purity CR having the same kinematics as the signal region exists for the DY+jets background, so the contribution from high mass DY lepton pairs produced in association with additional jets is estimated using simulated events. The DY+jets sample was normalized to the measured integrated luminosity and the SFs for lepton efficiencies discussed in Section 4.4 were applied.

DY+jets samples produced with MADGRAPH and aMC@NLO generators were considered for this analysis and the aMC@NLO one was chosen for the estimate, since it describes better the data. This is due to the better simulation of the additional jets coming from the hard interactions. Unfortunately, the aMC@NLO samples used in this analysis have low statistics at high $m_{\ell\ell\mathrm{jj}}$. On the other hand, the HT-binned MADGRAPH samples have more statistics in this same region, but they do not capture all the features seen in the data. The event selection of this analysis requires that the additional jets produced

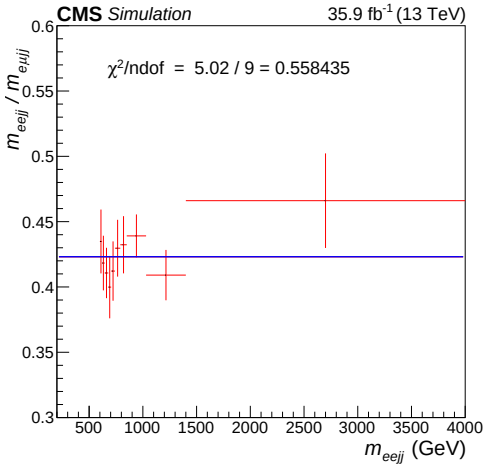

(a) *Constant fit to* $SF_{ee/e\mu}$

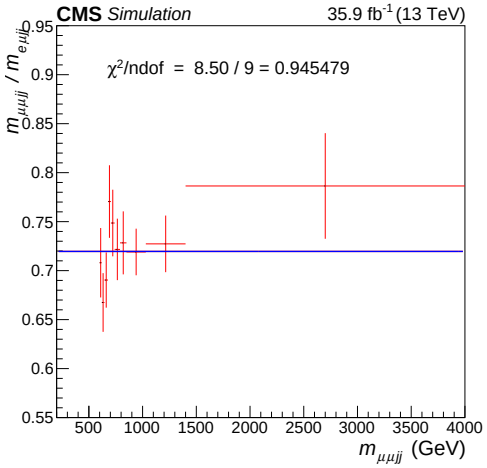

(b) *Constant fit to* $SF_{\mu\mu/e\mu}$

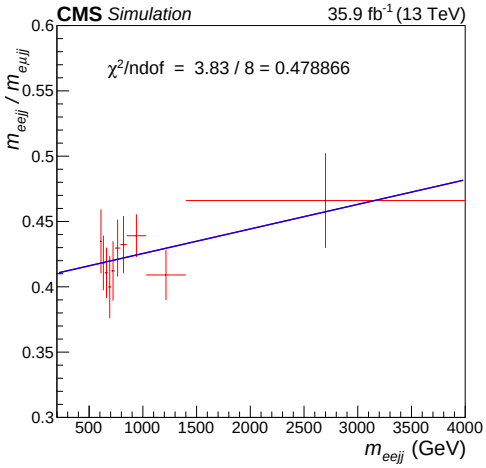

(c) *First order polynomial fit to* $SF_{ee/e\mu}$

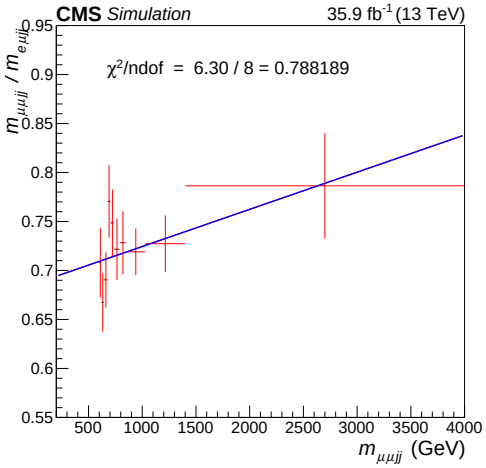

(d) *First order polynomial fit to* $SF_{\mu\mu/e\mu}$

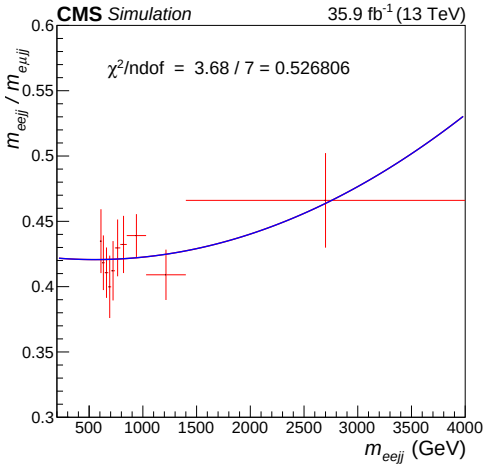

(e) *Second order polynomial fit to* $SF_{ee/e\mu}$

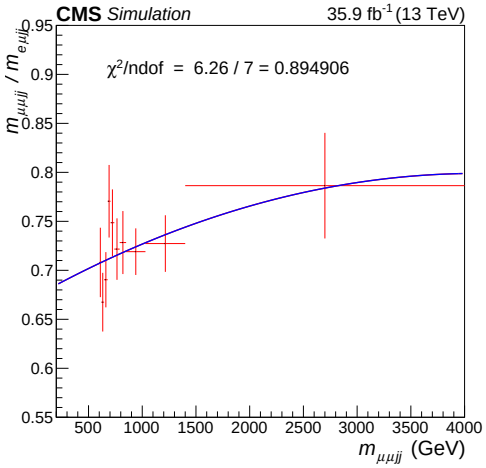

(f) *Second order polynomial fit to* $SF_{\mu\mu/e\mu}$

Figure 4.23: *$t\bar{t}$ SFs for the electron channel on the left and for the muon channel on the right as a function of $m_{\ell\ell jj}$ fitted with different functions.*

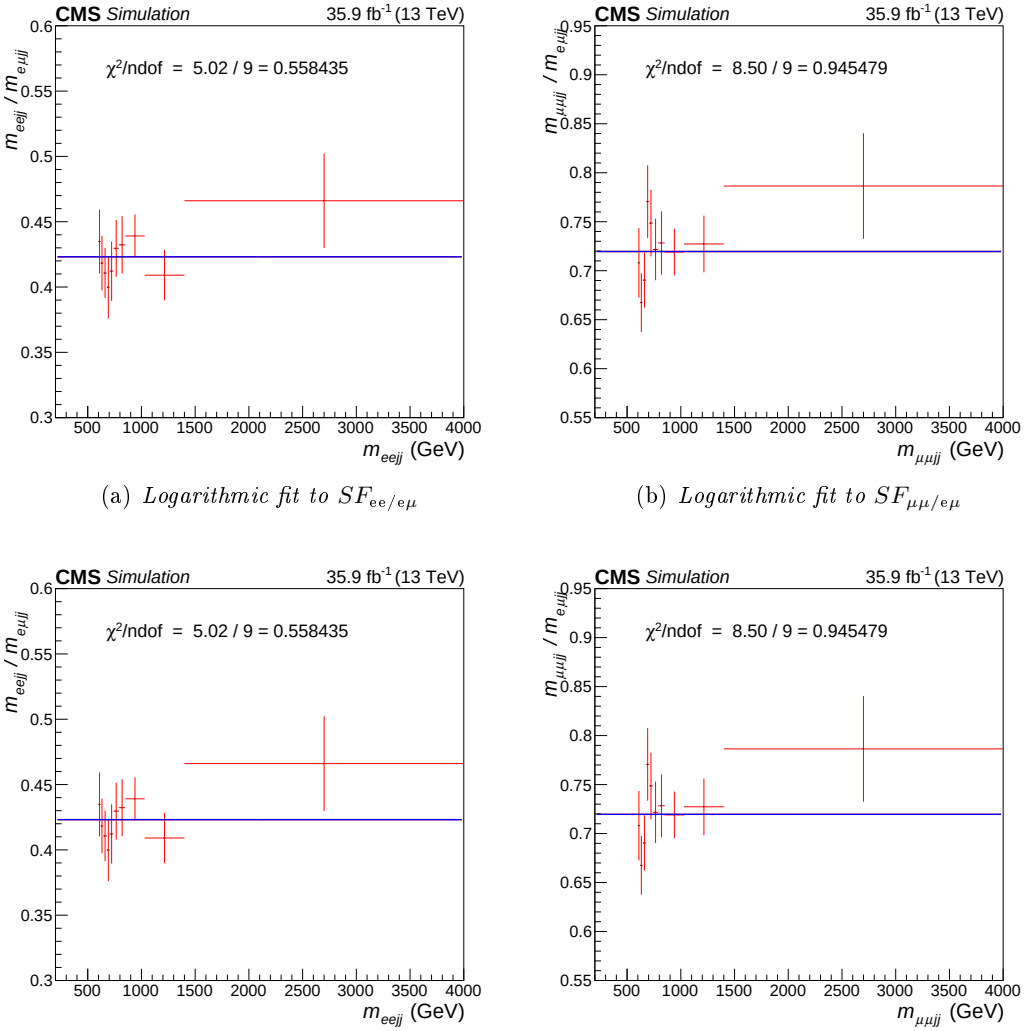

(a) *Logarithmic fit to* $SF_{\mathrm{ee}/\mathrm{e}\mu}$

(b) *Logarithmic fit to* $SF_{\mu\mu/\mathrm{e}\mu}$

(c) *Exponential fit to* $SF_{\mathrm{ee}/\mathrm{e}\mu}$

(d) *Exponential fit to* $SF_{\mu\mu/\mathrm{e}\mu}$

Figure 4.24: *$t\bar{t}$ SFs for the electron channel on the left and for the muon channel on the right as a function of $m_{\ell\ell\mathrm{jj}}$ fitted with different functions.*

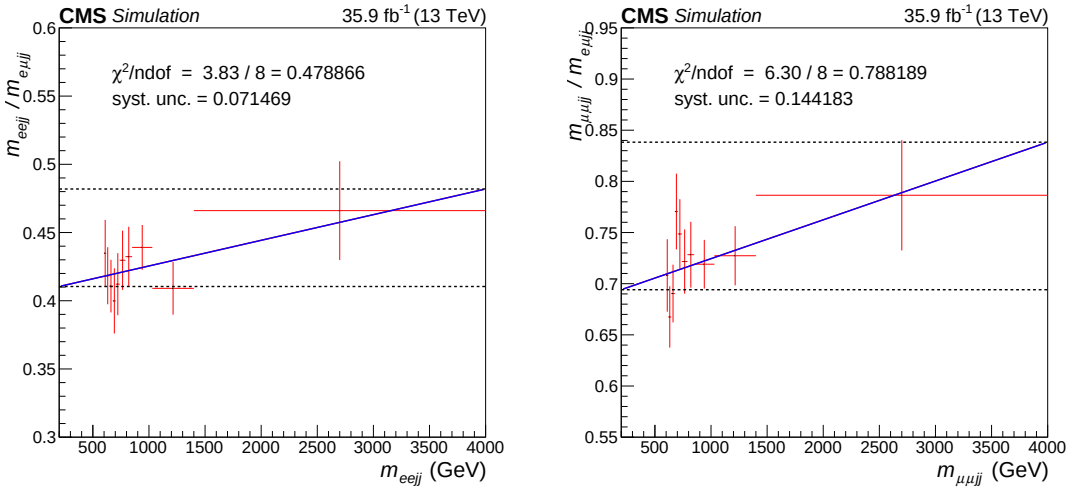

(a) *Systematic uncertainty band for* $SF_{\mathrm{ee}/\mathrm{e}\mu}$ (b) *Systematic uncertainty band for* $SF_{\mu\mu/\mathrm{e}\mu}$

Figure 4.25: *Systematic uncertainty band for the* $t\bar{t}$ *SFs (for the electron channel on the left and for the muon channel on the right) taken from the fit with a polynomial of first order to the bin-by-bin ratio of the* $m_{\ell\ell\mathrm{jj}}$ *and* $m_{\mathrm{e}\mu\mathrm{jj}}$ *distributions from* $t\bar{t}$ *simulations.*

as initial state radiation have p_T greater than 40 GeV. This region of phase space is not well modeled by MADGRAPH, as seen in Figure A.1 in Appendix A for both the electron and the muon channel, thus the aMC@NLO generator is used. More details about the MADGRAPH and aMC@NLO DY+jets samples are presented in Appendix A.
A comparison of the $m_{\ell\ell\mathrm{jj}}$ distribution in the signal region between the two generators is shown in Figure 4.26 for the electron and the muon channels. These distributions, scaled to 35.9 fb^{-1} of data, show that the two samples provide similar overall estimates for the DY+jets background with comparable statistical uncertainty, thus the statistics of the aMC@NLO MC sample is sufficient for a meaningful comparison with data. More details about the statistics of the aMC@NLO MC sample are presented in Appendix B.

The DY+jets sample was weighted applying the electroweak NLO corrections used in the CMS monojet analysis [162]. They have been derived in an inclusive way for Z events with one jet in the final state following what described in [163], where it is shown that changes versus jets multeplicity are small so they can be applied also to Z events with two jet in the final state. These electroweak effects tend to reduce the cross section estimate with increasing transverse momentum of the Z boson and are of the order of $\approx 1\%$ at 150 GeV and of ≈ 15–20% at 1 TeV.
The DY+jets contribution normalization in the simulation was then corrected to match the events in data by means of a SF measured in the *low-*$m_{\ell\ell}$ CR. The SF was calculated as the ratio of data and simulated events under the Z peak resonance in the range $80 < m_{\ell\ell} <$

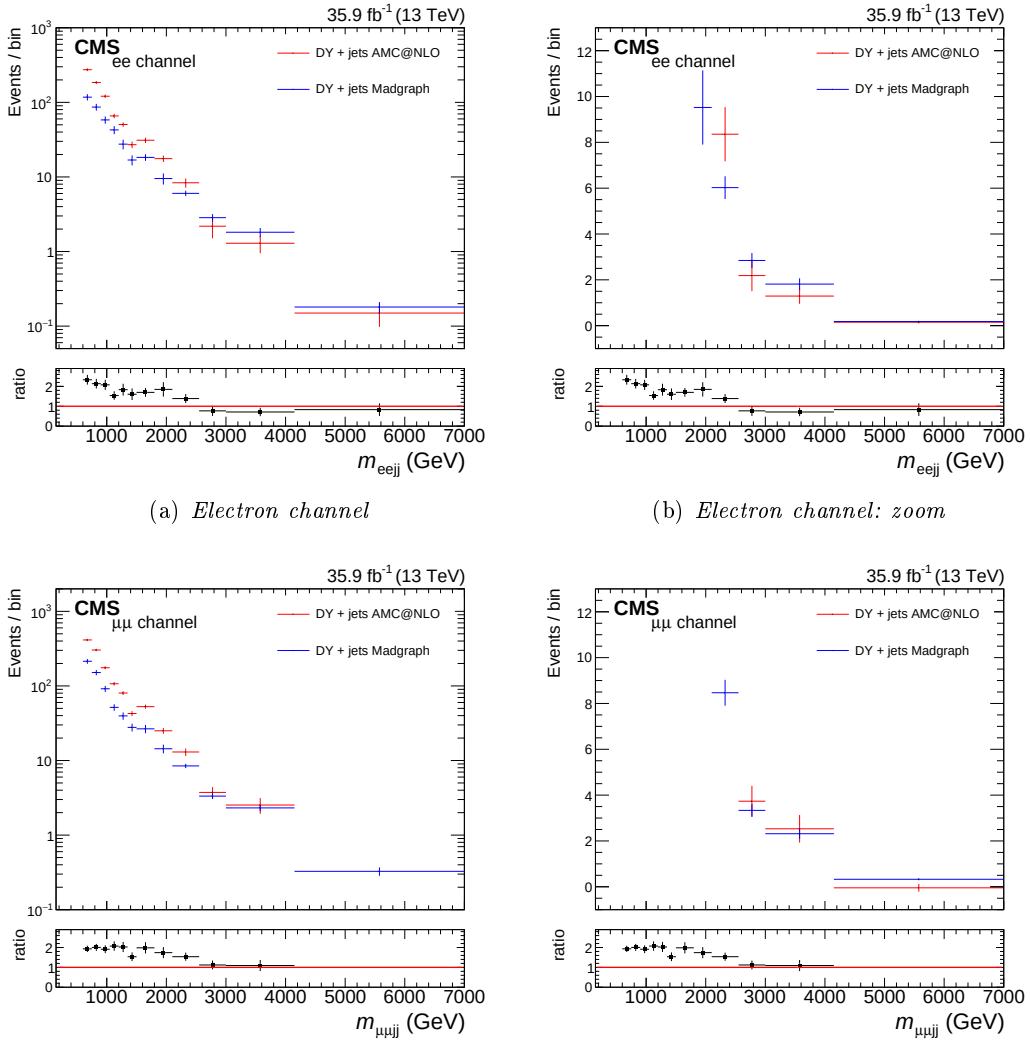

(a) *Electron channel* (b) *Electron channel: zoom*

(c) *Muon channel* (d) *Muon channel: zoom*

Figure 4.26: *The $m_{\ell\ell jj}$ distribution in the signal region for MC estimate from* AMC@NLO *and* MADGRAPH.

Table 4.9: *Fitted parameters and their errors for the different functions in the electron and muon channels.*

Function	Electron channel	Muon channel
pol0	$p_0 = 4.23142 \times 10^{-1} \pm 6.78942 \times 10^{-3}$	$p_0 = 7.19599 \times 10^{-1} \pm 9.97339 \times 10^{-3}$
pol1	$p_0 = 4.06674 \times 10^{-1} \pm 1.65238 \times 10^{-2}$ $p_1 = 1.88077 \times 10^{-5} \pm 1.72050 \times 10^{-5}$	$p_0 = 6.86513 \times 10^{-1} \pm 2.44170 \times 10^{-2}$ $p_1 = 3.79428 \times 10^{-5} \pm 2.55590 \times 10^{-5}$
pol2	$p_0 = 4.23556 \times 10^{-1} \pm 4.75597 \times 10^{-2}$ $p_1 = -1.02951 \times 10^{-5} \pm 7.87840 \times 10^{-5}$ $p_2 = 9.32428 \times 10^{-9} \pm 2.46324 \times 10^{-8}$	$p_0 = 6.73169 \times 10^{-1} \pm 7.01515 \times 10^{-2}$ $p_1 = 6.09820 \times 10^{-5} \pm 1.16391 \times 10^{-4}$ $p_2 = -7.39219 \times 10^{-9} \pm 3.64328 \times 10^{-8}$
log	$p_0 = 1.52675 \pm 1.03658 \times 10^{-2}$	$p_0 = 2.05361 \pm 2.04814 \times 10^{-2}$
exp	$p_0 = -8.60047 \times 10^{-1} \pm 1.60452 \times 10^{-2}$	$p_0 = -3.29061 \times 10^{-1} \pm 1.38597 \times 10^{-2}$

Table 4.10: *SF applied to the number of events in the* flavour-sideband *CR to estimate the number of $t\bar{t}$ events in the* eejj *and* $\mu\mu$jj *signal regions.*

channel	SF	stat. uncertainty	syst. uncertainty
eμjj $\rightarrow$ eejj	0.423	0.010	0.071
eμjj $\rightarrow$ $\mu\mu$jj	0.720	0.015	0.144

100 GeV in the dilepton invariant mass distribution, shown in Figures 4.12 and 4.15 for the electron and the muon channel, respectively, with the SF already applied. This SF takes into account residual mis-modeling between data and simulation including the signal region requirements on the jets. Table 4.11 shows the SFs that were applied in the estimate of the DY+jets contribution in this analysis. The systematic uncertainties on the SF are not taken into account because they are negligible with respect to the systematic uncertainties on the DY+jets estimation taken from the PDF, and factorization and renormalization factors, described in Section 4.7.1.
A comparison of the $m_{\ell\ell\text{jj}}$ distribution between data and MC is shown in Figure 4.27 in the *low-*$m_{\ell\ell}$ CR. Additional comparison plots for other kinematic variables are shown in Figure 4.28. The MC description of the data is reasonable even at high $m_{\ell\ell\text{jj}}$ in this sideband, which is essential to estimate the shape of the DY+jets background directly from simulation.

In order to verify that the SF measured for the DY+jets background around the Z peak in the *low-*$m_{\ell\ell}$ CR is valid also at higher masses, the *low-*$m_{\ell\ell jj}$ CR is used. Figure 4.29 shows a comparison between data and MC of the $m_{\ell\ell\text{jj}}$ distribution in events with high

Table 4.11: *$Z \rightarrow e^+e^-$ and $Z \rightarrow \mu^+\mu^-$ scale factors to normalize simulated events to data.*

channel	SF	stat. unc.
$Z \rightarrow e^+e^-$ (aMC@NLO)	1.069	0.008
$Z \rightarrow \mu^+\mu^-$ (aMC@NLO)	1.071	0.006

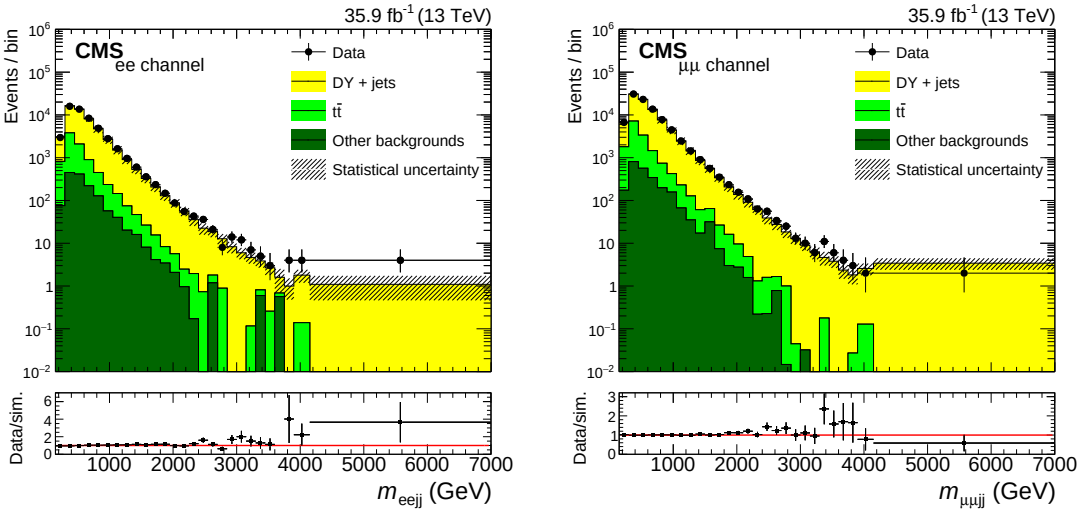

(a) m_{eejj} *events* (b) $m_{\mu\mu\mathrm{jj}}$ *events*

Figure 4.27: *The* $m_{\ell\ell\mathrm{jj}}$ *distribution in data and simulated events in the* low-$m_{\ell\ell}$ *CR with the DY SF applied. The uncertainty bands on the simulated background histograms only include statistical uncertainties. The uncertainty bars in the ratio plots represent combined statistical uncertainties of data and simulation.*

dilepton mass in the *low-*$m_{\ell\ell jj}$ CR. The agreement in this sideband is of great interest as the *low-*$m_{\ell\ell jj}$ CR resembles the signal region in describing the lepton kinematic characteristics without the constraint of the Z peak, since it is defined by the signal region selections, except for an inverted $m_{\ell\ell\mathrm{jj}} < 600$ GeV requirement.

As a further cross-check between data and simulation, the ratio between electron and muon distributions were studied. The efficiency to select muon events is higher, in part due to the trigger as well as the identification algorithm, but this overall difference should be approximately constant across $m_{\ell\ell\mathrm{jj}}$. This is confirmed by the two ratios for data and simulated events, shown in Figure 4.30. These ratios are compatible between data and the MC simulation as can be seen in Figure 4.31. Figure 4.32 shows the normalized cumulative distributions for electrons and muons in data and MC, and an overlay of the two flavour ratios is presented in Figure 4.33. The ratios of electrons and muons are thus consistent in data and MC with a flat distribution as a function of $m_{\ell\ell\mathrm{jj}}$.

Studies on high $m_{\ell\ell\mathrm{jj}}$ region

Basic quantities for leptons in the *low-*$m_{\ell\ell}$ CR with $m_{\ell\ell\mathrm{jj}} > 2.5$ TeV were checked in order to rule out a deficit of events at high dilepton mass as the one seen by the CMS Z' to muons analysis [84]. The kinematic variables for electrons and muons events with $m_{\ell\ell\mathrm{jj}}$ above 2.5 TeV are shown in Figures 4.34 and 4.35, respectively. The agreement between

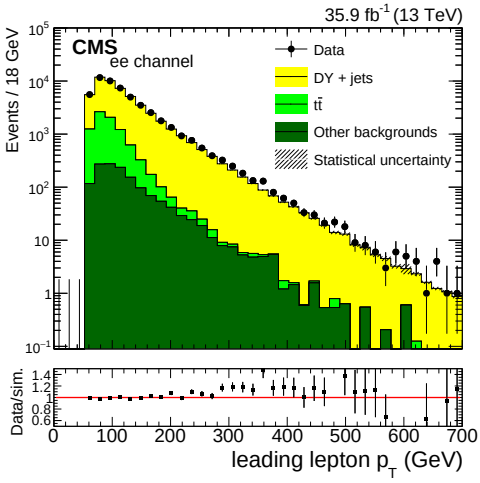

(a) *Electrons: leading lepton p_T*

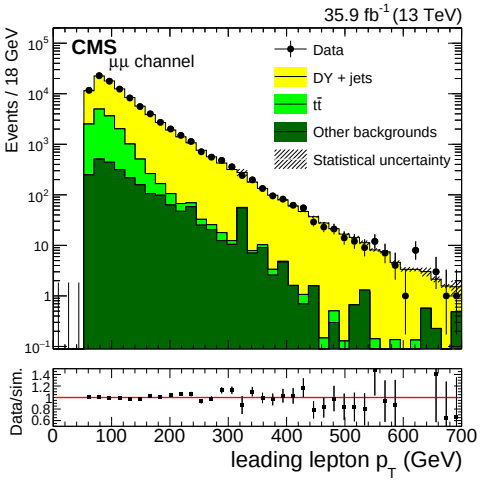

(b) *Muons: leading lepton p_T*

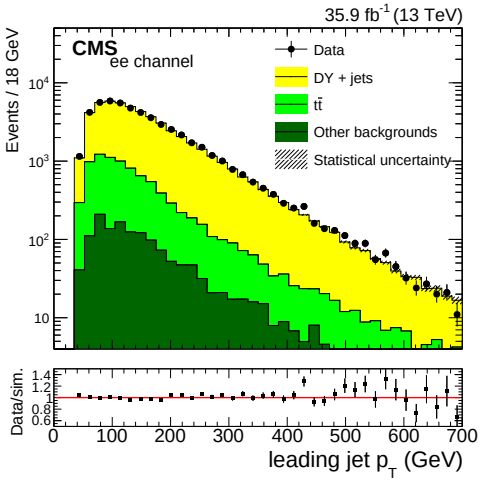

(c) *Electrons: leading jet p_T*

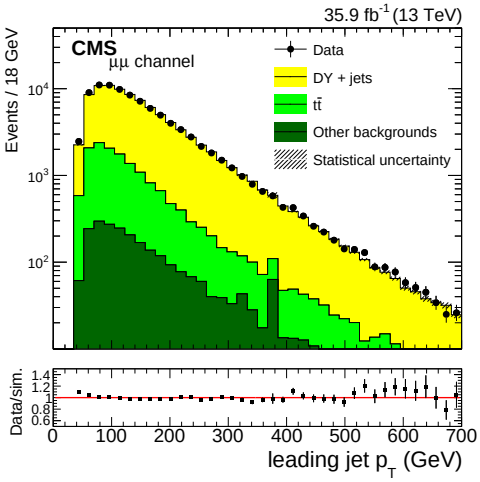

(d) *Muons: leading jet p_T*

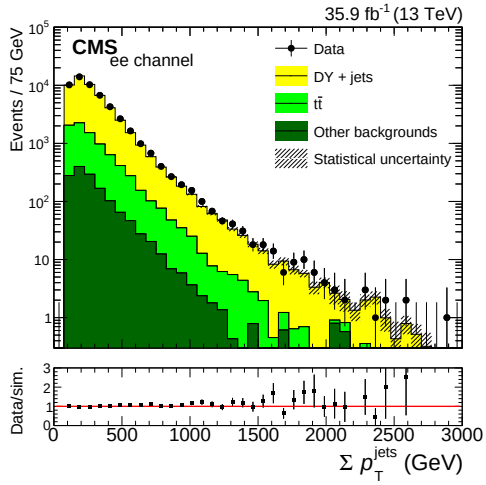

(e) *Electrons: sum p_T of jets*

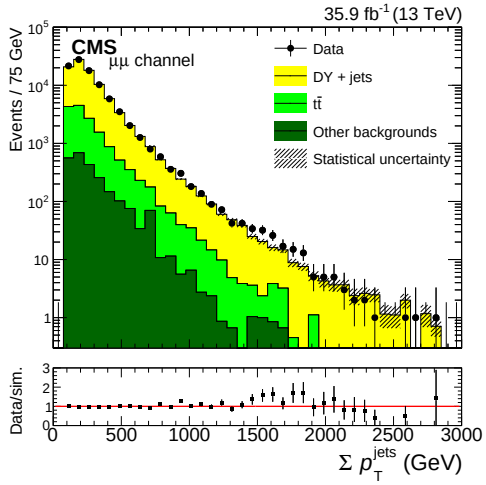

(f) *Muons: sum p_T of jets*

Figure 4.28: *Kinematic distributions for events in the* low-$m_{\ell\ell}$ *CR with the DY SF applied, for the electron channel on the left and for the muon channel on the right. The uncertainty bands on the simulated background histograms only include statistical uncertainties. The uncertainty bars in the ratio plots represent combined statistical uncertainties of data and simulation.*

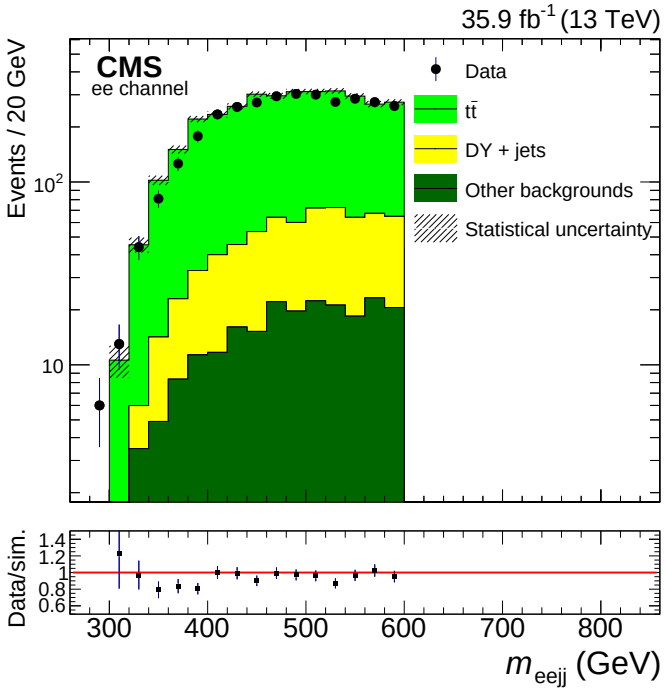

(a) Electron channel

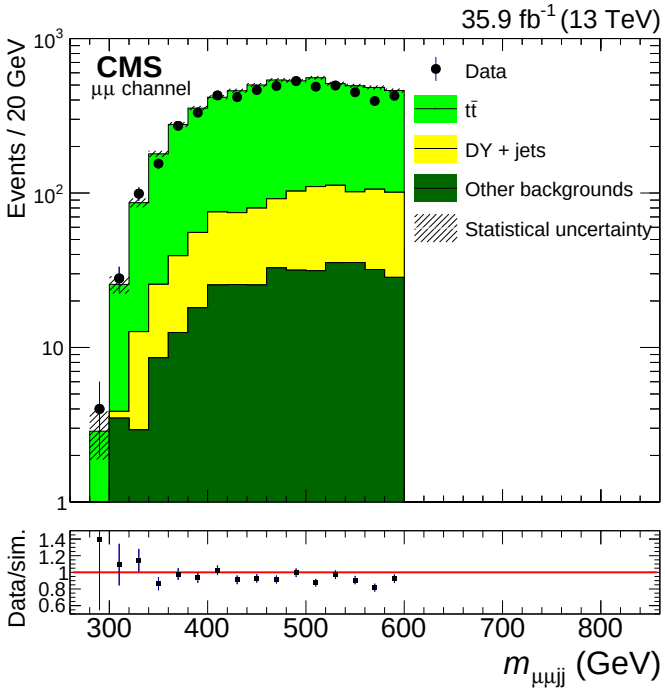

(b) Muon channel

Figure 4.29: *The $m_{\ell\ell jj}$ distribution for data and simulated events in the* low-$m_{\ell\ell jj}$ *CR with all SFs applied. The $t\bar{t}$ contribution is taken from the data-driven estimate as it is done in the signal region. The uncertainty bands on the simulated background histograms only include statistical uncertainties. The uncertainty bars in the ratio plots represent the combined statistical uncertainties of data and simulation.*

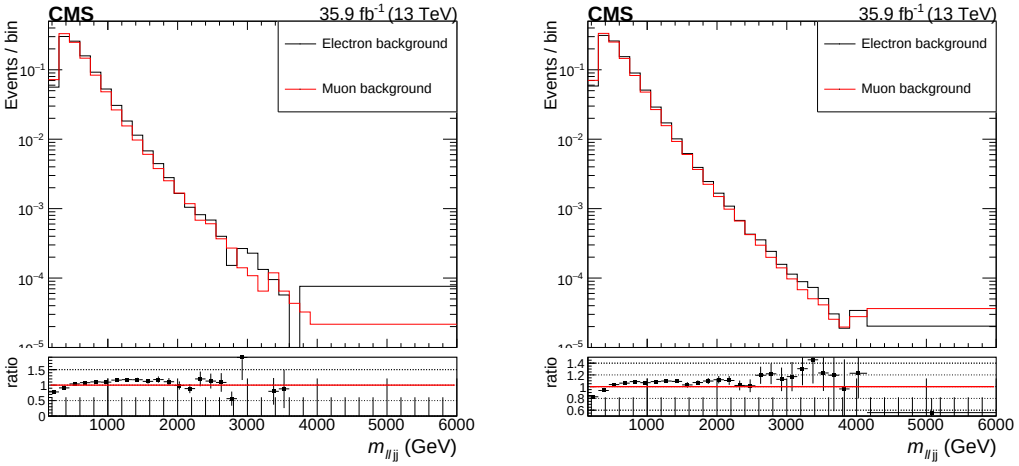

(a) *Data* (b) *MC simulation*

Figure 4.30: *The $m_{\ell\ell jj}$ distributions for electrons and muons and the ratio of electron events over muon events.*

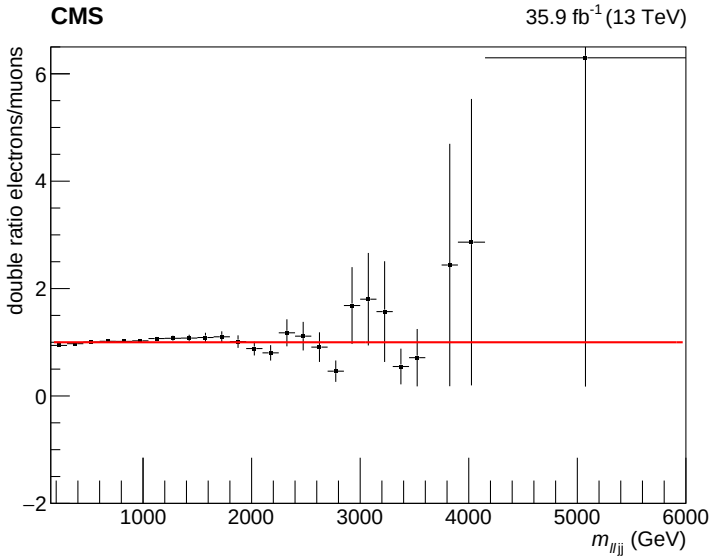

Figure 4.31: *Double ratio of data over MC simulation for electrons over muons in the $m_{\ell\ell jj}$ distribution.*

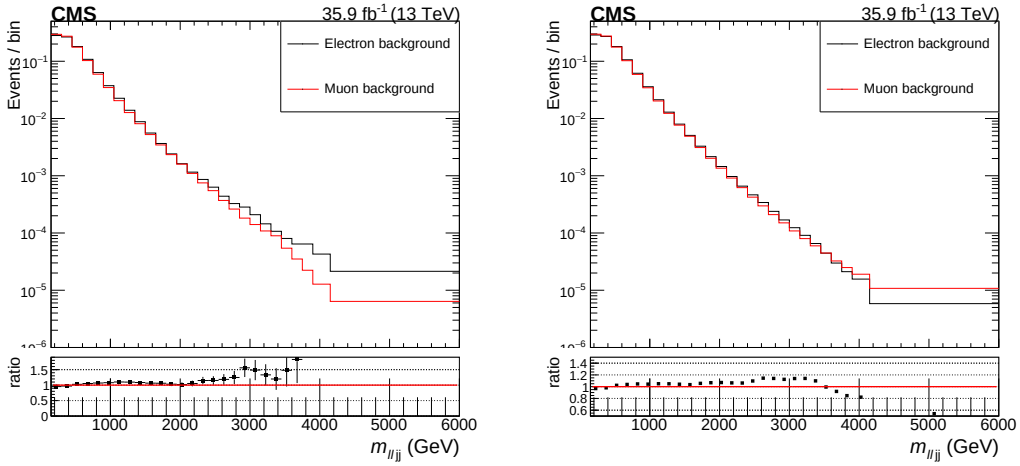

(a) *Data* (b) *MC simulation*

Figure 4.32: *The $m_{\ell\ell jj}$ cumulative distributions for electrons and muons and the ratio of electron events over muon events.*

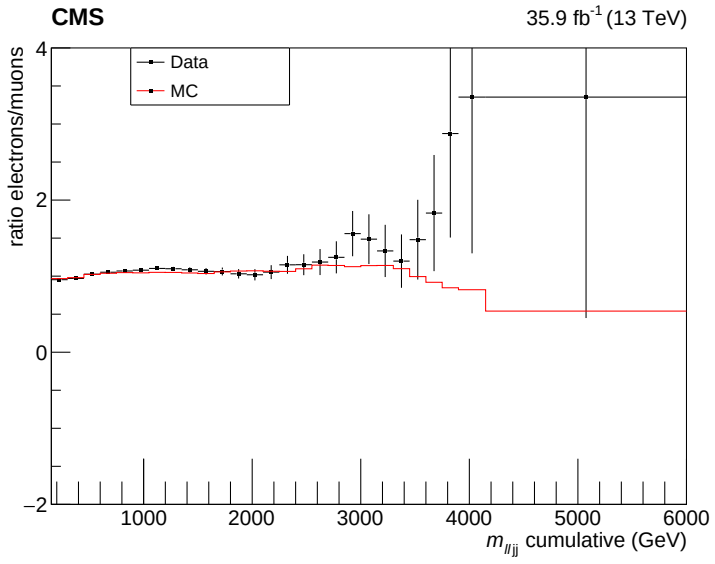

Figure 4.33: *Overlay of electron over muon ratios of cumulative $m_{\ell\ell jj}$ distributions for data and MC simulation.*

data and MC is reasonable given the low statistics, then the deficit of events seen by the Z' analysis is not confirmed by this analysis. This is due to the fact that this region does not represent the same exact kinematic space as the one studied by the Z' analysis. For muons events there is a deficit in the ϕ distribution, but this is not localized to any particular η region as can be seen in Figures 4.36 and 4.37.

4.7 Statistical analysis and systematic uncertainties

The strategy followed in this analysis is to search for deviations from the shape of the $m_{\ell\ell\mathrm{jj}}$ distribution expected in the standard model, that extends over a range of several TeV. While the LR symmetric models provide a motivation for the $\ell\ell$jj final state, we do not impose requirements on the signal shape specific to these scenarios, in order to maintain sensitivity to other models. The strategy to search for an excess of events in a wide mass range ("cut&count" approach) is effective in analyzing the data without making further assumptions about the characteristics of the benchmark signal model and, with respect to a "shape analysis", it reduces the effect of the uncertainties in the shapes of the backgrounds, especially in the high-$m_{\ell\ell\mathrm{jj}}$ region.

For each W_R mass hypothesis (m_{W_R}), the upper and lower limits of the mass window ($min < m_{\ell\ell\mathrm{jj}} < max$) are chosen as a function of m_{W_R} in order to obtain the most stringent expected cross section upper limits, calculated using the "standard" significance as was done in the previous iteration of the analysis [88]. Since the mass ranges are very wide and overlapping, additional studies, reported in Appendix C, were performed in order to estimate the ranges of mass windows by optimizing the signal Punzi significance [164]. No real improvement was observed, resulting in comparable mass windows, thus the 2015 approach was followed.
The boundaries of the windows are fitted as function of m_{W_R} with third degree polynomials to reduce the effect of statistical fluctuations in the optimization procedure. The fitted functions for the window edges are shown in Figure 4.38. The actual values for the upper and lower bounds are evaluated from the functions and rounded to the closest 10 GeV. These are shown in Table 4.12. The width of the mass window for the electron final state varies from 130 GeV at low masses ($m_{W_\mathrm{R}} \simeq 800$ GeV) to ≈ 3100 GeV at high masses ($m_{W_\mathrm{R}} \simeq 6000$ GeV). For muons, the mass window varies more, and becomes as large as ≈ 3800 GeV. The expected number of signal and background events is estimated by counting the events falling in a particular $m_{\ell\ell\mathrm{jj}}$ range.

The probability of observing a given number of events being produced by a combination of background and signal with a cross section σ is calculated using a Bayesian approach with a flat signal prior distribution and a fit model with nuisance parameters, introduced as log-normal prior distributions to address the systematic uncertainties.
Each limit for a specific m_{W_R} signal is calculated using the number of measured events (G) and predicted signal (S) and background (B) events in a specific $m_{\ell\ell\mathrm{jj}}$ window, together

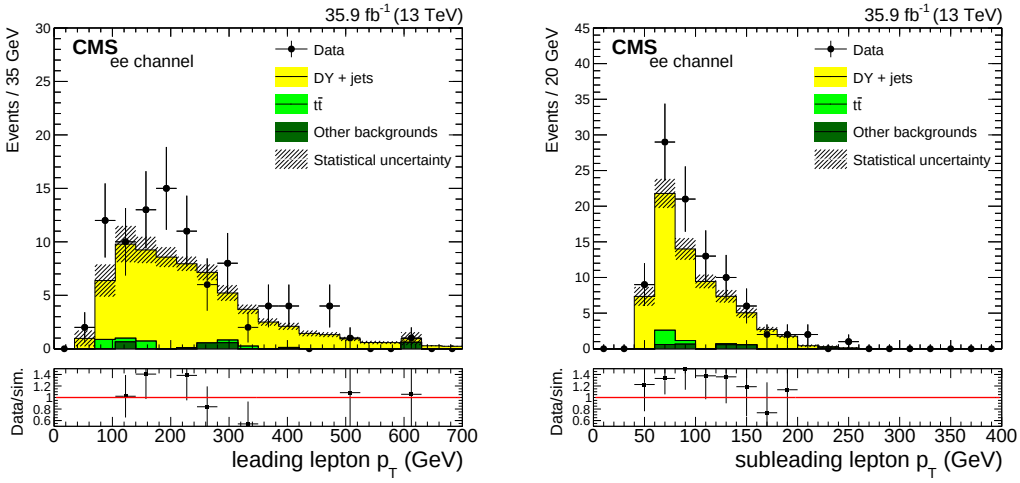

(a) *Leading lepton p_T*

(b) *Subleading lepton p_T*

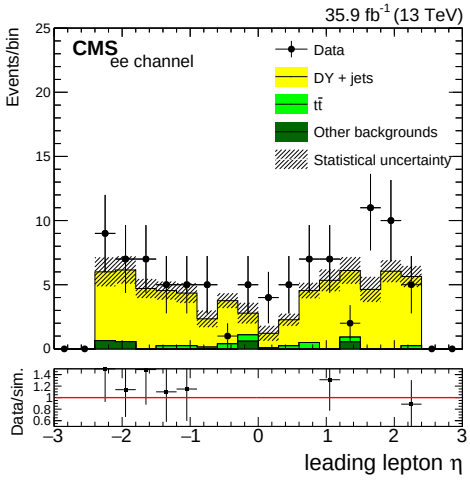

(c) *Leading lepton η*

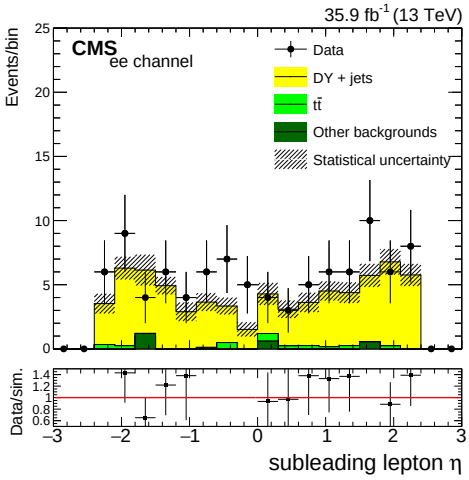

(d) *Subleading lepton η*

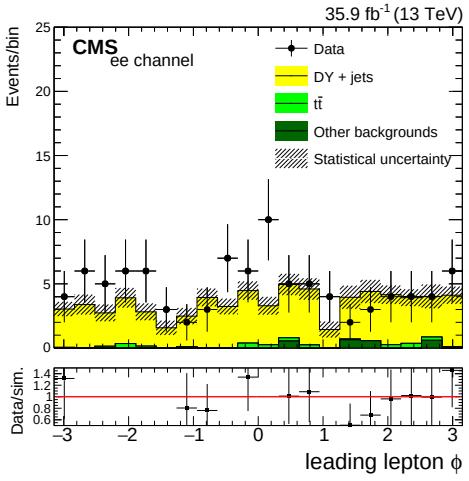

(e) *Leading lepton ϕ*

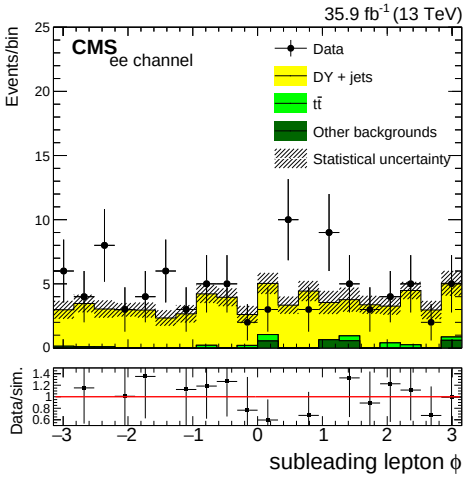

(f) *Subleading lepton ϕ*

Figure 4.34: *Comparison between data and simulation of different kinematic variables for electron events with $m_{\ell\ell jj} > 2.5$ TeV in the* low-$m_{\ell\ell}$ *CR.*

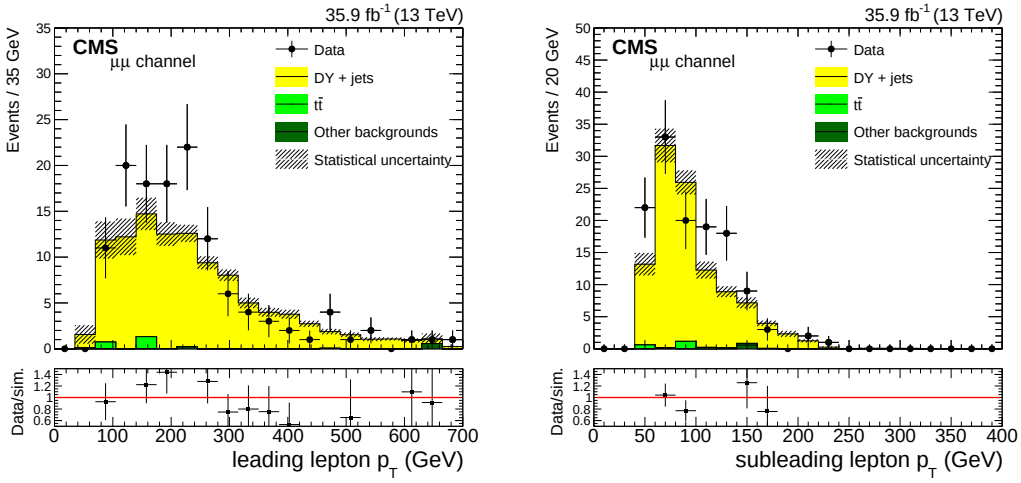

(a) *Leading lepton p_T*

(b) *Subleading lepton p_T*

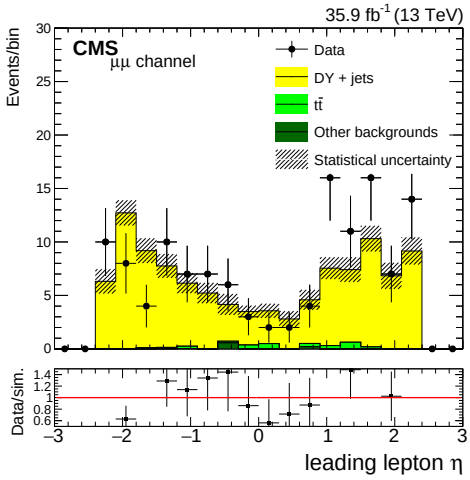

(c) *Leading lepton η*

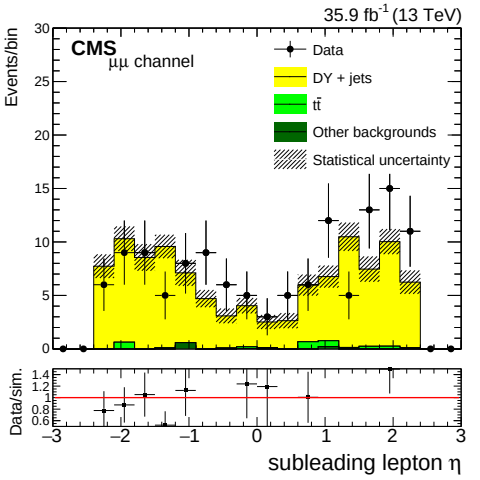

(d) *Subleading lepton η*

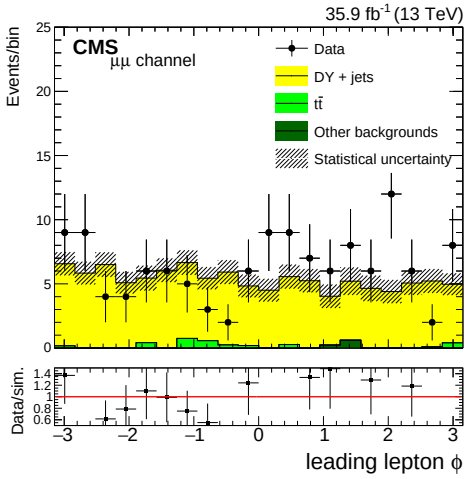

(e) *Leading lepton ϕ*

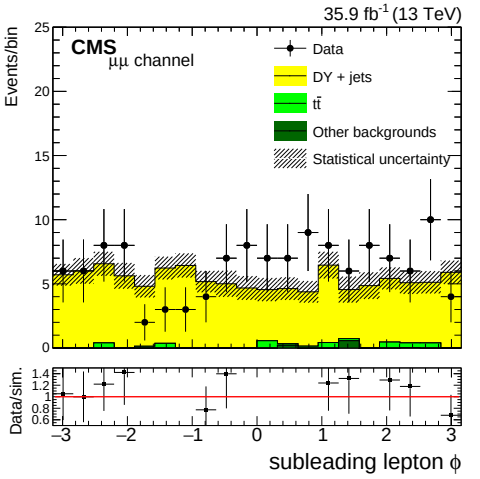

(f) *Subleading lepton ϕ*

Figure 4.35: *Comparison between data and simulation of different kinematic variables for muon events with $m_{\ell\ell jj} > 2.5$ TeV in the* low-$m_{\ell\ell}$ *CR.*

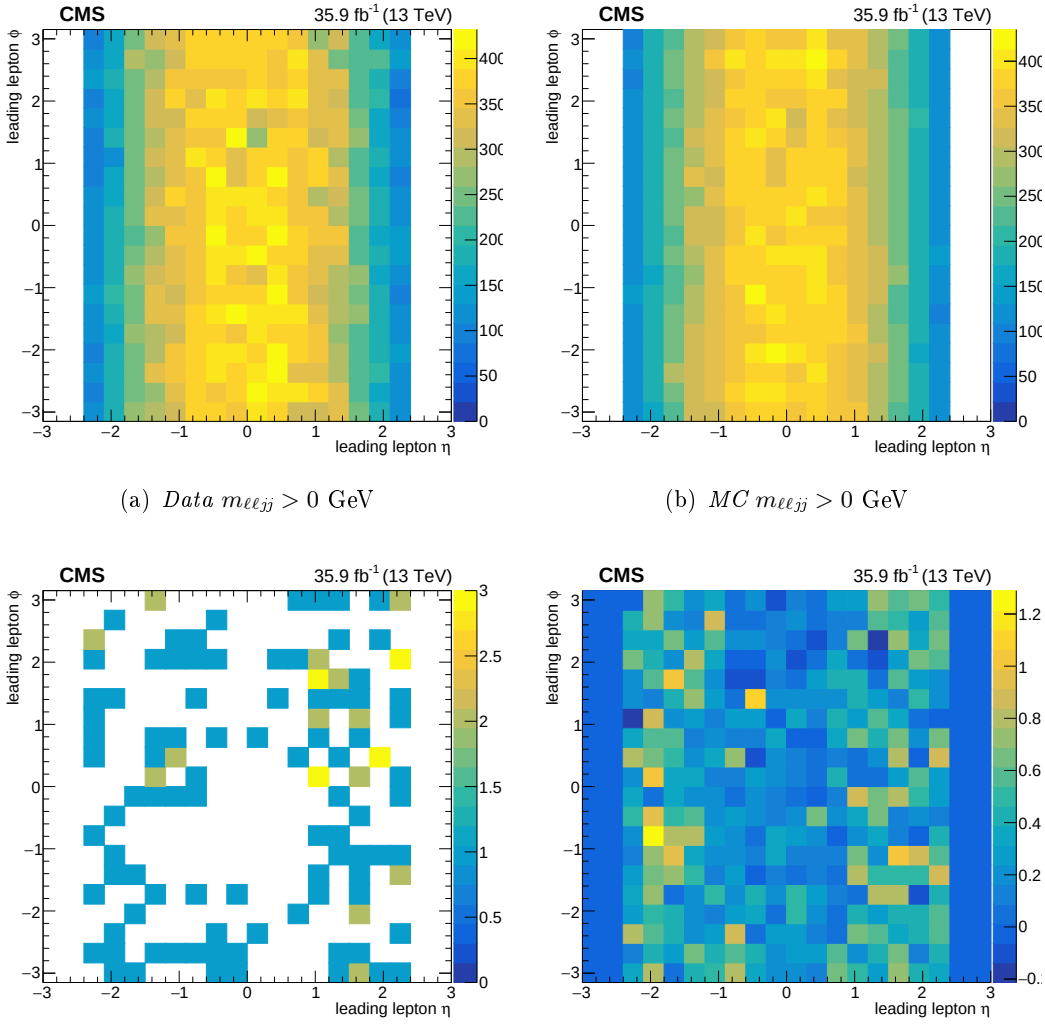

(a) *Data* $m_{\ell\ell jj} > 0$ GeV

(b) *MC* $m_{\ell\ell jj} > 0$ GeV

(c) *Data* $m_{\ell\ell jj} > 2500$ GeV

(d) *MC* $m_{\ell\ell jj} > 2500$ GeV

Figure 4.36: *2D distributions of leading muon* η *vs* ϕ *in events with* $m_{\ell\ell jj} > 2.5$ TeV *(bottom) and for all* $m_{\ell\ell jj}$ *(top) in the* low-$m_{\ell\ell}$ *CR.*

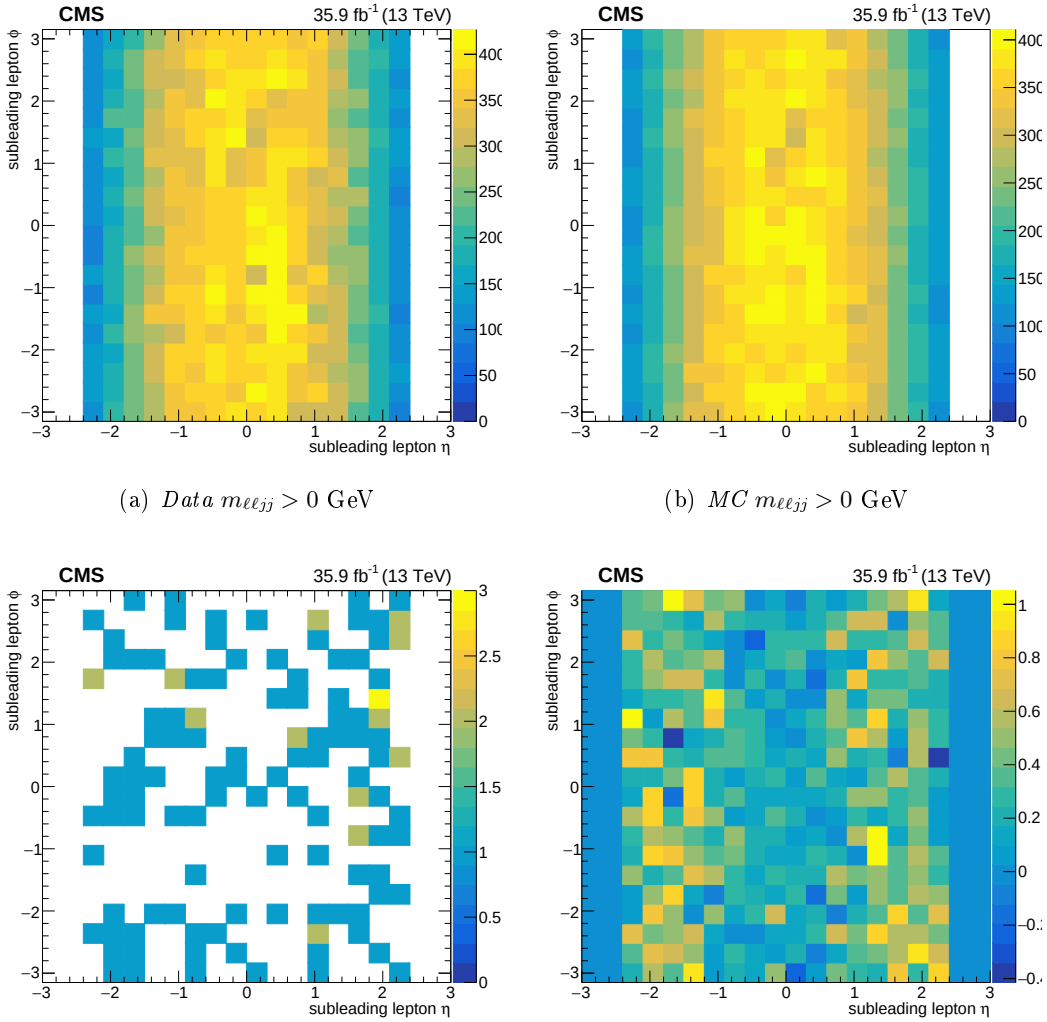

(a) *Data* $m_{\ell\ell jj} > 0$ GeV

(b) *MC* $m_{\ell\ell jj} > 0$ GeV

(c) *Data* $m_{\ell\ell jj} > 2500$ GeV

(d) *MC* $m_{\ell\ell jj} > 2500$ GeV

Figure 4.37: *2D distributions of subleading muon* η *vs* ϕ *in events with* $m_{\ell\ell jj} > 2.5$ TeV *(bottom) and for all* $m_{\ell\ell jj}$ *(top) in the* low-$m_{\ell\ell}$ *CR.*

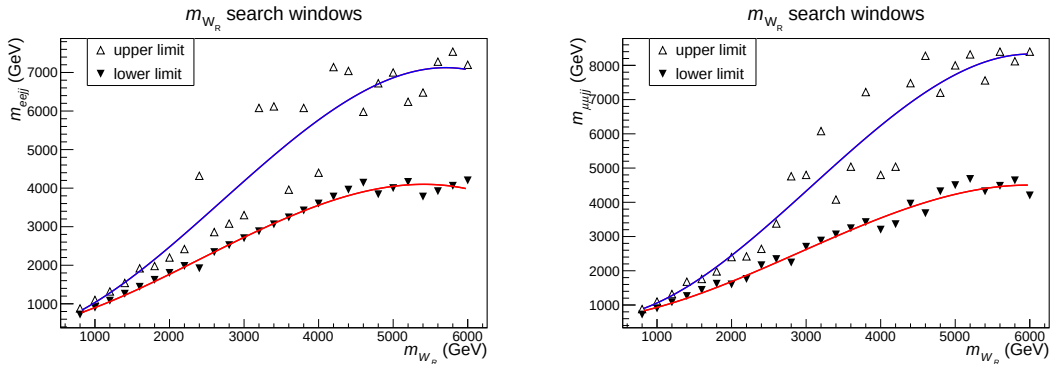

(a) $W_{\mathrm{R}} \to \mathrm{eejj}$ *windows* (b) $W_{\mathrm{R}} \to \mu\mu\mathrm{jj}$ *windows*

Figure 4.38: *Mass window edges optimized for cross section upper limits. Windows are smoothed out by fitting the upper and lower bounds with third degree polynomials, represented in blue and red, respectively.*

with their uncertainties δS and δB, described in Section 4.7.1. Expected limits were calculated at 95% CL using a Poisson model of the signal and background events,

$$Poisson(\mu, S(\theta), B(\theta)),$$

where μ is the dimensionless W_{R} signal strength, and θ represents the uncertainties δS and δB. Using Bayesian statistics, the probability distribution for μ given G measured events, $p(\mu|G)$, is obtained by evaluating the integral:

$$p(\mu|G) = \int p(\mu|\theta, G)\, p(\theta|G)\, d\theta,$$

where $p(\mu|\theta, G)$ is the probability distribution for μ given the uncertainties and the measurement G ("conditional posterior distributions"), and $p(\theta|G)$ is the probability distribution for the uncertainties given the measurement G ("marginal posterior distributions"). Functional forms of the conditional posterior distributions are derived from uniform prior distributions, while log-normal distributions are used for the functional forms of the marginal posterior distributions. The integrals of the conditional and marginal posterior distributions were evaluated numerically using MC methods to derive $p(\mu|G)$, generating many MC toys and computing the limit for each of them integrating $p(\mu|G)$ from $\mu = 0$ to $\mu = \mu_{max}$ such that the normalized integral equaled 0.95. The 95% CL upper limit on $\sigma(W_{\mathrm{R}}) \times BR(W_{\mathrm{R}} \to \ell\ell\mathrm{jj})$ is then defined as the value of $\sigma(W_{\mathrm{R}}) \times BR(W_{\mathrm{R}} \to \ell\ell\mathrm{jj})$ obtained from simulations multiplied by μ_{max}. This procedure is repeated for each mass hypothesis.

In order to take into account the statistical and systematic uncertainties, pseudo-experiments are performed varying the expected number of events from signal and background according to the uncertainties as described in the following Section. The median

of the distribution of the excluded cross section produced by pseudo-experiments and the intervals containing 68% and 95% of the pseudo-experiments are then quoted in the "expected" limits and their uncertainties.

Table 4.12: *Upper and lower limits of the mass windows that optimize the chance of discovery of a bump in the mass distribution for the electron and muon channels.*

m_{W_R} (GeV)	$m_{\ell\ell jj}$ window (GeV)	
	Electrons	Muons
800	720 - 860	720 - 880
1000	900 - 1030	930 - 1060
1200	1060 - 1280	1060 - 1280
1400	1220 - 1550	1200 - 1530
1600	1400 - 1850	1350 - 1810
1800	1580 - 2150	1510 - 2120
2000	1770 - 2470	1680 - 2450
2200	1960 - 2810	1860 - 2800
2400	2150 - 3150	2050 - 3170
2600	2340 - 3490	2240 - 3540
2800	2530 - 3840	2430 - 3930
3000	2720 - 4180	2620 - 4330
3200	2910 - 4520	2810 - 4720
3400	3080 - 4850	3000 - 5110
3600	3250 - 5170	3190 - 5500
3800	3410 - 5480	3370 - 5880
4000	3560 - 5770	3540 - 6240
4200	3690 - 6040	3700 - 6590
4400	3810 - 6290	3860 - 6910
4600	3910 - 6510	4000 - 7210
4800	3990 - 6700	4120 - 7490
5000	4050 - 6860	4230 - 7730
5200	4080 - 6990	4330 - 7930
5400	4100 - 7070	4400 - 8100
5600	4090 - 7120	4460 - 8220
5800	4050 - 7120	4490 - 8300
6000	3980 - 7070	4500 - 8330

4.7.1 Systematic uncertainties

There are two types of systematic uncertainties, one affecting the shape of the $m_{\ell\ell jj}$ distribution and one affecting the normalization of the $m_{\ell\ell jj}$ distribution, but since we use a "cut&count" approach all the uncertainties that affect the $m_{\ell\ell jj}$ shape also affect the number

of events in specific mass ranges and effectively become normalization uncertainties.
The systematic sources considered in this analysis are:

- Jet energy scale and resolution.
  The jet energy correction uncertainties, taken from the official recommendations [157] as described in Section 4.4.1, are provided as systematics sources that include correlations in p_T and η. Each of the corrections applied to data and simulation have certain systematic uncertainties, such as uncertainty in the initial and final state radiation corrections, the non-Gaussian tails of the energy measurements, and the pileup conditions. For the PF jets, JEC uncertainties $< 5\%$ are used, with an additional 2% uncertainty per rapidity unit. For the evaluation of the systematic errors due to jet resolutions effects, 10% uncertainties are used.

- Lepton energy scale and resolution.
  Electron scale and resolution uncertainties were taken from the official recommendations [158, 165], as described in Section 4.4.2. The residual differences between data and simulation in the electron energy scale are taken as systematic uncertainties. The uncertainties and correlations from the Gaussian fit used to smear the energy resolution in simulation to match the data are taken as systematic uncertainties.
  Muon scale and resolution uncertainties were taken from the official recommendations [99], as described is Section 4.4.3. For the small Rochester corrections, applied to data and simulation to correct for the remaining detector misalignment using the $Z \to \mu^+\mu^-$ events, the residual differences between the data and simulation are taken as the systematic uncertainty. For the muon momentum scale, uncertainties related to the corrections of the "generalized endpoint" method were also taken into account, as described in Section 4.4.3. For the muon resolution, an uncertainty of 1% in the barrel and of 2% in the endcaps is given by an additional smearing to the MC applied on the p_T of the single muon to account for the difference in resolution.

- Electron reconstruction, identification and trigger SF.
  SF and related uncertainties for electrons were discussed in Section 4.4.2. A *Tag-and-probe* procedure is used to measure the reconstruction and identification efficiency for electrons in $Z \to e^+e^-$ events. The uncertainties in the *Tag-and-probe* are taken as systematic uncertainties. For the high-p_T electrons, the prescriptions presented by the CMS Z' search [84] were followed for the trigger uncertainties, as described in Section 4.3.3.

- Muon identification, isolation and trigger SF.
  For muon identification and isolation, η dependent uncertainties were taken according to the official recipes, as described in Section 4.4.3. Uncertainties in muon reconstruction and identification are derived using a *Tag-and-probe* method in $Z \to \mu^+\mu^-$ events. One of the muons (the tag) is required to pass tight selection requirements,

while the second muon (the probe) has looser requirements. The uncertainty in the efficiency to reconstruct and identify these muons is taken as systematic. For the trigger uncertainties, the systematic uncertainties are taken from the official SFs, described in Section 4.3.3.

- $t\bar{t}$ background normalization.
  The uncertainty on the $t\bar{t}$ ee/eμ and $\mu\mu$/eμ extrapolation SFs is given by the sum in quadrature of the statistical and systematics uncertainties, evaluated as described in Section 4.6, of the transfer factors and affects only the normalization of $m_{\ell\ell \mathrm{jj}}$.
  An uncertainty on the DY+jets normalization scale factor is not considered, since it would be negligible with respect to the PDF, renormalization and factorization uncertainties used.

- PDF, factorization and renormalization factors.
  Two PDF sets, different for signal and DY+jets as described in Section 4.3, were used in simulated events to model the distribution of momenta amongst gluons, quarks, and their anti-quarks in the interacting protons. The coupling α_{QCD} was calculated at a renormalization energy scale μ_R in each simulated pp interaction, and a factorization energy scale μ_F was used to divide the QCD processes into two regions: a perturbative one, if the exchange momentum is $Q^2 \geq \mu_F^2$, and a not perturbative one, if the exchange momentum is $Q^2 \ll \mu_F^2$.
  To estimate the uncertainties on signal and DY+jets background coming from the choice of the PDF set used for the generation and the renormalization and factorization scales, each event was simulated different times varying the PDF or the renormalization and factorization scale weight. The relative yield variations after the re-weighting of the simulated samples events, implemented as a function of $m_{\ell\ell \mathrm{jj}}$ following the PDF4LHC prescription [166], were taken as systematic uncertainties. They affect both shape and normalization of $m_{\ell\ell \mathrm{jj}}$.

- Luminosity.
  The uncertainty on the integrated luminosity, estimated from data and officially provided [167], affects only the normalization of $m_{\ell\ell \mathrm{jj}}$.

In order to propagate the uncertainties in candidate reconstruction, affecting the shape of the $m_{\ell\ell \mathrm{jj}}$ distribution, a large number of pseudo-experiments was performed for each background process, varying all the uncertainty sources at the same time in an uncorrelated way, each of them according to a Gaussian distribution with mean equal to the nominal value of the single source and width equal to the uncertainty of the single source. For example, for the uncertainty related to the electron ID SF, the pseudo-experiments are sampled with Gaussian distributions where the mean is equal to 0.972 (0.983) and the width is equal to 0.006 (0.007) for electrons in the barrel (endcap). The variations were done before the event selection, so each pseudo-experiment was processed using the

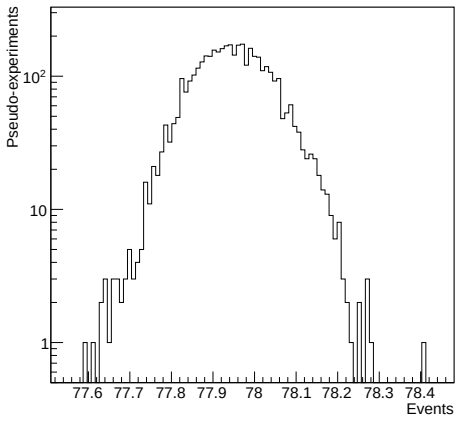

Figure 4.39: *The counted number of events for a* W_{R} *mass hypothesis of* 2 TeV *is shown for the signal sample after running* 5000 *pseudo-experiments.*

full analysis chain. The expected number of events for signal and background in a mass window was evaluated for each pseudo-experiment and its distribution drawn as shown in Figure 4.39, where the counted number of events for a W_{R} mass hypothesis of 2 TeV is shown for the signal sample after running 5000 pseudo-experiments. The values used to extract the limits are given for each search window by the mean (μ) of the integral of the WR mass distribution of the pseudo-experiments, and the standard deviation of the integral distribution is the propagated uncertainty (*syst.*). The uncertainties in candidate reconstruction are then implemented as nuisance parameters with log-normal priors ($lnN = 1 + syst./\mu$) in the limits evaluation. For example, for $m_{\ell\ell\mathrm{jj}} = 1000$ GeV in the electron channel, from the DY+jets toys we get $\mu = 120.708$ and $syst. = 19.539$ and from the $t\bar{t}$ toys we get $\mu = 340.936$ and $syst. = 29.439$, then the systematic uncertainties implemented in the limits evaluation correspond to $lnN = 1.1619$ for the DY+jets background and to $lnN = 1.0863$ for the $t\bar{t}$ background. The effects of these uncertainties on the signal and background yields are listed in Table 4.13.

The overall integrated luminosity, the uncertainty in the $t\bar{t}$ extrapolation SFs and the uncertainties in the estimation of the DY+jets background are also included in the evaluation of the limits as nuisance parameters with log-normal priors. For example, for the integrated luminosity we have $lnN = 1.025$. The range of values of these uncertainties are shown in Table 4.14. Concerning the uncertainties in the signal arising from the PDF and scale uncertainties, only the effect on the W_{R} signal acceptance is considered in the expected limit calculation.

In Table 4.15, the expected number of events (weighted in simulation), the statistical uncertainty and the propagated systematic uncertainty for the W_{R} signal, the DY+jets and $t\bar{t}$ background events, the other smaller backgrounds and the total of all the backgrounds

Table 4.13: *Effect of systematic uncertainties in candidate reconstruction efficiencies, energy scale and resolutions on the signal and background yields. The "Signal" column shows the range of uncertainties computed at each of the W_R mass points. The "Background" column indicates the range of the uncertainties for the backgrounds.*

Uncertainty	Signal (%)	Background (%)
Jet energy resolution	3.2–26	0.90–25
Jet energy scale	0.20–29	4.8–27
Electron energy resolution	3.7–4.8	2.7–4.5
Electron energy scale	3.7–6.4	4.9–5.9
Electron reco/trigger/ID	8.7–11	6.1–10
Muon energy resolution	4.7–10	6.9–12
Muon energy scale	4.7–10	6.2–12
Muon trigger/ID/iso	2.3–4.7	1.9–5.2

Table 4.14: *Values for uncertainties in $t\bar{t}$, DY+jets and luminosity. The uncertainties in the $t\bar{t}$ SFs affect the $t\bar{t}$ background, the uncertainties in the DY PDF and the DY factorization and renormalization scales affect the DY+jets background, and the uncertainty in the integrated luminosity affects both signal and backgrounds. In the table it is indicated if the uncertainty is statistical only or includes systematics.*

Uncertainty source	Magnitude (%)
$t\bar{t}$ extrapolation ee/eμ SF	17 (stat+syst)
$t\bar{t}$ extrapolation $\mu\mu$/eμ SF	20 (stat+syst)
DY ee PDF	15–70 (syst)
DY ee renormalization/factorization	5.0–40 (syst)
DY $\mu\mu$ PDF	10–70 (syst)
DY $\mu\mu$ renormalization/factorization	10–50 (syst)
Integrated luminosity	2.5 (stat+syst)

are reported, together with the observed number of events.
The values of the systematic uncertainties for a sample W_R mass point are also presented in Table 4.16 and Table 4.17.

Implementation of the uncertainties in the limit evaluation

To include the statistical uncertainties for each signal and background process in the evaluation of the limits, Gamma distributions, continuous version of the Poisson distribution with parameters N (≥ 0) and α (> 0), are used [168]. In the limit estimation, pseudo-experiments are generated based on the expected number of events, sampled according to a Gamma distribution and multiplied by the log-normal distributions of the systematics uncertainties. Given the two parameters of the Gamma distribution, N and α, the rate of each process (number of expected events in the signal region) is given by $N \cdot \alpha$. For the $t\bar{t}$ background estimated from data in a specific CR, the parameter N corresponds to the number of data events in this CR and α is the scale factor from the CR to the signal region. For the DY+jets and the others backgrounds estimated with simulation, the parameter N corresponds to the number of MC events passing the selections in the signal region and α is the overall scaling factor, equal to the integrated luminosity multiplied by the cross section of the process and divided by the number of total events of the process. For example, for $m_{\ell\ell jj} = 1000$ GeV in the electron channel, for the $t\bar{t}$ background we have $N = 810$ and $\alpha = 0.423$, while for the DY+jets background $N = 836$ and $\alpha = 0.14435$.
In the aMC@NLO DY+jets sample there are negative event weights at high $m_{\ell\ell jj}$, leading to a negative value for the N parameter. In this case, we set $N = 0$ and replace the rate of the process with a very small positive value (0.0001).

4.8 Results

The observed $m_{\ell\ell jj}$ distributions in the signal region including the expected backgrounds and the signal shape for $m_{W_R} = 4$ TeV are shown in Figure 4.40 for both the electron and the muon channel after the unblinding of the data. All the systematic uncertainties are estimated as a function of $m_{\ell\ell jj}$ and shown in the plot. No significant deviations are seen in the data with respect to expectation.

Expected and observed exclusion limits on the signal cross section at 95% CL are set as described in Section 4.7, using only the signal and background predictions for the expected upper limits, while for the observed ones also the data are used. They are shown in Figure 4.41 for both the electron and muon channel, taking into account all the systematic and statistical uncertainties described in Section 4.7.1. For the W_R model with $m_{N_R} = \frac{1}{2} m_{W_R}$, the observed lower limit at 95% CL on the mass of the right-handed W boson is 4.4 TeV for both channels, while the expected exclusion limit is 4.4 TeV for the electron channel and 4.5 TeV for the muon channel. The most significant excess, of $\approx 1.5\sigma$,

Table 4.15: *Number of expected events for signal, DY+jets, $t\bar{t}$, Other, and All backgrounds, as well as the observed number of events in the different W_R mass windows defined in Table 4.12. All uncertainties are included in the expected number of events.*

	Electron channel					
m_{W_R} (GeV)	Observed	Signal (mean ± stat ± syst)	Z/γ^* (mean ± stat ± syst)	Top quark (mean ± stat ± syst)	Other (mean ± stat ± syst)	All BG (mean ± stat ± syst)
800	1264	25849.4 ± 280.4 ± 2846.3	$260.64^{+17.17}_{-16.13} \pm 49.73$	$948.56^{+31.81}_{-30.79} \pm 111.92$	$105.51^{+11.3}_{-10.26} \pm 21.49$	$1314.71^{+37.87}_{-36.25} \pm 124.34$
1000	505	10264.3 ± 110.5 ± 1067.2	$120.71^{+12.05}_{-10.97} \pm 24.14$	$340.94^{+19.48}_{-18.46} \pm 38.11$	$44.47^{+7.74}_{-6.64} \pm 10.03$	$506.11^{+24.16}_{-22.48} \pm 46.22$
1200	383	6460.9 ± 59.1 ± 648.4	$104.26^{+11.24}_{-10.19} \pm 20.72$	$263.28^{+17.25}_{-16.22} \pm 32.16$	$40.51^{+7.42}_{-6.34} \pm 10.19$	$408.05^{+22.1}_{-20.18} \pm 39.59$
1400	286	3943.7 ± 32.6 ± 385.2	$92.09^{+10.63}_{-9.58} \pm 18.17$	$189.99^{+14.81}_{-13.77} \pm 23.82$	$38.91^{+7.29}_{-6.21} \pm 9.39$	$320.98^{+19.63}_{-17.89} \pm 31.40$
1600	174	2235.6 ± 18.0 ± 215.8	$54.55^{+8.43}_{-7.36} \pm 10.48$	$101.74^{+11.12}_{-10.07} \pm 12.77$	$23.50^{+5.92}_{-4.81} \pm 6.05$	$179.79^{+15.16}_{-13.37} \pm 17.59$
1800	129	1365.5 ± 10.5 ± 130.2	$42.73^{+7.39}_{-6.51} \pm 8.27$	$71.6^{+9.5}_{-8.4} \pm 8.5$	$11.54^{+4.49}_{-3.35} \pm 2.23$	$125.88^{+12.96}_{-11.17} \pm 12.07$
2000	84	796.4 ± 6.1 ± 75.0	$28.71^{+6.42}_{-5.33} \pm 5.71$	$40.51^{+7.42}_{-6.34} \pm 4.50$	$10.32^{+4.32}_{-3.16} \pm 2.42$	$79.55^{+10.72}_{-8.86} \pm 7.67$
2200	56	473.9 ± 3.7 ± 44.7	$15.72^{+5.05}_{-3.92} \pm 3.04$	$23.56^{+5.92}_{-4.82} \pm 2.84$	$9.06^{+4.12}_{-2.95} \pm 2.29$	$48.34^{+8.81}_{-6.88} \pm 4.75$
2400	36	238.4 ± 2.1 ± 22.8	$9.58^{+4.2}_{-3.04} \pm 1.88$	$12.53^{+4.63}_{-3.49} \pm 2.01$	$8.24^{+3.98}_{-2.81} \pm 2.15$	$30.34^{+7.42}_{-5.42} \pm 3.49$
2600	20	184.4 ± 1.4 ± 17.2	$7.07^{+3.78}_{-2.6} \pm 1.37$	$7.01^{+3.77}_{-2.58} \pm 1.11$	$6.20^{+3.62}_{-2.42} \pm 1.71$	$20.28^{+6.45}_{-4.39} \pm 2.45$
2800	15	114.1 ± 0.9 ± 10.6	$4.12^{+3.19}_{-1.95} \pm 0.79$	$5.82^{+3.55}_{-2.34} \pm 0.78$	$4.01^{+3.17}_{-1.92} \pm 0.83$	$13.95^{+5.73}_{-3.6} \pm 1.39$
3000	10	71.5 ± 0.6 ± 6.7	$2.20^{+2.70}_{-1.37} \pm 0.38$	$3.59^{+3.07}_{-1.81} \pm 0.45$	$2.67^{+2.83}_{-1.53} \pm 0.43$	$8.46^{+4.97}_{-2.73} \pm 0.73$
3200	7	45.7 ± 0.4 ± 4.3	$1.68^{+2.54}_{-1.16} \pm 0.28$	$1.77^{+2.57}_{-1.2} \pm 0.27$	$0.55^{+2.12}_{-0.52} \pm 0.26$	$4.01^{+4.19}_{-1.75} \pm 0.46$
3400	7	30.4 ± 0.2 ± 2.8	$1.41^{+2.45}_{-1.04} \pm 0.25$	$1.00^{+2.30}_{-0.83} \pm 0.23$	$0.39^{+2.04}_{-0.39} \pm 0.05$	$2.81^{+3.93}_{-1.39} \pm 0.34$
3600	3	19.2 ± 0.2 ± 1.8	$0.98^{+2.29}_{-0.81} \pm 0.18$	$0.42^{+2.06}_{-0.41} \pm 0.03$	$0.20^{+1.95}_{-0.20} \pm 0.02$	$1.60^{+3.65}_{-0.94} \pm 0.19$
3800	2	12.9 ± 0.1 ± 1.2	$0.95^{+2.28}_{-0.8} \pm 0.22$	$0.42^{+2.06}_{-0.41} \pm 0.03$	$0.0^{+1.84}_{-0.0} \pm 0.0$	$1.38^{+3.58}_{-0.9} \pm 0.23$
4000	2	8.9 ± 0.1 ± 0.8	$0.72^{+2.19}_{-0.65} \pm 0.16$	$0.0^{+1.8}_{-0.0} \pm 0.0$	$0.0^{+1.8}_{-0.0} \pm 0.0$	$0.72^{+3.40}_{-0.65} \pm 0.16$
4200	2	6.3 ± 0.1 ± 0.6	$0.62^{+2.15}_{-0.57} \pm 0.14$	$0.0^{+1.8}_{-0.0} \pm 0.0$	$0.0^{+1.8}_{-0.0} \pm 0.0$	$0.62^{+3.37}_{-0.57} \pm 0.14$
4400	1	4.20 ± 0.03 ± 0.37	$0.46^{+2.08}_{-0.45} \pm 0.12$	$0.0^{+1.8}_{-0.0} \pm 0.0$	$0.0^{+1.8}_{-0.0} \pm 0.0$	$0.46^{+3.33}_{-0.45} \pm 0.12$
4600	1	2.60 ± 0.02 ± 0.23	$0.34^{+2.02}_{-0.34} \pm 0.11$	$0.0^{+1.8}_{-0.0} \pm 0.0$	$0.0^{+1.8}_{-0.0} \pm 0.0$	$0.34^{+3.29}_{-0.34} \pm 0.11$
4800	1	2.00 ± 0.01 ± 0.19	$0.22^{+1.96}_{-0.22} \pm 0.07$	$0.0^{+1.8}_{-0.0} \pm 0.0$	$0.0^{+1.8}_{-0.0} \pm 0.0$	$0.22^{+3.26}_{-0.22} \pm 0.07$
5000	1	1.40 ± 0.01 ± 0.12	$0.17^{+1.94}_{-0.17} \pm 0.04$	$0.0^{+1.8}_{-0.0} \pm 0.0$	$0.0^{+1.8}_{-0.0} \pm 0.0$	$0.17^{+3.24}_{-0.17} \pm 0.04$
5200	1	0.90 ± 0.01 ± 0.08	$0.17^{+1.94}_{-0.17} \pm 0.04$	$0.0^{+1.8}_{-0.0} \pm 0.0$	$0.0^{+1.8}_{-0.0} \pm 0.0$	$0.17^{+3.24}_{-0.17} \pm 0.04$
5400	1	0.580 ± 0.004 ± 0.051	$0.15^{+1.92}_{-0.15} \pm 0.04$	$0.0^{+1.8}_{-0.0} \pm 0.0$	$0.0^{+1.8}_{-0.0} \pm 0.0$	$0.15^{+3.24}_{-0.15} \pm 0.04$
5600	1	0.450 ± 0.003 ± 0.039	$0.17^{+1.94}_{-0.17} \pm 0.04$	$0.0^{+1.8}_{-0.0} \pm 0.0$	$0.0^{+1.8}_{-0.0} \pm 0.0$	$0.17^{+3.24}_{-0.17} \pm 0.04$
5800	1	0.300 ± 0.002 ± 0.027	$0.17^{+1.94}_{-0.17} \pm 0.04$	$0.0^{+1.8}_{-0.0} \pm 0.0$	$0.0^{+1.8}_{-0.0} \pm 0.0$	$0.17^{+3.24}_{-0.17} \pm 0.04$
6000	1	0.210 ± 0.001 ± 0.019	$0.22^{+1.96}_{-0.22} \pm 0.07$	$0.0^{+1.8}_{-0.0} \pm 0.0$	$0.0^{+1.8}_{-0.0} \pm 0.0$	$0.22^{+3.26}_{-0.22} \pm 0.07$
	Muon channel					
m_{W_R} (GeV)	Observed	Signal (mean ± stat ± syst)	Z/γ^* (mean ± stat ± syst)	Top quark (mean ± stat ± syst)	Other (mean ± stat ± syst)	All BG (mean ± stat ± syst)
800	2064	38953.8 ± 356.9 ± 2234.0	$412.56^{+21.33}_{-20.3} \pm 45.10$	$1614.56^{+41.19}_{-40.18} \pm 277.85$	$156.09^{+13.52}_{-12.48} \pm 12.14$	$2183.21^{+48.32}_{-46.72} \pm 281.75$
1000	921	16470.6 ± 146.2 ± 1249.8	$216.47^{+15.74}_{-14.7} \pm 25.16$	$580.32^{+25.1}_{-24.08} \pm 97.44$	$86.03^{+10.31}_{-29.7} \pm 6.95$	$882.82^{+31.37}_{-29.7} \pm 100.87$
1200	626	9205.2 ± 73.5 ± 539.3	$165.47^{+13.89}_{-12.85} \pm 18.07$	$448.14^{+22.19}_{-21.16} \pm 78.41$	$66.52^{+9.2}_{-8.14} \pm 8.06$	$680.13^{+27.74}_{-26.06} \pm 80.87$
1400	465	5486.6 ± 40.0 ± 308.0	$132.31^{+12.53}_{-11.49} \pm 16.25$	$323.38^{+19.0}_{-17.97} \pm 57.32$	$46.37^{+7.86}_{-6.79} \pm 5.40$	$502.06^{+23.18}_{-22.38} \pm 59.83$
1600	310	3347.6 ± 23.0 ± 194.6	$100.23^{+11.04}_{-9.99} \pm 11.22$	$173.17^{+14.18}_{-13.15} \pm 30.71$	$34.0^{+6.9}_{-5.8} \pm 3.1$	$307.39^{+19.25}_{-17.5} \pm 32.84$
1800	207	2062.8 ± 13.4 ± 116.6	$79.45^{+9.95}_{-8.9} \pm 10.45$	$121.88^{+12.07}_{-11.02} \pm 21.04$	$25.88^{+6.15}_{-5.05} \pm 2.27$	$227.21^{+16.81}_{-15.04} \pm 23.60$
2000	140	1274.3 ± 8.0 ± 71.3	$55.04^{+8.46}_{-7.4} \pm 7.35$	$68.95^{+9.34}_{-8.28} \pm 11.55$	$19.55^{+5.5}_{-4.38} \pm 1.92$	$143.55^{+13.75}_{-11.94} \pm 13.83$
2200	74	743.8 ± 4.7 ± 47.5	$35.04^{+6.98}_{-5.89} \pm 4.82$	$40.10^{+7.39}_{-6.31} \pm 6.98$	$11.98^{+4.36}_{-3.41} \pm 1.30$	$87.12^{+11.13}_{-9.28} \pm 8.58$
2400	36	447.2 ± 2.9 ± 32.3	$20.20^{+5.57}_{-4.46} \pm 3.18$	$21.33^{+5.69}_{-4.58} \pm 4.34$	$7.55^{+3.87}_{-2.69} \pm 0.67$	$49.08^{+8.85}_{-6.93} \pm 5.42$
2600	26	290.4 ± 1.8 ± 19.9	$13.19^{+4.72}_{-3.59} \pm 2.04$	$11.92^{+4.55}_{-3.4} \pm 2.41$	$4.48^{+3.27}_{-2.04} \pm 0.86$	$29.59^{+7.33}_{-5.35} \pm 3.27$
2800	18	177.0 ± 1.1 ± 13.1	$8.34^{+4.0}_{-2.83} \pm 1.28$	$9.91^{+4.25}_{-3.09} \pm 1.82$	$2.66^{+2.83}_{-1.53} \pm 0.30$	$20.91^{+6.49}_{-4.46} \pm 2.24$
3000	12	110.1 ± 0.7 ± 9.2	$5.53^{+3.49}_{-2.28} \pm 0.81$	$6.12^{+3.61}_{-2.4} \pm 1.09$	$1.74^{+2.56}_{-1.19} \pm 0.15$	$13.39^{+5.63}_{-3.52} \pm 1.36$
3200	7	69.0 ± 0.5 ± 6.2	$3.76^{+3.11}_{-1.85} \pm 0.66$	$3.02^{+2.92}_{-1.64} \pm 0.59$	$1.20^{+2.37}_{-0.94} \pm 0.28$	$7.97^{+4.88}_{-2.64} \pm 0.93$
3400	6	43.1 ± 0.3 ± 4.3	$2.39^{+2.75}_{-1.44} \pm 0.47$	$1.71^{+2.55}_{-1.17} \pm 0.45$	$0.23^{+1.96}_{-0.23} \pm 0.06$	$4.33^{+4.23}_{-1.87} \pm 0.65$
3600	4	29.2 ± 0.2 ± 2.8	$1.63^{+2.52}_{-1.14} \pm 0.46$	$0.72^{+2.19}_{-0.65} \pm 0.10$	$0.21^{+1.96}_{-0.21} \pm 0.01$	$2.56^{+3.87}_{-1.33} \pm 0.47$
3800	4	18.6 ± 0.1 ± 1.8	$1.08^{+2.33}_{-0.87} \pm 0.21$	$0.72^{+2.19}_{-0.65} \pm 0.10$	$0.21^{+1.96}_{-0.21} \pm 0.01$	$2.01^{+3.75}_{-1.11} \pm 0.24$
4000	4	12.3 ± 0.1 ± 1.2	$0.76^{+2.20}_{-0.67} \pm 0.16$	$0.0^{+1.8}_{-0.0} \pm 0.0$	$0.21^{+1.96}_{-0.21} \pm 0.01$	$0.97^{+3.47}_{-0.71} \pm 0.16$
4200	3	8.1 ± 0.1 ± 0.8	$0.43^{+2.06}_{-0.42} \pm 0.17$	$0.0^{+1.8}_{-0.0} \pm 0.0$	$0.19^{+1.93}_{-0.19} \pm 0.07$	$0.61^{+3.38}_{-0.46} \pm 0.18$
4400	2	5.37 ± 0.04 ± 0.51	$0.18^{+1.94}_{-0.18} \pm 0.10$	$0.0^{+1.8}_{-0.0} \pm 0.0$	$0.04^{+1.86}_{-0.04} \pm 0.08$	$0.22^{+3.26}_{-0.18} \pm 0.13$
4600	2	3.63 ± 0.02 ± 0.33	$-0.03^{+1.82}_{-0.03} \pm 0.07$	$0.0^{+1.8}_{-0.0} \pm 0.0$	$0.0^{+1.8}_{-0.0} \pm 0.01$	$-0.03^{+3.18}_{-0.03} \pm 0.07$
4800	2	2.53 ± 0.02 ± 0.20	$-0.03^{+1.82}_{-0.03} \pm 0.07$	$0.0^{+1.8}_{-0.0} \pm 0.0$	$0.0^{+1.8}_{-0.0} \pm 0.0$	$-0.03^{+3.18}_{-0.03} \pm 0.07$
5000	2	1.74 ± 0.01 ± 0.12	$-0.04^{+1.82}_{-0.04} \pm 0.15$	$0.0^{+1.8}_{-0.0} \pm 0.0$	$0.0^{+1.8}_{-0.0} \pm 0.0$	$-0.04^{+3.18}_{-0.04} \pm 0.15$
5200	2	1.18 ± 0.01 ± 0.08	$-0.05^{+1.81}_{-0.05} \pm 0.09$	$0.0^{+1.8}_{-0.0} \pm 0.0$	$0.0^{+1.8}_{-0.0} \pm 0.0$	$-0.05^{+3.17}_{-0.05} \pm 0.09$
5400	2	0.80 ± 0.01 ± 0.05	$-0.07^{+1.80}_{-0.07} \pm 0.07$	$0.0^{+1.8}_{-0.0} \pm 0.0$	$0.0^{+1.8}_{-0.0} \pm 0.0$	$-0.07^{+3.17}_{-0.07} \pm 0.07$
5600	2	0.550 ± 0.003 ± 0.030	$-0.06^{+1.81}_{-0.06} \pm 0.07$	$0.0^{+1.8}_{-0.0} \pm 0.0$	$0.0^{+1.8}_{-0.0} \pm 0.0$	$-0.06^{+3.17}_{-0.06} \pm 0.07$
5800	2	0.380 ± 0.002 ± 0.019	$-0.06^{+1.81}_{-0.06} \pm 0.07$	$0.0^{+1.8}_{-0.0} \pm 0.0$	$0.0^{+1.8}_{-0.0} \pm 0.0$	$-0.06^{+3.17}_{-0.06} \pm 0.07$
6000	2	0.260 ± 0.002 ± 0.012	$-0.05^{+1.81}_{-0.05} \pm 0.09$	$0.0^{+1.8}_{-0.0} \pm 0.0$	$0.0^{+1.8}_{-0.0} \pm 0.0$	$-0.05^{+3.17}_{-0.05} \pm 0.09$

Table 4.16: *Systematic uncertainties for signal and background in the electron channel for* $m_{W_R} = 2200$ GeV.

Uncertainty	Signal (%)	Background (%)
Jet energy resolution	3.29	6.34
Jet energy scale	0.66	25.57
Electron energy resolution	4.39	4.32
Electron energy scale	4.1	5.4
Electron reco/trigger/ID	9.38	6.62
$t\bar{t}$ extrapolation SF	-	17
DY PDF	-	15.6
DY renormalization/factorization	-	7.0
Integrated luminosity	2.5	2.5

Table 4.17: *Systematic uncertainties for signal and background in the muon channel for* $m_{W_R} = 2200$ GeV.

Uncertainty	Signal (%)	Background (%)
Jet energy resolution	3.29	1.42
Jet energy scale	0.66	26.24
Muon energy resolution	5.16	9.27
Muon energy scale	5.27	7.17
Muon trigger/ID/iso	2.71	4.27
$t\bar{t}$ extrapolation SF	-	20
DY PDF	-	11.5
DY renormalization/factorization	-	10.5
Integrated luminosity	2.5	2.5

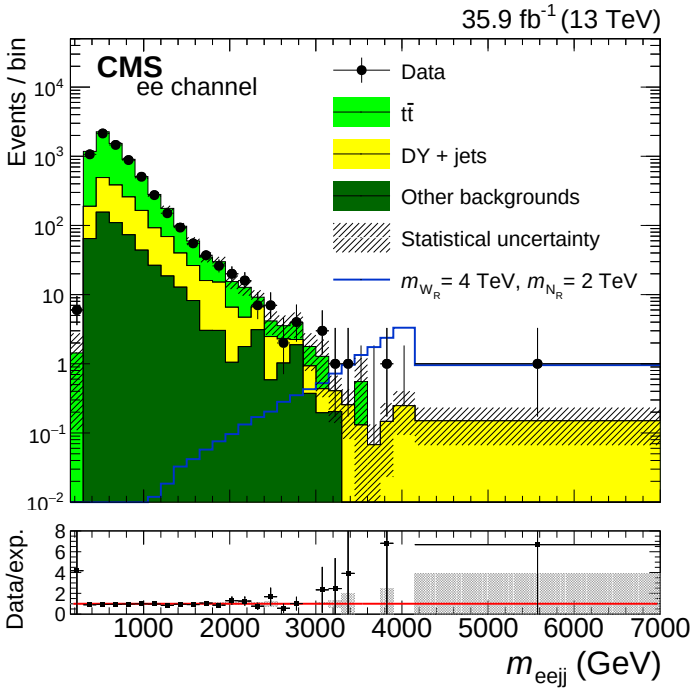

(a) *Electron channel*

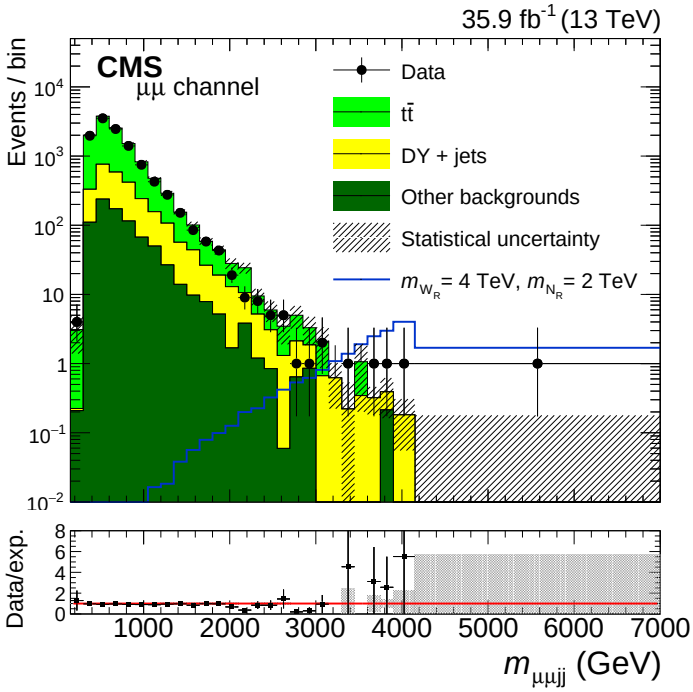

(b) *Muon channel*

Figure 4.40: *The $m_{\ell\ell jj}$ distribution in the signal region. The uncertainty bands on the simulated background histograms only include statistical uncertainties. The uncertainty bars in the ratio plots represent the combined statistical uncertainties of data and simulation. The gray error band around unity represents instead the systematic uncertainty of the simulation.*

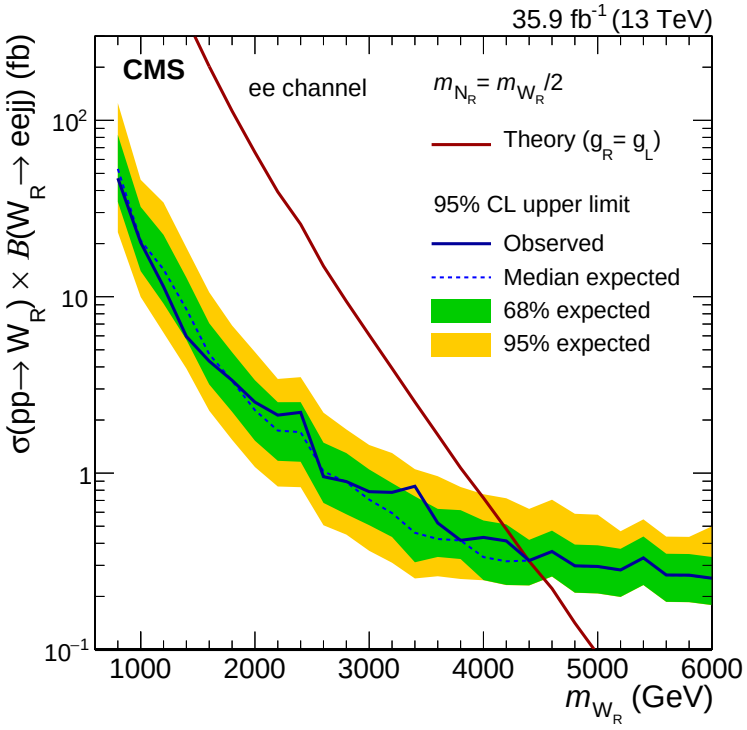

(a) *Electron channel*

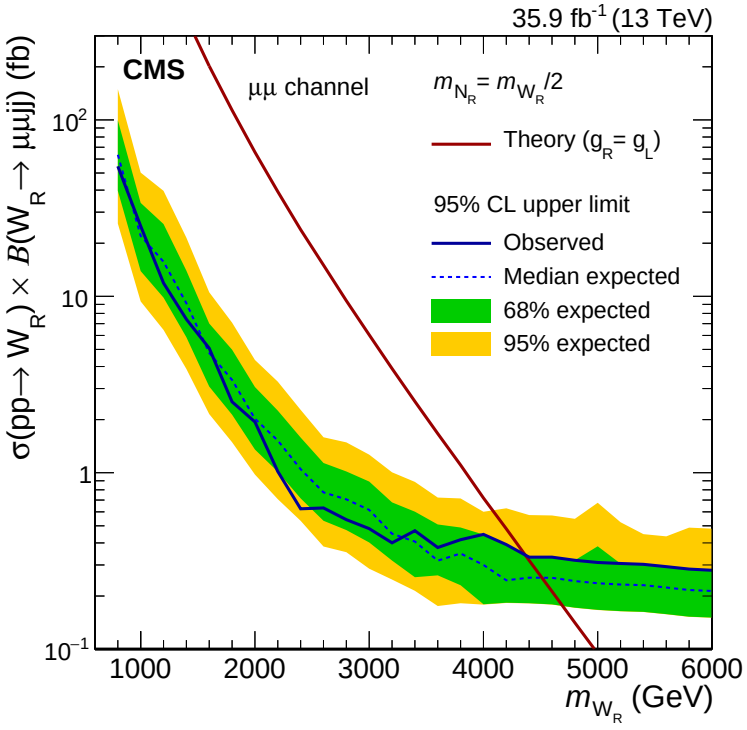

(b) *Muon channel*

Figure 4.41: *Expected and observed 95% CL upper limits on the product of* $\sigma(pp \to W_{\mathrm{R}})$ *and branching fraction* $B(W_{\mathrm{R}} \to \ell\ell jj)$. *The inner (green) band and the outer (yellow) band indicate, respectively, the expected 68% and 95% CL exclusion regions.*

is observed at $m_{\ell\ell jj} \simeq 3.4$ TeV in the electron channel. The lower edge of the 95% CL band disappears at high masses because of the small number of events in that region.

To extend these expected exclusion limits to a two-dimensional (m_{W_R}, m_{N_R}) mass plane covering a large range of neutrino masses below the W_R boson mass, the following procedure is used.
The cross section limit at a fixed W_R mass is calculated for $m_{N_R} = \frac{1}{2} m_{W_R}$ using fully reconstructed events. GEN-only W_R samples, produced as discussed in Section 4.3.2.1, are independently generated at the same fixed W_R mass, with 800 GeV $< m_{W_R} <$ 6000 GeV in steps of 100 GeV, for 100 GeV $< m_{N_R} < m_{W_R}$ in steps of 100 GeV, including $m_{N_R} = \frac{1}{2} m_{W_R}$. For each sample with $m_{N_R} \neq \frac{1}{2} m_{W_R}$ the cross section is calculated with PYTHIA. The full offline signal region selection (including the mass window selection) presented in Section 4.5 is applied to these W_R events at the generator level in order to get the GEN offline selection efficiencies shown in Figure 4.42, representing the fraction of events passing all the signal selections at each mass point. These efficiencies are used to calculate the ratio r of the kinematic offline selections efficiencies between the $m_{N_R} = \frac{1}{2} m_{W_R}$ sample and the samples with $m_{N_R} \neq \frac{1}{2} m_{W_R}$:

$$r = \frac{\text{eff}(m_{W_R}, m_{N_R})}{\text{eff}(m_{W_R}, m_{W_R}/2)}. \tag{4.1}$$

This m_{W_R}- and m_{N_R}-dependent factor, that accounts for the change in the W_R acceptance and efficiency as m_{N_R} changes for a fixed m_{W_R}, is applied to the cross section limit obtained for $m_{N_R} = \frac{1}{2} m_{W_R}$ to rescale it to the other m_{N_R} hypotheses for one specific m_{W_R}. This can be done because the cross section limit for a specific m_{N_R} is linearly proportional to the signal selection efficiency at that m_{N_R} multiplied by the W_R cross section. At a given m_{W_R}, since the background prediction is the same for all m_{N_R}, the cross section limit for a certain m_{N_R} is then related to the limit for $m_{N_R} = \frac{1}{2} m_{W_R}$ by the ratio of their signal efficiencies. The limit obtained for a particular m_{N_R} is then compared to the cross section calculated for that m_{N_R}.
This process is repeated for all W_R mass values to create the expected exclusion limits for neutrino mass hypotheses different from $\frac{1}{2} m_{W_R}$ presented in Figure 4.43, for both the electron and the muon channel.
The official fully reconstructed W_R signal samples only have W_R masses which are integer multiples of 200 GeV. The cross section limit for W_R masses which are non-integer multiples of 200 GeV are then obtained using linear interpolation between the two nearest, fully reconstructed W_R mass points.
The limits for $m_{W_R} = 2400$ GeV, 4600 GeV and 5400 GeV in the electron channel are calculated using privately generated, fully reconstructed W_R signal events.
For the efficiency scaling factor, GEN particles can be used in place of reconstructed objects because, as shown in Figure 4.44, taken from the 2015 iteration of the search [88], the scaling factors obtained using generator level events are consistent with the scaling

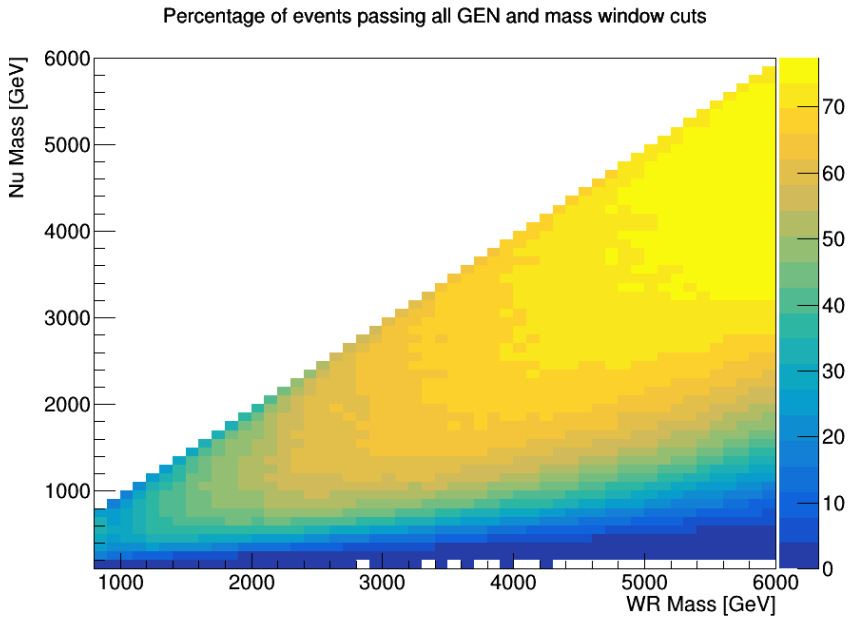

(a) *Electron channel*

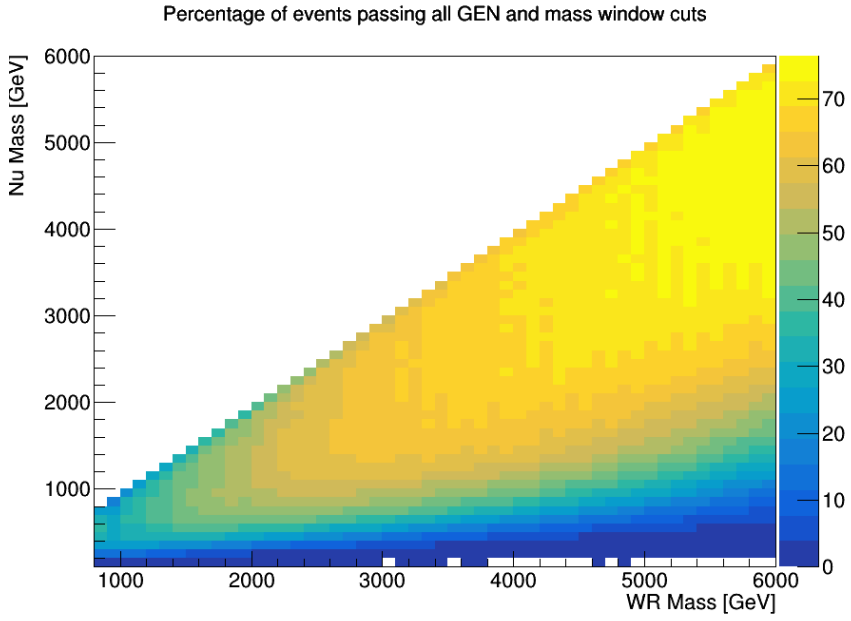

(b) *Muon channel*

Figure 4.42: *GEN efficiencies showing the GEN W_{R} events passing all the signal region selections, including the mass window selection, as a function of $m_{W_{\mathrm{R}}}$ and $m_{N_{\mathrm{R}}}$.*

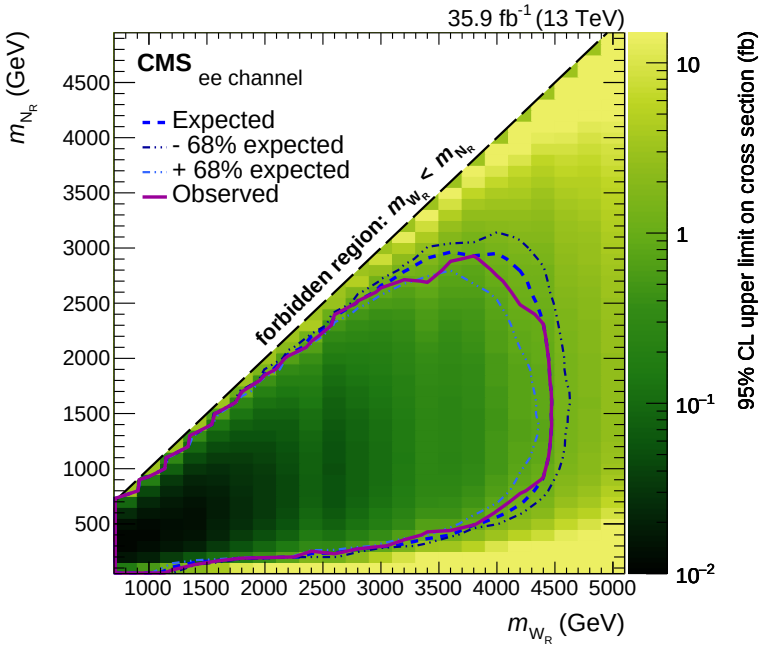

(a) *Electron channel*

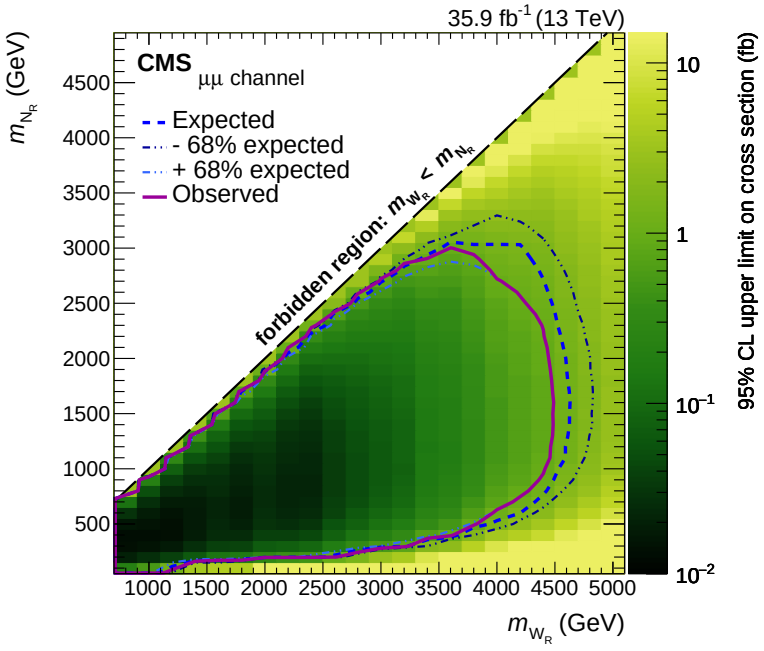

(b) *Muon channel*

Figure 4.43: *Upper limit on the cross section for different* W_{R} *and* N_{R} *mass hypotheses. The expected and observed exclusions are shown as the dotted (blue) curve and the solid (magenta) curve, respectively. The thin dotted (blue) curves indicate the region in the* $(m_{W_{\mathrm{R}}}, m_{N_{\mathrm{R}}})$ *parameter space that is expected to be excluded at 68% CL in the case that no signal is present in the data.*

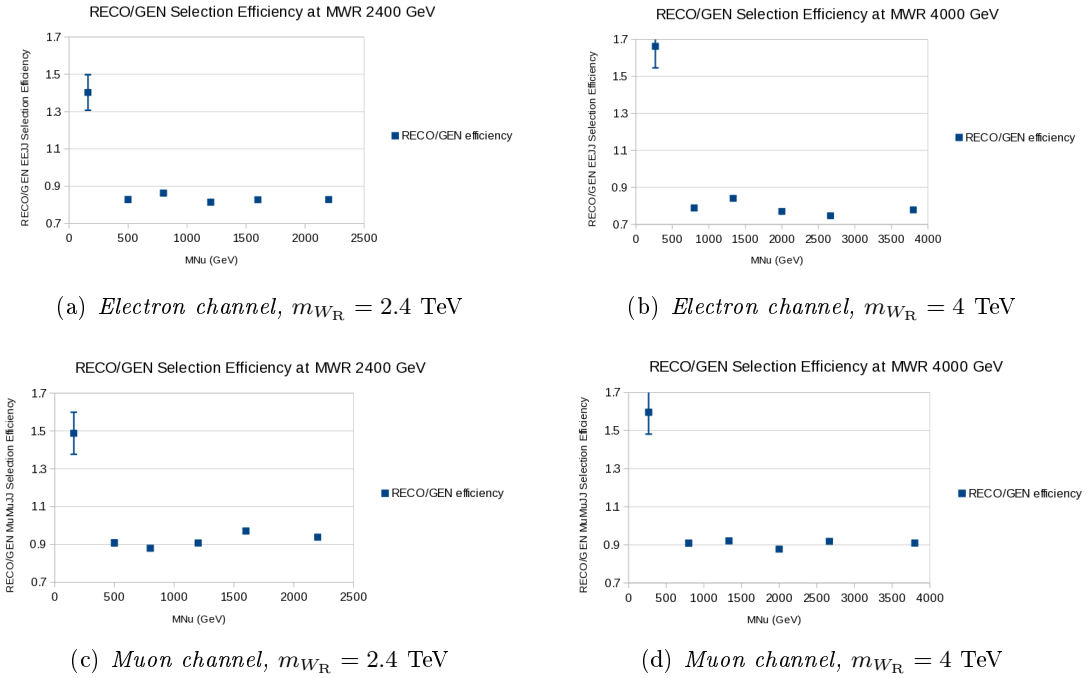

(a) *Electron channel,* $m_{W_\mathrm{R}} = 2.4$ TeV

(b) *Electron channel,* $m_{W_\mathrm{R}} = 4$ TeV

(c) *Muon channel,* $m_{W_\mathrm{R}} = 2.4$ TeV

(d) *Muon channel,* $m_{W_\mathrm{R}} = 4$ TeV

Figure 4.44: *Ratio of efficiencies, used to calculate the 2D limits for the 2015 analysis, obtained with RECO* W_R *events and GEN events as a function of the neutrino mass.*

factors obtained using fully reconstructed events.
The ratio between RECO and GEN efficiencies is constant versus the neutrino mass, then the generator level events can be used to rescale the limits. In the $m_{N_\mathrm{R}} \lesssim \frac{1}{8} m_{W_\mathrm{R}}$ region, the selection efficiency is higher in fully reconstructed W_R events than in generator level events, because jets produced by pileup interactions in RECO events can pass the jet offline selection at low m_{N_R}, whereas this is not possible in the GEN selection of GEN samples. At low m_{N_R}, the 2D exclusion limits obtained using GEN W_R events are then less stringent than the limit obtained using RECO W_R events.

4.8.1 Comparison with 2015 results

The 35.9 fb^{-1} of data collected in 2016 are more than 10 times what was collected in 2015 and thus the 2016 exclusion upper limits on the W_R mass are expected to extend the exclusion from approximately 3.2 TeV of the 2015 data to 4.5 TeV. Given that the analysis strategy did not change between the two iterations of the analysis, the improvement is expected to be proportional to the increase in luminosity, given by a square root factor.
The ratio of the 2016 and 2015 limits is shown in Figure 4.45. The 2015 limits have been scaled by square root of luminosity, so the expected value is 1. The ratio shows that at high mass, for $m_{W_\mathrm{R}} > 2$ TeV, the 2016 expected limits are better than the 2015 limits even

after scaling by the luminosity increase.

For the 2015 iteration of the analysis, a MADGRAPH sample was used for the Drell–Yan background estimation instead of the aMC@NLO one used in this analysis. The background estimates as well as the signal efficiencies were compared for the 2015 and 2016 datasets and their distributions are shown in Figure 4.46, where the 2015 estimates have been scaled by the increase in luminosity. In 2015 the expected backgrounds were higher than those in 2016 while the signal efficiencies were about the same. The 2016 limits at high mass are then better than those calculated in 2015 because the larger 2015 backgrounds with similar signal efficiencies lead to a less stringent limit on the 2015 signal cross section.

At low mass the 2016 limits are slightly worse because the systematics uncertainties are larger in 2016 (more factors, ignored in 2015, were included in the limits calculation). When systematics are included in the calculation, the improvement at high $m_{\ell\ell\mathrm{jj}}$ is particularly important since this is the region of interest in this iteration of the W_R search.

The 2016 expected limits are better than the 2015 ones even at lower masses if the systematic uncertainties are not included in the calculation of the limits. This is shown in Figure 4.47. Note that the window sizes were optimized separately for the best limit, including the effect of systematics, for both 2015 and 2016. The residual difference at low mass, $m_{W_\mathrm{R}} < 1$ TeV, is then presumably due to the optimization which includes the systematics.

If we do not apply the scaling, the limits ratio calculated without systematics, shown in Figure 4.48, is between 1/lumi (green line) and $1/\sqrt{\mathrm{lumi}}$ (red line). It is equal to 1/lumi when the backgrounds are zero and only the signal efficiency matters, while it is $1/\sqrt{\mathrm{lumi}}$ when backgrounds have enough statistics.

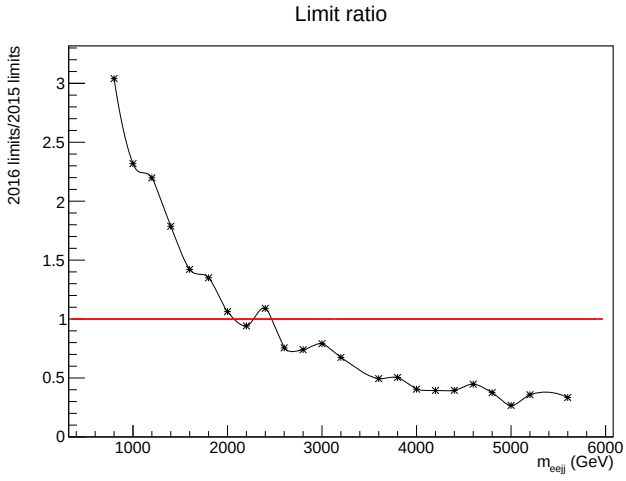

(a) *Electrons*

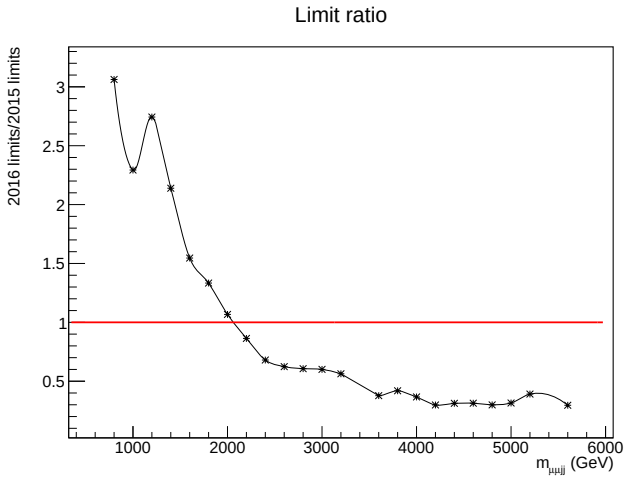

(b) *Muons*

Figure 4.45: *Ratio of 2015 and 2016 expected cross section limits. The 2015 limits have been scaled by square root of luminosity to compare with the 2016 limits and the expected ratio is 1.*

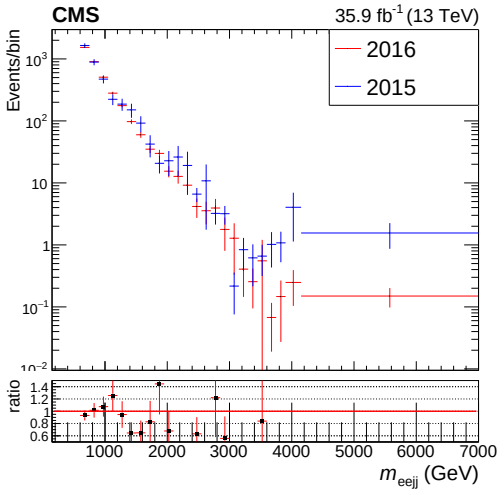

(a) *Electron background*

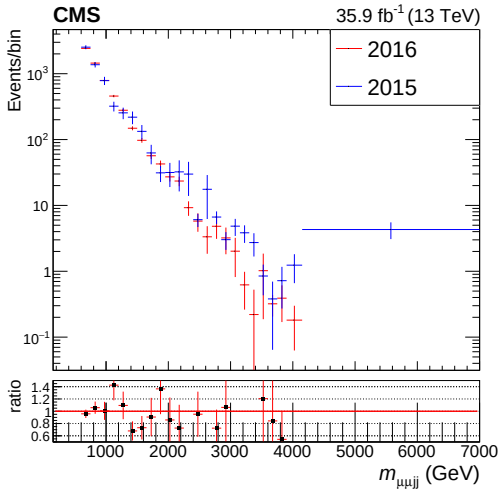

(b) *Muon background*

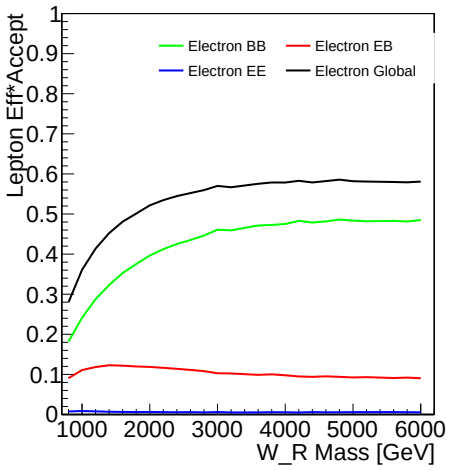

(c) *Electron signal efficiency in 2015*

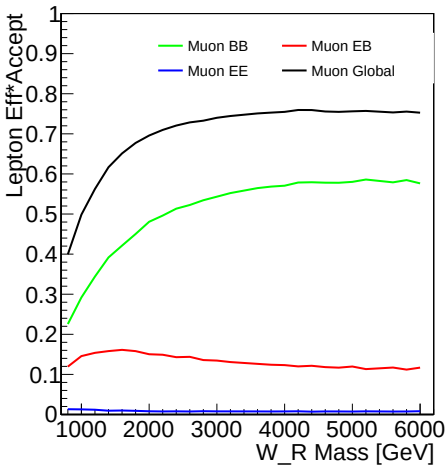

(d) *Muon signal efficiency in 2015*

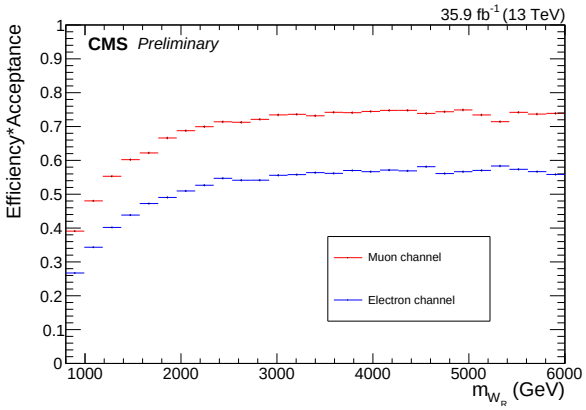

(e) *Signal efficiency in 2016*

Figure 4.46: *Comparison of expected backgrounds and signal efficiencies for 2015 and 2016.*

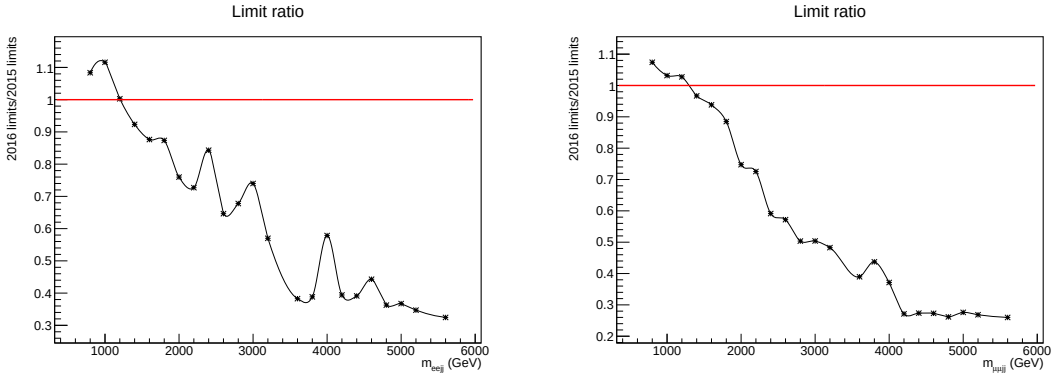

(a) *Electrons* (b) *Muons*

Figure 4.47: *Ratio of 2015 and 2016 expected cross section limits. The 2015 limits have been scaled by square root of luminosity to compare with the 2016 limits and the expected ratio is* 1*. Limit calculation is done without including systematic uncertainties.*

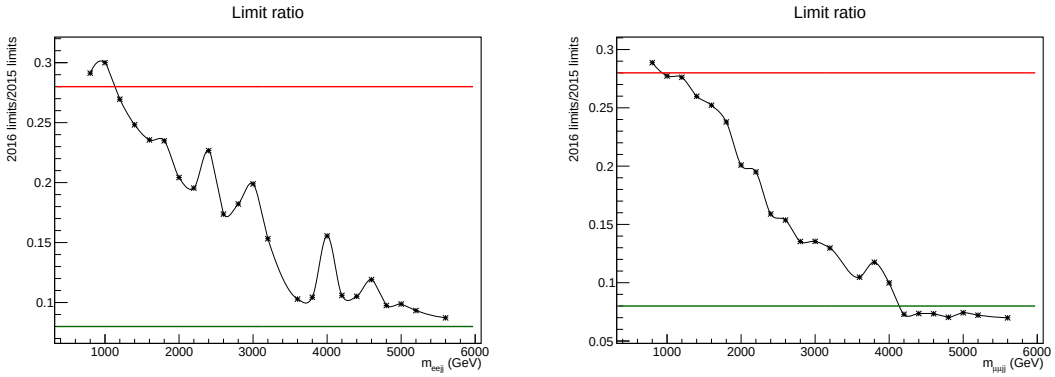

(a) *Electrons* (b) *Muons*

Figure 4.48: *Ratio of 2015 and 2016 expected cross section limits without a square root of luminosity scaling. Systematic uncertainties are not included in the limit calculation. The green line represents* $1/lumi$*, while the red line represents* $1/\sqrt{lumi}$*.*

4.9 Conclusions

The search for a heavy W_R boson and a heavy neutrino with the 2016 data at 13 TeV has been presented in this chapter. The results of this analysis have been published in a recent CMS paper [169].

As explained in Section 4.8, the observed lower limit at 95% CL on the mass of the W_R boson, for a model with $m_{N_R} = \frac{1}{2}m_{W_R}$, is 4.4 TeV for both the electron and the muon channels. The expected exclusion limit is 4.4 TeV for the electron channel and 4.5 TeV for the muon channel. These results provide the most stringent limits to date, giving an improvement of ≈ 1.4 TeV with respect to the results of the previous analysis at 8 TeV [87].

No significant excess over the standard model background expectations has been observed in the invariant mass distribution of the dilepton plus dijet system. The biggest deviation is in the electron channel at $m_{\ell\ell jj} \simeq 3.4$ TeV, with a local significance of $\approx 1.5\sigma$. The 2.8σ excess seen in the electron channel at $m_{\ell\ell jj} \simeq 2.1$ TeV with the 8 TeV analysis is thus not confirmed by the present data.

At high masses, region of interest for the W_R search, the uncertainties on these results are dominated by the statistical component. The main systematic uncertainties components are the theoretical uncertainties on the PDFs, and on the factorization and renormalization factors. The main experimental systematic uncertainties are coming from jet energy scale and resolution.

The slight fluctuation in the electron channel at $m_{\ell\ell jj} \simeq 3.4$ TeV is of $\approx 1.5\sigma$ but it seems above 2σ in the p-value plot shown in Figure 4.49. The reason why the same excess is not seen in the mass plot is linked to the different mass regions considered for the p-value plot, which uses the W_R mass windows described in Section 4.7, and for the $m_{\ell\ell jj}$ distribution, which uses different mass bins. The number of observed and expected events are presented in Table 4.18 for the mass bins used in the $m_{\ell\ell jj}$ distribution, and in Table 4.19 for the W_R mass search windows used for the limits calculation and for the p-value plot.

The events within the W_R mass search windows for the electron and muon channels are shown in Figure 4.50.

In the muon channel, one event is observed in the last $m_{\ell\ell jj}$ bin where there are zero predicted events but the statistical uncertainties are very large, as shown in Figure 4.40. In fact, in Figure 4.41 it is visible that the muon events in the tail of W_R mass are consistent with the expected limit at $+1\sigma$. Besides the event in the last bin of the $m_{\ell\ell jj}$ plot, at $m_{W_R} = 5815.35$ GeV, there is also an event in the over-flow bin, at $m_{W_R} = 7074.14$ GeV. The event displays of these events can be seen in Figures 4.51 and 4.52, respectively.

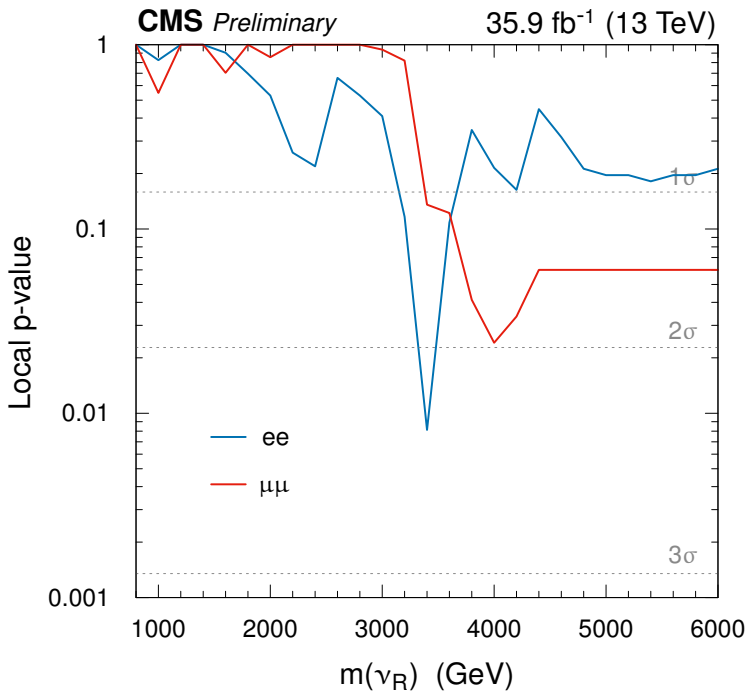

Figure 4.49: *Local p-value as a function of m_{N_R} for the electron (blue) and the muon (red) channels.*

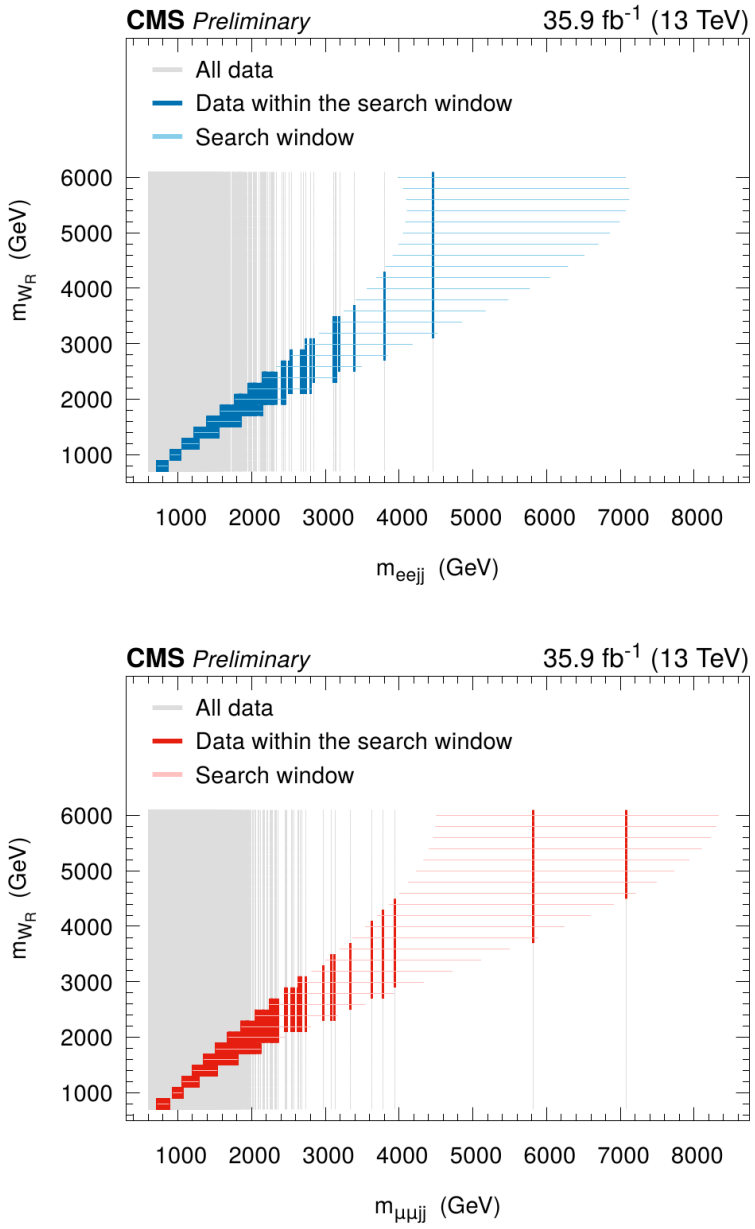

Figure 4.50: *Events within the W_R mass search windows for the electron channel on the top and for the muon channel on the bottom.*

Table 4.18: *Number of observed and expected signal (m_{W_R} = 4 TeV, m_{N_R} = 2 TeV) and background events for the $m_{\ell\ell jj}$ bins in the electron channel.*

Low limit (GeV)	High limit (GeV)	Observed	Signal (m_{W_R} = 4 TeV)	Background
150	300	6	0	1.4354
300	450	1065	0	1176.18
450	600	2133	0.0005	2260.54
600	750	1457	0.0006	1533.40
750	900	880	0.0041	903.046
900	1050	505	0.0054	507.341
1050	1200	274	0.0119	280.500
1200	1350	150	0.0185	176.482
1350	1500	93	0.0327	97.3851
1500	1650	55	0.0418	59.7550
1650	1800	37	0.0575	35.0059
1800	1950	26	0.0757	29.9317
1950	2100	20	0.0963	15.4457
2100	2250	16	0.1327	12.7367
2250	2400	7	0.1697	9.18297
2400	2550	7	0.2036	4.16667
2550	2700	2	0.2820	3.55631
2700	2850	4	0.3512	3.93591
2850	3000	0	0.4294	1.77754
3000	3150	3	0.5245	1.28185
3150	3300	1	0.7217	0.406534
3300	3450	1	0.9671	0.255177
3450	3600	0	1.3401	0.553389
3600	3750	0	1.7434	0.067561
3750	3900	1	2.3745	0.146848
3900	4150	0	3.3222	0.247999
4150	7000	1	0.9557	0.149646

Table 4.19: *Number of observed and expected signal and background events for different W_R mass search windows in the electron channel.*

W_R window mass point (GeV)	Low limit (GeV)	High limit (GeV)	Observed	Signal	Background
3000	2720	4180	10	71.5	8.46
3200	2910	4520	7	45.7	4.01
3400	3080	4850	7	30.4	2.81
3600	3250	5170	3	19.2	1.60
3800	3410	5480	2	12.9	1.38
4000	3560	5770	2	8.9	0.72

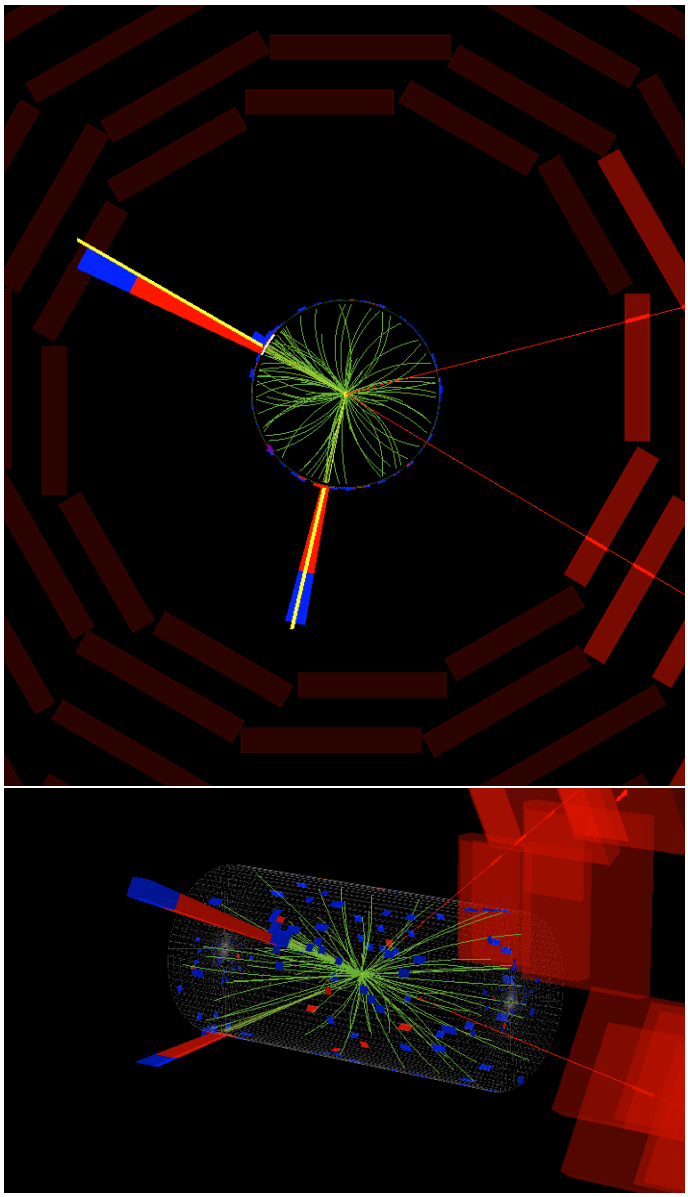

Figure 4.51: *Event display for run 282800, lumisection 174, event 315780535 with* $m_{\mu\mu jj} =$ 5815.35 GeV.

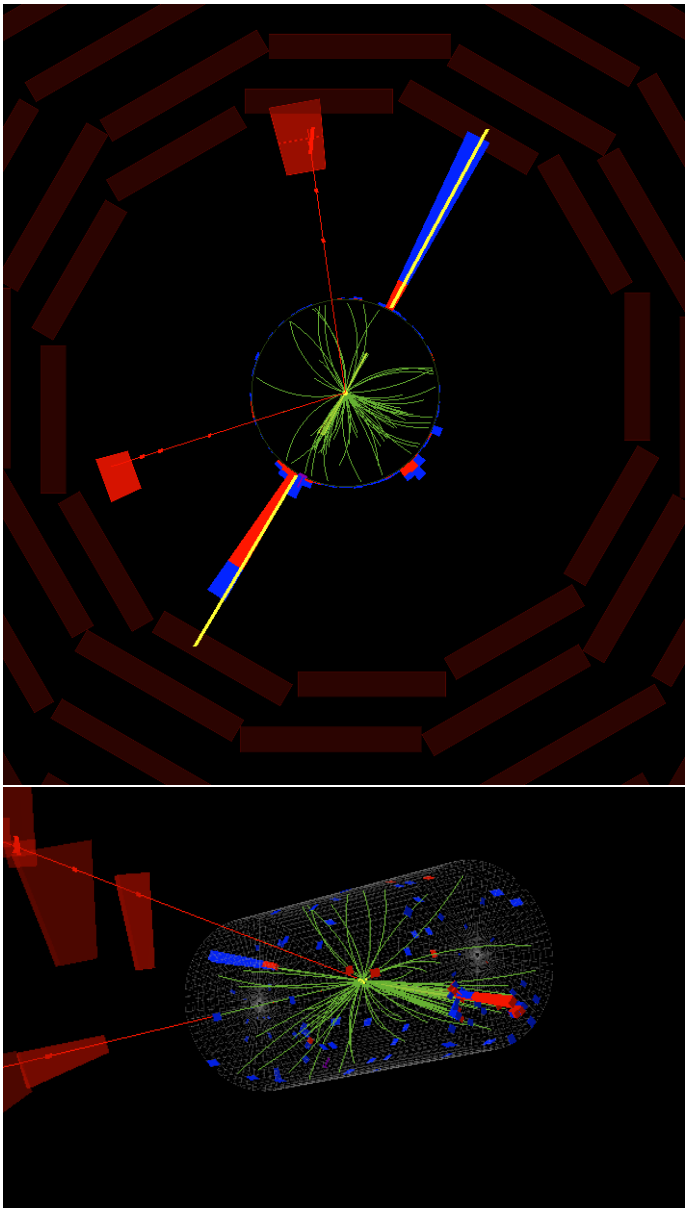

Figure 4.52: *Event display for run 276811, lumisection 25, event 41218301 with* $m_{\mu\mu jj} =$ 7074.14 GeV.

Chapter 5

Outlook and perspectives

An overview of the heavy neutrino physics at the LHC and future experiments is presented in this chapter.

5.1 Other searches at CMS

Besides the search for a heavy right-handed W boson and a heavy neutrino presented in the previous chapter, other searches for heavy neutrinos [170–172] have been carried out by the CMS experiment using the 2016 data at 13 TeV with a luminosity of 35.9 fb^{-1}.

5.1.1 Search for heavy neutral leptons in trilepton channel

The search for heavy neutral leptons (HNL) in the trilepton channel [170] considers the decay of a W boson into three leptons and a light neutrino, shown in Figure 1.3 on the left. This analysis looks for three leptons with $p_T > 5$ GeV and for missing E_T in the final state. Due to the presence of the neutrino, the reconstruction of the full HNL mass, and thus the hunt for a mass peak, is impossible but the trilepton final state helps in probing very low HNL masses, since a reconstruction of very soft leptons is possible.
The main backgrounds, estimated through data-driven methods, are events with non-prompt leptons coming from DY+jets and $t\bar{t}$, events with three prompt leptons coming from $WZ \to 3\ell\nu$ and $ZZ \to 4\ell$, and conversions $X\gamma$ (i.e. $Z\gamma^*$ with γ^* going into two leptons).
This analysis refers to the neutrino Minimal Standard Model (νMSM) described in Section 1.2.2. Since in this model the HNL is a Majorana particle, its decay can violate lepton number allowing events without a pair of leptons with opposite sign and same flavor (OSSF). These events are analyzed separately with respect to the events with an OSSF pair. The analysis considers two orthogonal categories: the *low-mass region* for $m_N < m_W$, and the *high-mass region* for $m_N > m_W$. These two regions are divided into multiple bins of the minimum mass out of all lepton pairs of opposite charge, $M^{min}_{2\ell OS}$, which is strongly

correlated to m_N in signal events. In the high-mass region, each of the $M_{2\ell OS}^{min}$ bins is further subdivided into bins of the transverse mass (M_T) of the lepton not present in the pair forming $M_{2\ell OS}^{min}$, since M_T tends to be much larger in signal events than in SM processes. The observed and expected yields in these categories are shown in Figure 5.1, from where it is visible that no statistically significant excess above the SM expectation is observed. Upper limits at 95% CL are then set on the mixing parameters between the HNL and electrons or muons. As shown in Figure 5.2, they vary between 1.5×10^{-5} and 1.8 for HNL with masses between 1 GeV and 1.2 TeV.

5.1.2 Search for heavy neutral leptons in dilepton-dijet channel

The same-sign (SS) dilepton search of HNL [171] considers the decay of a W boson into two SS leptons and a pair of jets, shown in Figure 1.3 on the right, which is possible if the HNL is a Majorana particle as considered in the context of a Type I seesaw model. This analysis looks for two leptons with $p_T > 8$ GeV and two jets.
The main backgrounds are events with prompt leptons coming from WZ and ZZ decays, estimated from simulation, events with misidentified leptons coming from DY+jets, $t\bar{t}$, and W+jets, estimated through a data-driven method, and events with a mismeasured charge from DY, estimated from simulation.
The strategy used in this analysis is to search for an excess of events in the dilepton-dijet invariant mass distribution, using a "cut&count" approach and considering two different regions: the *low-mass region* for $m_N < m_W$ and the *high-mass region* for $m_N > m_W$. As shown in Figure 5.3, no significant excess is observed in these distributions.
Upper limits at 95% CL are then set on the mixing parameters between HNL and electrons or muons, varying between 2.3×10^{-5} and 1 for HNL with masses between 20 GeV and 1600 GeV, as shown in Figure 5.4.

Comparing these results with the ones of the analysis in the trilepton channel, it can be noted that the trilepton channel has more stringent limits for low masses of HNL, while the SS dilepton channel has higher sensitivity at high masses, giving the most restrictive direct limits for $m_N > 100$ GeV and the first limits for Majorana neutrinos with $m_N > 1.2$ TeV.

5.1.3 Search for heavy neutrinos in diτ-dijet channel

The search for heavy neutrinos in the diτ-dijet channel [172] considers the decay of a W_{R} boson into two high-p_T τ leptons decaying hadronically, two high-p_T jets, and missing transverse momentum (p_T^{miss}) from the τ lepton decays.
This analysis looks for two τ leptons with $p_T > 32$ GeV, two jets with $p_T > 50$ GeV, and $p_T^{miss} > 50$ GeV. The main backgrounds are $t\bar{t}$, Z+jets and QCD multijets processes, estimated with data-driven techniques.
This search refers to a Left-Right symmetric model which considers the heavy right-handed

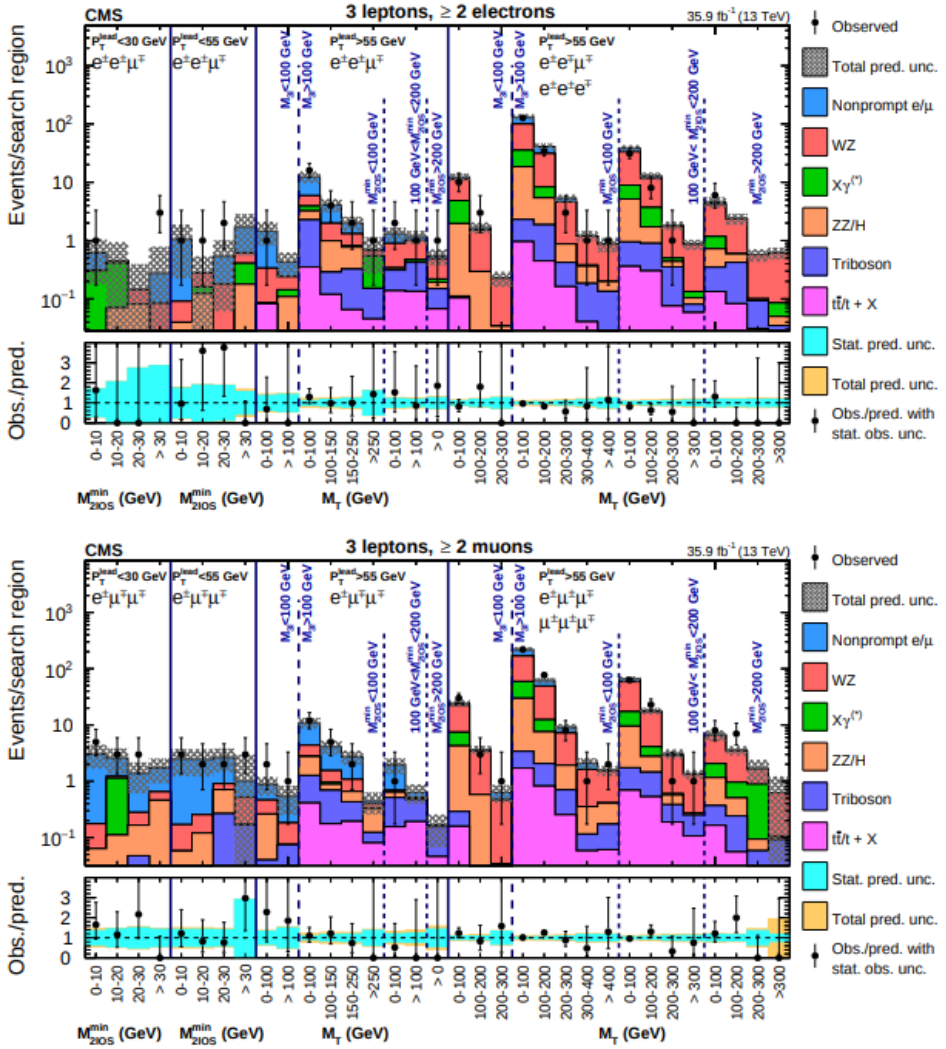

Figure 5.1: *Observed and expected event yields as a function of $M_{2\ell OS}^{min}$ and M_T for events with at least two electrons (top), and with at least two muons (bottom) in the trilepton channel. The contribution of each background source is shown. The first 8 bins of each figure correspond to the low-mass region, while the rest displays the high-mass region. [170]*

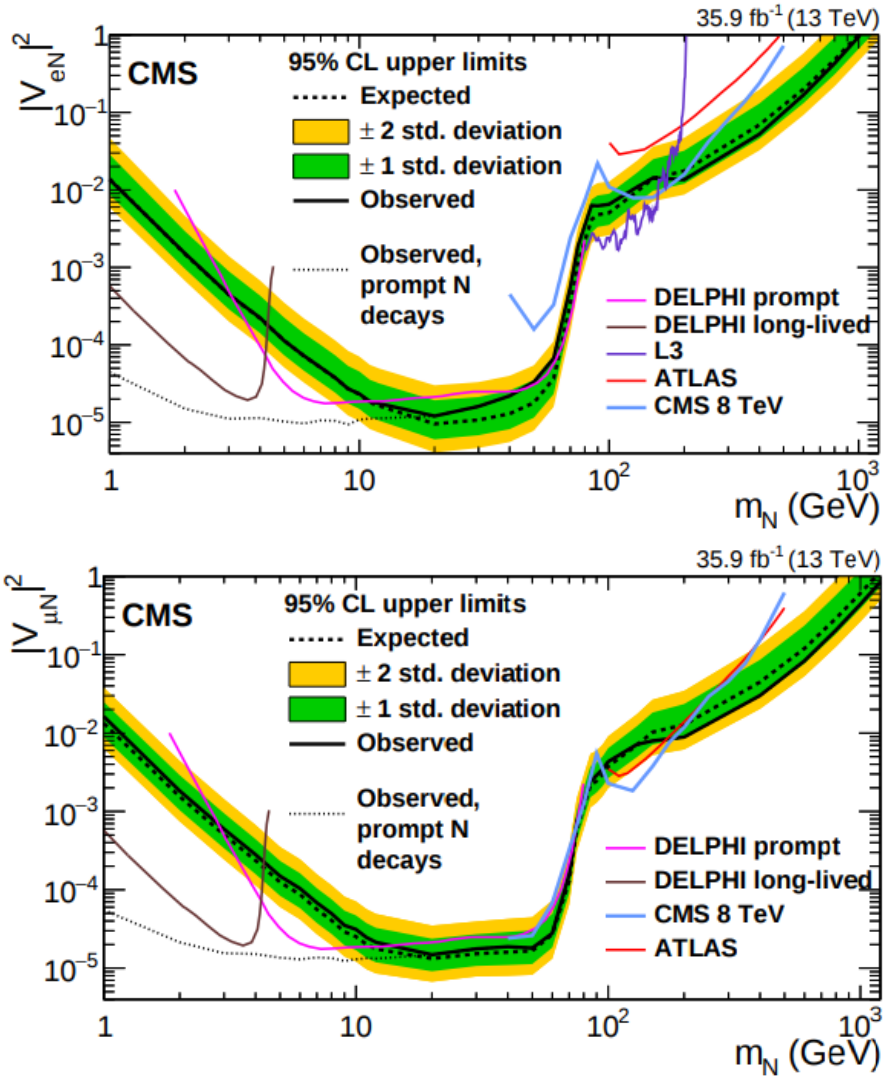

Figure 5.2: *Observed and expected upper limits at 95% CL on mixing parameter between HNL and electron (top) or muon (bottom) as a function of the HNL mass in the trilepton channel. The dashed black curve is the expected upper limit, with one and two standard-deviation bands shown in dark green and light yellow, respectively. The solid black curve is the observed upper limit, while the dotted black curve is the observed limit in the approximation of prompt N decays. The best upper limits at 95% CL from other collider searches in L3, DELPHI, ATLAS, and CMS are also shown. [170]*

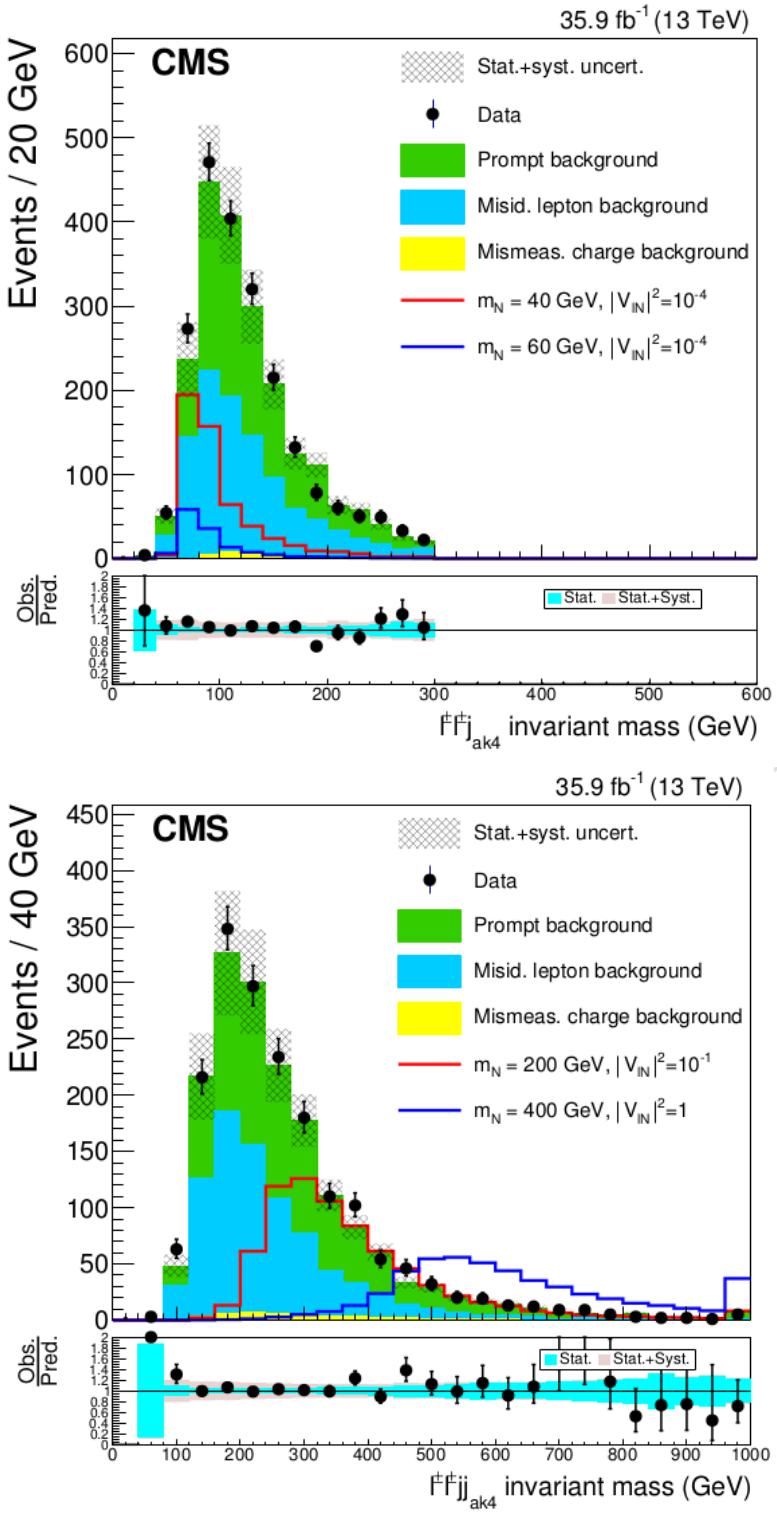

Figure 5.3: *Dilepton-dijet invariant mass distributions for the low-mass (top) and the high-mass (bottom) signal region for data, background samples, and two signal hyphotheses in the SS dilepton channel. [171]*

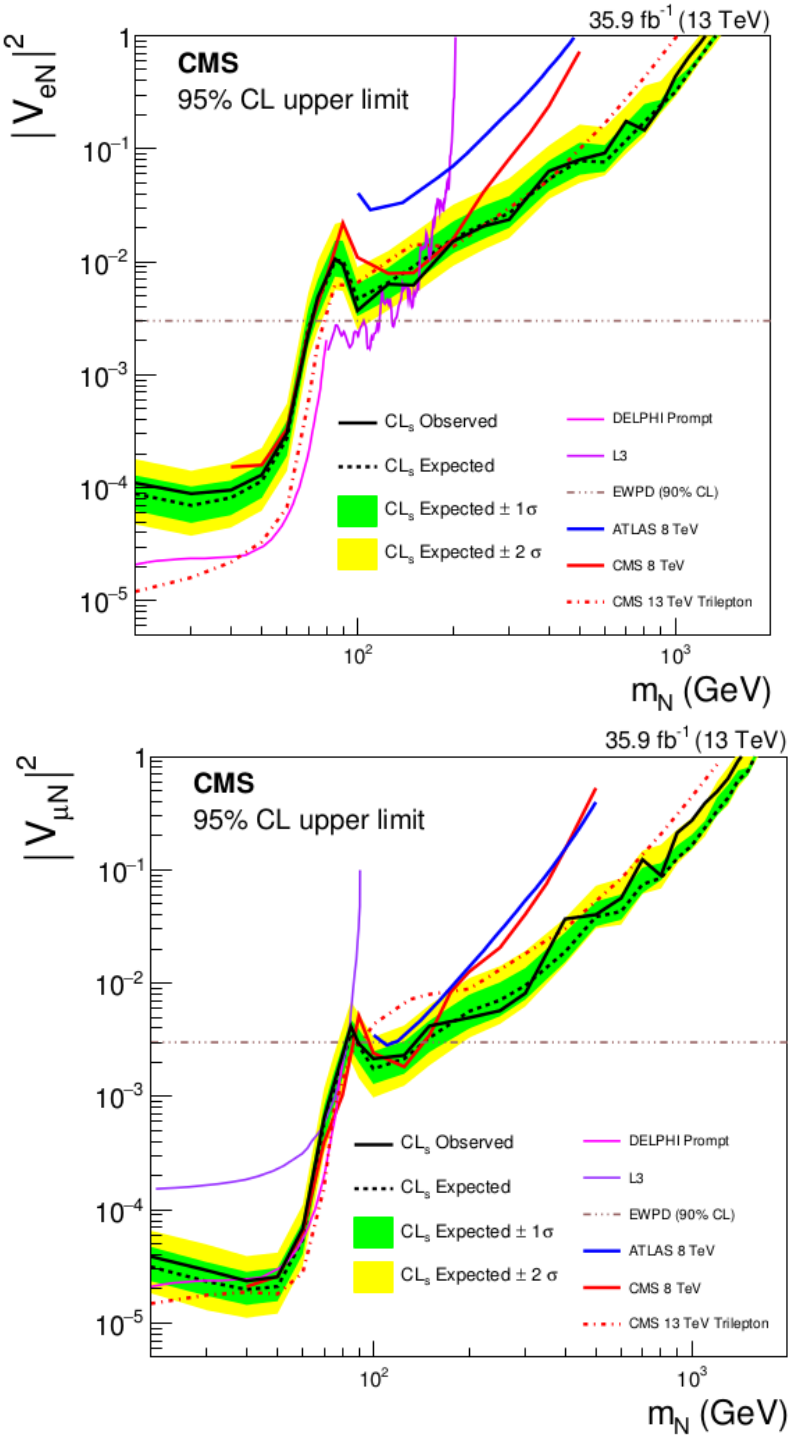

Figure 5.4: *Observed and expected upper limits at 95% CL on mixing parameter between HNL and electron (top) or muon (bottom) as a function of the HNL mass in the SS dilepton channel. The dashed black curve is the expected upper limit, with one and two standard-deviation bands shown in dark green and light yellow, respectively. The solid black curve is the observed upper limit. The upper limits from other direct searches in DELPHI, L3, and ATLAS, the upper limits from the CMS 2012 data at* $\sqrt{s} = 8$ TeV*, and the trilepton analysis based on the same 2016 data set used in this analysis are also shown. [171]*

neutrinos N_e and N_μ too heavy to be detected at the LHC, and assumes that only the N_τ flavor contributes significantly to the W_R decay.
The W_R resonance mass cannot be fully reconstructed in the $\tau\tau jj$ channel because of the presence of neutrinos from the τ lepton decays. The search strategy is thus to look for a broad enhancement of events above the expected background in the distribution of the partial mass reconstructed by the τ decay products, the two highest p_T jets and the p_T^{miss}.
The observed data yield, of 117 events, is consistent with the SM background expectation, of 126.2 ± 11.8 events, therefore upper limits at 95% CL are set on the signal production cross-section, as shown in Figure 5.5 (top).
Considering different scenarios for the mass ratio between N_τ and W_R, the 95% CL upper limits on the product of the production cross section and the branching fraction as a function of m_{W_R} and $m_{N_\tau}/m_{W_\mathrm{R}}$ are presented in Figure 5.5 (bottom). Assuming that the N_τ mass is 0.8 (0.2) times the mass of the W_R boson, W_R masses below 3.45 (2.75) TeV are excluded at 95% CL, giving the most stringent limits to date in $\tau\tau jj$ final states.

5.2 Direct searches at future experiments

As said in Section 1.2.2, the lifetime of heavy neutrinos can vary from very small values, leading to *prompt decays* that are the ones explored so far at the LHC, to very large ones, leading to *displaced decays* that are possible for lower couplings at low masses.
In Figure 5.6, the existing constraints from different experiments and the projections for future experiments on the mixing angle between a heavy neutral lepton (HNL) and a muon as a function of the HNL mass are represented. The LHC has probed a large portion of the parameter space for prompt decays of HNLs in the mass range between ≈ 1 GeV and few TeV, corresponding to the right top region of the plot, but it has just started to probe the region not excluded by the EW precision data.
So far no evidence for BSM physics has been found at the LHC, whose searches are limited by the available integrated luminosity and by the difficulties to probe short lifetimes in hadronic environments. The focus should thus be on displaced decay signatures. Heavy neutrinos with masses below the W boson mass and with very small active-sterile mixings behave as long-lived neutral particles with a measurable decay length that leads to a displacement of the decay products from the interaction point. This gives an opportunity to probe their signatures by taking advantage of the displaced vertex techniques.
The available parameter space is limited theoretically by the observations of baryon asymmetry of the universe, big bang nucleosynthesis and "see-saw" model, as shown in Figure 5.7, but the remaining allowed parameter space can be explored with direct searches at future experiments.
The heavy neutrinos can be looked for at fixed target experiments like SHiP [173], described in Section 5.2.1, or NA62, a CERN experiment already taking data [174, 175], or at some new proposed detectors at the LHC like MATHUSLA or FASER [176, 177], described

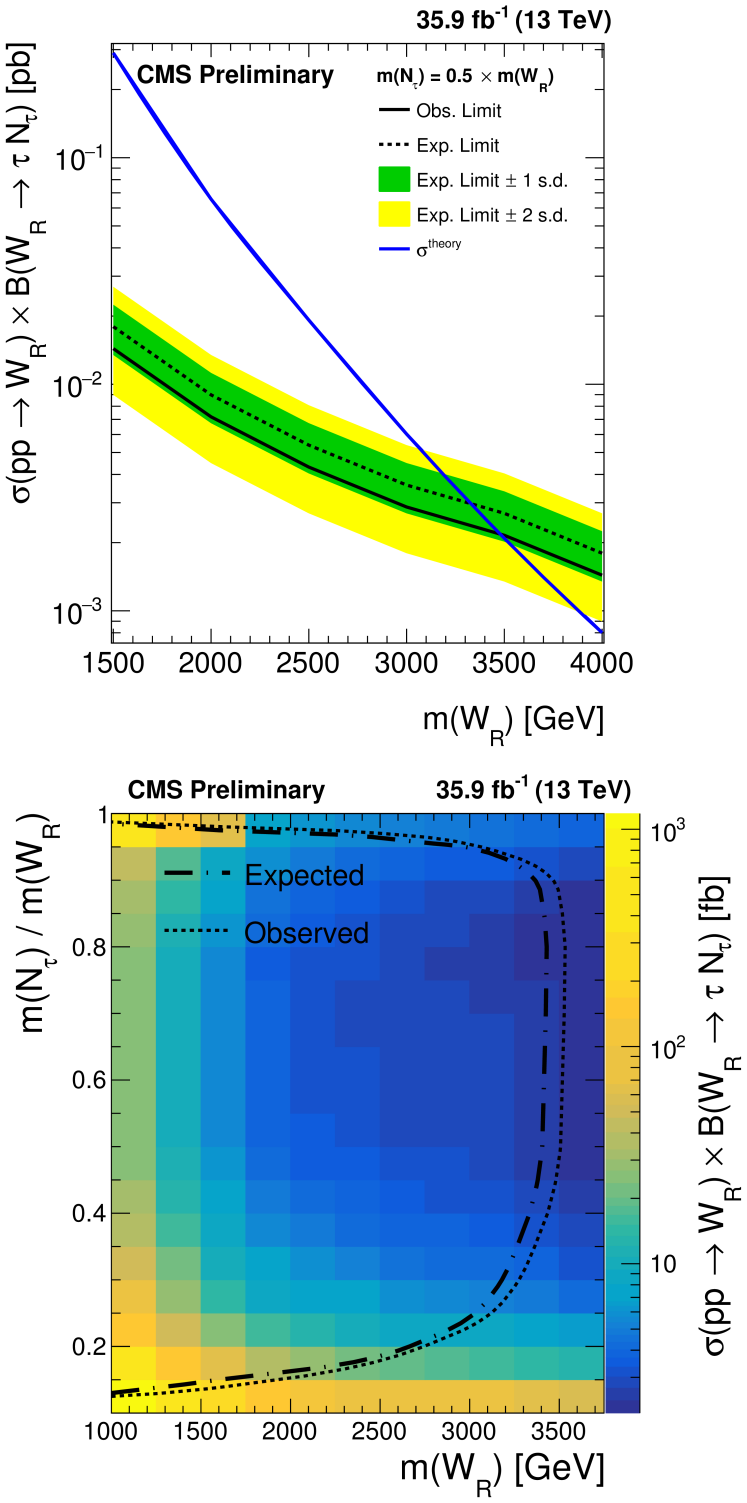

Figure 5.5: *Top: Observed and expected upper limits at 95% CL on the cross section times branching fraction for production of a W_R decaying to N_τ as a function of the W_R mass. The observed limits are shown as solid black lines, while expected limits and their one- (two-) standard deviation limits are shown by dashed lines with green (yellow) bands. The theoretical cross sections are indicated by the solid blue lines. Bottom: Expected and observed limits at 95% CL as a function of m_{W_R} and m_{N_τ}/m_{W_R}. [172]*

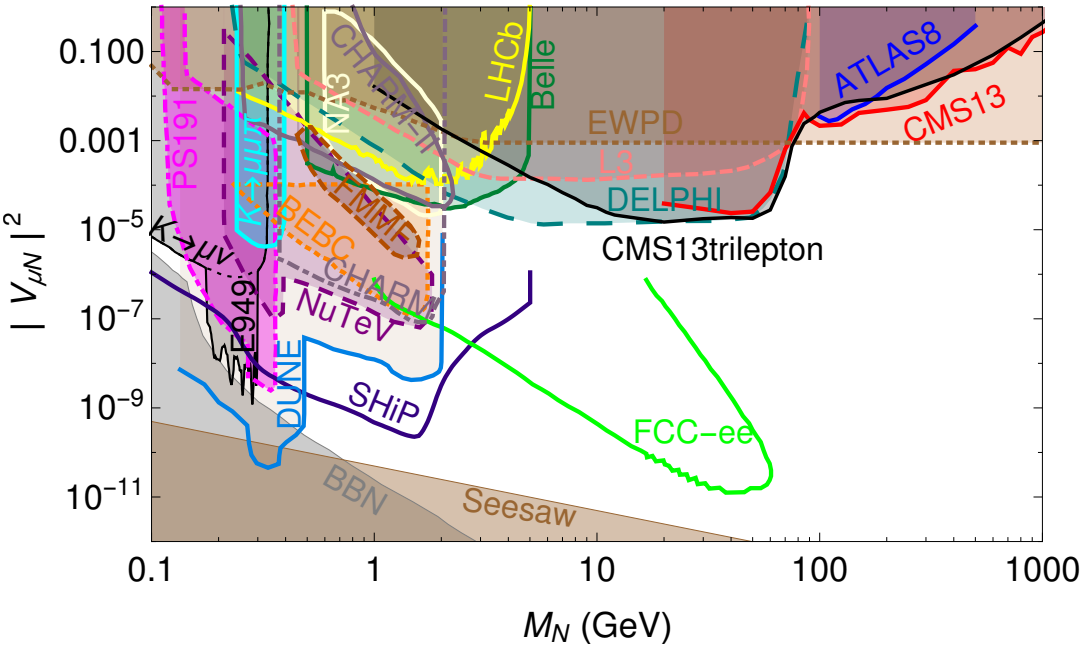

Figure 5.6: *Constraints (filled area) and projections (contours) on the mixing angle between a HNL and a muon as a function of the HNL mass for different experiments. [182]*

in Section 5.2.2. The HNLs can also be searched at electron-positron circular colliders like FCC-*ee* [178], described in Section 5.2.3, or the Circular Electron Positron Collider (CEPC) [179], and at linear colliders like the International Linear Collider (ILC) [180], described in Section 5.2.4. Moreover, also indirect signatures can be sensitive to HNLs, such as neutrinoless double beta decay [181].

5.2.1 SHiP

The Search for Hidden Particles (SHiP) experiment is a proposed fixed-target experiment at the CERN SPS using a 400 GeV proton beam and 2×10^{20} proton-target expected interactions in 5 years [173]. The beamline and the detector will be installed starting from 2021 and the data-taking will not start earlier than 2026. By then, LHC should have delivered 300 fb^{-1} to CMS and ATLAS, so SHiP will provide complementary sensitivity to searches for new physics.
The SHiP experiment, shown in Figure 5.8, is composed of:

- a heavy target to maximize the heavy flavour production and minimize the production of neutrinos in $\pi/K \to \mu\nu$ decays, that are sources of background;

- a hadron absorber after the target to stop most SM particles, except μ and ν;

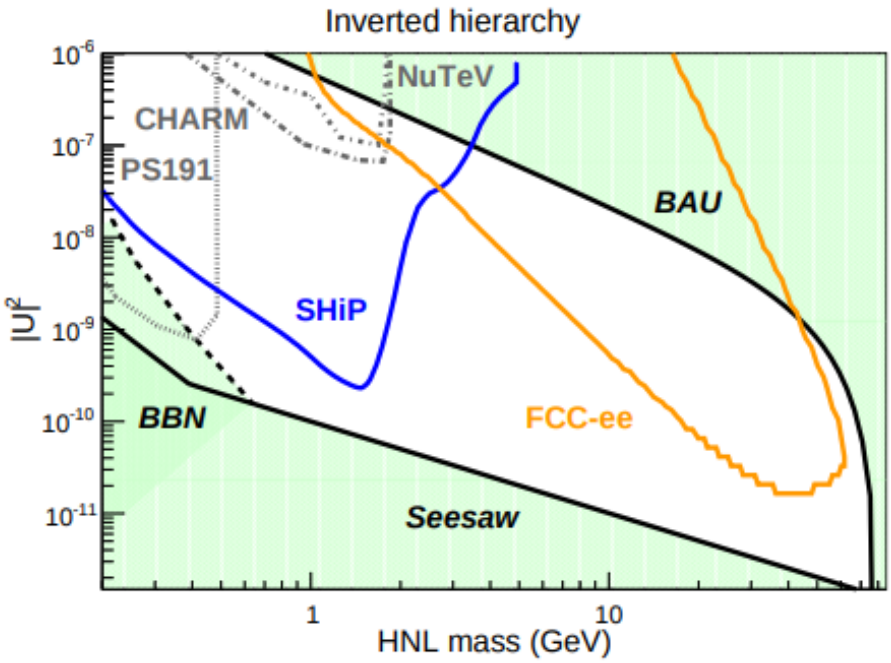

Figure 5.7: *Constraints on the mixing angle between a HNL and a muon as a function of the HNL mass given by future experiments projections and theoretical models. [183]*

- an active muon shield with a magnetic deflection away from the detectors to reduce μ-induced backgrounds;
- an emulsion spectrometer to detect tau neutrinos and search for dark matter;
- a long decay volume ($\approx$ 50 m) under vacuum to prevent neutrino interactions within the fiducial volume;
- a spectrometer with standard detectors to detect the "Hidden-Particles" (HP detectors): a tracking system, a magnet, a timing detector, calorimeters, and a muon system.

The beam extraction is slow ($\approx$ 1 s) and uniform to reduce occupancy in the detector, which has a total length of about 115 m with a 5 m diameter.

The experiment aims to search for very weakly interacting long-lived particles with masses up to $O(10)$ GeV and couplings down to 10^{-10}, including Heavy Neutral Leptons (right-handed partners of the active neutrinos), vector, scalar, and axion portals to the Hidden Sector, and light supersymmetric particles like sgoldstinos, superpartners of the goldstino. The high intensity of the SPS, and in particular the large production of charm mesons and photons with the 400 GeV beam, enables a wide variety of light long-lived exotic particles of different models. The hidden sector models share a number of unique and common

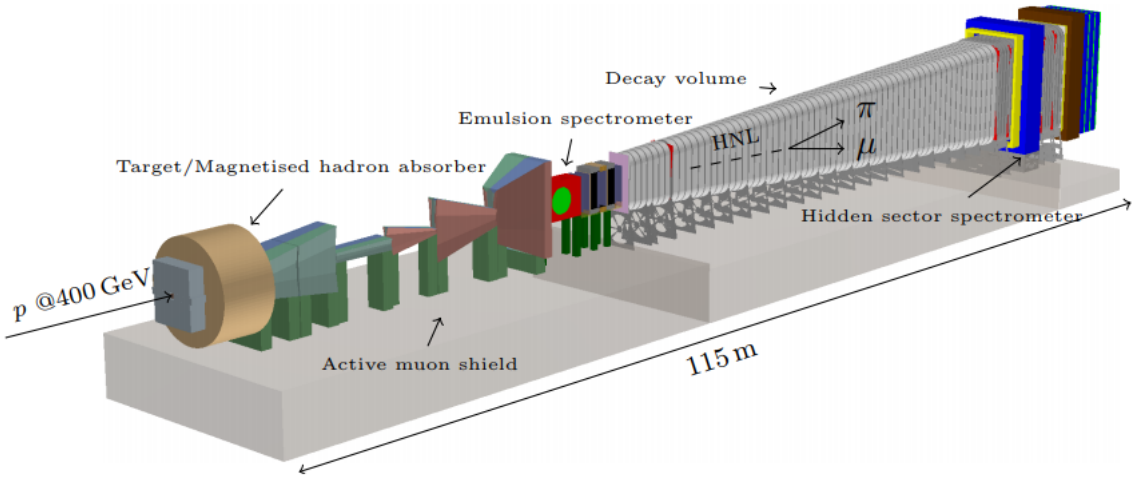

Figure 5.8: *Layout of the SHiP detector.*

Table 5.1: *Final states for different hidden particles.*

Particles	Final states
HNL, SUSY neutralino	$\ell^{\pm}\pi^{\mp}$, $\ell^{\pm}K^{\mp}$, $\ell^{\pm}\rho^{\mp}$, $\rho^{\pm} \to \pi^{\pm}\pi^{0}$
Vector, scalar, axion portals, SUSY sgoldstino	$\ell^{\pm}\ell^{\mp}$, $\pi^{\pm}\pi^{\mp}$, $K^{\pm}K^{\mp}$
HNL, SUSY neutralino, axino	$\ell^{\pm}\ell^{\mp}\nu_{\ell}$
Axion portal, SUSY sgoldstino	$\gamma\gamma$
SUSY sgoldstino	$\pi^{0}\pi^{0}$

physics phenomenologies [184], shown in Table 5.1.
The hidden particles can be detected inside SHiP through their decay in SM particles. The detector must be sensitive to as many decay modes as possible, so a full reconstruction and particle identification are essential to minimize the model dependencies.
Having a production branching ratio of $O(10^{-10})$, hidden particles production is strongly suppressed with respect to ordinary SM processes. Moreover, these objects are long-lived, since they can travel unperturbated through the ordinary matter with a lifetime of $O(\mu s)$, leading to a challenging background suppression.
To reject the background sources, mainly ν- and μ-induced backgrounds, random combination of tracks, and cosmic muons from deep inelastic scattering on the cavern and vessel walls, the following strategies are used: the reconstructed momentum must point back to the proton target, the reconstructed vertex must be in the decay volume, there must be a veto upstream the decay volume and a timing veto with a precision of $O(100$ ps).
The backgrounds are investigated with extensive MC studies. As shown in Figure 5.9, less than 0.1 background events are expected in 5 years.
Regarding the HNLs, SHIP could scan most of the experimentally unexplored and cosmologically allowed region below the charm mass, as shown in Figure 5.10. For the two heavier HNLs with $m_{N_{2/3}} \approx 1$ GeV, which typically have lifetimes > 10 μs and decay distances of O(km), 120 events are expected.
Thanks to a significant contribution from B meson decays, SHiP can improve the sensitivity to HNLs with masses up to ≈ 3 GeV by several orders of magnitude. This region, above the charm kinematic limit, is unique and complementary to the region that could be probed at the future circular collider (FCC) in e^+e^- mode.
The sensitivity to HNLs will allow for the first time to probe, in the mass range above the kaon mass, a coupling range for which baryogenesis and active neutrino masses could also be explained.

Background source	Statistical factor	Expected background
ν ($p > 10.0$ GeV/c)	35.	< 0.07
ν (4.0 GeV/c$< p < 10.0$ GeV/c)	~ 1	0 (MC)
ν (2.0 GeV/c$< p < 4.0$ GeV/c)	0.07	0 (MC)
μ DIS HS	~ 1	0 (MC)
μ DIS wall	0.001	0 (MC)
μ Combinatorial	10^4	< 0.1
μ Cosmics ($p < 100$ GeV/c)	0.2	0 (MC)
μ Cosmics ($p > 100$ GeV/c)	800.	< 0.1
μ Cosmics DIS ($p > 100$ GeV/c)	10^3	< 0.1
μ Cosmics DIS (10 GeV/c$< p < 100$ GeV/c)	~ 1	0 (MC)

Figure 5.9: *Expected background sources in SHIP.*

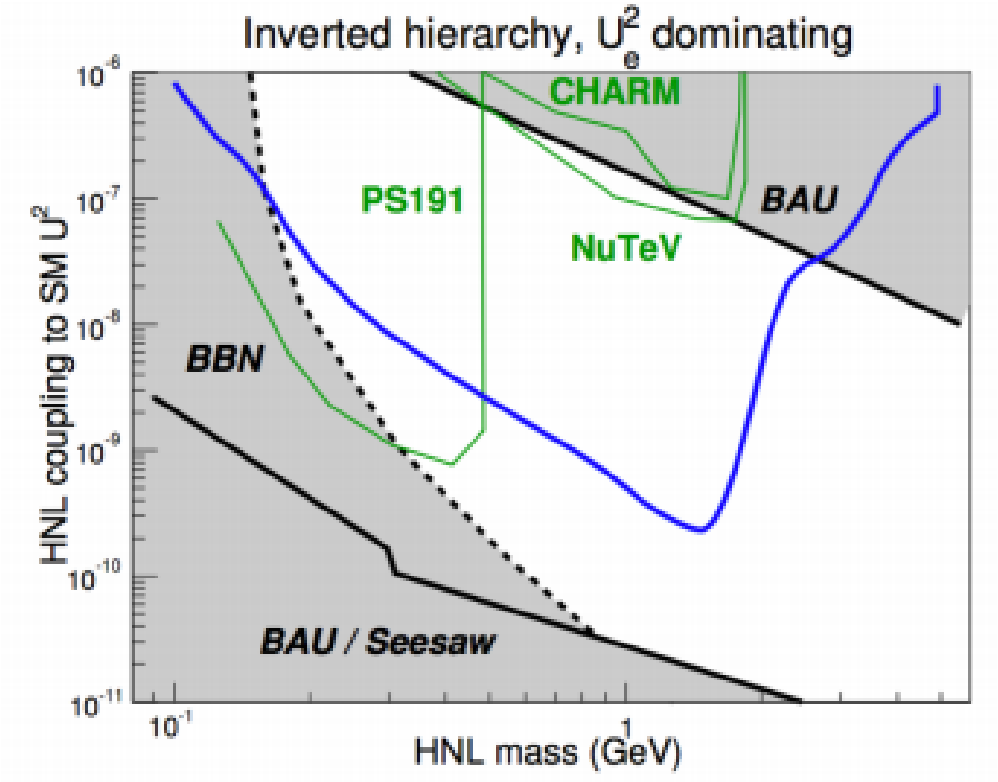

Figure 5.10: *Experimental and cosmological bounds on the search for heavy neutral leptons. The exclusion limit at 90% CL SHiP could set in the case of no signal, assuming a model [185] with inverted hierarchy and a dominant electron coupling,* $U_e^2 : U_\mu^2 : U_\tau^2 = 48 : 1 : 1$*, is represented by the blue line.*

5.2.2 HL-LHC

The HL-LHC, described in Section 2.1.3, is expected to deliver up to 3000 $fb^{-1}$of data. Searches for sterile neutrinos in dedicated experiments like FASER or MATHUSLA [176, 177] could thus probe the parameter space of heavy neutrino models with unprecedented sensitivity.
MATHUSLA ("MAssive Timing Hodoscope for Ultra Stable neutraL pArticles") [186] is a proposed surface detector above the ATLAS interaction point, with a distance of $140-320$ m from it. This distance from the LHC beams will allow to test for rather long life-times of the neutrinos, up to $c\tau \lesssim 10^7 - 10^8$ m, but requires a huge detection volume, with dimensions of $\approx 200 \times 200 \times 20$ m^3. Since this detector will be above ground, the cosmic rays background is a serious concern but it can be kept under control surrounding the decay volume with veto detectors such as scintillators and resistive plate chambers. This background can be reduced to negligible levels thanks to the excellent timing resolution of these anti-coincidence detectors.
FASER ("ForwArd Search ExpeRiment") [187] is a proposed cylindrical detector situated in the very forward direction, few hundred meters downstream of the ATLAS or CMS interaction point (IP). There are several options for the position and size of the detector: FASER^r, the small FASER with radius 0.2 m, FASER^R with radius of 1 m, and FASER^n ("near") with small radius 0.04 m and at a shorter distance.

The sensitivity to sterile neutrinos can be estimated considering all possible production channels: D-mesons, B-mesons, W and Z bosons, as well as Higgs boson. The sensitivity measured in the branching ratio versus $c\tau$ plane is shown in Figure 5.11 for D-mesons (on the left) and B-mesons (on the right), in Figure 5.12 for W (on the left) and Z (on the right) bosons, and in Figure 5.13 for the Higgs boson.
As visible in Figure 5.11, despite being at similar distances from the IP, FASER^R and MATHUSLA are sensitive to different regions in $c\tau$. Mesons flying in the forward direction receive typically much larger boosts than mesons produced at mid-rapidity, thus FASER is less sensitive at large $c\tau$. At the LHC, charm quark production is strongly peaked in the forward direction, thus the FASER experiment performs particularly well for D-mesons, while MATHUSLA does significantly better than FASER for B-mesons.
For the W and Z boson production, shown in Figure 5.12, the sensitivity is ≈ 5 orders of magnitude lower, reflecting the larger number of D-mesons produced at the LHC with respect to gauge bosons. For gauge bosons there is much less boost into the forward direction than for D-mesons, therefore MATHUSLA is again the most sensitive detector. As expected, the production from Higgs decays gives only a negligible contribution to the sensitivity, shown in Figure 5.13.

The sensitivity measured in the plane of the mixing angle $|V_{\alpha N}|^2$ between the sterile neutrino N and a lepton α (electron or muon) versus m_N is shown in Figure 5.14 for different experiments. As visible from the plot on the left, FASER^R always performs better

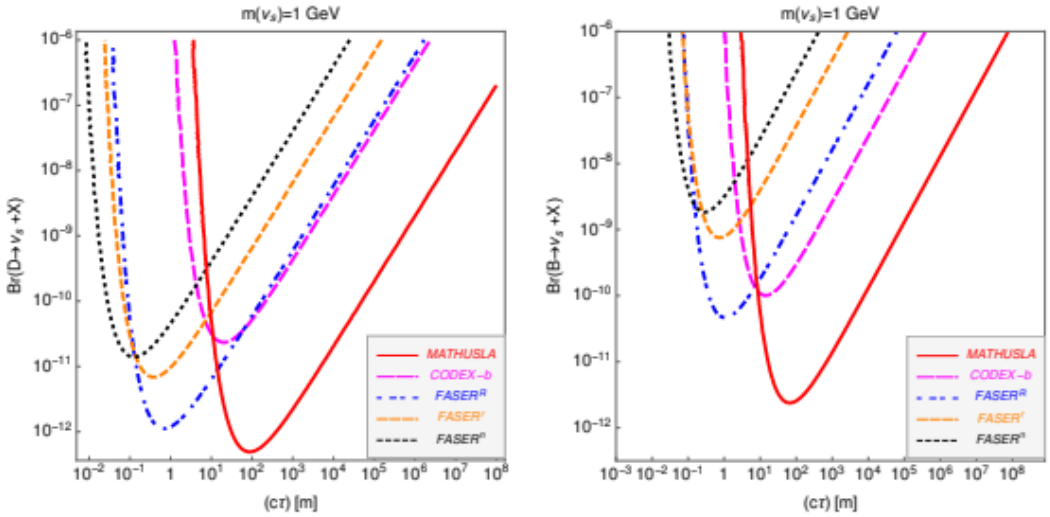

Figure 5.11: *Sensitivity estimates in the branching ratio versus decay length plane for FASER, MATHUSLA, and CODEX-b for neutrinos from D-meson (B-mesons) decays on the left (right).*

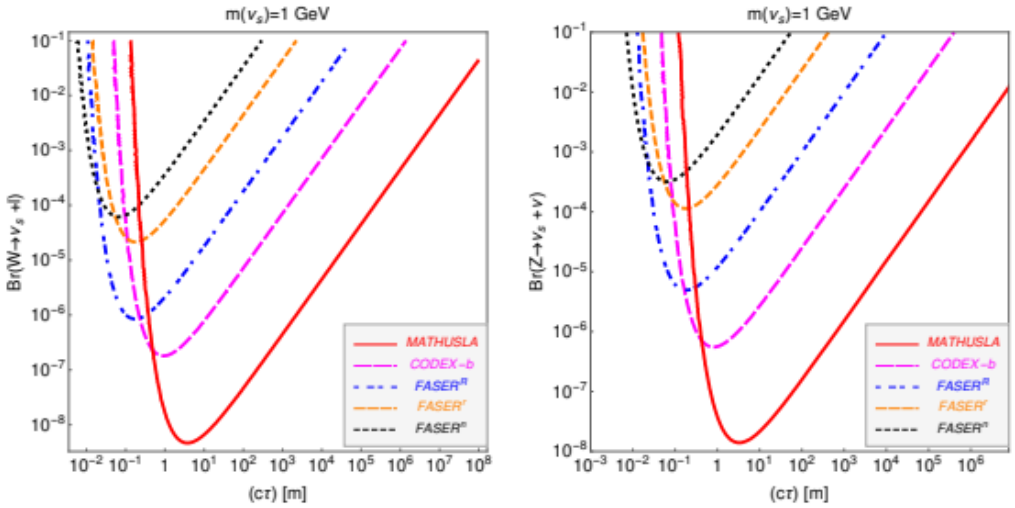

Figure 5.12: *Sensitivity estimates in the branching ratio versus decay length plane for FASER, MATHUSLA, and CODEX-b for neutrinos from W (Z) boson production on the left (right).*

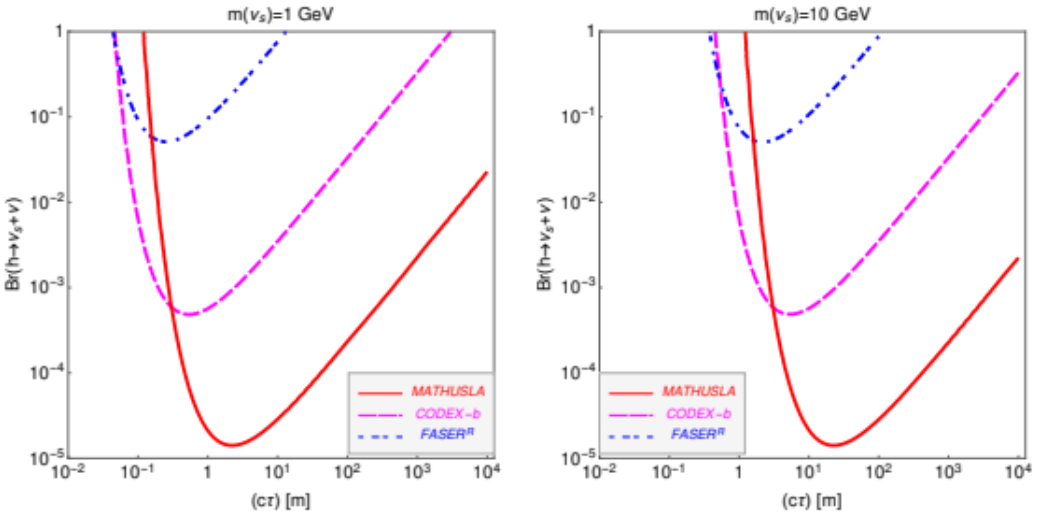

Figure 5.13: *Sensitivity estimates in the branching ratio versus decay length plane for FASER, MATHUSLA, and CODEX-b for neutrinos from H boson production: for* $m_N = 1$ GeV *on the left and for* $m_N = 10$ GeV *on the right.*

than the other FASER variants, is competitive with NA62 for $m_N \lesssim 2$ GeV, and has even better sensitivity than NA62 for $m_N \gtrsim 2$ GeV, while the fixed target experiment SHiP is more sensitive than FASER^R in the whole mass range.
From the plot on the right it is visible that FASER^R and CODEX-b[1] have similar sensitivities for $m_N \lesssim 3.2$ GeV, while MATHUSLA performs better than both in most parts of the parameter space. For $m_N \lesssim 0.5$ GeV, LBNE[2] has the best expected sensitivity, while for $m_N \gtrsim 0.5$ GeV SHiP is the most sensitive experiment, except for the $2 \lesssim m_N \lesssim 4$ GeV region where MATHUSLA is even better. MATHUSLA is competitive with SHiP also for $m_N \lesssim 2$ GeV, where it is only slightly less sensitive than SHiP. For larger masses, FASER^R and CODEX-b are worse than SHiP only by approximately one order of magnitude.

Regarding the already existing CMS and ATLAS experiments, sensitivity projections for new physics searches with 3000 fb^{-1}of data at the HL-LHC are being estimated [190–192]. In particular, a search for heavy composite Majorana neutrinos at the HL-LHC, in a final state with two leptons and at least one large-radius jet, is being carried out by the CMS experiment [193].
In a composite scenario, the heavy composite Majorana neutrino, N, is a particular case of excited states with masses lower than or equal to the compositeness scale Λ, interacting via contact interactions or gauge couplings with the ordinary SM fermions [194]. This study

[1]"Compact detector for Exotics at LHCb" [188], proposed detector for LLPs installed near the LHCb experiment and consisting of a cubic box with approximate dimensions of $10 \times 10 \times 10$ m^3.
[2]Long-Baseline Neutrino Experiment, near detector of the future DUNE experiment [189].

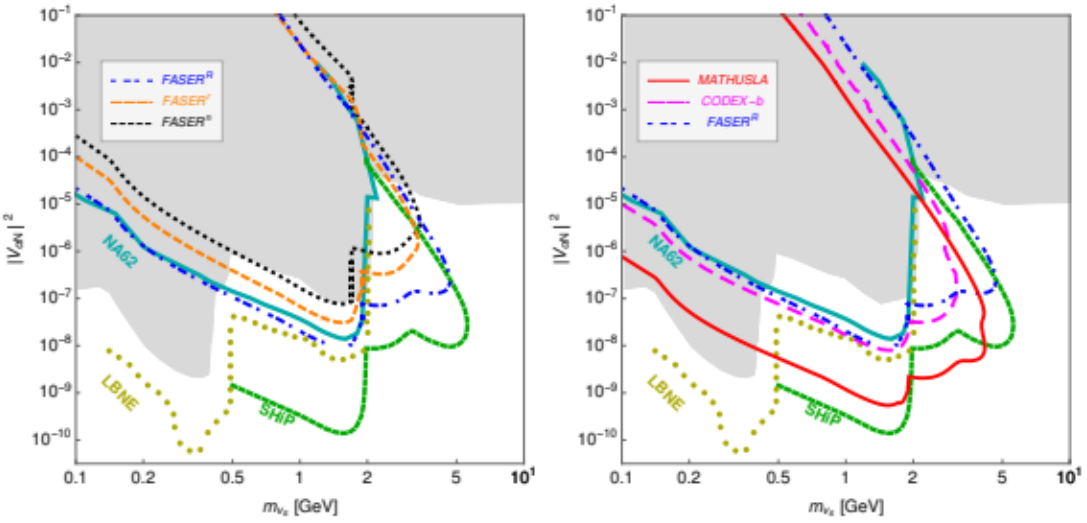

Figure 5.14: *Sensitivity estimates in the mixing angle $|V_{\alpha N}|^2$ versus neutrino mass m_N for the different variants of FASER on the left, and for FASER, MATHUSLA, CODEX-b, SHiP, NA62 and LBNE on the right.*

considers a heavy composite Majorana neutrino produced in association with a lepton and decaying into a same-flavour lepton plus two quarks, requiring two leptons and at least one large-radius jet in the signal region. The production cross section of the heavy composite Majorana neutrino for gauge and contact interaction at $\Lambda = 12$ TeV is presented in Figure 5.15. The heavy composite Majorana neutrino can decay through both gauge and contact interactions in:

$$N \to \ell q\bar{q},\ N \to \ell^+\ell^-\nu(\bar{\nu}),\ N \to \nu(\bar{\nu})q\bar{q}.$$

In this work, the final state considered is $\ell\ell q\bar{q}$ ($\ell = e, \mu$), which has the highest sensitivity and has already been studied in a previous search on Run 2 data [195], excluding heavy composite Majorana neutrinos with masses up to 4.6 TeV (4.7 TeV) in the electron (muon) channel, for the representative case $\Lambda = M_N$.
The projection study uses samples generated at $\sqrt{s} = 14$ TeV and processed through the Delphes [196] simulation of the Phase 2 CMS detector response. A shape-based analysis is performed looking at the invariant mass formed by the two leptons and the leading large-radius jet, $M(\ell\ell J)$, which provides a good discrimination between the signal and the SM backgrounds, as shown in Figure 5.16.
An upper limit at 95% CL on the cross section of the heavy composite Majorana neutrino produced in association with a lepton times its branching fraction to a same flavour lepton and two quarks, $\sigma(pp \to \ell N) \times B(N \to \ell qq)$, is then set and shown in Figure 5.17.

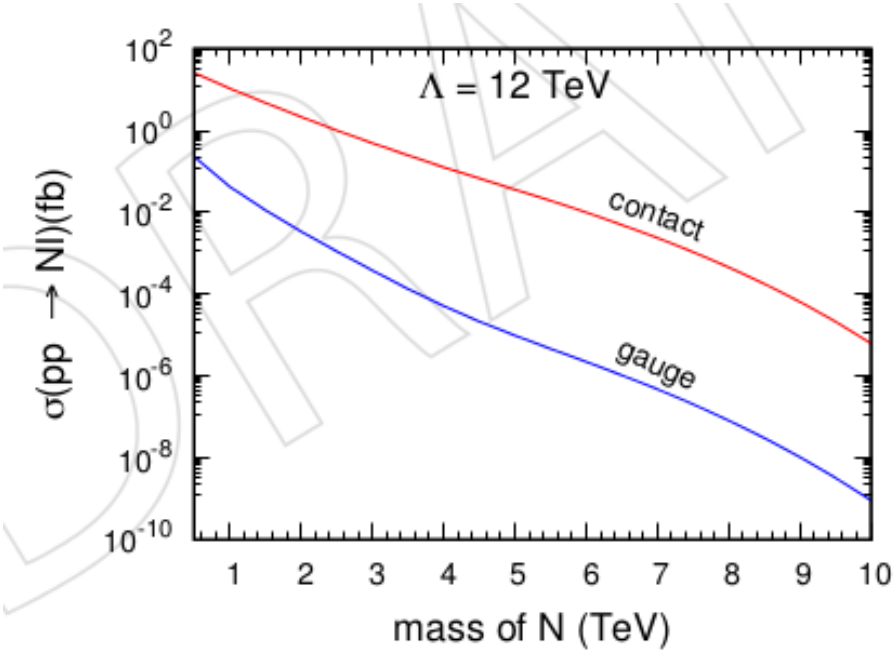

Figure 5.15: *Production cross section of the heavy composite Majorana neutrino for gauge and contact interaction at* $\Lambda = 12$ TeV *for pp collisions at* $\sqrt{s} = 14$ TeV. *[193]*

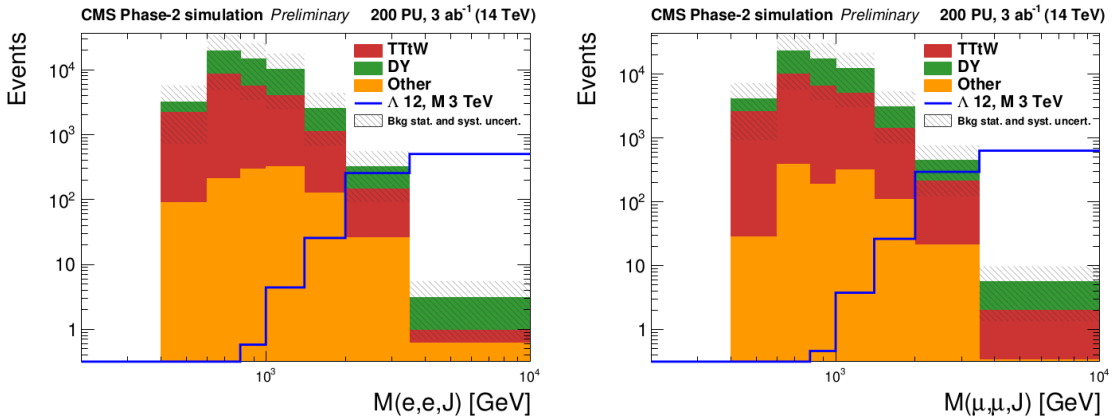

Figure 5.16: *Distribution of the variable* $M(\ell\ell J)$ *for backgrounds (stacked plots) and expected signal (blue line) in the signal region, considering the model parameters* $\Lambda = 12$ TeV *and* $M_N = 3$ TeV, *for the eeqq channel (left) and for the μμqq channel (right). The background uncertainties are the combined statistical and systematic uncertainties. [193]*

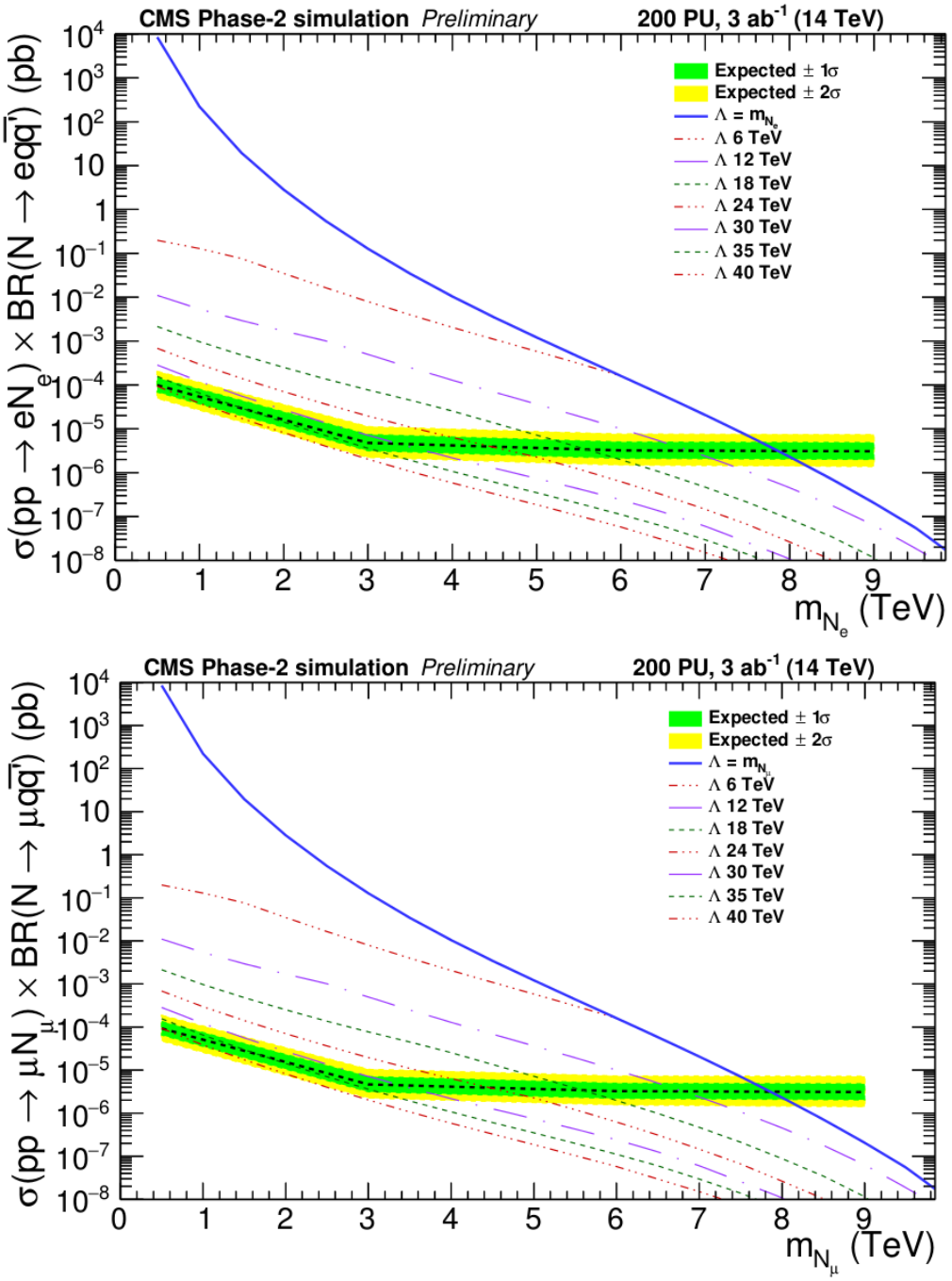

Figure 5.17: *The expected* 95% *CL upper limits (dashed black line) on* $\sigma(pp \to \ell N) \times B(N \to \ell qq)$*, for the eeqq (top) and the μμqq (bottom) final states, as a function of the mass of the heavy composite Majorana neutrino. The green and yellow bands represent the expected variation of the limit to one and two standard deviation(s), respectively. The solid blue curve indicates the theoretical prediction of* $\Lambda = M_N$*. The textured curves give the theoretical predictions for seven* Λ *values ranging from* 6 *to* 40 TeV*. [193]*

The HL-LHC, with a centre of mass energy of 14 TeV and with an integrated luminosity of 3000 fb^{-1}, will allow to extend significantly the region of the parameter space which can be probed, improving the sensitivity to cross-sections of order of $10^{-}6$ pb for heavy neutrino masses M_N ranging from 3 to 9 TeV for the $\ell\ell qq$ channel, where ℓ is an electron or a muon. For the compositeness scale $\Lambda = M_N$, the existence of a heavy Majorana neutrino could then be excluded for masses up to 8 TeV at 95% CL.

5.2.3 FCC-ee

The Future Circular Collider (FCC) is a proposed 100 km circular collider at CERN [178], shown in Figure 5.18. It can explore the $10 - 100$ TeV energy scale with precision measurements of W, Z, H, and top properties and can discover very weakly coupled particles in the $5 - 100$ GeV mass range.
There is a strong scientific case for an electron positron collider, complementary to the LHC, that can study the properties of the Higgs boson and other particles with unprecedented precision and whose energy can be upgraded. By the end of 2019 there will be a full proposal giving priority to a pp collider, with a timeline constrained by the evolution of magnet technology and by the HL-LHC timeline. The focus is thus on an initial $90 - 400$ GeV e^+e^- machine, and the aim is to achieve a 100 TeV hadron-hadron (hh) collider.

FCC-ee is a clean experimental environment that can probe complicated signatures such as displaced vertices and disappearing tracks, and scenarios with small masses, lifetimes, or couplings. The foreseen luminosity will enable to cover almost all the parameter space at any energy and the highest sensitivity is expected for $m_N < m_W$ ("low-mass" regime) which allows to test model predictions.
Long-lived particles (LLPs) searches at FCC-ee take advantage from full event reconstruction, much less (QCD) background, and no triggering issues but suffer from low center of mass energy (E_{CM}) and production rates. The searches for LLPs with very short lifetimes ($\approx$ mm) are thus advantaged but they are severely limited by E_{CM}.

The electron-proton collider FCC-eh has a good sensitivity for softly decaying, short-lived ($\approx \mu$m) LLPs because of very low PU, good tracking resolution, and boosted final states with larger center of mass energy than most lepton colliders. With respect to FC-hh it has a clean environment with smaller background, forward objects, and detection of BSM signal which looks like hadronic noise at hh colliders, but also small production due to smaller $\sqrt{s}$.
It has specialized scenarios with large signal rate for leptoquarks, heavy neutrinos, and W_{R} from LR symmetry but the corresponding hh program has greater reach.
FCC-hh and -eh are sensitive to the "high-mass" regime with direct tests of lepton-flavor violation (LFV) and lepton-number violation (LNV), useful to shed light on the number

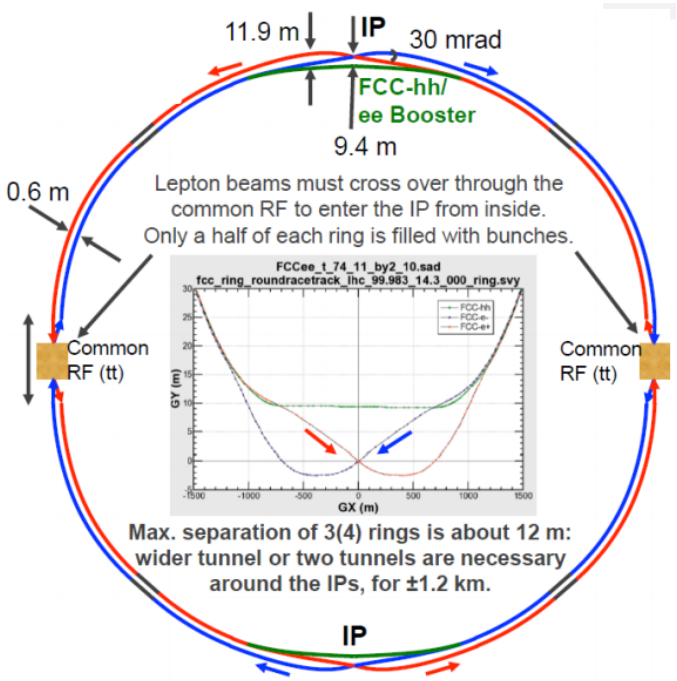

Figure 5.18: *Layout of the FCC collider.*

of heavy neutrino generations and their masses, and with indirect tests via measurements of Higgs potential.

The production and decay channels for sterile neutrinos are summarized in Figure 5.19: the final states visible on the right constitute the different signatures for direct searches of sterile neutrinos at the FCC colliders [197]. The most promising search strategies at the different colliders are the following:

- for FCC-ee: displaced vertices, electroweak precision measurements (mostly at the Z-pole), and H production and decay modes;
- for FCC-hh: displaced vertices, LNV and LFV dileptons-dijets ($\ell_\alpha \ell_\beta jj$), and LNV dileptons ($\ell_\alpha \ell_\beta \nu\nu$);
- for FCC-eh: LFV lepton-trijet ($\ell_\alpha^- jjj$), and LNV antilepton-trijets ($\ell_\alpha^+ jjj$).

The combination of ee with hh and eh colliders provides complementary tests for the sterile neutrino mass mechanism. The combination of direct and indirect signatures at all FCCs will pin down the parameters and test model specific predictions, testing in this way the origin of neutrino masses. Preliminary studies show a good potential for these searches, but a confirmation based on an accurate detector simulation is needed.
Searches for sterile neutrinos in Z decays look for $Z \to N\nu$, with $N \to W^*\ell$ or $Z^*\nu$ and very displaced secondary vertex. The number of events depends on the mixing between

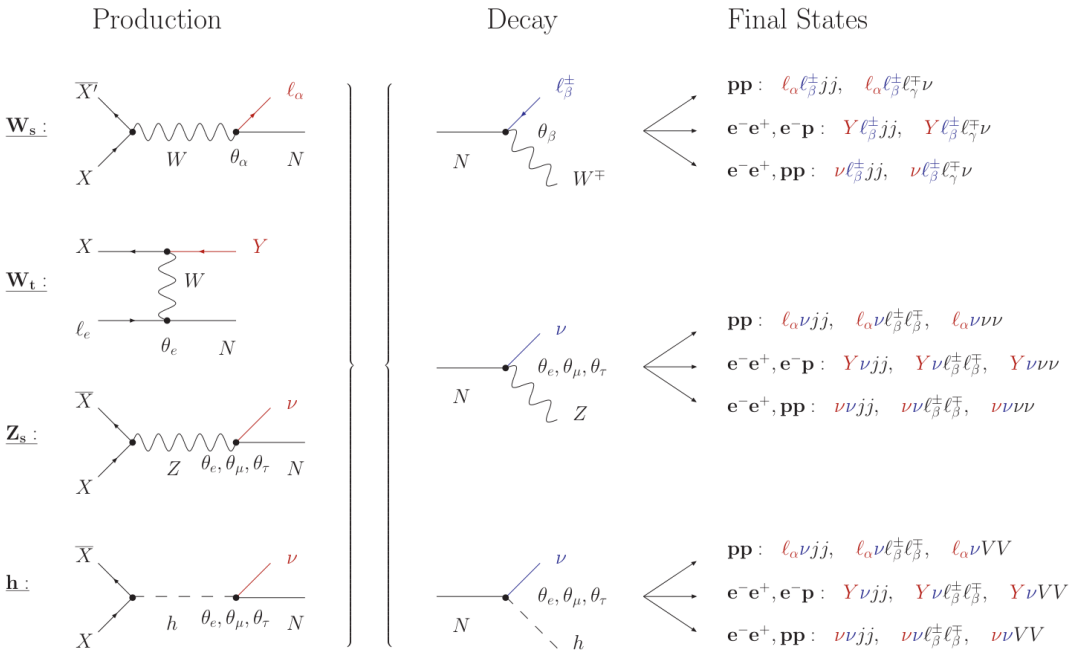

Figure 5.19: *Representation of different heavy neutrino production and decay channels at leading order, including the dependency of the active-sterile mixing parameters, with the possible final states for direct sterile neutrino searches at the FCC colliders.*

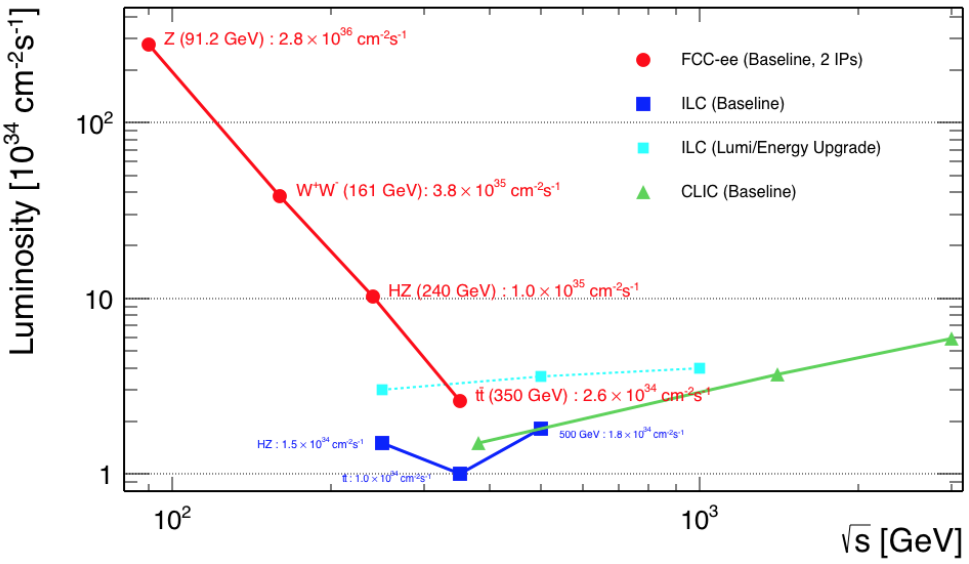

Figure 5.20: *Luminosity as a function of mass for different experiments.*

heavy N and light ν and on the mass of N. At the Z pole there will be very high luminosity for FCC-ee, as shown in Figure 5.20, allowing a total of 10^{12} Z bosons to be produced in a few years.
The direct searches appear very promising since, as shown in Figure 5.21, a sensitivity down to a heavy-light mixing of $|\theta|^2 \approx 10^{-12}$ is obtained for heavy neutrino masses between 10 and 80 GeV, and a sensitivity down to $|\theta|^2 \approx 10^{-14}$ is obtained for heavy neutrino masses up to 200 GeV [198].
For the sensitivity of the displaced vertex searches, the projections on the mixing angle between one HNL and a lepton as a function of the HNL mass are shown in Figures 5.22, 5.23, and 5.24 for FCC-ee, FCC-hh, and FCC-eh respectively [197].

5.2.4 ILC

The International Linear Collider (ILC) [199] is a proposed linear electron-positron collider that can initially achieve center-of-mass energies of $200 - 500$ GeV, with a later upgrade to ≈ 1 TeV.
Heavy neutrinos can be searched in a $m_N < 30$ GeV region, where the dominant decay mode of the Majorana neutrino is $N \to \gamma + \nu$ [200], whose Feynman diagrams are shown in Figure 5.25. The cross section of this process at ILC increases with the increase of m_N and with the increase of center-of-mass energy, as shown in Figure 5.26, since the contribution from the third production diagram of Figure 5.25 is greatly enhanced by a large center-of-mass energy.
The integrated luminosities necessary to observe the Majorana neutrinos at 3σ and 5σ with $\sqrt{s} = 350$ GeV and $\sqrt{s} = 500$ GeV at ILC are shown in Figure 5.27 as a function of m_N. The observation capability will decrease with the decrease of m_N, but since the integrated luminosity expected with $\sqrt{s} = 500$ GeV at ILC is of 3500 fb^{-1}, Majorana neutrinos may be easily detected in future linear colliders.

For the seesaw mechanism at the TeV scale or lower, the Dirac Yukawa coupling is too small ($Y_D \approx 10^{-6} - 10^{-5}$) to produce an observable amount of heavy neutrinos at the colliders. These can be produced at high energy colliders considering the inverse seesaw scenario [201], through sizable mixing with the SM neutrinos. The ILC can produce heavy neutrinos in the process $e^+e^- \to \bar{\nu}_l N_l$ exchanging W or Z bosons.
The total production cross sections for this process at the ILC with $\sqrt{s} = 500$ GeV and 1 TeV are shown in Figure 5.28.
The final state considered is a single isolated lepton plus dijet with large missing energy: $e^+e^- \to \bar{\nu}_l N_l$ is followed by the decays $N \to lW$ and $W \to q\bar{q}'$, through which the heavy neutrino production cross sections and the heavy neutrino mass can be reconstructed. The main backgrounds are $e\nu W \to e\nu q\bar{q}$ and $WW \to l\nu q\bar{q}$, which can be reduced by kinematic selections. The production cross sections for these processes are shown as a function of the heavy neutrino mass in Figure 5.29.

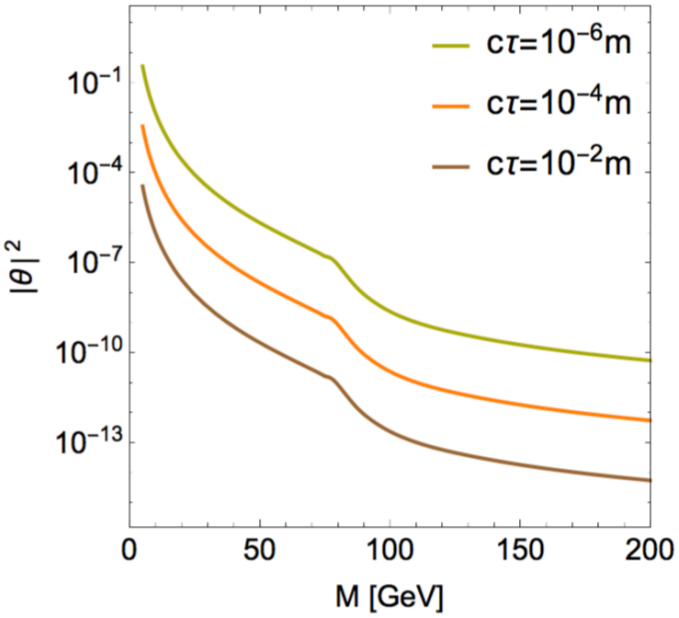

Figure 5.21: *Projections on the mixing angle between one HNL and a lepton as a function of the HNL mass for different lifetimes.*

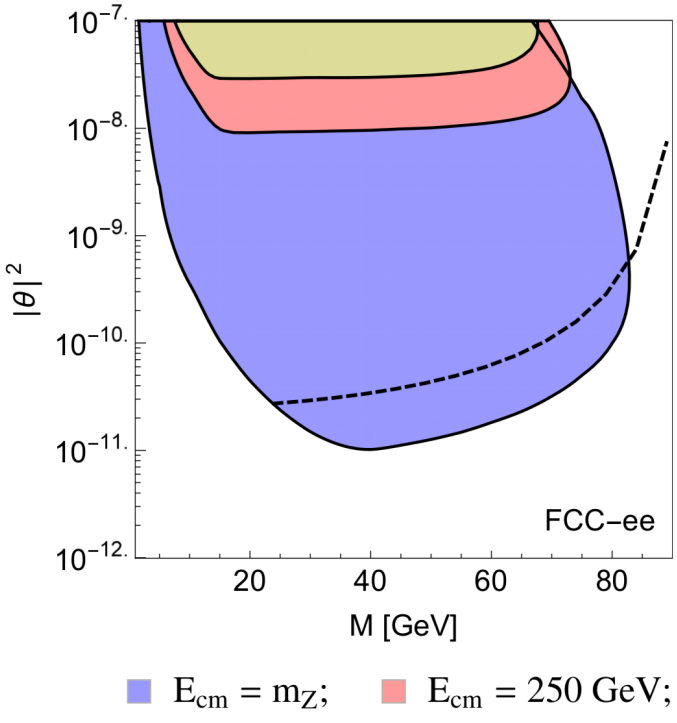

Figure 5.22: *Projections on the mixing angle between one HNL and a lepton as a function of the HNL mass for FCC-ee.*

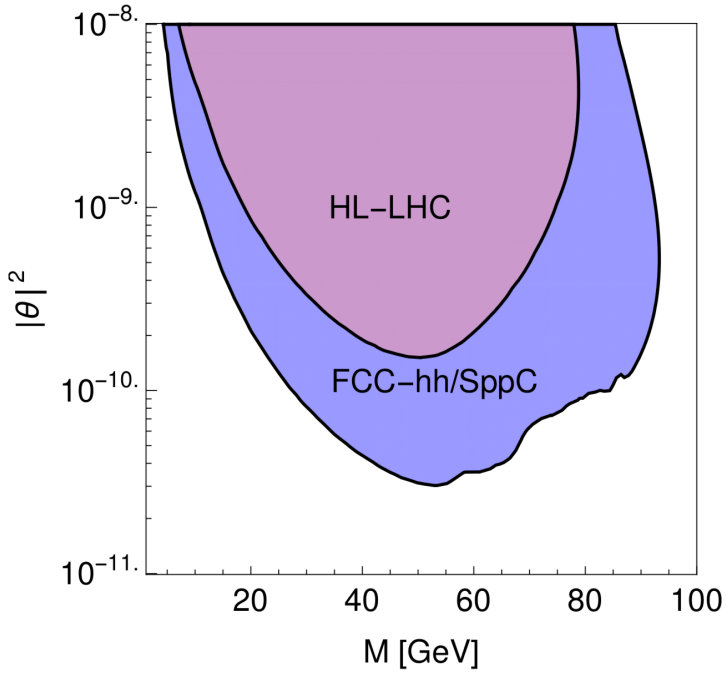

Figure 5.23: *Projections on the mixing angle between one HNL and a lepton as a function of the HNL mass for FCC-hh and HL-LHC.*

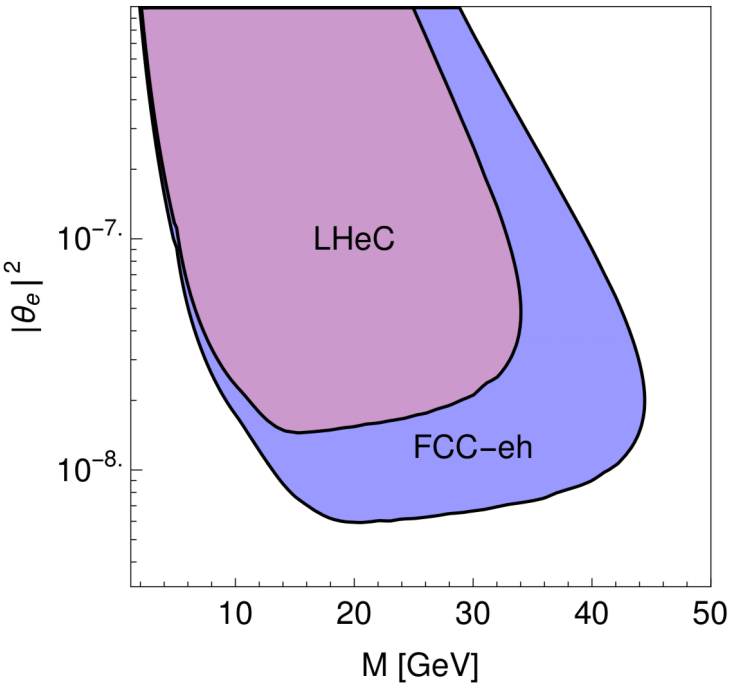

Figure 5.24: *Projections on the mixing angle between one HNL and a lepton as a function of the HNL mass for FCC-eh.*

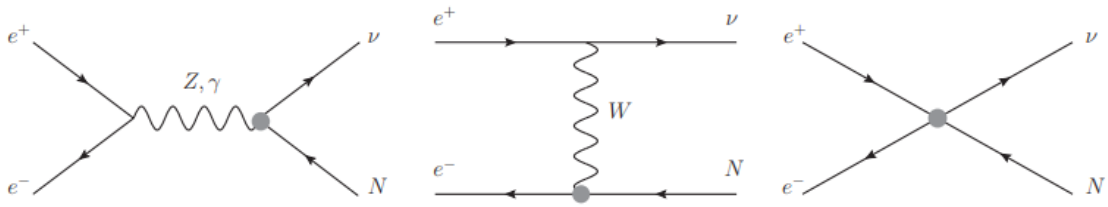

Figure 5.25: *Feynman diagrams for the $e^+e^- \to \nu N$ process.*

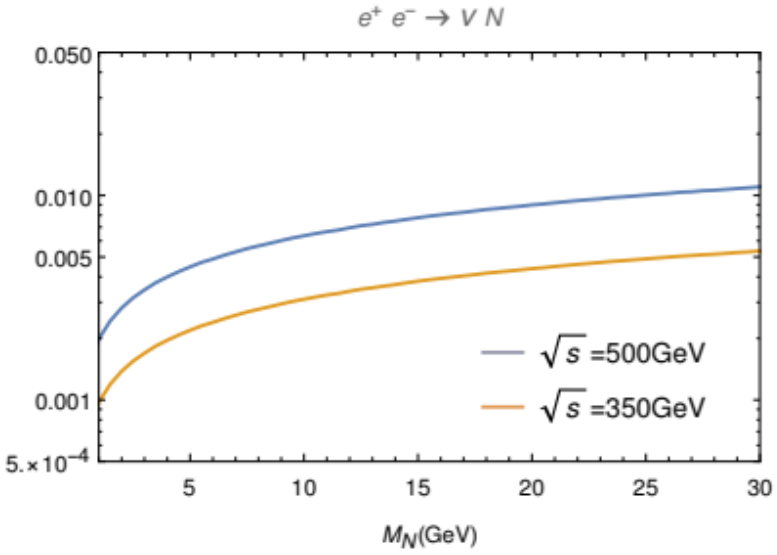

Figure 5.26: *Cross sections of $e^+e^- \to \nu N$ as a function of m_N at ILC.*

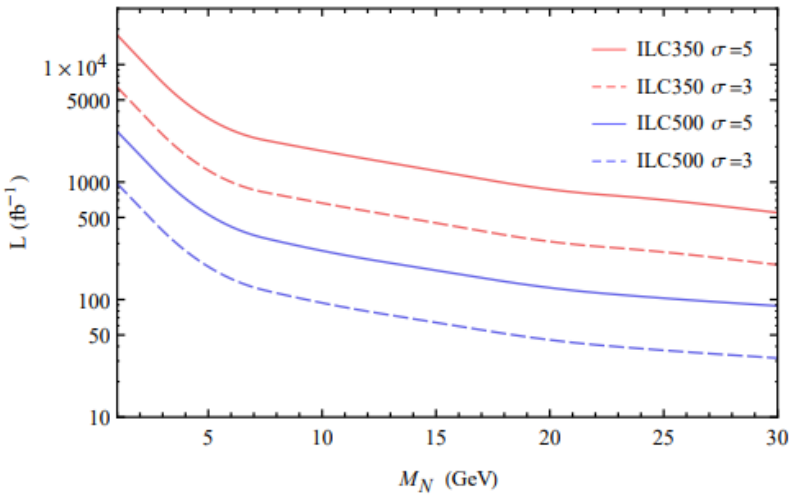

Figure 5.27: *Integrated luminosity necessary for observing the Majorana neutrino at the* 3σ *(dashed line) and* 5σ *(solid line) levels at ILC with* $\sqrt{s} = 350$ GeV *(red) and* $\sqrt{s} = 500$ GeV *(blue).*

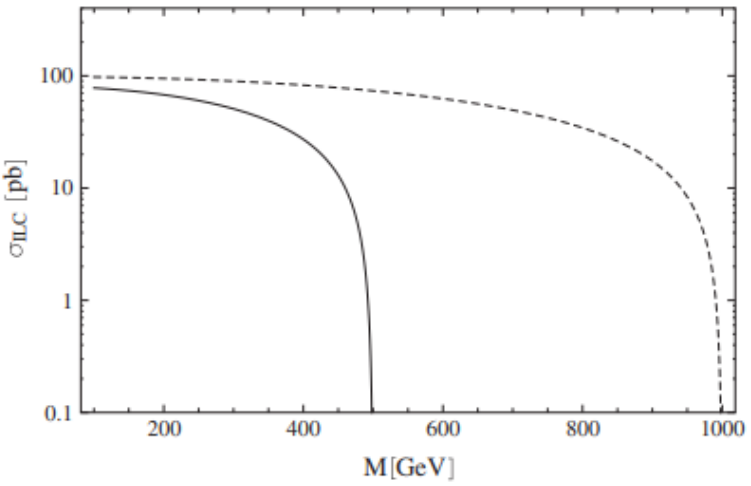

Figure 5.28: *Total production cross section of the* $e^+e^- \to \bar{\nu}_l N_l$ *process at the ILC with* $\sqrt{s} = 500$ GeV *(solid line) and* 1 TeV *(dashed line).*

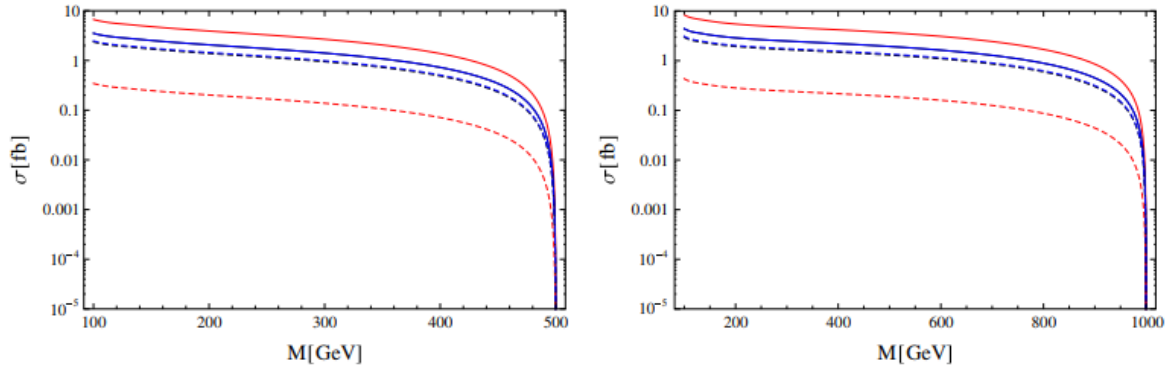

Figure 5.29: *Production cross section of the* $e^+e^- \to n\bar{u}_l N_l$ *process, followed by the decays* $N \to lW$ $(l = e, \mu, \tau)$ *and* $W \to q\bar{q}'$*, as a function of the heavy neutrino mass at* $\sqrt{s} =$ 500 GeV *on the left and at* 1 TeV *on the right.*

5.3 Conclusions

LHC is still a developing area of research with new techniques, new specific triggers and more data to collect. Moreover, a lot of channels have still to be explored, like other production modes and displaced decays which will increase the sensitivity to HNLs with low mass and low couplings. Future searches at LHC will then allow to significantly extend the parameter space probed so far.

The synergy between experiments like SHiP and FCC-*ee* will allow the exploration of a large parameter space for sterile neutrinos, providing great prospects for right-handed neutrino searches also at future experiments.

A comparison of the estimated sensitivities for the different colliders is shown in Figure 5.30 [197]. For masses below m_W, the best sensitivity of $|\theta|^2 \approx 10^{-11}$ can be reached via displaced vertex searches by electron-positron colliders like FCC-*ee*. Above the W mass, the best sensitivity of $|\theta|^2 \approx 10^{-6}$ for $m \approx 200$ GeV can be achieved by electron-positron colliders like FCC-*eh*, while proton-proton colliders like FCC-*hh* can reach $|\theta|^2 \approx 10^{-5}$ for $m \approx 200$ GeV.

Via the direct searches, the HL-LHC and FCC-*hh* can thus test heavy neutrinos with masses up to ≈ 450 GeV and 2 TeV, respectively. The electron-proton colliders LHeC and FCC-*eh* can extend the mass reach of the proton-proton colliders and test heavy neutrinos masses up to ≈ 1 TeV and 2.7 TeV, respectively.

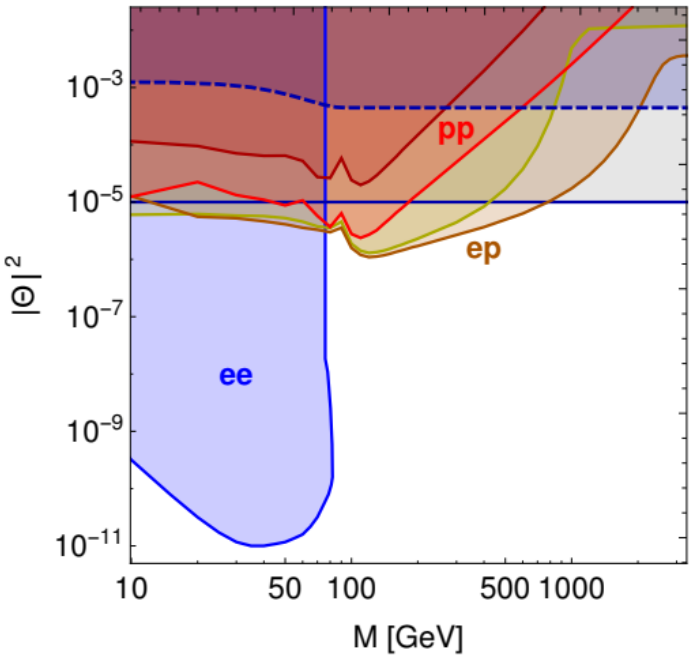

Figure 5.30: *Sensitivities of the FCC-ee (blue line), FCC-hh (red line), and FCC-eh (brown line) colliders, including the HL-LHC (dark-red line) and the LHeC (yellow line) [197]. The solid and dashed horizontal blue line denotes the sensitivity to* $|\theta_e|^2 + |\theta_\mu|^2$ *and* $|\theta_\tau|^2$*, respectively.*

Appendix A

Drell–Yan Monte Carlo studies

As already seen in the 2015 analysis, the aMC@NLO generator for the DY+jets samples describes better the data. The event selection of this analysis requires that the additional jets produced as initial state radiation have p_T greater than 40 GeV. This region of phase space is not well modeled by MADGRAPH, as seen in Figure A.1 for both the electron and the muon channel in the *low-*$m_{\ell\ell}$ CR, then the aMC@NLO generator is used.

A possible solution to the small disagreement visible in the comparison between the data and the MADGRAPH DY+jets MC is to reweight the MC as a function of some variable instead of a flat scale factor. As seen in Figure A.1, the disagreement is mostly in the jet momenta and thus in the HT distribution. The MC is then reweighted to the data in the *low-*$m_{\ell\ell}$ CR so that the HT distributions match. The weighted distributions for the electron and the muon channels are shown in Figure A.2, where the binning was chosen so that the statistical uncertainty in each data bin is about 1%. The results of the reweighting are shown in Figure A.3. Even though the HT was corrected to match the data, it is clear that the $m_{\ell\ell\mathrm{jj}}$ distribution is still not well modeled by the MADGRAPH generator in this region of phase space. By reweighting the MC, the over-estimation seen in $m_{\ell\ell\mathrm{jj}} > 1000$ GeV is now seen slightly below 1000 GeV. The choice of using the aMC@NLO generator is thus well motivated.

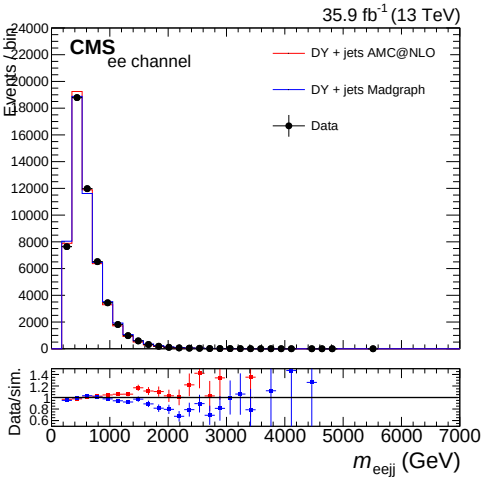

(a) *Electron channel:* $m_{\ell\ell\mathrm{jj}}$

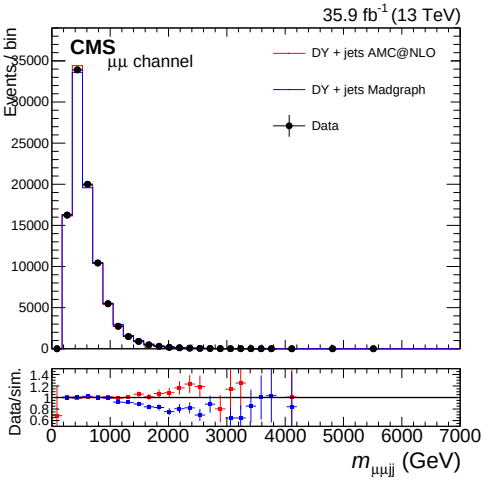

(b) *Muon channel:* $m_{\ell\ell\mathrm{jj}}$

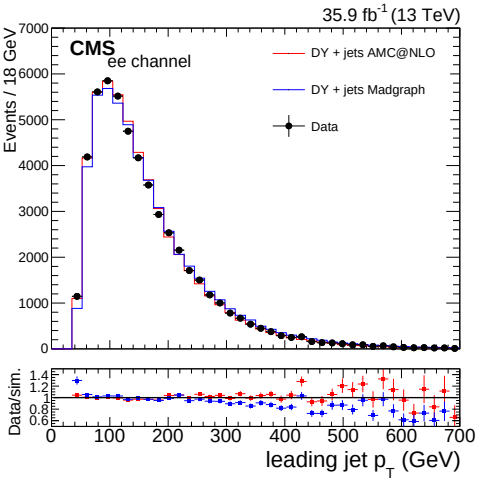

(c) *Electron channel: leading jet* p_T

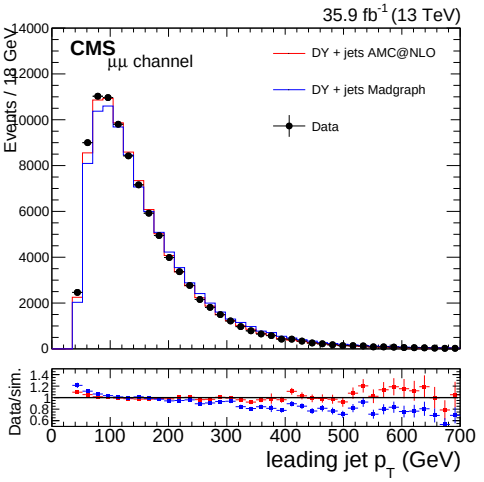

(d) *Muon channel: leading jet* p_T

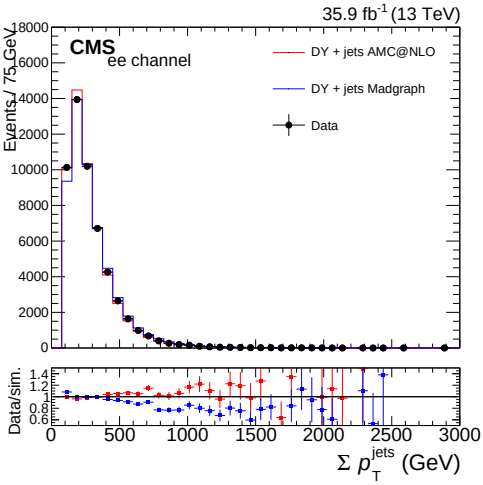

(e) *Electron channel: HT*

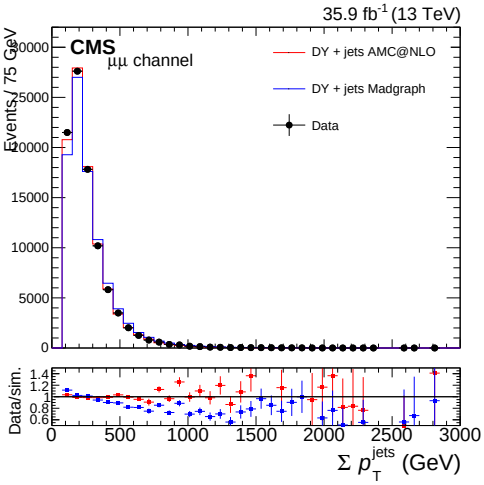

(f) *Muon channel: HT*

Figure A.1: *Comparison between the data and the* MADGRAPH *and* aMC@NLO *DY MC samples in the* low-$m_{\ell\ell}$ *CR.*

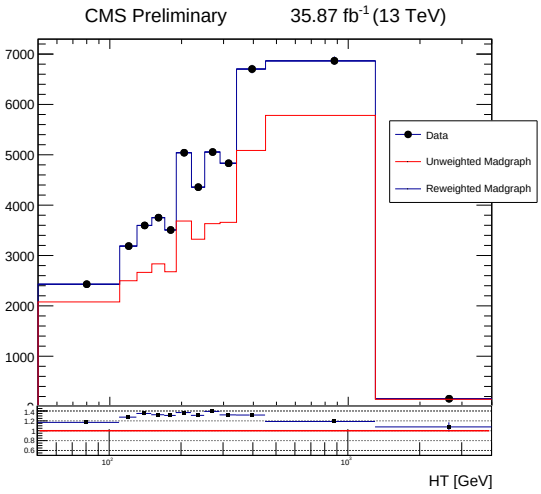

(a) *Electron channel*

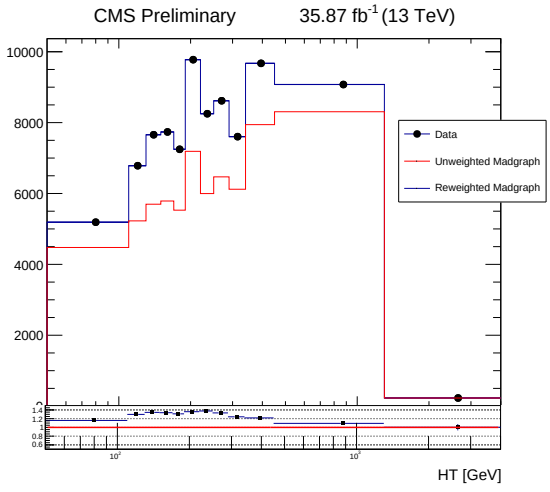

(b) *Muon channel*

Figure A.2: *Reweighted HT distributions for* MADGRAPH *in the* low-$m_{\ell\ell}$ *CR.*

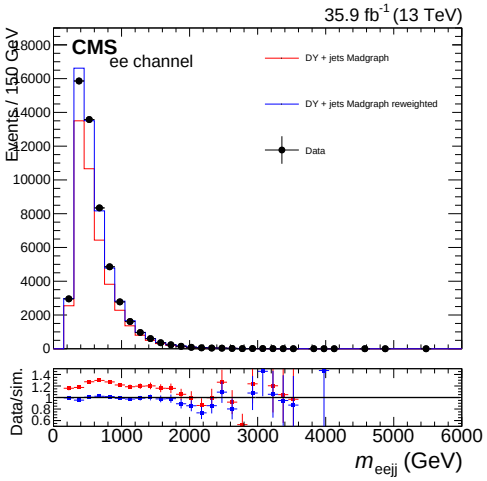

(a) *Electron channel:* $m_{\ell\ell\mathrm{jj}}$

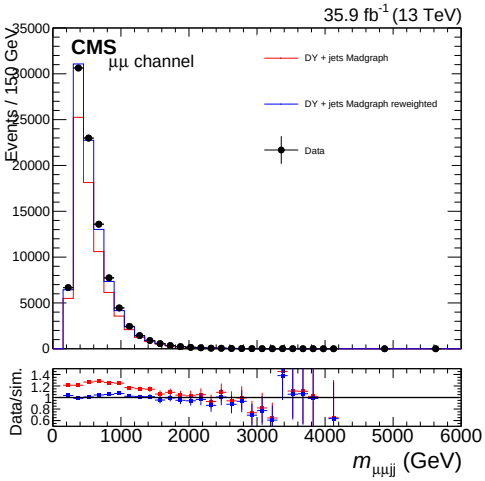

(b) *Muon channel:* $m_{\ell\ell\mathrm{jj}}$

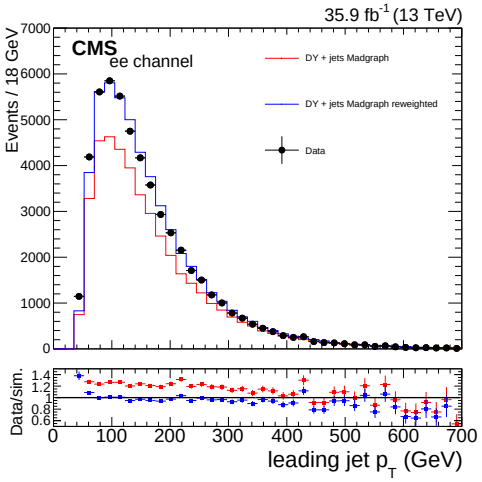

(c) *Electron channel: leading jet* p_T

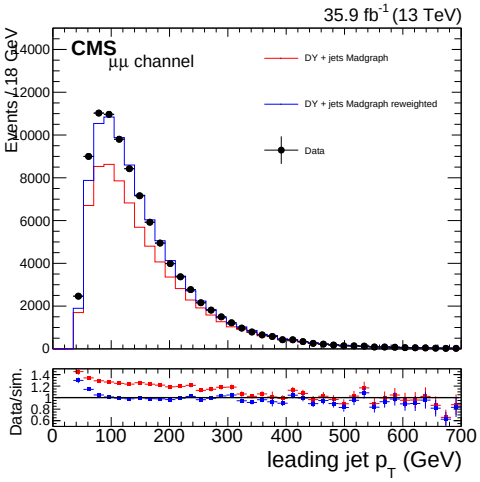

(d) *Muon channel: leading jet* p_T

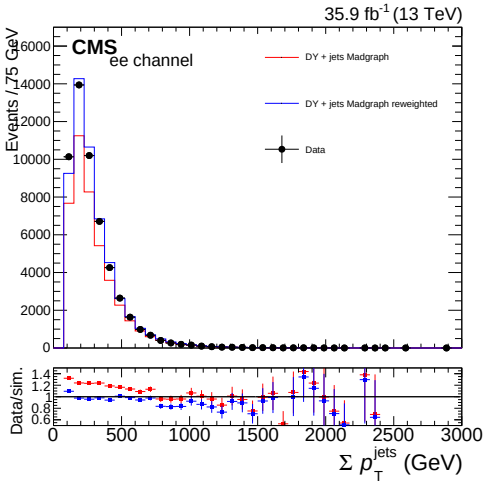

(e) *Electron channel: HT*

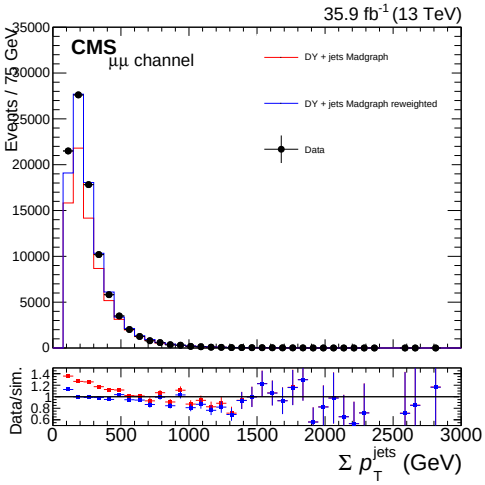

(f) *Muon channel: HT*

Figure A.3: *Comparison between the data and the DY* MADGRAPH *samples before and after reweighting in the* low-$m_{\ell\ell}$ *CR.*

Appendix B

Statistics of DY aMC@NLO sample

It was seen that the DY+jets MC samples were limited by the low statistics at high $m_{\ell\ell\mathrm{jj}}$ masses. This problem is more evident in the aMC@NLO sample because of the negative generator weights. The statistical errors for weighted events are calculated as $\sqrt{\Sigma w_i^2}$, where w_i is the weight of event i and the sum runs over all events in a $m_{\ell\ell\mathrm{jj}}$ window, leading to a worse uncertainty than the one expected from a simple Poisson distribution. The rates for the different mass windows are presented in Table B.1 for the electron channel and in Table B.2 for the muon channel.

Table B.1: *Event counts in each of the $m_{\ell\ell jj}$ mass windows for the DY+jets* aMC@NLO *sample in the electron channel. The raw number of events is presented, as well as the actual event rate with the corresponding statistical uncertainty.*

W_R mass (GeV)	Raw events	Actual rate	Stat. uncertainty
1000	64950	1174.46	21.84
1200	66022	1177.74	21.85
1400	64091	1064.72	20.02
1600	53570	649.28	14.48
1800	39362	362.31	9.87
2000	24835	170.34	6.16
2200	18060	96.90	4.37
2600	9274	32.44	2.27
2800	6507	16.83	1.67
3000	4022	9.74	1.20
3200	2752	5.80	0.97
3400	2036	3.37	0.76
3600	1409	1.99	0.50
3800	1062	1.67	0.37
4200	610	1.00	0.28
4400	508	1.00	0.26
4800	366	0.75	0.20
5000	328	0.71	0.20
5200	301	0.68	0.20
5600	369	0.72	0.20
5800	415	0.89	0.23
6000	520	0.98	0.26

Table B.2: *Event counts in each of the $m_{\ell\ell jj}$ mass windows for the DY+jets* aMC@NLO *sample in the muon channel. The raw number of events is presented, as well as the actual event rate with the corresponding statistical uncertainty.*

W_R mass (GeV)	Raw events	Actual rate	Stat. uncertainty
1000	86117	1847.98	29.22
1200	93587	1888.07	29.35
1400	96836	1898.21	29.37
1600	97992	1886.68	29.16
1800	86592	1360.19	22.93
2000	72349	904.85	17.33
2200	46231	433.29	10.76
2400	32084	250.71	7.50
2600	21623	124.72	4.86
2800	16085	72.77	3.72
3000	10590	38.70	2.53
3200	6756	19.08	1.69
3400	4662	11.16	1.31
3600	2921	6.42	0.91
3800	1992	4.39	0.76
4000	1383	2.91	0.66
4200	1058	2.04	0.57
4400	810	1.37	0.43
4600	623	0.89	0.40
4800	508	0.77	0.25
5000	438	0.50	0.22
5200	405	0.48	0.22
5400	405	0.48	0.22
5600	439	0.50	0.22
5800	510	0.77	0.25
6000	626	0.91	0.40

Appendix C

Punzi mass range optimization

The Punzi significance, which provides an estimate for a signal significance alternative to the one used in this analysis, is described in [164]. It performs better when there are low background yields and it is independent of signal cross section, being independent of a-priori expectations about the presence of a signal. As described in the reference, assuming that the Poisson distribution of observed events is approximated by a Gaussian distribution, and that the efficiency of the selections on the signal is independent of the cross section of the process, the optimal set of selections (t) can be optimized by maximizing

$$\text{sig} = \frac{\epsilon(t)}{a/2 + \sqrt{B(t)}},$$

where a is the expected number of sigmas corresponding to the one-sided Gaussian tests with significance level α, $\epsilon(t)$ is the signal efficiency as a function of the selections, and $B(t)$ is the number of expected background events as a function of the selections.

In the case of finding the optimal mass ranges to calculate the cross section limits of the W_{R} signal, the signal efficiency and background number of events are functions of the window sizes. The Punzi significance was optimized to determine the upper and lower bounds of the mass windows and the results are shown in Figure C.1.
There is a feature in the electron channel where the window size gets much larger after a certain W_{R} mass hypothesis ($m_{W_{\mathrm{R}}} \sim 3400$ GeV). The windows were recalculated using the Punzi significance and a new background estimate, taken from a smooth distribution where an exponential function was fitted in the low $m_{\ell\ell\mathrm{jj}}$ region and extrapolated to high masses. The results, presented in Figure C.2, show the same feature, so this is a feature of the Punzi significance rather than a statistical effect caused by the lack of events in the high $m_{\ell\ell\mathrm{jj}}$ region. This can be interpreted as that, when the background estimate is low enough, the optimal upper window should be as large as possible as to include as much signal since the background contribution is negligible.

The limits on the W_{R} cross section, with mass windows optimized for the Punzi sig-

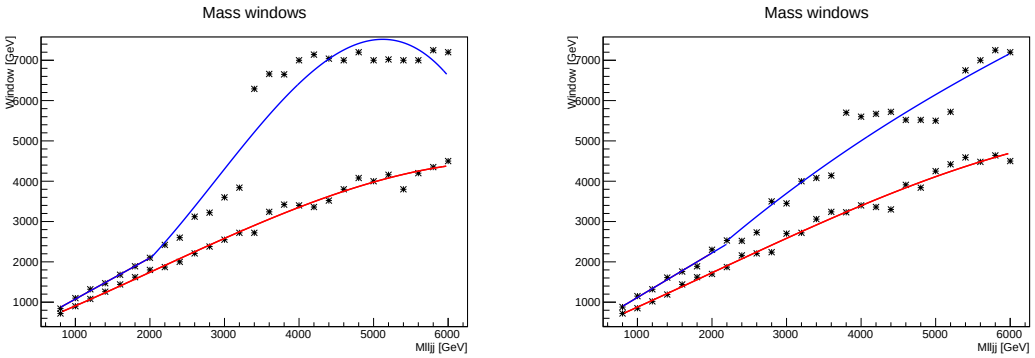

(a) $W_R \to$ eejj *windows* (b) $W_R \to \mu\mu$jj *windows*

Figure C.1: *Mass window edges optimized for Punzi signal significance. Windows are smoothed out by fitting a third degree polynomial.*

nificance, were calculated and are shown in Figure C.3. The limits obtained with this procedure are consistent with those obtained when the mass windows are optimized for the cross section upper limit as was done in the previous iteration of this analysis.
The Punzi significance is a useful tool, but it was not shown to provide large enough improvements on the limit calculation thus it was not pursued for this analysis.

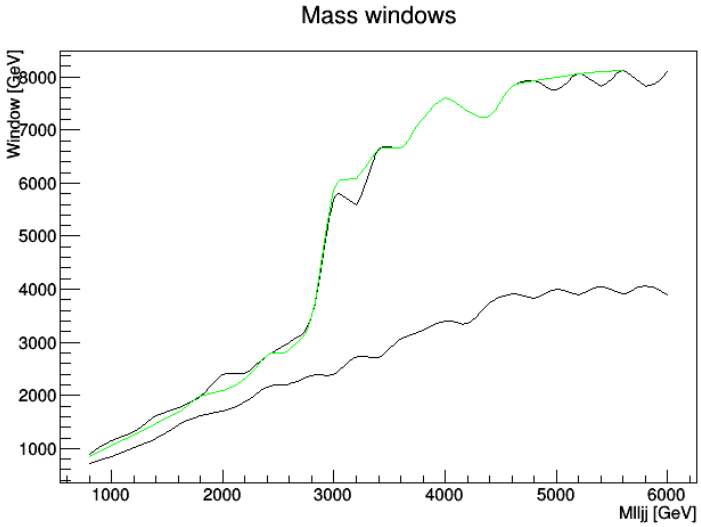

Figure C.2: *Mass window edges optimized for Punzi signal significance using an analytical approximation of the background estimate. The green curve corresponds to the exponential fit while the black curve uses a combined electron/muon MC estimate.*

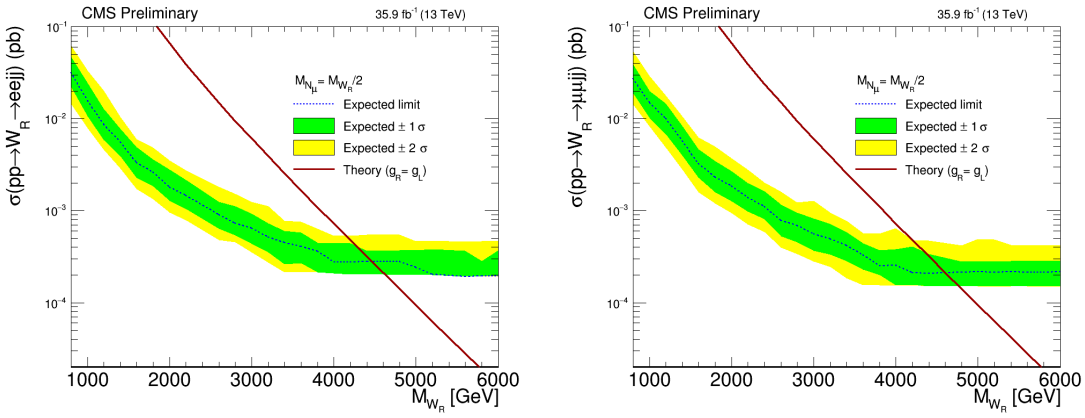

(a) *Electron channel* (b) *Muon channel*

Figure C.3: *Expected limit on* $\sigma(pp \to W_{\mathrm{R}}) \times BR(W_{\mathrm{R}} \to \ell\ell\mathrm{jj})$ *with systematic uncertainties obtained for the Punzi significance optimization.*

Bibliography

[1] Steven Weinberg. A Model of Leptons. *Phys. Rev. Lett.*, 19:1264–1266, 1967.

[2] S. L. Glashow. Partial Symmetries of Weak Interactions. *Nucl. Phys.*, 22:579–588, 1961.

[3] Georges Aad et al. Observation of a new particle in the search for the Standard Model Higgs boson with the ATLAS detector at the LHC. *Phys. Lett.*, B716:1–29, 2012.

[4] Serguei Chatrchyan et al. A New Boson with a Mass of 125 GeV Observed with the CMS Experiment at the Large Hadron Collider. *Science*, 338:1569–1575, 2012.

[5] Georges Aad et al. Combined Measurement of the Higgs Boson Mass in pp Collisions at $\sqrt{s} = 7$ and 8 TeV with the ATLAS and CMS Experiments. *Phys. Rev. Lett.*, 114:191803, 2015.

[6] F. Halzen and Alan D. Martin. *QUARKS AND LEPTONS: AN INTRODUCTORY COURSE IN MODERN PARTICLE PHYSICS*. 1984.

[7] F. J. Hasert et al. Observation of Neutrino Like Interactions Without Muon Or Electron in the Gargamelle Neutrino Experiment. *Phys. Lett.*, B46:138–140, 1973. [,5.15(1973)].

[8] G. Arnison et al. Experimental Observation of Lepton Pairs of Invariant Mass Around 95-GeV/c**2 at the CERN SPS Collider. *Phys. Lett.*, B126:398–410, 1983. [,7.55(1983)].

[9] P. Bagnaia et al. Evidence for Z0 —> e+ e- at the CERN anti-p p Collider. *Phys. Lett.*, B129:130–140, 1983. [,7.69(1983)].

[10] G. Arnison et al. Experimental Observation of Isolated Large Transverse Energy Electrons with Associated Missing Energy at s**(1/2) = 540-GeV. *Phys. Lett.*, B122:103–116, 1983. [,611(1983)].

[11] M. Banner et al. Observation of Single Isolated Electrons of High Transverse Momentum in Events with Missing Transverse Energy at the CERN anti-p p Collider. *Phys. Lett.*, B122:476–485, 1983. [,7.45(1983)].

[12] G. Arnison et al. Observation of the Muonic Decay of the Charged Intermediate Vector Boson. *Phys. Lett.*, 134B:469–476, 1984.

[13] G. Abbiendi et al. Measurement of the mass and width of the W boson. *Eur. Phys. J.*, C45:307–335, 2006.

[14] S. Schael et al. Measurement of the W boson mass and width in e^+e^- collisions at LEP. *Eur. Phys. J.*, C47:309–335, 2006.

[15] P. Achard et al. Measurement of the mass and the width of the W boson at LEP. *Eur. Phys. J.*, C45:569–587, 2006.

[16] J. Abdallah et al. Measurement of the Mass and Width of the W Boson in e^+e^- Collisions at $\sqrt{s}$ = 161-GeV - 209-GeV. *Eur. Phys. J.*, C55:1–38, 2008.

[17] B. Abbott et al. A measurement of the W boson mass. *Phys. Rev.*, D58:092003, 1998.

[18] B. Abbott et al. A measurement of the W boson mass using large rapidity electrons. *Phys. Rev.*, D62:092006, 2000.

[19] T. Affolder et al. Measurement of the W boson mass with the Collider Detector at Fermilab. *Phys. Rev.*, D64:052001, 2001.

[20] Roel Aaij et al. Observation of the resonant character of the $Z(4430)^-$ state. *Phys. Rev. Lett.*, 112(22):222002, 2014.

[21] Roel Aaij et al. Observation of $J/\psi p$ Resonances Consistent with Pentaquark States in $\Lambda_b^0 \to J/\psi K^- p$ Decays. *Phys. Rev. Lett.*, 115:072001, 2015.

[22] Makoto Kobayashi and Toshihide Maskawa. CP Violation in the Renormalizable Theory of Weak Interaction. *Prog. Theor. Phys.*, 49:652–657, 1973.

[23] Nicola Cabibbo. Unitary Symmetry and Leptonic Decays. *Phys. Rev. Lett.*, 10:531–533, 1963. [,648(1963)].

[24] Ziro Maki, Masami Nakagawa, and Shoichi Sakata. Remarks on the unified model of elementary particles. *Prog. Theor. Phys.*, 28:870–880, 1962. [,34(1962)].

[25] Georges Aad et al. Measurements of the Higgs boson production and decay rates and constraints on its couplings from a combined ATLAS and CMS analysis of the LHC pp collision data at $\sqrt{s} = 7$ and 8 TeV. *JHEP*, 08:045, 2016.

[26] Alesandro Bravar. The Mu3e Experiment at PSI. *PoS*, ICHEP2016:552, 2016.

[27] L. A. Winslow. Discovering the majorana neutrino: The next generation of experiments. *AIP Conference Proceedings*, 1666(1):170005, 2015.

[28] S. Dawson. Introduction to Electroweak Symmetry Breaking. *AIP Conf. Proc.*, 1116:11–34, 2009.

[29] F. Englert and R. Brout. Broken Symmetry and the Mass of Gauge Vector Mesons. *Phys. Rev. Lett.*, 13:321–323, 1964. [,157(1964)].

[30] Peter W. Higgs. Broken Symmetries and the Masses of Gauge Bosons. *Phys. Rev. Lett.*, 13:508–509, 1964. [,160(1964)].

[31] G. S. Guralnik, C. R. Hagen, and T. W. B. Kibble. Global Conservation Laws and Massless Particles. *Phys. Rev. Lett.*, 13:585–587, 1964. [,162(1964)].

[32] J. Goldstone. Field Theories with Superconductor Solutions. *Nuovo Cim.*, 19:154–164, 1961.

[33] Jeffrey Goldstone, Abdus Salam, and Steven Weinberg. Broken Symmetries. *Phys. Rev.*, 127:965–970, 1962.

[34] J. Beringer et al. Review of Particle Physics (RPP). *Phys. Rev.*, D86:010001, 2012.

[35] Antonio Pich. The Standard Model of Electroweak Interactions. In *Proceedings, High-energy Physics. Proceedings, 18th European School (ESHEP 2010): Raseborg, Finland, June 20 - July 3, 2010*, pages 1–50, 2012. [,1(2012)].

[36] Paul Langacker. *The standard model and beyond*. 2010.

[37] M. Persic and P. Salucci. Dark and visible matter in spiral galaxies. *Mon. Not. Roy. Astron. Soc.*, 234:131–154, 1988.

[38] Stephen P. Martin. A Supersymmetry primer. pages 1–98, 1997. [Adv. Ser. Direct. High Energy Phys.18,1(1998)].

[39] D. S. Akerib et al. First results from the LUX dark matter experiment at the Sanford Underground Research Facility. *Phys. Rev. Lett.*, 112:091303, 2014.

[40] Xin Wu. The Silicon-Tungsten Tracker of the DAMPE Mission. *PoS*, ICRC2015:1192, 2016.

[41] B. Pontecorvo. Neutrino Experiments and the Problem of Conservation of Leptonic Charge. *Sov. Phys. JETP*, 26:984–988, 1968. [Zh. Eksp. Teor. Fiz.53,1717(1967)].

[42] K. S. Hirata et al. Observation of B-8 Solar Neutrinos in the Kamiokande-II Detector. *Phys. Rev. Lett.*, 63:16, 1989.

[43] John N. Bahcall. Two solar neutrino problems. *Physics Letters B*, 338(2):276 – 281, 1994.

[44] P. Adamson et al. First measurement of electron neutrino appearance in NOvA. *Phys. Rev. Lett.*, 116(15):151806, 2016.

[45] Ch. Kraus et al. Final results from phase II of the Mainz neutrino mass search in tritium beta decay. *Eur. Phys. J.*, C40:447–468, 2005.

[46] K. Abe et al. The T2K Experiment. *Nucl. Instrum. Meth.*, A659:106–135, 2011.

[47] F. P. An et al. Observation of electron-antineutrino disappearance at Daya Bay. *Phys. Rev. Lett.*, 108:171803, 2012.

[48] F. Reines and C. L. Cowan. Detection of the free neutrino. *Phys. Rev.*, 92:830–831, 1953.

[49] G. Danby, J. M. Gaillard, Konstantin A. Goulianos, L. M. Lederman, Nari B. Mistry, M. Schwartz, and J. Steinberger. Observation of High-Energy Neutrino Reactions and the Existence of Two Kinds of Neutrinos. *Phys. Rev. Lett.*, 9:36–44, 1962.

[50] K. Kodama et al. Observation of tau neutrino interactions. *Phys. Lett.*, B504:218–224, 2001.

[51] C. S. Wu, E. Ambler, R. W. Hayward, D. D. Hoppes, and R. P. Hudson. Experimental Test of Parity Conservation in Beta Decay. *Phys. Rev.*, 105:1413–1414, 1957.

[52] Q. R. Ahmad et al. Direct evidence for neutrino flavor transformation from neutral current interactions in the Sudbury Neutrino Observatory. *Phys. Rev. Lett.*, 89:011301, 2002.

[53] Y. Fukuda et al. Evidence for oscillation of atmospheric neutrinos. *Phys. Rev. Lett.*, 81:1562–1567, 1998.

[54] Ivan Esteban, M. C. Gonzalez-Garcia, Michele Maltoni, Ivan Martinez-Soler, and Thomas Schwetz. Updated fit to three neutrino mixing: exploring the accelerator-reactor complementarity. *JHEP*, 01:087, 2017.

[55] P. Adamson et al. Combined analysis of ν_μ disappearance and $\nu_\mu \to \nu_e$ appearance in MINOS using accelerator and atmospheric neutrinos. *Phys. Rev. Lett.*, 112:191801, 2014.

[56] N. Agafonova et al. Discovery of τ Neutrino Appearance in the CNGS Neutrino Beam with the OPERA Experiment. *Phys. Rev. Lett.*, 115(12):121802, 2015.

[57] K. Abe et al. Measurements of neutrino oscillation in appearance and disappearance channels by the T2K experiment with 6.6×10^{20} protons on target. *Phys. Rev.*, D91(7):072010, 2015.

[58] P. Adamson et al. Measurement of the neutrino mixing angle θ_{23} in NOvA. *Phys. Rev. Lett.*, 118(15):151802, 2017.

[59] J. K. Ahn et al. Observation of Reactor Electron Antineutrino Disappearance in the RENO Experiment. *Phys. Rev. Lett.*, 108:191802, 2012.

[60] Y. Abe et al. Reactor electron antineutrino disappearance in the Double Chooz experiment. *Phys. Rev.*, D86:052008, 2012.

[61] D. N. Spergel et al. First year Wilkinson Microwave Anisotropy Probe (WMAP) observations: Determination of cosmological parameters. *Astrophys. J. Suppl.*, 148:175–194, 2003.

[62] Massimiliano Lattanzi. Planck 2015 constraints on neutrino physics. *Journal of Physics: Conference Series*, 718(3):032008, 2016.

[63] Nathalie Palanque-Delabrouille et al. Neutrino masses and cosmology with Lyman-alpha forest power spectrum. *JCAP*, 1511(11):011, 2015.

[64] C. E. Aalseth et al. The IGEX Ge-76 neutrinoless double beta decay experiment: Prospects for next generation experiments. *Phys. Rev.*, D65:092007, 2002.

[65] M. Agostini et al. Results on Neutrinoless Double-β Decay of ^{76}Ge from Phase I of the GERDA Experiment. *Phys. Rev. Lett.*, 111(12):122503, 2013.

[66] Takehiko Asaka and Mikhail Shaposhnikov. The nuMSM, dark matter and baryon asymmetry of the universe. *Phys. Lett.*, B620:17–26, 2005.

[67] Takehiko Asaka, Steve Blanchet, and Mikhail Shaposhnikov. The nuMSM, dark matter and neutrino masses. *Phys. Lett.*, B631:151–156, 2005.

[68] Murray Gell-Mann, Pierre Ramond, and Richard Slansky. Complex Spinors and Unified Theories. *Conf. Proc.*, C790927:315–321, 1979.

[69] Rabindra N. Mohapatra and Goran Senjanovic. Neutrino mass and spontaneous parity violation. *Phys. Rev. Lett.*, 44:912, 1980.

[70] R. N. Mohapatra and Jogesh C. Pati. A Natural Left-Right Symmetry. *Phys. Rev.*, D11:2558, 1975.

[71] Wai-Yee Keung and Goran Senjanovic. Majorana Neutrinos and the Production of the Right-handed Charged Gauge Boson. *Phys. Rev. Lett.*, 50:1427, 1983.

[72] Alessio Maiezza, Miha Nemevsek, Fabrizio Nesti, and Goran Senjanovic. Left-Right Symmetry at LHC. *Phys. Rev.*, D82:055022, 2010.

[73] Jogesh C. Pati and Abdus Salam. Lepton Number as the Fourth Color. *Phys. Rev.*, D10:275–289, 1974. [Erratum: Phys. Rev.D11,703(1975)].

[74] G. Senjanovic and Rabindra N. Mohapatra. Exact Left-Right Symmetry and Spontaneous Violation of Parity. *Phys. Rev.*, D12:1502, 1975.

[75] Goran Senjanovic. Spontaneous Breakdown of Parity in a Class of Gauge Theories. *Nucl. Phys.*, B153:334–364, 1979.

[76] Rabindra N. Mohapatra and Goran Senjanović. Neutrino mass and spontaneous parity nonconservation. *Phys. Rev. Lett.*, 44:912–915, Apr 1980.

[77] Victor Mukhamedovich Abazov et al. Evidence for an anomalous like-sign dimuon charge asymmetry. *Phys. Rev.*, D82:032001, 2010.

[78] Yosef Nir. CP violation in and beyond the standard model. In *Proceedings, 27th SLAC Summer Institute on Particle Physics: CP Violation in and Beyond the Standard Model (SSI 99): Stanford, USA, July 7-16, 1999*, pages 165–243, 1999.

[79] J. Chakrabortty, J. Gluza, T. Jelinski, and T. Srivastava. Theoretical constraints on masses of heavy particles in Left-Right Symmetric Models. *Phys. Lett.*, B759:361–368, 2016.

[80] Yue Zhang, Haipeng An, Xiangdong Ji, and Rabindra N. Mohapatra. General CP Violation in Minimal Left-Right Symmetric Model and Constraints on the Right-Handed Scale. *Nucl. Phys.*, B802:247–279, 2008.

[81] CMS Collaboration. Measurement of the production cross section for pp to Z(nu nu) gamma at sqrt(s) = 13 TeV at CMS. 2016.

[82] Vardan Khachatryan et al. Searches for invisible decays of the Higgs boson in pp collisions at $\sqrt{s} = 7$, 8, and 13 TeV. *JHEP*, 02:135, 2017.

[83] Roberto Contino. Z', Z_{KK}, Z^* and all that: Current bounds and theoretical prejudices on heavy neutral vector bosons. *Nuovo Cim.*, B123:511–515, 2008.

[84] Albert M Sirunyan et al. Search for high-mass resonances in dilepton final states in proton-proton collisions at $\sqrt{s} = 13$ TeV. 2018.

[85] Morad Aaboud et al. Search for new high-mass phenomena in the dilepton final state using 36 fb^{-1} of proton-proton collision data at $\sqrt{s} = 13$ TeV with the ATLAS detector. *JHEP*, 10:182, 2017.

[86] Serguei Chatrchyan et al. Search for heavy neutrinos and W[R] bosons with right-handed couplings in a left-right symmetric model in pp collisions at sqrt(s) = 7 TeV. *Phys. Rev. Lett.*, 109:261802, 2012.

[87] Vardan Khachatryan et al. Search for heavy neutrinos and W bosons with right-handed couplings in proton-proton collisions at $\sqrt{s} = 8\,\text{TeV}$. *Eur. Phys. J.*, C74(11):3149, 2014.

[88] Search for heavy neutrinos and W bosons with right handed couplings in proton-proton collisions at $\sqrt{s} = 13$ TeV. Technical Report CMS-PAS-EXO-16-045, CERN, Geneva, 2017.

[89] Georges Aad et al. Search for heavy neutrinos and right-handed W bosons in events with two leptons and jets in pp collisions at $\sqrt{s} = 7$ TeV with the ATLAS detector. *Eur. Phys. J.*, C72:2056, 2012.

[90] Georges Aad et al. Search for heavy Majorana neutrinos with the ATLAS detector in pp collisions at $\sqrt{s} = 8$ TeV. *JHEP*, 07:162, 2015.

[91] Oliver S. Bruning, P. Collier, P. Lebrun, S. Myers, R. Ostojic, et al. LHC Design Report. 1. The LHC Main Ring. 2004.

[92] Lyndon Evans and Philip Bryant. LHC Machine. *JINST*, 3:S08001, 2008.

[93] S. Chatrchyan et al. The CMS Experiment at the CERN LHC. *JINST*, 3:S08004, 2008.

[94] G. Aad et al. The ATLAS Experiment at the CERN Large Hadron Collider. *JINST*, 3:S08003, 2008.

[95] W.J. Stirling. Parton luminosity and cross section plots. *Private communication*, 2016.

[96] G. Apollinari, I. Béjar Alonso, O. Brüning, M. Lamont, and L. Rossi. *High-Luminosity Large Hadron Collider (HL-LHC): Preliminary Design Report.* CERN Yellow Reports: Monographs. CERN, Geneva, 2015.

[97] CMS, the Compact Muon Solenoid: Technical proposal. 1994.

[98] CMS Collaboration. CMS, tracker technical design report. 1998.

[99] Serguei Chatrchyan et al. Performance of CMS muon reconstruction in pp collision events at $\sqrt{s} = 7$ TeV. *JINST*, 7:P10002, 2012.

[100] CMS: The electromagnetic calorimeter. Technical design report. 1997.

[101] CMS: The hadron calorimeter technical design report. 1997.

[102] Victor Daniel Elvira. Measurement of the Pion Energy Response and Resolution in the CMS HCAL Test Beam 2002 Experiment. 2004.

[103] *The CMS muon project: Technical Design Report.* Technical Design Report CMS. CERN, Geneva, 1997.

[104] S. Dasu et al. CMS. The TriDAS project. Technical design report, vol. 1: The trigger systems. 2000.

[105] B. Kreis et al. Run 2 Upgrades to the CMS Level-1 Calorimeter Trigger. *JINST*, 11(01):C01051, 2016.

[106] P. Sphicas. CMS: The TriDAS project. Technical design report, Vol. 2: Data acquisition and high-level trigger. 2002.

[107] A. M. Sirunyan et al. Particle-flow reconstruction and global event description with the CMS detector. *JINST*, 12(10):P10003, 2017.

[108] Commissioning of the Particle-flow Event Reconstruction with the first LHC collisions recorded in the CMS detector. 2010.

[109] Serguei Chatrchyan et al. Description and performance of track and primary-vertex reconstruction with the CMS tracker. *JINST*, 9(10):P10009, 2014.

[110] Pierre Billoir. Progressive track recognition with a Kalman like fitting procedure. *Comput. Phys. Commun.*, 57:390–394, 1989.

[111] Pierre Billoir and S. Qian. Simultaneous pattern recognition and track fitting by the Kalman filtering method. *Nucl. Instrum. Meth.*, A294:219–228, 1990.

[112] A. Strandlie and W. Wittek. Propagation of covariance matrices of track parameters in homogeneous magnetic fields in CMS. 2006.

[113] Jan Myrheim and Lars Bugge. A fast runge-kutta method for fitting tracks in a magnetic field. *Nuclear Instruments and Methods*, 160(1):43 – 48, 1979.

[114] D Contardo, M Klute, J Mans, L Silvestris, and J Butler. Technical Proposal for the Phase-II Upgrade of the CMS Detector. Technical Report CERN-LHCC-2015-010. LHCC-P-008. CMS-TDR-15-02, Geneva, Jun 2015. Upgrade Project Leader

Deputies: Lucia Silvestris (INFN-Bari), Jeremy Mans (University of Minnesota) Additional contacts: Lucia.Silvestris@cern.ch, Jeremy.Mans@cern.ch.

[115] CMS Collaboration. The Phase-2 Upgrade of the CMS Tracker. Technical Report CERN-LHCC-2017-009. CMS-TDR-014, CERN, Geneva, Jun 2017.

[116] CMS Collaboration. The Phase-2 Upgrade of the CMS L1 Trigger Interim Technical Design Report. Technical Report CERN-LHCC-2017-013. CMS-TDR-017, CERN, Geneva, Sep 2017. This is the CMS Interim TDR devoted to the upgrade of the CMS L1 trigger in view of the HL-LHC running, as approved by the LHCC.

[117] CMS Collaboration. The Phase-2 Upgrade of the CMS Barrel Calorimeters Technical Design Report. Technical Report CERN-LHCC-2017-011. CMS-TDR-015, CERN, Geneva, Sep 2017. This is the final version, approved by the LHCC.

[118] CMS Collaboration. The Phase-2 Upgrade of the CMS Endcap Calorimeter. Technical Report CERN-LHCC-2017-023. CMS-TDR-019, CERN, Geneva, Nov 2017. Technical Design Report of the endcap calorimeter for the Phase-2 upgrade of the CMS experiment, in view of the HL-LHC run.

[119] CMS Collaboration. The Phase-2 Upgrade of the CMS Muon Detectors. Technical Report CERN-LHCC-2017-012. CMS-TDR-016, CERN, Geneva, Sep 2017. This is the final version, approved by the LHCC.

[120] CMS Collaboration. TECHNICAL PROPOSAL FOR A MIP TIMING DETECTOR IN THE CMS EXPERIMENT PHASE 2 UPGRADE. Technical Report CERN-LHCC-2017-027. LHCC-P-009, CERN, Geneva, Dec 2017. This document describes a MIP timing detector for the Phase-2 upgrade of the CMS experiment, in view of HL-LHC running.

[121] Vardan Khachatryan et al. Observation of the diphoton decay of the Higgs boson and measurement of its properties. *Eur. Phys. J.*, C74(10):3076, 2014.

[122] Vardan Khachatryan et al. Search for narrow resonances in dilepton mass spectra in proton-proton collisions at $\sqrt{s} = 13$ TeV and combination with 8 TeV data. *Phys. Lett.*, B768:57–80, 2017.

[123] Vardan Khachatryan et al. Measurement of the ZZ production cross section and $Z \to \ell^+\ell^-\ell'^+\ell'^-$ branching fraction in pp collisions at $\sqrt{s}$=13 TeV. *Phys. Lett.*, B763:280–303, 2016. [Erratum: Phys. Lett.B772,884(2017)].

[124] A. M. Magnan. HGCAL: a High-Granularity Calorimeter for the endcaps of CMS at HL-LHC. *JINST*, 12(01):C01042, 2017.

[125] Z. Antunovic, I. Britvitch, K. Deiters, N. Godinovic, Q. Ingram, A. Kuznetsov, Y. Musienko, I. Puljak, D. Renker, S. Reucroft, R. Rusack, T. Sakhelashvili, A. Singovski, I. Soric, and J. Swain. Radiation hard avalanche photodiodes for the cms detector. *Nuclear Instruments and Methods in Physics Research Section A: Accelerators, Spectrometers, Detectors and Associated Equipment*, 537(1):379 – 382, 2005. Proceedings of the 7th International Conference on Inorganic Scintillators and their Use in Scientific adn Industrial Applications.

[126] S Michelis, B Allongue, G Blanchot, F Faccio, C Fuentes, S Orlandi, S Saggini, S Cengarle, and F Ongaro. Dc-dc converters in 0.35μm cmos technology. *Journal of Instrumentation*, 7(01):C01072, 2012.

[127] S. Baccaro et al. Radiation damage effect on avalanche photodiodes. *Nucl. Instrum. Meth.*, A426:206–211, 1999.

[128] P. Adzic et al. Energy resolution of the barrel of the CMS electromagnetic calorimeter. *JINST*, 2:P04004, 2007.

[129] Joshua Berger, Jeff Asaf Dror, and Wee Hao Ng. Sneutrino Higgs models explain lepton non-universality in $eejj, e\nu jj$ excesses. *JHEP*, 09:156, 2015.

[130] Arindam Das, Natsumi Nagata, and Nobuchika Okada. Testing the 2-TeV Resonance with Trileptons. *JHEP*, 03:049, 2016.

[131] P. S. Bhupal Dev, Chang-Hun Lee, and R. N. Mohapatra. Leptogenesis Constraints on the Mass of Right-handed Gauge Bosons. *Phys. Rev.*, D90(9):095012, 2014.

[132] Jack H Collins and Wee Hao Ng. A 2TeV W_R , supersymmetry, and the Higgs mass. *JHEP*, 01:159, 2016.

[133] Bogdan A. Dobrescu and Zhen Liu. W' Boson near 2 TeV: Predictions for Run 2 of the LHC. *Phys. Rev. Lett.*, 115(21):211802, 2015.

[134] Bogdan A. Dobrescu and Patrick J. Fox. Signals of a 2 TeV W' boson and a heavier Z' boson. *JHEP*, 05:047, 2016.

[135] Paramita Adhya, D. Rai Chaudhuri, and Amitava Raychaudhuri. Decay and decoupling of heavy right-handed Majorana neutrinos in the L-R model. *Eur. Phys. J. C*, 19:183, 2001.

[136] P. S. Bhupal Dev, Rabindra N. Mohapatra, and Yongchao Zhang. Heavy right-handed neutrino dark matter in left-right models. *Mod. Phys. Lett. A*, 32:1740007, 2017.

[137] Arindam Das, P. S. Bhupal Dev, and Rabindra N. Mohapatra. Same sign versus opposite sign dileptons as a probe of low scale seesaw mechanisms. *Phys. Rev. D*, 97:015018, 2018.

[138] S. Agostinelli et al. GEANT4—a simulation toolkit. *Nucl. Instrum. Meth. A*, 506:250, 2003.

[139] Torbjörn Sjöstrand, Stefan Ask, Jesper R. Christiansen, Richard Corke, Nishita Desai, Philip Ilten, Stephen Mrenna, Stefan Prestel, Christine O. Rasmussen, and Peter Z. Skands. An introduction to PYTHIA 8.2. *Comput. Phys. Commun.*, 191:159, 2015.

[140] Richard D. Ball et al. Parton distributions with LHC data. *Nucl. Phys. B*, 867:244, 2013.

[141] J. Alwall, R. Frederix, S. Frixione, V. Hirschi, F. Maltoni, O. Mattelaer, H. S. Shao, T. Stelzer, P. Torrielli, and M. Zaro. The automated computation of tree-level and next-to-leading order differential cross sections, and their matching to parton shower simulations. *JHEP*, 07:079, 2014.

[142] Richard D. Ball et al. Parton distributions for the LHC run II. *JHEP*, 04:040, 2015.

[143] Paolo Nason. A new method for combining NLO QCD with shower Monte Carlo algorithms. *JHEP*, 11:040, 2004.

[144] Stefano Frixione, Paolo Nason, and Carlo Oleari. Matching NLO QCD computations with Parton Shower simulations: the POWHEG method. *JHEP*, 11:070, 2007.

[145] Simone Alioli, Paolo Nason, Carlo Oleari, and Emanuele Re. A general framework for implementing NLO calculations in shower Monte Carlo programs: the POWHEG BOX. *JHEP*, 06:043, 2010.

[146] Emanuele Re. Single-top Wt-channel production matched with parton showers using the POWHEG method. *Eur. Phys. J. C*, 71:1547, 2011.

[147] Vardan Khachatryan et al. Event generator tunes obtained from underlying event and multiparton scattering measurements. *Eur. Phys. J.*, C76(3):155, 2016.

[148] J. Alwall, S. Höche, F. Krauss, N. Lavesson, L. Lönnblad, F. Maltoni, M. L. Mangano, M. Moretti, C. G. Papadopoulos, F. Piccinini, S. Schumann, M. Treccani, J. Winter, and M. Worek. Comparative study of various algorithms for the merging of parton showers and matrix elements in hadronic collisions. *Eur. Phys. J. C*, 53:473, 2008.

[149] Rikkert Frederix and Stefano Frixione. Merging meets matching in MC@NLO. *JHEP*, 12:061, 2012.

[150] Stan Bentvelsen and Irmtraud Meyer. The Cambridge jet algorithm: Features and applications. *Eur. Phys. J.*, C4:623–629, 1998.

[151] Matteo Cacciari, Gavin P. Salam, and Gregory Soyez. The anti-k_t jet clustering algorithm. *JHEP*, 04:063, 2008.

[152] Particle-Flow Event Reconstruction in CMS and Performance for Jets, Taus, and MET. 2009.

[153] Commissioning of the Particle-Flow reconstruction in Minimum-Bias and Jet Events from pp Collisions at 7 TeV. 2010.

[154] Matteo Cacciari and Gavin P. Salam. Pileup subtraction using jet areas. *Phys. Lett. B*, 659:119, 2008.

[155] Jet algorithms performance in 13 TeV data. Technical Report CMS-PAS-JME-16-003, CERN, Geneva, 2017.

[156] Jet Performance in pp Collisions at 7 TeV. 2010.

[157] Vardan Khachatryan et al. Jet energy scale and resolution in the CMS experiment in pp collisions at 8 TeV. *JINST*, 12(02):P02014, 2017.

[158] Vardan Khachatryan et al. Performance of Electron Reconstruction and Selection with the CMS Detector in Proton-Proton Collisions at $\sqrt{s} = 8$ TeV. *JINST*, 10(06):P06005, 2015.

[159] Wolfgang Adam, R. Frühwirth, Are Strandlie, and T. Todor. Reconstruction of Electrons with the Gaussian-Sum Filter in the CMS Tracker at the LHC. 2005.

[160] Andreas Hocker et al. TMVA - Toolkit for Multivariate Data Analysis. *PoS*, ACAT:040, 2007.

[161] A. Bodek, A. van Dyne, J. Y. Han, W. Sakumoto, and A. Strelnikov. Extracting Muon Momentum Scale Corrections for Hadron Collider Experiments. *Eur. Phys. J.*, C72:2194, 2012.

[162] Albert M Sirunyan et al. Search for new physics in final states with an energetic jet or a hadronically decaying W or Z boson and transverse momentum imbalance at $\sqrt{s} = 13$ TeV. 2017.

[163] J. M. Lindert et al. Precise predictions for V+jets dark matter backgrounds. 2017.

[164] Giovanni Punzi. Sensitivity of searches for new signals and its optimization. *eConf*, C030908:MODT002, 2003. [,79(2003)].

[165] Vardan Khachatryan et al. Performance of Photon Reconstruction and Identification with the CMS Detector in Proton-Proton Collisions at sqrt(s) = 8 TeV. *JINST*, 10(08):P08010, 2015.

[166] PDF4LHC Working Group. PDF4LHC recommendations. 2011.

[167] CMS Luminosity Measurements for the 2016 Data Taking Period. Technical Report CMS-PAS-LUM-17-001, CERN, Geneva, 2017.

[168] ATLAS and CMS Collaborations. Procedure for the LHC Higgs boson search combination in summer 2011. Technical Report CMS-NOTE-2011-005, ATL-PHYS-PUB-2011-11, 2011.

[169] Albert M Sirunyan et al. Search for a heavy right-handed W boson and a heavy neutrino in events with two same-flavor leptons and two jets at $\sqrt{s} = 13$ TeV. *JHEP*, 05(05):148, 2018.

[170] Albert M Sirunyan et al. Search for heavy neutral leptons in events with three charged leptons in proton-proton collisions at $\sqrt{s} = 13$ TeV. *Phys. Rev. Lett.*, 120(22):221801, 2018.

[171] Search for heavy Majorana neutrinos in the same-sign dilepton channel in proton-proton collisions at sqrt(s) = 13 TeV. Technical Report CMS-PAS-EXO-17-028, CERN, Geneva, 2018.

[172] Search for heavy neutrinos and third-generation leptoquarks in final states with two hadronically decaying τ leptons and two jets in proton-proton collisions at $\sqrt{s} = 13$ TeV. Technical Report CMS-PAS-EXO-17-016, CERN, Geneva, 2018.

[173] A. Di Crescenzoon. The SHiP experiment at CERN SPS. *Nuovo Cim.*, C39(1):226, 2016.

[174] Eduardo Cortina Gil et al. Search for heavy neutral lepton production in K^+ decays. *Phys. Lett.*, B778:137–145, 2018.

[175] Marco Drewes, Jan Hajer, Juraj Klaric, and Gaia Lanfranchi. NA62 sensitivity to heavy neutral leptons in the low scale seesaw model. 2018.

[176] Juan Carlos Helo, Martin Hirsch, and Zeren Simon Wang. Heavy neutral fermions at the high-luminosity LHC. 2018.

[177] Felix Kling and Sebastian Trojanowski. Heavy Neutral Leptons at FASER. *Phys. Rev.*, D97(9):095016, 2018.

[178] Salim Ogur, A. Barnyakov, K. Furukawa, N. Iida, A. Levichev, F. Miyahara, D. Nikiforov, K. Oide, Y. Papaphilippou, and F. Zimmermann. Preliminary design of FCC-ee pre-injector complex. *J. Phys. Conf. Ser.*, 874(1):012003, 2017. [,TUPAB014(2017)].

[179] Stefan Antusch, Eros Cazzato, Marco Drewes, Oliver Fischer, Bjorn Garbrecht, Dario Gueter, and Juraj Klaric. Probing Leptogenesis at Future Colliders. 2017.

[180] Stefan Antusch, Eros Cazzato, Marco Drewes, Oliver Fischer, Björn Garbrecht, Dario Gueter, and Juraj Klaric. Probing the Seesaw Mechanism and Leptogenesis with the International Linear Collider. In *International Workshop on Future Linear Collider (LCWS2017) Strasbourg, France, October 23-27, 2017*, 2018.

[181] Marco Drewes and Shintaro Eijima. Neutrinoless double β decay and low scale leptogenesis. *Phys. Lett.*, B763:72–79, 2016.

[182] Frank F. Deppisch, P. S. Bhupal Dev, and Apostolos Pilaftsis. Neutrinos and Collider Physics. *New J. Phys.*, 17(7):075019, 2015.

[183] Alain Blondel, E. Graverini, N. Serra, and M. Shaposhnikov. Search for Heavy Right Handed Neutrinos at the FCC-ee. *Nucl. Part. Phys. Proc.*, 273-275:1883–1890, 2016.

[184] Annarita Buonaura. The SHiP experiment and its detector for neutrino physics. (CERN-SHiP-PROC-2016-002), Feb 2016.

[185] G. De Lellis. Search for hidden particles: a new experiment proposal. *Nuclear and Particle Physics Proceedings*, 265-266:165 – 170, 2015. Proceedings of the Neutrino Oscillation Workshop.

[186] John Paul Chou, David Curtin, and H. J. Lubatti. New Detectors to Explore the Lifetime Frontier. *Phys. Lett.*, B767:29–36, 2017.

[187] Jonathan L. Feng, Iftah Galon, Felix Kling, and Sebastian Trojanowski. ForwArd Search ExpeRiment at the LHC. *Phys. Rev.*, D97(3):035001, 2018.

[188] Vladimir V. Gligorov, Simon Knapen, Michele Papucci, and Dean J. Robinson. Searching for Long-lived Particles: A Compact Detector for Exotics at LHCb. *Phys. Rev.*, D97(1):015023, 2018.

[189] C. Adams et al. The Long-Baseline Neutrino Experiment: Exploring Fundamental Symmetries of the Universe. 2013.

[190] A Liss and J Nielsen. Physics at a High-Luminosity LHC with ATLAS. Technical Report ATL-PHYS-PUB-2013-007, CERN, Geneva, Jul 2013.

[191] Estimated Sensitivity for New Particle Searches at the HL-LHC. Technical Report CMS-PAS-FTR-16-005, CERN, Geneva, 2017.

[192] K. Hoepfner. Updated Projections for BSM Studies. *ECFA HL-LHC Workshop*, October 2016.

[193] Search for heavy composite Majorana neutrinos at the High-Luminosity LHC. Technical Report CMS-PAS-FTR-18-006, CERN, Geneva, 2018.

[194] R. Leonardi, L. Alunni, F. Romeo, L. Fanò, and O. Panella. Hunting for heavy composite Majorana neutrinos at the LHC. *Eur. Phys. J.*, C76(11):593, 2016.

[195] A. M. Sirunyan et al. Search for a heavy composite Majorana neutrino in the final state with two leptons and two quarks at $\sqrt{s} = 13$ TeV. *Phys. Lett.*, B775:315–337, 2017.

[196] J. de Favereau, C. Delaere, P. Demin, A. Giammanco, V. Lemaître, A. Mertens, and M. Selvaggi. DELPHES 3, A modular framework for fast simulation of a generic collider experiment. *JHEP*, 02:057, 2014.

[197] Stefan Antusch, Eros Cazzato, and Oliver Fischer. Sterile neutrino searches at future e^-e^+, pp, and e^-p colliders. *Int. J. Mod. Phys.*, A32(14):1750078, 2017.

[198] Stefan Antusch, Eros Cazzato, and Oliver Fischer. Heavy neutrino-antineutrino oscillations at colliders. 2017.

[199] Barry Barish and James E. Brau. The International Linear Collider. *Int. J. Mod. Phys.*, A28(27):1330039, 2013.

[200] Chong-Xing Yue, Yu-Chen Guo, and Zhen-Hua Zhao. Majorana neutrino signals at Belle-II and ILC. *Nucl. Phys.*, B925:186–194, 2017.

[201] Arindam Das and Nobuchika Okada. Inverse seesaw neutrino signatures at the LHC and ILC. *Phys. Rev.*, D88:113001, 2013.

université PARIS-SACLAY | ÉCOLE DOCTORALE PHENIICS

Titre : Recherche de neutrinos lourds dans l'expérience CMS et études pour l'amélioration de son calorimètre électromagnétique

Mots-clés : *neutrinos lourds, CMS, LHC, calorimètre électromagnétique, upgrade*

Résumé : Dans cette thèse, la recherche de neutrinos lourds droitiers à travers la désintégration d'un boson W droitier (W_R) en deux leptons et deux jets avec l'expérience CMS au Grand Collisionneur de Hadrons (LHC) est présentée. Le boson W_R se désintègre en un lepton et un neutrino massif (N_R), et le neutrino se désintègre en un autre lepton de la même saveur et en une paire de jets. Les données recueillies par l'expérience CMS dans les collisions proton-proton à 13 TeV en 2016 correspondant à une luminosité totale intégrée de 35.9 fb^{-1} ont été utilisés pour cette analyse. Ces neutrinos lourds manquent dans le Modèle Standard (SM) de la physique des particules et ils sont donc importants pour faire la lumière sur la physique au-delà du SM. Mes principales contributions ont été la simulation et la validation des échantillons de signaux, l'estimation de l'un des principaux bruit de fonds, la production des limites 1D et 2D sur la section transversale du W_R (en fonction de la masse du W_R et de la masse du W_R par rapport à la masse du N_R), et l'analyse statistique et systématique. Les résultats obtenus avec cette analyse donnent les limites les plus strictes à ce jour.

Des études pour l'amélioration du calorimètre électromagnétique de CMS pour la Phase II du LHC, qui prévoit un remplacement partiel de l'électronique dans le barrel, sont également présentés. Mes principales contributions ont été dans la préparation de l'installation et dans la prise de données des test beams réalisée à la ligne de faisceau H4 dans la zone SPS Nord du CERN, dont le but était d'étudier la performance du prototype pour les nouvelles Very-Front-End cartes (CATIA chips avec un ADC de 160 MHz), et dans l'étude des formes et bruit des signaux recueillis par une matrice de 5×5 cristaux pour calculer leur timing et leur résolution énergétique.

Le document commence par une introduction théorique sur le Modèle Standard et sur la physique au delà du Modèle Standard, en particulier sur les neutrinos lourds, suivi d'une description du détecteur CMS et de son calorimètre électromagnétique. Les études pour l'amélioration du calorimètre électromagnétique sont présentées dans un chapitre dédié, puis l'analyse sur la recherche de neutrinos lourds et un aperçu de la physique des neutrinos au LHC et autres expériences sont décrits.

Title : Search for heavy neutrinos with the CMS experiment and studies for the upgrade of its electromagnetic calorimeter

Keywords: *heavy neutrinos, CMS, LHC, electromagnetic calorimeter, upgrade*

Abstract: In this thesis, the search for heavy right-handed neutrinos through the decay of a right-handed W (W_R) boson into two leptons and two jets with the CMS experiment at the Large Hadron Collider is presented. The W_R boson decays into a lepton and a massive neutrino (N_R), and the neutrino decays into another lepton of the same flavor and into a pair of jets. The data collected by the CMS experiment in proton-proton collisions at 13 TeV during 2016 and corresponding to a total integrated luminosity of 35.9 fb^{-1} were used for this analysis. These heavy neutrinos are missing in the Standard Model (SM) of particle physics and thus they are important to shed light on physics beyond the SM. My main contributions were the simulation and validation of the signal samples, the estimation of one of the main backgrounds, the production of the 1D and 2D limits on the W_R cross section (as a function of the W_R mass and of the W_R mass versus N_R mass), and the systematics and statistical analysis. The results obtained with this analysis give the most stringent limits to date.

Studies on the upgrade of the CMS electromagnetic calorimeter for the LHC Phase II, that foresees a partial replacement of the electronics in the barrel, are also presented. My main contributions were in the preparation of the setup and in the data taking of test beams performed at the H4 beam line in the SPS North Area of CERN, whose goal was to study the performance of the prototype for the new Very-Front-End boards (CATIA chips with 160 MHz ADC), and in studying the shapes and noise of the signals collected by a matrix of 5×5 crystals calculating their timing and energy resolution.

The document starts with a theoretical introduction about the Standard Model and the physics beyond the Standard Model, in particular on heavy neutrinos, followed by a description of the CMS detector and its electromagnetic calorimeter. The upgrade studies on the electromagnetic calorimeter are presented in a dedicated chapter, then the analysis on the search for heavy neutrinos and an overview on the overall neutrino physics at the LHC and other experiments are described.

Université Paris-Saclay
Espace Technologique / Immeuble Discovery
Route de l'Orme aux Merisiers RD 128 / 91190, Saint-Aubin, France